High-precision ^{26}Al-^{26}Mg systematics of basaltic achondrites, chondrites and ultramafic achondrites

by

Martin Schiller

A thesis
submitted to Victoria University of Wellington
in fulfilment of the
requirements for the degree of
Doctor of Philosophy
in Earth Sciences.

Victoria University of Wellington
2010

Abstract

A precise and accurate chronology of events that shaped the early Solar System is crucial in understanding its formation. One of the high-resolution chronometers that can be used to establish a relative chronology is the short-lived ^{26}Al-to-^{26}Mg clock ($t_{1/2}$ = 0.73 Myr). This study developed new Mg chemical separation techniques for complex meteoritic matrices that produces Mg purities $>$ 99% with $>$ 99% yields. Mg was analysed by pseudo-high resolution multiple collector inductively coupled plasma mass spectrometry. These techniques make it possible to measure the mass-independent abundance of ^{26}Mg (δ^{26}Mg*) that is related to ^{26}Al decay to very high-precision ($\pm$ 0.0025 to 0.0050‰). These new techniques were then applied to three research objectives.

The first part of this study presents Mg isotope data for thirteen bulk basaltic achondrites from at least 3 different parent bodies, as well as mineral isochrons for the angrites Sahara 99555 and D'Orbingy and the ungrouped NWA 2976. Model ^{26}Al-^{26}Mg ages based on bulk rock δ^{26}Mg* excesses for basaltic magmatism range from 2.6-4.1 Myr, respectively, after formation of calcium-aluminium-rich inclusions (CAIs) and the mineral isochrons for the angrites Sahara 99555 and D'Orbigny, and the ungrouped NWA 2976 yield apparent crystallisation ages of $5.06^{+0.06}_{-0.05}$ Myr and $4.86^{+0.10}_{-0.09}$ Myr after CAI formation. The elevated initial δ^{26}Mg* of the mineral isochron of NWA 2976 (+0.0175 $\pm$ 0.0034‰) likely reflects thermal resetting during an impact event and slow cooling on its parent body. However, in the case of the angrites, the marginally elevated initial δ^{26}Mg* (+0.0068 $\pm$ 0.0058‰) could reflect δ^{26}Mg* in-growth in a magma

ocean prior to eruption and crystallisation or in an older igneous protolith with super-chondritic Al/Mg prior to impact melting and crystallisation of these angrites, or partial internal re-equilibration of Mg isotopes after crystallisation. ^{26}Al-^{26}Mg model ages and an olivine+pyroxene+whole rock isochron for the angrites Sahara 99555 and D'Orbigny are in good agreement with age constraints from ^{53}Mn-^{53}Cr and ^{182}Hf-^{182}W short-lived chronometers. This suggests that the ^{26}Al-^{26}Mg feldspar-controlled isochron ages for these angrites may be compromised by the partial re-setting of feldspar Mg isotope systematics. However, even the ^{26}Al-^{26}Mg angrite model ages cannot be reconciled with Pb-Pb ages for Sahara 99555/D'Orbigny and CAIs, which are ca. 1.0 Myr too old (angrites) or too young (CAIs) for reasons that are not clear. This discrepancy might indicate that ^{26}Al was markedly lower (ca. 40%) in the planetesimal- and planet-forming regions of the proto-planetary disk as compared to CAIs, or that CAI Pb-Pb ages may not accurately date CAI formation.

The second part of this thesis focuses on investigating the homogeneity of $(^{26}Al/^{27}Al)_0$ and Mg isotopes in the proto-planetary disk and to test the validity of the short-lived ^{26}Al-to-^{26}Mg chronometer applied to meteorites. Nineteen chondrites representing nearly all major chondrite classes were analysed, including a step-leaching experiment on the CM2 chondrite Murchison. δ^{26}Mg* variations in leachates of Murchison representing acid soluble material are $\leq$ 30 times smaller than reported for neutron-rich isotopes of Ti and Cr and do not reveal resolvable deficits in δ^{26}Mg* (-0.002 to +0.118‰). Very small variations in δ^{26}Mg* anomalies in bulk chondrites (-0.006 to +0.019‰) correlate with increasing $^{27}Al/^{24}Mg$ ratios and δ^{50}Ti, reflecting the variable presence of CAIs in some types of carbonaceous chondrites. Overall, the observed variations in δ^{26}Mg* are small and potential differences beyond those resulting from the presence of CAI-like material could not be detected. The results do not allow radical heterogeneity of ^{26}Al ($\geq \pm$ 30%) or measurable

Mg nucleosynthetic heterogeneity ($\geq \pm$ 0.005‰) to have existed on a planetesimal scale in the proto-planetary disk. The data imply that planets (i.e. chondrite parent bodies) accreted from material with initial $(^{26}Al/^{27}Al)_0$ in the range of 2.1 to 6.7 $\times$ 10^{-5}. The average stable Mg isotope composition of all analysed bulk chondrites is $\delta^{25}Mg_{DSM-3}$ = -0.152 $\pm$ 0.079‰ (2 sd) and is indistinguishable from that of Earth's mantle.

The third part of this study comprises a high-precision Mg isotope and mineral major and trace element study of 24 diogenites. Diogenites are ultramafic pyroxene and olivine cumulate rocks that are presumed to have resulted from magmatic differentiation on the howardite-eucrite-diogenite (HED) parent body. There are, however, no precise and independent age constraints on the formation of diogenites and, in particular, their age relationships to the basaltic eucrites. Mg isotope analysis of diogenites showed significant variability in δ^{26}Mg* anomalies that range from -0.0108 $\pm$ 0.0018 to +0.0128 $\pm$ 0.0018‰. These anomalies generally correlate with the mineral major and trace element chemistry and demonstrate active ^{26}Al decay during magmatic differentiation. Furthermore, it also suggests that diogenites are products of fractional crystallisation from a large scale magmatic system. Heating and melting of the HED parent body was driven by ^{26}Al decay and led to diogenite formation 0.7 to 1.3 Myr after CAIs depending on whether a heterogeneous or homogeneous $(^{26}Al/^{27}Al)_0$ distribution is assumed between the proto-planetary disk and CAIs. These data show that diogenite formation pre-dates eucrite formation and indicate HED parent body accretion and core formation occurred within the first Myr of the Solar System. The lifetime of the magmatic evolution is less well constrained. The data suggest that the complete range of diogenites may have formed as quickly as $\sim$ 0.2 Myr.

Acknowledgments

At the end of three years working on this project and five years of my life in New Zealand it has been mostly good times with a lot of great people. First of all, I would like to thank my main supervisor, Professor Joel Baker, who gave me the chance to conduct this study, supported me with never ending interest, and helped me in any regard necessary to get this project done in a successful way. I learned a lot since I arrived in New Zealand and much has been due to his support throughout my entire stay. Thanks Joel, most of the time it has been a true pleasure and you have become a good friend.

Thanks also to my co-supervisor Professor Martin Bizzarro for inviting me to spend half a year at Starplan in Copenhagen. It was great to finally have a chance to talk in person, get in contact with the Starplan group and use the great facilities. I am looking forward to continue this amazing opportunity.

Also my thanks to John Creech, Marc-Alban Millet, John Patterson and Monica R. Handler for their support in the laboratories at Victoria University, especially I am in debt to Monica for her invaluable comments on the final draft of this thesis. I also want to thank Warren Dickinson for his continued support and friendship following my MSc studies with him, Warren is probably the greatest friend I made in New Zealand and I will dearly miss my regular chocolate and tea in his office. At this place I also

like to thank all the people that I have met throughout my time at Victoria University, cheers to this big crowd of good friends.

I gratefully acknowledge the financial support of this project by the Marsden Fund and am thankful to NASA and Anton Irving for providing several meteorite samples for analysis.

Last, but most importantly, I want to thank my family for their continuous support and interest in my studies.

Contents

List of Figures

List of Tables

This doctoral thesis consists of 3 first-authored papers forming chapters 3 to 5, 2 co-authored papers and a synthesis. The papers forming chapters 3 to 5 are listed below:

1. Paper I: **^{26}Al-^{26}Mg dating of asteroidal magmatism in the young Solar System**, Schiller M., Baker J. A. & Bizzarro M., *Geochimica et Cosmochimica Acta*, in review.

2. Paper II: **High precision Mg isotopic systematics of bulk chondrites**, Schiller M., Handler M. R. & Baker J. A., *Earth and Planetary Science Letters*, in review.

3. Paper III: **Timing and mechanisms of the evolution of the magma ocean on the HED parent body**, Schiller M., Baker J. A., Bizzarro M., Creech J. & Irving A., in preparation for submission to Earth and Planetary Science Letters.

Chapter 1

Introduction

A general understanding of Solar System formation can be elucidated through astronomical observations and astrophysical models. Meteorites from asteroids, Mars and the Moon however, are the only samples which directly record the processes that occurred in the very early Solar System. Examining and measuring the physical, petrographic, chemical and isotopic properties of meteorites makes it possible to test and refine models for Solar System formation. A key piece of information for understanding the nature of planet-forming processes is the precise timing of both the formation of the precursor solids from which planetesimals and planets accreted, as well as of processes that occurred on the meteorite parent bodies themselves, such as core-mantle differentiation and asteroidal magmatism.

Some meteoritic materials such as calcium-aluminium-rich inclusions (CAIs) are favorably suited to precise dating using absolute chronometers such as the ^{207}Pb-^{206}Pb dating system due to their volatile depleted nature and, thus, high parent/daughter (U/Pb) ratios (e.g., Amelin et al., 2002). Unfortunately, with the exception of CAIs, chondrules, and some volatile-depleted basaltic meteorites (e.g., Amelin et al., 2002; Amelin, 2008a; Connelly et al., 2008a), many meteoritic materials cannot be absolutely dated to the necessary precision ($\leq$ 1 Myr) to be able to establish

a high resolution chronology of early Solar System processes. However, a number of short-lived isotope systems (e.g., ^{26}Al-^{26}Mg, ^{53}Mn-^{53}Cr, ^{129}I-^{129}Xe, ^{182}Hf-^{182}W) can be used to construct relative age information from meteorites and their constituents (e.g., Russell et al., 1996; Lugmair and Shukolyukov, 1998; Brazzle et al., 1999; Kleine et al., 2002). For example, the ^{182}Hf-^{182}W chronometer is ideally suited to dating the relative timing of metal-silicate segregation and thus core-mantle differentiation of planetesimals and planets (e.g., Kleine et al., 2005a).

The ^{26}Al-^{26}Mg decay system, which is the focus of this study, is particularly suited to tracking and potentially precisely dating silicate differentiation, such as crust formation on planetesimals, for three reasons. (1) Mg and Al are both abundant elements; (2) Mg and Al are fractionated strongly during magmatic differentiation processes and between different mineral phases in igneous meteorites, and (3) the short half-life of ^{26}Al ($\sim$0.73 Myr; Walker et al., 1989) makes it ideal for generating high-precision ages in the first few million years of the Solar System, when planetesimal accretion and differentiation is thought to have occurred (Kleine et al., 2002; Amelin, 2008b,a). Additionally, the former abundance and distribution of ^{26}Al is of particular interest as it is the only short-lived radionuclide that was apparently abundant enough to have driven planetesimal melting in the early Solar System (Urey, 1955).

In addition to providing a means to date early Solar System processes, the presence or absence of short-lived radionuclides and their homogeneity in early Solar System materials provides clues as to the astrophysical conditions under which our Solar System formed as the short life span of some of these isotopes requires the processes that formed them to have only shortly pre-dated Solar System formation. For example, the former existence of the short-lived isotope ^{10}Be ($t_{1/2}$ = 1.5 Myr) in CAIs of the Allende meteorite (McKeegan et al., 2000), which can only be produced through spallation reactions, demonstrates that some short-lived radionuclides were at least in part produced within or just prior to the formation

of the Solar System.

1.1 Objectives and structure of this thesis

This thesis is part of a project funded by a Royal Society of New Zealand Marsden grant to examine stellar nucleosynthetic inputs, solid formation and planet building in the first few million years of the Solar System using Mg and Ni isotopes in meteorites. The main focus of this thesis is a high-precision study of Mg isotopes in various meteoritic materials to 1) confirm small mass-independent ^{26}Mg (δ^{26}Mg*) anomalies in differentiated meteorites, (2) examine the former distribution of ^{26}Al/^{27}Al in the planet-forming region of the proto-planetary disk, and (3) understand the importance of ^{26}Al decay throughout early planetesimal silicate-silicate differentiation. In order to achieve this, a refined separation technique for Mg from meteoritic materials was developed that allows near complete purification of Mg from meteorites with high yields, along with improved pseudo-high resolution mass spectrometric techniques for measurement of Mg isotopes. Chapter 1 presents an introduction to current models of early Solar System formation and evolution, early Solar System chronology, and the importance and role of ^{26}Al in the early Solar System. It concludes with a discussion of meteorites as samples of the early Solar System, and specifically those classes studied here. The analytical protocols developed and used for this work are described and discussed in Chapter 2.

Chapter 3 applies these newly developed techniques to basaltic achondrites, some of which were previously studied by Bizzarro et al. (2005) and Baker et al. (2005). This work confirms the presence of small mass-independent ^{26}Mg anomalies that are related to the former presence of ^{26}Al in these meteorites and the elevated Al/Mg ratio of basaltic meteorites. Chapter 3 also demonstrates the limitations of ^{26}Al-^{26}Mg model ages (as used by Bizzarro et al., 2005; Baker et al., 2005), which use only

the bulk rock and an arbitrary Solar System initial composition to retrieve age information from the samples. This is because the model age approach does not consider the complex magmatic history of most achondrites, for example, protracted magma ocean evolution on planetesimals. In addition to the whole rock model ages, mineral isochrons for the angrites Sahara 99555 and D'Orbigny improve the precision of previously reported Mg isotope data for these meteorites and demonstrate the offset between model and isochron ages. A ^{26}Al-^{26}Mg mineral isochron age for the ungrouped achondrite NWA 2976 precisely dates this unusual meteorite and also has a resolvable excess in initial δ^{26}Mg* abundance, which in this case likely reflects later thermal resetting (Yamaguchi et al., 2002).

In Chapter 4 the focus of the work is on the distribution of ^{26}Al and mass-independent -dependent variations in Mg isotopes in bulk chondrites. Chondrites represent primitive, undifferentiated, Solar System material and may provide the best insights into the homogeneity or heterogeneity of ^{26}Al and Mg isotopes *on a planetesimal scale* in the chondrite- and planet-forming region of the proto-planetary disk. This information is valuable as it constrains the potential variability of ^{26}Al among different meteorite parent bodies. The results of this investigation demonstrate that, given the precision and accuracy of the mass-biased-corrected ^{26}Mg/^{24}Mg isotope measurements ($\sim$0.0050‰), there is only very limited mass-independent ^{26}Mg isotope variability among chondrites produced mainly by variable ^{27}Al/^{24}Mg ratios and not through ^{26}Al heterogeneity. However, because of the limitations in the analytical uncertainties and the large uncertainties of CAI isochrons at chondritic ^{27}Al/^{24}Mg ratios (e.g., Jacobsen et al., 2008) it is still possible that a significant difference in ^{26}Al exists between chondrites and CAIs, with the latter being routinely used to provide the best initial ^{26}Al abundance of the early Solar System.

Chapter 5 investigates the theoretical model of the evolution of mass-independent ^{26}Mg isotope variations in magma oceans on planetesimals developed in Chapter 3 by characterising a large number of diogenites

from the HED parent body for their chemical and Mg isotope compositions. Diogenites are ideally suited to providing a detailed record of the magmatic history of their parent body and of the Mg isotopic composition of their parental magma as these chemically diverse, cumulate, orthopyroxenite rocks span a wide compositional range of pyroxene (En = 85.3 to 65.4) (Mittlefehldt, 2007). The mineralogical change reflects changes in the composition of the parental magma(s) on the HED parent body and hence changes in the $^{27}Al/^{24}Mg$ ratio of the parent magma over time. These changes in mineralogy, combined with very precise Mg isotope measurements that were produced using newly developed MC-ICP-MS techniques that make the measurement of the mass independent ^{26}Mg abundance ($\delta 26Mg^*$) to less than 0.0025‰ possible (Bizzarro et al., 2010), demonstrate that the parent magmas of diogenites evolved rapidly while ^{26}Al was still extant in the early Solar System and constrain the timing and processes of earliest silicate differentiation on the HED parent body. Finally, Chapter 6 provides a brief synthesis of the main results of this study and their implications as well as some suggestions for future work.

1.2 Astrophysical environment of Solar System formation

1.2.1 Meteorites as samples of early Solar System evolution

Evidence of and understanding the astrophysical conditions and stages that led to the formation of our Solar System come from astronomical observations and astrophysical predictions. A likely evolutionary sequence of the formation of our Solar System is schematically shown in Figure 1.1. While astronomical observations and astrophysical models can predict how our Solar System might have formed and evolved, meteorites

and their constituents provide the only direct constraints on these models by providing:

1. Insights into the stellar nucleosynthetic inputs into the molecular cloud or earliest Solar System through isotopic study of the isotopic abundances of different elements in meteorites, including those produced by short-lived radionuclides (SLRs; $t_{1/2} < 100$ Myr) (e.g., Wasserburg et al., 2006).

2. Information about the chemical, physical, and thermodynamic properties at different locations within the proto-planetary disk through study of stable isotopic variations of elements (e.g., Clayton, 1993; Greenwood et al., 2005; Trinquier et al., 2009).

3. Timescales for formation of solids (CAIs and chondrules) and planetesimals and planets in the Solar System, as well as the differentiation and evolution of planetary objects (Halliday, 2003; McKeegan and Davis, 2007, and references therein).

Of particular importance are the decay products of SLRs in meteorites that reveal the former presence of these SLRs in the young Solar System, offering insights into the type of astrophysical environment in which our Sun and Solar System formed (Table 1.1). Although the former existence of a wide range of SLRs has been demonstrated (McKeegan and Davis, 2007), ^{10}Be, ^{26}Al and ^{60}Fe play a particularly important role in the understanding of Solar System formation. The isotopes of most elements in the Solar System, apart from hydrogen and helium, are the products of stars that formed and died prior to Solar System formation. A number of SLRs however, must have formed shortly prior to or after our Sun's birth and therefore yield information about the processes that occurred immediately prior to the formation of our Solar System and, potentially, within the proto-planetary disk.

It has been suggested that SLRs may have been formed by spallation reactions in the Sun's proto-planetary disk due to cosmic rays from solar

flares (Gounelle et al., 2001), or by nucleosynthesis in nearby stars and then injected into the formation environment of the Sun by supernovae or other means prior to or after the collapse of the molecular cloud (e.g., Ouellette et al., 2009). To address this question, various isotope systems have been studied. In particular, the ^{60}Fe-^{60}Ni system has been of recent focus, and the now established widespread existence of ^{60}Fe (Tachibana et al., 2006; Regelous et al., 2008; Dauphas et al., 2008) has been taken to be a strong indicator of supernova contribution to the SLR budget of the proto-planetary disk. However, the recently revised half-life of ^{60}Fe to 2.62 Myr (Rugel et al., 2009) and the abundance of ^{60}Fe in stellar objects point to the possibility that the ^{60}Fe abundance is related to the galactic background (Regelous et al., 2008; Gounelle and Meibom, 2008; Gounelle et al., 2009), which weakens the potential role of ^{60}Fe as a 'smoking gun' regarding the formation mechanism of the Solar System.

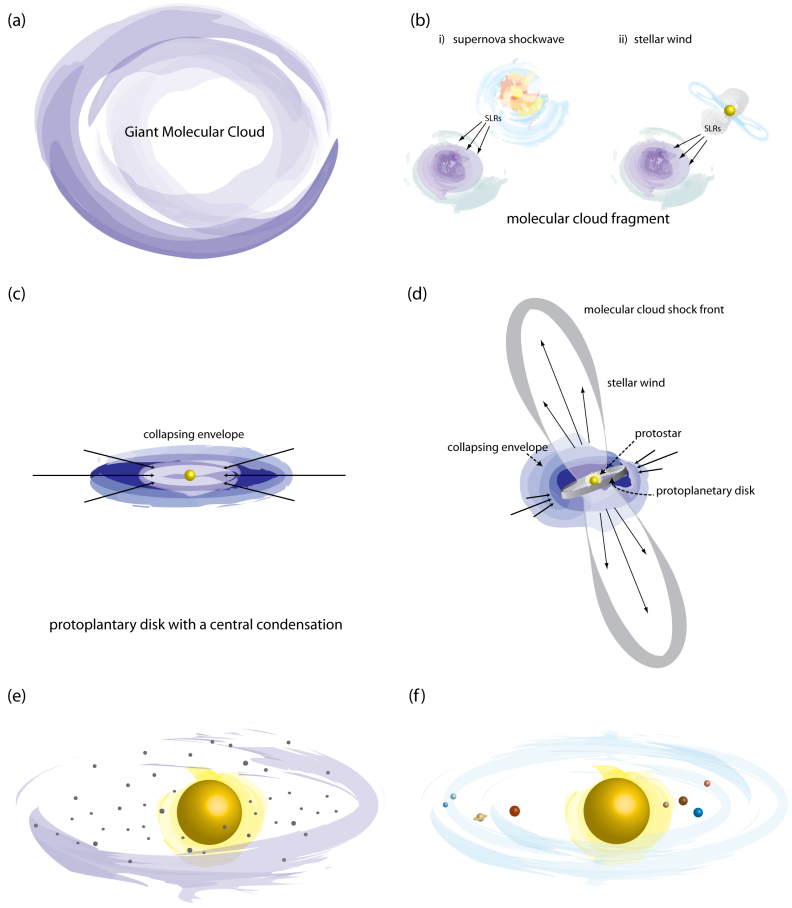

Figure 1.1: A simplified illustration of Solar System formation taken from Andrews (2009). a) A schematic of a giant molecular cloud in which smaller areas are dense enough to form cores. (b) A fragment of the molecular cloud is condensed through supernovae or stellar winds to become gravitationally instable, while other areas of the molecular cloud are dispersed by the same processes. Both supernovae and stellar winds can also introduce short lived radionuclides into the dense cloud core. (c) Through collapse a solar nebula forms, consisting of an accreting planetary disk and a central primitive star. (d) Mass now flows from the disk onto the growing proto-star. Bipolar jets of outflows are created along the system's axis of rotation. In the X-wind model short-lived radionuclide production occurs mainly in this stage. (e) The bipolar winds from the young star efficiently expel gas from the nebula, causing dust particles to settle to the midplane of the disk and allowing planetary accretion to begin. (f) A Solar System is formed.

Table 1.1: Short-lived radionuclides that have been demonstrated to have existed in Solar System materials. Table adapted from McKeegan and Davis (2007).

Fractionation[a]	Parent-daughter	Half-life[b]	Estimated initial solar system abundance	Objects found in	Ref.
Neb	^{7}Be-^{7}Li	53.1 days	10^{-3} ^{9}Be	CAIs	(1)
Neb	^{41}Ca-^{41}K	102 kyr	10^{-8} ^{40}Ca	CAIs	(2)
Plan	^{36}Cl-^{36}S,^{36}Ar	301 kyr	($\sim$4 $\times10^{-6}$) ^{35}Cl	CAIs, chondrites	(3)
Neb	^{26}Al-^{26}Mg	717 kyr	(5.21 $\times10^{-5}$) ^{27}Al	CAIs, chondrules, achondrite	(4)
Neb, Plan	^{60}Fe-^{60}Ni	2.52 Myr (15)	($\sim$5-10 $\times10^{-7}$) ^{56}Fe	Achondrites, chondrites	(6)
Neb	^{10}Be-^{10}B	1.51 Myr	($\sim$1.0 $\times10^{-3}$) ^{9}Be	CAIs	(5)
Neb, Plan	^{53}Mn-^{53}Cr	3.74 Myr	(1.0 $\times10^{-5}$) ^{55}Mn	CAIs, chondrules, carbonates, achondrites	(7)
Plan	^{107}Pd-^{107}Ag	6.5 Myr	($\sim$5 $\times10^{-5}$) ^{108}Pd	Iron meteorites, pallasites	(8)
Plan	^{182}Hf-^{182}W	8.90 Myr	(1.07 $\times10^{-4}$) ^{180}Hf	Planetary differentiates	(9)
Plan	^{129}I-^{129}Xe	15.7 Myr	10^{-4} ^{127}I	Chondrules, secondary minerals	(10)
Plan	^{205}Pb-^{205}Tl	17.3 Myr	($\sim$1-2 $\times10^{-4}$) ^{204}Pb	Iron meteorites	(11)
Plan	^{92}Nb-^{92}Zr	34.7 Myr	10^{-4} ^{93}Nb	Chondrites, mesosiderites	(12)
Plan	^{244}Pu - Fission products	80.0 Myr	(7 $\times10^{-3}$) ^{238}U	CAIs, chondrites	(13)
Plan	^{146}Sm-^{142}Nd	103 Myr	(9 $\times10^{-4}$) ^{147}Sm	Chondrites	(14)

References: (1) Chaussidon et al. (2006); (2) Srinivasan et al. (1994), Srinivasan et al. (1996); (3) Lin et al. (2005), Hsu et al. (2006); (4) (MacPherson et al., 1995), Jacobsen et al. (2008); (5) Chaussidon et al. (2006); (6) Mostefaoui et al. (2005), Tachibana et al. (2006); (7) Dauphas et al. (2005); (8) Chen and Wasserburg (1990); (9) Kleine et al. (2005a); (10) Jeffery and Reynolds (1961); (11) Nielsen et al. (2006); (12) Schönbachler et al. (2002); (13) Hudson et al. (1989); (14) Lugmair et al. (1983); (15) Rugel et al. (2009).

a Environment in which most significant parent-daughter fractionation processes occur.

b Half-lives from National Nuclear Data Center, Brookhaven National Laboratory (National Nuclear Data Center, 2006).

1.2.2 X-wind model

Based on observations of x-ray emissions of pulsating proto-stars, Shu et al. (1996, 1997) developed the "X-wind" model to explain the formation of chondrules and CAIs (Fig. 1.2). Because pre-main-sequence solar mass stars are likely to emit orders of magnitude more energy through X-ray emissions from solar flare activity than our current sun (Feigelson et al., 2002a), proton radiation from the early Sun may provide a source for early heated and volatile depleted objects such as CAIs and chondrules (Lee et al., 1998; McKeegan et al., 2000; Gounelle et al., 2001; Feigelson et al., 2002b; Leya et al., 2003) and may have contributed to the Solar System budget of SLRs during this stage. Strong support for this model came with the discovery of ^{10}Be in CAIs (McKeegan et al., 2000), which can only effectively be produced through cosmic ray induced spallation reactions such as predicted by the X-wind model for the CAI formation region. However, a significant shortcoming of this model is the special circumstances needed to balance the production of ^{53}Mn and ^{26}Al in CAIs (e.g., Gounelle et al., 2001). While it is likely that the general model correctly predicts events in the early Solar System and may even be the correct model for flash-melting of CAIs and for some SLR abundances (Feigelson et al., 2002b), its failure to adequately explain isotopic abundances of SLRs means that this process is unlikely to be the main source for at least some SLRs, particularly for the more recently discovered ^{60}Fe, which requires a supernova origin (Tachibana and Huss, 2003; Tachibana et al., 2006). The presence of ^{10}Be in CAIs has been proposed as providing a clear indicator of a local origin for the SLRs in our Solar System (e.g., McKeegan et al., 2000; Gounelle et al., 2001), but this conclusion has subsequently been questioned by Desch et al. (2004) who suggested that the majority of ^{10}Be in CAIs could have been produced by galactic cosmic rays in the molecular cloud prior to the formation of our Solar System. The apparent evidence for the former existence of very short-lived ^{7}Be ($t_{1/2}$ = 53.12 days) in CAIs (Chaussidon et al., 2006), however, also requires local production of ^{7}Be in the CAI-forming

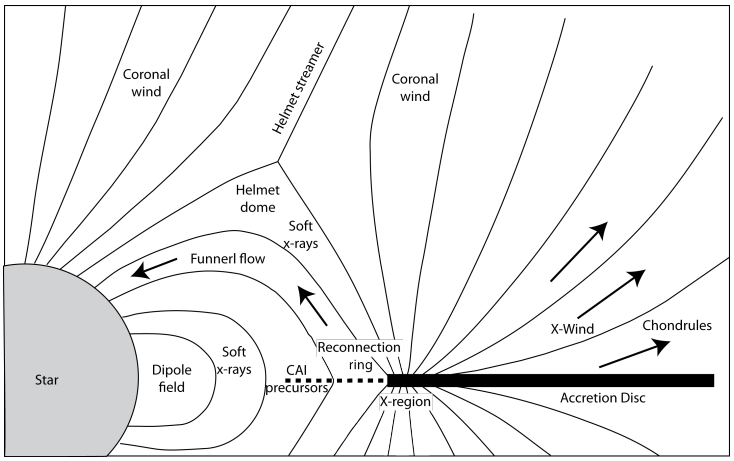

Figure 1.2: Schematic drawing of the magnetic field geometry and gas flow in the X-wind model for the production of CAIs and chondrules. Figure taken from Shu et al. (1997).

region, supporting a cosmic ray origin for at least some of the beryllium isotope anomalies if the former existence of ^{7}Be can be confirmed.

1.2.3 Supernova injection model

A competing model to the X-wind model for explaining the abundances of SLRs in our Solar System is the supernova injection model. Two sub-models exist - the supernova trigger and the aerogel model - where a supernova either induces the molecular cloud collapse while injecting SLRs or introduces the SLRs to the newly formed proto-planetary disk shortly after the collapse (Ouellette et al., 2009).

Supernova trigger model

In this model, a nearby supernova is the cause of the collapse of a dense part of the molecular cloud that forms the proto-planetary disk and most SLRs found in the early Solar System were formed by this single super-

nova (Cameron and Truran, 1977). This suggestion was based on the discovery of live ^{26}Al in CAIs by Lee et al. (1976), which suggests that shortly prior to the formation of the Solar System ^{26}Al was introduced to the collapsing molecular cloud. The short half-life and high initial abundance of ^{26}Al led Cameron and Truran (1977) to suggest that the time interval between nucleosynthesis and incorporation of ^{26}Al in CAIs was < 1 Myr. A major complication of the supernova trigger model is that the supernova shock front has to be sufficiently slow (5-70 km s^{-1}; Boss et al., 2010) to be able to simultaneously trigger collapse and inject SLRs into the presolar cloud core and therefore the presolar cloud core needs to be sufficiently far away from the supernova. While Boss et al. (2010) could generate models that suggest triggering of collapse and injection of SLRs at the same time is possible, their calculations failed to produce the injection efficiencies desired to satisfy the former abundance levels of SLRs inferred from the meteoritic record. Furthermore, these are one- and two-dimensional models, and it is not yet entirely clear how injection of SLRs would work in a three-dimensional cloud whilst at the same time triggering collapse of the cloud (Ouellette et al., 2009).

Aerogel model

This model is based on the observation that low-mass stars often form in close proximity to massive stars, while star formation generally occurs in clusters and most low-mass stars also form in clusters that contain at least one star sufficiently massive to undergo a supernova (Lada and Lada, 2003). In the aerogel model, a nearby proto-planetary disk is seeded by SLR-containing supernova ejecta, injecting the SLRs (mostly isotopes of refractory elements) incorporated in dust grains into the disk (Ouellette et al., 2010). The correct distance of the proto-planetary disk from the supernova here is quite important as, if too close, the proto-planetary disk would be destroyed by the supernova and, if too far, not enough SLRs would reach the proto-planetary disk to satisfy the former abundances of

SLRs found in meteoritic material. These problems have led some authors to conclude that it is unlikely that a proto-planetary disk will be the correct distance from a supernova to survive and still receive the correct amount of SLRs (e.g., Gounelle and Meibom, 2008). Major questions with the aerogel model are the survivability of the proto-planetary disk and the amount of supernova dust that can be retained by the disk.

Both these problems have been addressed in Ouellette et al. (2007, 2009). Ouellette et al. (2007) found that a proto-planetary disk can survive even nearby supernova with minimal mass loss because they are much denser than cloud cores. However, supernova material in the gaseous phase also passes through the proto-planetary disk with virtually no retention, which in turn means that if SLRs are found in the gas phase they can not be injected by a supernova. Astronomical observations however, suggest that dust is formed shortly after a supernova (Colgan et al., 1994) and calculations by Ouellette et al. (2009) show that the retention efficiency of this dust, presumably containing SLRs, into a proto-planetary disk can be quite high. Another difficulty for the aerogel model is that the injection of SLRs occurs after the formation of the proto-planetary disk and introduced SLRs have to be efficiently mixed on a short timescale within the proto-planetary disk to satisfy the meteoritic evidence. Model calculations predict that two different mechanisms could potentially achieve this: disk instabilities, and turbulent diffusion with radial flows (Ouellette et al., 2009). A potential test of the validity of the aerogel model is isotopic shifts in stable isotope ratios, especially oxygen isotopes, introduced to the proto-planetary disk from the supernova ejecta (Gounelle and Meibom, 2007). However, Ouellette et al. (2009) point out that there are some complications in the approach using the oxygen isotopes as a marker for supernova input and that it is currently not possible to predict the magnitude of stable isotope variations arising from an inhomogeneous distribution of supernova ejecta in the early Solar System.

1.2.4 Supernova propagation: Molecular cloud and star formation

It is known that star formation occurs in molecular clouds (e.g., Lada and Lada, 2003). However, the close relationship of molecular cloud and stellar life cycles is a relatively new paradigm. Molecular clouds form from the diffuse hot interstellar medium (H_I regions) and have a relatively short life cycle of 10-20 Myr (Hartmann et al., 2001; Hennebelle et al., 2007). The time spent in the molecular phase (H_{II} regions), when the column density is high enough to shield H_2 and CO from dissociating ultraviolet radiation, is only about a quarter of this (Hartmann et al., 2001). In general, it is thought that molecular clouds are the post-shock regions of converging flows that originate from earlier star forming regions (Hartmann et al., 2001; Hennebelle et al., 2007). At high enough column densities, gravitational forces become important and allow gravitational collapse to occur. Star formation occurs nearly simultaneously with the cloud formation and is probably mainly driven by these gravitational instabilities. Molecular clouds are then quickly dispersed through the forming stellar winds and supernovae (Hartmann and Burkert, 2007).

In the supernova propagation model of star formation, supernovae of former star-forming regions condense and trigger the formation of new dense molecular clouds and star forming clusters. While the X-wind model has difficulties explaining the abundance of ^{60}Fe in our Solar System, and the supernova trigger model requires a relative specific setting of Solar System formation, in the supernova propagation model SLRs are continuously produced and introduced to the molecular cloud either in Wolf Rayet or supernovae winds. For example, the ^{60}Fe levels expected in the early Solar System can be achieved in this model in a reasonable astrophysical setting (Gounelle et al., 2009), although it is not ruled out that a single supernova could have supplied the majority of the SLR in the early Solar System.

1.3 Early Solar System chronology

1.3.1 Formation of the central star and the proto-planetary disk

After collapse of the molecular cloud and during the nebular phase, the still growing Sun was an embedded young stellar object (YSO) enshrouded by gas and dust, which was first distributed in an extended envelope and later evolved into an accretion disk that ultimately defined the ecliptic plane (Fig. 1.1; Halliday, 2003; McKeegan and Davis, 2007). While the timescales for this stage are poorly constrained, increasingly, observational data show that around young stars this stage is of the order of a few million years (e.g., McCaughrean and O'Dell, 1996). It is expected that planetesimal and planets form at an early stage in the midplane of such optically thick disks (Podosek and Cassen, 1994; Wetherill and Stewart, 1993; Weidenschilling, 2000).

Stars with solar masses are thought to accrete rapidly from a collapsing cloud core in $\sim 10^5$ yr and develop into class I YSOs with accretion disks within a few hundred thousand years (Hartmann, 2000). In the subsequent T-Tauri stage these stars can have many of the characteristics of our Sun but are much brighter and have outflows that produce strong stellar winds. It has been argued that the T-Tauri stage is an early phase of heating of the inner portions of the disk and that the T-Tauri stage may last a few million years. During the T-Tauri stage, temperatures in excess of 1,500 K could be expected in the terrestrial planet-forming region (Boss, 1990; Nelson et al., 1998, 2000), with the main heating taking place at the midplane. Temperatures later drop quickly on timescales of 10^5 yr and, in the midplane, where planetesimals are likely to form, temperatures can reach 300 K at 1 AU on these timescales (Boss, 1990; Cassen, 2001).

1.3.2 Solid formation

Our understanding of the first solids to form in the Solar System is largely based on the components present in undifferentiated meteorites i.e., chondrites. Chondrites probably accreted in the region of the asteroid belt and contain important components that record the conditions in the early Solar System (Scott and Krot, 2007) . Next to the dominant chondrules and the matrix, chondrites still contain their iron component, which suggest they were never heated enough to segregate the iron. Apart from chondrules, a number of chondrite types also contain CAIs that probably formed as free-floating objects within the solar nebula, and very fine-grained dust that contains presolar grains (McKeegan and Davis, 2007). Given that presolar grains are unstable in a silicate matrix above a few hundred degrees Celsius (e.g., Mendybaev et al., 2002) they cannot have experienced the heating of the CAI and chondrule components in these meteorites. As chondrites are aggregates of various diverse components of different ages, it is likely that these components did not form at the same place or at the same time during the nebular phase of Solar System formation. Presolar grains must have survived the hot nebula phase unscathed while chondrules and CAIs experienced various degrees of high temperatures, which is a central argument for a high temperature gradient within the proto-planetary disk along with the correlated depletion of moderately volatile elements and Cr and Ti isotopes (Trinquier et al., 2009) in carbonaceous chondrites. In order to better understand the processes that formed the early Solar System it is important to constrain the timing and nature of the processes that formed refractory inclusions and chondrules as they are preserved in chondrites today.

Refractory inclusions

There are two main types of refractory inclusions: CAIs and amoeboid olivine aggregates (AOAs). CAIs are the oldest solids in chondrites that

formed within our Solar System and are believed to have formed during the most energetic phase of protosolar disk evolution (e.g., Ireland and Fegley, 2000; Wood, 2000). CAIs that have not experienced later melting have irregular shapes, fluffy textures, mineral assemblages and a trace element chemistry all of which suggest that most formed as condensates from a cooling gas phase, while some also show signs that they formed as evaporative residue. Ireland and Fegley (2000) suggested that CAIs may represent mixtures of solar nebula condensates and refractory residue materials formed by evaporating material of presolar origin. In CV chondrites, CAIs are subdivided into Types A, B and C based on their mineralogy. Type A CAIs are further subdivided into fluffy and compact types, with compact CAIs probably having once been molten (Scott and Krot, 2007). CAIs are commonly surrounded by a Wark-Lovering rim, which is a thin sequence of nearly monominerallic layers that duplicate the mineralogy found within the CAI (MacPherson, 2007). The outermost part of CAIs is made up an accretionary rim consisting of fine-grained olivine and pyroxene that fills the topography of the enclosed CAI. CAIs occur mostly in carbonaceous chondrites (Scott and Krot, 2007), however, the abundance and mineralogy of CAIs differs greatly between the various chondrite groups and, for example, type B CAIs are almost exclusively found in CV chondrites. In general, CAIs in most chondrite groups have ^{16}O-rich isotopic compositions (Fig. 1.3a) that suggested they formed in a single and restricted part of the nebular from which they were redistributed unevenly prior to chondrite accretion (McKeegan et al., 2000; Guan et al., 2000). However, Krot et al. (2007) suggested that in order to better satisfy the observed varieties, CAIs formed in multiple events in the CAI-forming region while the external conditions such as the dust/gas ratio and peak heating temperatures varied. Variations in oxygen isotopic compositions within single CAIs in CV and CO chondrites require isotopic exchange (Clayton, 2003). The mechanism for this is poorly understood and the suggested mechanisms include gas- solid and/or gas-melt exchange in the so-

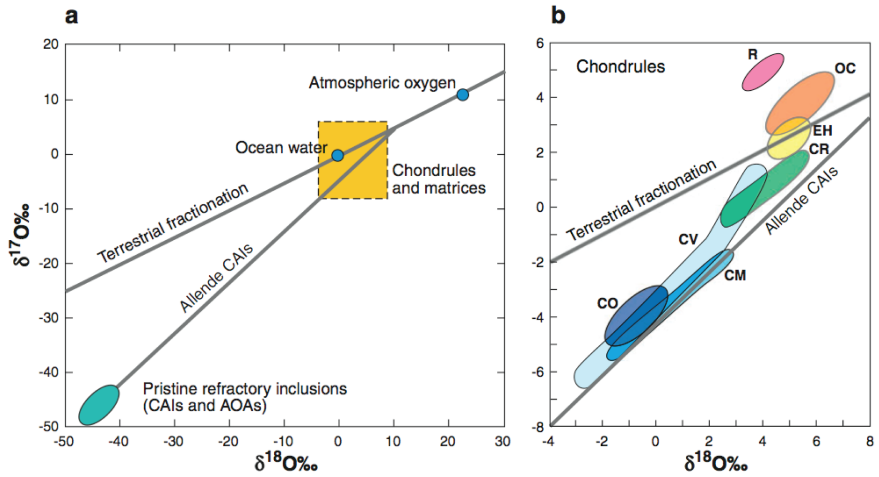

Figure 1.3: Three oxygen isotope plot for meteorites and their components, where isotopic compositions are plotted in δ notation with reference to standard ocean water. (a) Terrestrial samples plot on the terrestrial fractionation line, whereas CAIs and other refractory inclusions plot along a distinct line clustering in the lower left of the plot. (b) Enlarged view of the yellow chondrule and matrices' box in (a), showing the ranges of oxygen isotopic compositions of chondrules from carbonaceous (CO, CV, CM, CR), enstatite (EH) and ordinary (OC) chondrites. This figure is originally from Scott and Krot (2007) modified by Andrews (2009).

lar nebula (Clayton, 1993) and solid-fluid exchange in an asteroidal setting (Wasson et al., 2001). Igneous ^{16}O-poor CAIs in CR, CH, and CB chondrites suggest that oxygen isotope exchange occurred during melting, although it is not clear at what time and in what region of the protoplanetary disk the exchange occurred (Scott and Krot, 2007). The observation of ^{16}O-rich and -poor CAIs can be interpreted to reflect either temporal variations in the nebular gas compositions from which CAIs formed or physical transport of CAI precursors into a region with ^{16}O-poor gas (Scott and Krot, 2001).

A special group of CAIs are FUN CAIs (Wasserburg et al., 1977), where FUN stands for Fractionation and Unidentified Nuclear effects. These are characterised by little or no excess of ^{26}Mg from the decay of ^{26}Al, large mass-dependent isotopic fractionation effects in both magnesium and oxygen, and relatively large non-radiogenic nuclear anomalies in a variety of elements including barium, titanium, calcium, and others (MacPherson, 2007). Typical FUN inclusions can only be recognised by their isotopic composition, in all other properties they are identical to normal Type B CAIs. The origin of the mass-dependent isotopic fractionation in FUN CAIs is commonly assumed to be the result of Rayleigh-type distillation, however such an origin is problematic for FUN CAIs with bulk compositions identical to normal CAIs (MacPherson, 2007).

The existence of FUN inclusions is difficult to explain in the presence of normal CAIs. Models explaining the formation of normal CAIs generally fail to explain FUN CAIs, in particular the absence of ^{26}Al in the latter. An alternative model that could potentially resolve this difficulty is that ^{26}Al was injected into the solar system in a very time-restricted event, and that FUN and non-FUN CAIs were formed shortly before and after this event, respectively (e.g., Wood, 1998). To confirm this however, precise absolute ages of FUN CAIs are needed to establish a relative chronology for FUN and normal CAI formation.

Amoeboid olivine aggregates (AOAs) are irregular shaped objects that can make up a few percent of carbonaceous chondrites. In unaltered chondrites, AOAs consist of anhedral, fine-grained (1-20 mm) forsterite (Fa,1-3), Fe,Ni-metal, and a refractory component composed of aluminian diopside, spinel, anorthite, and rare melilite (Scott and Krot, 2007). AOAs have variable size, shape, distribution and modal mineralogy and some AOAs show triple junctions between forsterite grains and coarse-grained shells surrounding finer-grained cores, indicating high-temperature annealing (Komatsu et al., 2001). In the least altered chondrites, they are porous aggregates with mineralogy matching that expected for high-temperature

nebular condensates. They appear to have no mineralogical and isotopic differences between chondrite groups (Scott and Krot, 2007). The mineralogy, petrology, ^{16}O-rich compositions, and depletion in moderately volatile elements of AOAs suggests that they are aggregates of material that formed in an ^{16}O-rich gaseous reservoir and are refractory objects. Because the mineralogy and chemical composition of AOAs and accretionary rims around CAIs are similar it is considered likely that both formed contemporaneously in the CAI-forming region (Scott and Krot, 2007).

Chondrules

Chondrules are the most abundant consituent in chondrites. They are thought to be molten droplets of 0.0110 mm in size that that formed freefloating from dust in the protoplanetary disc. Chondrules are divided into porphyritic and fine-grained types. Porphyritic chondrules crystallized from melts that had peak temperatures that were close to the liquidus temperature for only short periods of time resulting in incomplete melting of the precursor material, whereas non-porphyritic chondrules crystallized from melts that were heated sufficiently to result in complete melting (Lofgren, 1996; Hewins and Connolly, 1996; Connolly et al., 1998). Oxygen isotopic compositions of large individual chondrules suggest that chondrules formed from several different reservoirs that were poorer in ^{16}O than the CAI source (Fig. 1.3b). Iron-rich chondrules have been suggested to represent chondrules that formed in a closed-system through flash-melting dust, whereas the majority of chondrules, which are iron-poor, are more likely to have formed through open system crystallization in the nebular gas, where the chemical composition was volatility controlled (Scott and Krot, 2007).

1.3.3 Planetary accretion and differentiation

The process of planetesimal accretion is considered to be gravitational. However, before gravitational accretion can occur bodies of sufficient size ($\sim$ 1 km; Chambers, 2007) have to form to allow gravitational forces to exert a major role. The mechanism responsible for this transition from gas and dust to large, km-sized, bodies is not yet understood and to date, none of the proposed mechanisms successfully satisfy all the requirements to form our Solar System as it is observed today (Halliday, 2003). The process of planetesimal accretion after formation of the first kilometer-sized objects is much better understood. This stage is the so-called runaway gravitational growth producing Mercury- and Mars-sized objects and should have only lasted for timescales of a few $\sim 10^5$ yr with faster accretion rates closer to the sun (e.g., Lissauer, 1987; Wetherill and Stewart, 1993; Weidenschilling, 2000). The final stage forms the terrestrial planets through large collisions. The timescale of this stage is vastly model dependent and different models have been proposed (Cameron, 1978; Hayashi et al., 1979; Safronov, 1954), where the main difference between the models is the amount of solar nebula gas present, which strongly affects the rate of accretion.

1.3.4 Chronological constraints on early Solar System processes

One of the most important factors in understanding the early processes in the formation of our Solar System is the chronology, as this provides key constraints on the rates and timescales for the processes of solid and planetary formation as well as for differentiation of the planets. Apart from the absolute Pb-Pb chronometer based on the decay-chains from ^{235}U, ^{238}U and ^{232}Th, there are several short-lived radionuclides that can provide relative age constraints on the formation of solids and planets and differentiation of the latter (Table 1.1). The most important chronometers recently

used to investigate the transition from the first Solar System solids to planetesimal bodies of the size of a few 100 km, occurring within 10 Myr of CAI formation, are the ^{207}Pb-^{206}Pb, ^{182}Hf-^{182}W, ^{53}Mn-^{53}Cr and ^{26}Al-^{26}Mg chronometers.

Timing of solid formation in the young Solar System

Amelin et al. (2002, 2006) reported what is currently the most precise absolute Pb-Pb age for a CAI from the CV3 chondrite Efremovka: 4567.11 $\pm$ 0.16 Ma. Similar ages were also obtained for CAIs from the CV3 chondrite Allende by Jacobsen et al. (2008) and Connelly et al. (2008a). Absolute Pb-Pb ages have now been reported for several chondrules (Amelin et al., 2002; Amelin and Krot, 2007; Connelly et al., 2008a) and are generally 2 Myr younger than CAI ages. This age difference is consistent with inferred initial ^{26}Al/^{27}Al ratios in chondrules relative to the abundance of ^{26}Al/^{27}Al in CAIs (Kita et al., 2000; Mostefaoui et al., 2002; Villeneuve et al., 2009). However, with the demonstration of ^{238}U/^{235}U variations in CAIs (Brennecka et al., 2010b) it is possible that the apparent Pb-Pb age difference between CAIs and chondrules is partly an artifact of different ^{238}U/^{235}U ratios in chondrules and CAIs and new Pb-Pb ages that also incorporate ^{238}U/^{235}U measurements are needed to demonstrate this apparent age difference is real.

Timing of planetesimal accretion and differentiation

The oldest achondrite (differentiated meteorite) dated using the Pb-Pb chronometer so far is the unique meteorite Asuka 881394 (4566.5 $\pm$ 0.2 Ma, Wadhwa et al., 2009a). Two other, much more precise Pb-Pb ages come from the basaltic meteorites Sahara 99555 (4564.58 $\pm$ 0.14 Ma, Connelly et al., 2008b) and D'Orbigny (4564.42 $\pm$ 0.12 Ma, Amelin, 2008a). Both are thought to have come from the angrite parent body and have quenched textures with strongly zoned mineral phases indicating that they cooled

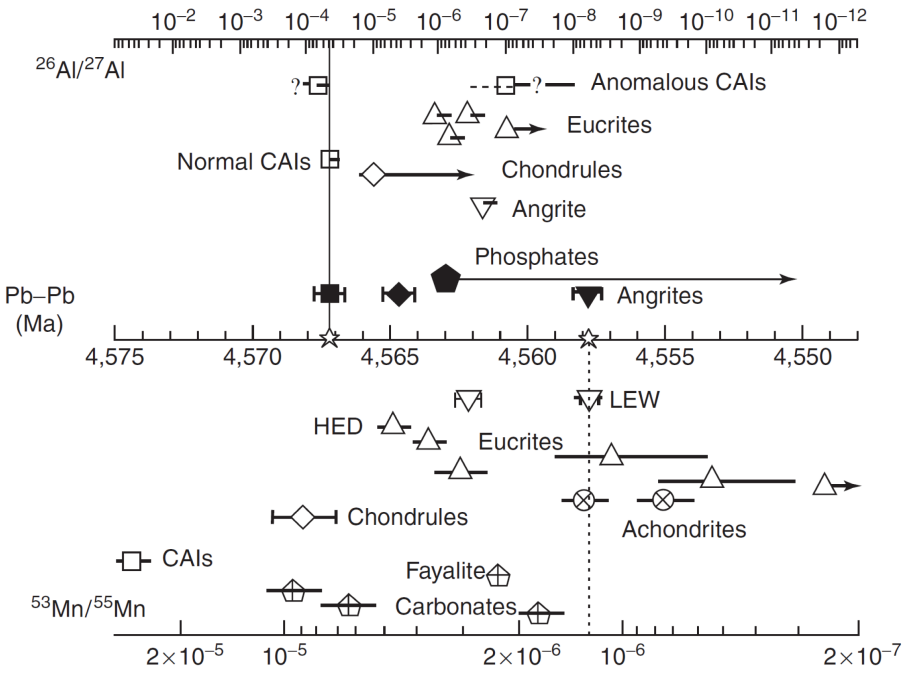

Figure 1.4: Comparison of the timeline for early solar system events of ^{26}Al-^{26}Mg and ^{53}Mn-^{53}Cr short-lived chronometers with the absolute timescale provided by the Pb-Pb chronometer. The anchor points (vertical dashed lines) are (1) the Pb-Pb age of CAIs (Amelin et al., 2002) with 'canonical' ^{26}Al/^{27}Al and (2) the Pb-Pb age of angrites (Lugmair and Galer, 1992) with the ^{53}Mn/^{55}Mn ratio in the angrite meteorite LEW 86010 (Lugmair and Shukolyukov, 1998). Pb-Pb ages are indicated by filled symbols read against the absolute timescale (central axis); the top axis shows the initial ^{26}Al/^{27}Al values measured in various phases (open symbols) and the bottom axis refers to initial ^{53}Mn/^{55}Mn for the open symbols in the bottom panel. Squares - CAIs, diamonds - chondrules, upright triangles - eucrites (basaltic achondrites), inverted triangles - angrites, crossed circles - pallasites and Acapulco, and pentagons - secondary minerals in chondrites (phosphates, carbonates, and fayalite). The datum labeled 'HED' represents the Mn-Cr correlation line for bulk eucrites. 'LEW' refers to the anchor point for ^{53}Mn/^{55}Mn and Pb-Pb; the remaining angrite data represent Mn-Cr and Al-Mg analyses of D'Orbigny (Nyquist et al., 2003). 'Anomalous CAIs' refers to those that apparently formed with no live ^{26}Al. Figure taken from (McKeegan and Davis, 2007).

rapidly (Greenwood et al., 2005; Mittlefehldt, 2007). These absolute ages indicate that planetesimals accreted, melted and differentiated within 3 Myr of the condensation of the oldest known solids (CAIs) in our Solar System.

All short-lived chronometers rely on the Pb-Pb absolute chronometer to provide at least one anchorpoint to construct an absolute chronology and timescale for early Solar System processes. While the general chronological constraints from the ^{182}Hf-^{182}W, ^{53}Mn-^{53}Cr and ^{26}Al-^{26}Mg chronometers are consistent, there is no agreement between these short-lived chronometers and the Pb-Pb chronometer over the absolute age differences (e.g., McKeegan and Davis, 2007).

For example, the ^{182}Hf-^{182}W chronometer can be used to date metal-silicate differentiation of planetesimals as Hf is lithophile whereas W is moderately siderophile, resulting in super-chondritic Hf/W ratios in the silicate part of planets producing ^{182}W excesses and complementary deficits in the low Hf/W metal if core formation occurs during the life time of ^{182}Hf ($t_{1/2}$ = 8.9 Myr; National Nuclear Data Center, 2010). An early metal core formation and silicate-silicate differentiation within 1-2 Myr after CAI formation as established by the Pb-Pb ages of angrites and CAIs is in general agreement with ^{182}Hf-^{182}W ages for CAIs, achondrites, and iron meteorites (Kleine et al., 2002, 2004, 2005a; Markowski et al., 2006b, 2007; Schersten et al., 2006; Burkhardt et al., 2008). However, in order to have consistent relative age differences between CAIs and angrites for both the ^{182}Hf-^{182}W and Pb-Pb chronometers, the Pb-Pb age of angrites would have to be ca. 1-2 Myr younger or that of CAIs to be 1-2 Myr older than their published Pb-Pb ages. The recent discovery of variable ^{238}U/^{235}U ratios in CAIs (Brennecka et al., 2010b) suggested a potential solution to this problem. However, the preliminary report of similar ^{238}U/^{235}U ratios for the D'Orbigny angrite as CAIs (Brennecka et al., 2010a) indicates that potential shifts in the absolute Pb-Pb ages are likely to be similar for both, that is CAIs and angrites, preserving the offset between absolute Pb-Pb ages and

relative ^{182}Hf-^{182}W ages.

Another short-lived chronometer suited to studying the formation of the first solids and planetesimals is the ^{53}Mn-^{53}Cr chronometer ($t_{1/2}$ = 3.7 Myr). Studies by Lugmair and Shukolyukov (1998, 2001) and Trinquier et al. (2008) have resulted in a similar chronology to ^{182}Hf-^{182}W, however, tying the ^{53}Mn-^{53}Cr timeline to Pb-Pb dated angrites (LEW 86010, NWA 4801) (Lugmair and Galer, 1992; Amelin and Irving, 2007) also results in a discrepancy between absolute Pb-Pb ages for CAIs and the relative ^{53}Mn-^{53}Cr ages requiring the Pb-Pb dates for CAIs to be older (Fig. 1.4). This discrepancy between the different chronometers, mainly between the short-lived chronometers and the absolute Pb-Pb ages, may indicate that certain assumptions, such as the homogeneity of all isotopic systems throughout the early Solar System, are flawed. However, with addition of the ^{26}Al-^{26}Mg chronometer the situation becomes more problematic. Relative age differences between chondrules and CAIs from Pb-Pb and ^{26}Al-^{26}Mg ages are generally consistent, whereas the relative age difference between precisely ^{26}Al-^{26}Mg dated angrites (Sahara 99555 and D'Orbigny) and CAIs indicates that either the Pb-Pb age of the CAIs is too young or the angrite Pb-Pb ages are too old by ca. 1 Myr.

1.4 The role of ^{26}Al in the early Solar System

^{26}Al is one of 14 extinct short-lived radionuclides that have been demonstrated to have existed in the early Solar System (Table 1.1, McKeegan and Davis, 2007). These SLRs are generally characterised by their relatively short half-life of $\leq$ 100 million years and that SLRs existed during the early parts of the formation of our Solar System but have since decayed. The evidence for the former presence of SLRs in the Solar System comes from isotopic enrichments in their daughter products in meteorites. ^{26}Al was first demonstrated to have formerly been present in the Solar System by Lee et al. (1976) in Ca-Al-rich minerals of Allende. Since then an

initial, so-called 'canonical' $(^{26}Al/^{27}Al)_0$ abundance of 5×10^{-5} in CAIs (MacPherson et al., 1995), the oldest material thought to have formed in our Solar System (Amelin et al., 2002), has been established. However, this canonical abundance has been called into question by in situ laser ablation Mg isotope data (Young et al., 2005) and whole rock CAI isochrons (Thrane et al., 2006) that suggested evidence for supra canonical $(^{26}Al/^{27}Al)_0$ abundances in the early Solar System. This dispute has not been entirely resolved, but newer Mg isotope data for whole rock and internal mineral CAI isochrons reinstated the canonical abundance and provide the most precise value of $^{26}Al/^{27}Al = (5.23 \pm 0.13) \times 10^{-5}$ in CAIs so far reported (Jacobsen et al., 2008).

Using the 'canonical' abundance of $^{26}Al/^{27}Al$ subsequent studies have used the ^{26}Al-^{26}Mg clock to establish the former distribution of ^{26}Al in high Al/Mg phases in CAIs, chondrules and some achondrites principally using in situ ion probe techniques (e.g., Srinivasan et al., 1999; Nyquist et al., 2003). Only relatively recent developments in multiple-collector inductively coupled plasma mass spectrometry (MC-ICP-MS) techniques over the past decade or so have made it possible to investigate material with much lower Al/Mg ratios and hence much smaller ^{26}Al induced ^{26}Mg isotopic anomalies (Bizzarro et al., 2004, 2005; Baker et al., 2005).

This improvement in the precision of Mg isotope measurements has resulted in a shift in the focus of ^{26}Al-^{26}Mg dating from the investigation of mainly nebular processes (i.e. CAIs and chondrules) to that of the relative ages of achondrites and differentiated meteorites that represent the products of silicate differentiation on planetesimals (e.g., Spivak-Birndorf et al., 2009). One key assumption of ^{26}Al-^{26}Mg dating is a homogeneous distribution of ^{26}Al within the proto-planetary disk, based on the 'canonical' abundance of ^{26}Al in most CAIs as well as evidence for the former presence of ^{26}Al in chondrules and some basaltic achondrites (MacPherson et al., 1995; Russell et al., 1996; Villeneuve et al., 2009). If this assumption is correct, ^{26}Al with its short half-life would be a very powerful chronome-

ter within its life span for dating silicate-silicate fractionation events in the first few million years of our Solar System as the analytical techniques theoretically allow a high temporal resolution ($\sim$ 100 kyr).

1.4.1 Origin of ^{26}Al in the early Solar System

Although there is unequivocal evidence for the presence of live ^{26}Al in the early Solar System, the ultimate origin of the ^{26}Al remains a debated issue as it can potentially be produced in different ways.

^{26}Al can potentially be produced through irradiation by the energetic young Sun in the proto-planetary disk or through stellar nucleosynthesis in massive stars with ^{26}Al injected shortly prior to, during or possibly even shortly after formation of the Solar System. Both stellar nucleosynthetic processes (Gaidos et al., 2009) and an irradiation origin during intense magnetic flaring within the early Solar System have been proposed to have produced sufficient ^{26}Al to explain the 'canonical' abundance found in CAIs (see Sahijpal and Gupta, 2009, and references therein). However, it currently seems most likely that the majority of ^{26}Al was produced prior to the collapse of the molecular cloud and was either present in the molecular cloud at time of the molecular cloud collapse or was introduced to the early Solar System shortly after collapse.

A complete understanding of the source of ^{26}Al is hampered by the lack of understanding of the astrophysical setting of and the trigger mechanism for formation of our Solar System. The source of SLRs in our Solar System has been investigated by looking for the former existence of 'smoking gun' isotopes such as ^{10}Be, ^{7}Be and ^{60}Fe that can only be produced by a single mechanism.

For example, the former existence of ^{10}Be in CAIs has been demonstrated by McKeegan et al. (2000), and has been used to argue for an irradiation origin of SLRs within the proto-planetary disk. However, this has been challenged by the possibility that ^{10}Be can be sufficiently produced

by galactic cosmic rays in the molecular cloud (Desch et al., 2004). This argument has in turn been questioned by the apparent discovery of the very short-lived ^{7}Be ($t_{1/2}$ = 57 days; Chaussidon et al., 2006), which would require this isotope at least to be produced within the Solar System. The presence of another SLR in meteorites, ^{60}Fe, that can only be produced in supernovae, has been used as an argument for a stellar source of SLRs (Tachibana et al., 2006). With the recently re-evaluated half-life of ^{60}Fe of $t_{1/2}$ = 2.62 Myr (Rugel et al., 2009), however, it is quite likely that this is not evidence for a supernova injection (Bizzarro et al., 2007), but rather a remnant of galactic background (Gounelle et al., 2009). Currently, evidence does favor an external source of ^{26}Al, with contributions from internal X-wind irradiation estimated to have potentially produced around 10% of the observed ^{26}Al abundance (Sahijpal and Gupta, 2009), while all such calculations so far are based on a homogeneous, canonical ^{26}Al abundance in the early Solar System.

1.4.2 ^{26}Al-^{26}Mg chronometer

Magnesium has three stable isotopes (^{24}Mg, 2^{25}Mg, and ^{26}Mg) that are produced in stellar environments through explosive hydrogen burning (^{24}Mg) and neon burning in the α-process, carbon burning, and explosive nucleosynthesis (^{25}Mg and ^{26}Mg; Burbidge et al., 1957). In addition ^{26}Mg is the decay product of ^{26}Al. ^{26}Al decays with a half-life of 0.73 Myr through positron emission and electron capture to ^{26}Mg releasing 3.12 MeV per decay (Castillo-Rogez et al., 2009). Since the former presence of ^{26}Al was demonstrated in CAIs, the ^{26}Al-^{26}Mg decay system has been used to date the relative timing of CAI and chondrule formation as well as some basaltic achondrites (e.g., Srinivasan et al., 1999; Kita et al., 2000). With the exception of a small number of thermal ionization mass spectrometry studies (e.g., Lee et al., 1977), most early constraints on the former ^{26}Al abundance in meteoritic material was produced by in situ ion probe mea-

surements that require high Al phases to be able to detect ^{26}Mg excesses resulting from ^{26}Al decay. However, recent application of MC-ICP-MS to Mg isotope analysis has opened up a new range of dating opportunities. In particular, Bizzarro et al. (2005) and Baker et al. (2005) apparently demonstrated that it is possible to use the presence of small ^{26}Mg excesses in bulk basaltic meteorites to calculate model ages to date the increase in Al/Mg associated with the formation of basaltic magmas (see also Chapter 3). Previously, many of these basaltic meteorites lacked evidence for the former presence of ^{26}Al as, presumably, either the basaltic meteorites crystallized after extinction of ^{26}Al or because ^{26}Mg excesses in the high Al/Mg phase (feldspar) in these meteorites had been lost by secondary events and diffusive equilibration with low Al/Mg mineral phases.

Conversely, Al/Mg of essentially zero in some types of differentiated meteorites and their minerals should allow ^{26}Mg deficits to place age constraints on their formation if differentiation took place within 2 Myr of CAI formation (see Baker and Schiller, 2010). The ^{26}Mg excesses and deficits expected from such processes will be ca. $\leq \pm 0.050‰$ and require both the precision and accuracy of Mg isotope measurements to be $\leq \pm 0.005‰$ if the full potential of the ^{26}Al-to-^{26}Mg dating system is to be utilised.

Model ages are used in this study in the same manner as in Bizzarro et al. (2005) and Baker et al. (2005), and are the the result of a regression through the bulk rock composition of a sample and the chondritic composition of the Solar System (^{27}Al/^{24}Mg = 0.1, δ^{26}Mg* = 0) to give an age that is likely to be close to the true crystallisation age (see Chapter 3). This approach is inferior to internal mineral isochrons as it ignores any previous history of the precursor material. However, model ages are also much less susceptible to secondary resetting events and are much more likely to preserve their age information.

A problem for both mineral isochron ages and model ages, is that in order to retrieve ages relative to CAIs the general assumption is that the entire proto-planetary disk had the same initial ^{26}Al abundance as CAIs.

This assumption is not easy to test because an $^{26}Al/^{27}Al$ abundance of 5 $\times 10^{-5}$ is equivalent to only $\sim 0.037‰$ difference in the $^{26}Mg/^{24}Mg$ ratio for material that has a Solar System $^{27}Al/^{24}Mg$ ratio. The distribution of $\delta^{26}Mg^*$ anomalies in bulk chondrites and their relationship with anomalies in CAI-material can be used as an indicator of the level of heterogeneity within the chondrite forming region (see Chapter 4), but given the maximum range of potential anomalies and the precision achieved for most samples in this study, $\sim$0.0050‰, it is only possible to place limits on the potential ^{26}Al heterogeneity between the chondrite- and the CAI-forming regions.

1.4.3 ^{26}Al as a heat source in the early Solar System

The widespread evidence for early differentiation of small planetesimals in the early Solar System requires an adequate heat source to provide the thermal energy to produce rapid and large scale melting. Several heat sources have been proposed.

Proposed heat sources include impact energy during accretion, electromagnetic induction and decay of short-lived radionuclides. Impact melting can provide large amounts of thermal energy but Keil et al. (1997) showed that melting of a whole planetesimal could not be achieved through impacts without fragmentation of the planetesimal, and impact melting is therefore unlikely to have been the main heat source driving planetesimal magmatism. Similarly, electromagnetic induction heating of planetesimals moving around the magnetically active protosun as suggested by Sonett et al. (1968) has been shown in laboratory experiments to not be able to supply enough energy alone (Marsh et al., 2006). This leaves the radiogenic decay energy of short-lived radionuclides as the only plausible, currently identifiable, mechanism for driving planetesimal melting and differentiation in the early Solar System. Urey (1955) initially suggested that decay of ^{26}Al could have provided the required heat source and

since the former widespread presence of ^{26}Al in the early Solar System has been demonstrated (e.g., Lee et al., 1976; MacPherson et al., 1995; Bizzarro et al., 2005, and reference therein), decay of short-lived nuclides appears to be the most likely source of heat for the differentiation and/or thermal metamorphism of planetesimals. The role of SLRs has also been supported by revised estimates of the initial (^{60}Fe/^{56}Fe) ratio in the early Solar System (Tachibana and Huss, 2003; Mostefaoui et al., 2004, 2005; Cook et al., 2006; Regelous et al., 2008), however with the recently revised half-life of ^{60}Fe (Rugel et al., 2009), the potential importance of ^{60}Fe decay as a heat source has been significantly reduced. In summary, ^{26}Al or both ^{60}Fe and ^{26}Al decay most likely provided the necessary thermal energy to drive melting and differentiation of small planetesimals in the early Solar System.

1.5 Meteorite samples analysed in this study

1.5.1 Classification of meteorites

Meteorites are generally divided into two groups - chondrites and non-chondrites - where non-chondrites can be further subdivided into achondrites, irons and stony irons (Table 1.2). Chondrites are considered the most primitive meteorites as their parent bodies never melted and differentiated, which is why their elemental composition (for most non-volatile elements) is similar to the solar photosphere. Non-chondrites are meteorites that originated from parent bodies that have experienced various degrees of melting and differentiation. Meteorites with characteristics transitional between those of chondrites and achondrites are called primitive achondrites and still contain high amounts of metal and siderophile elements and their parent body probably never differentiated into a core and a mantle. The most evolved achondrites appear to be products of crust-mantle differentiation and have some similarities to basalts found on Earth. Iron meteorites represent remnants of cores from small plan-

etesimals that did melt and differentiate to form Fe-Ni metal cores and silicate mantles. Stony-iron meteorites contain roughly equal amounts of silicate (dominantly olivine), metal, and troilite and are thought to have come from the core-mantle boundary region of small planetesimals. As both Al and Mg, the focus of this study, are lithophile elements concentrated into the silicate mantle during planetesimal differentiation, the subsequent summary excludes iron meteorites, which are not ideally suited for the application of the ^{26}Al-^{26}Mg chronometer. In-depth discussions of the classification and the specific characteristics of the different classes of meteorites can be found in Krot et al. (2007), Scott and Krot (2007), Mittlefehldt (2007), Haack and McCoy (2007) and references therein.

Table 1.2: Classification of meteorites taken from Scott and Krot (2007), Krot et al. (2007) and Mittlefehldt (2007).

Chondrites															
class	carbonaceous								ordinary			enstatite			
group	CI	CM	CO	CR	CB	CH	CV	CK	H	L	LL	EH	EL	R	K
Petrological type	1	1-2	3-4	1-2	3	3	3-4	3-6	3-6			3-6		3-6	3
subgroups					CB_a		CV_A								
					CB_b		CV_B								
							CV_{RED}								
(vol. %):															
CAI and AOA	<0.01	5	13	0.5	<0.1	0.1	10	4	0.01-0.2	<0.1	<0.1	<0.1		<0.1	
Chondrules	<5	20	40	50-60	30-40	~70	45	15		60-80		60-80		>40	20-30
Metal	<0.01	0.1	1-5	5-8	60-70	20	0-5	<0.01	8	3	1.5	15	8	<0.1	6-9

Non-chondrites	origin	rock type
primitive		
Acapulcoites, Lodranites	Metamorphism ± partial melting	Chondritic ultramafic
Winonaites, IAB silicate inclusions, IIICD silicate inclusion	Metamorphism ± partial melting	Chondritic ultramafic
differentiated		
Achondrites		
Angrites	Melt crystallization	Mafic
Aubrites	Melt crystallization, melt residue (?)	Nonchondritic ultramafic
Brachinites	Melt crystallization,Metamorphosed chondrite (?)	Chondritic and nonchondritic ultramafic
Ureilites	Melt crystallization, melting residue	Nonchondritic ultramafic
HED		
Howardites, Eucrites, Diogenites	Melt crystallization, impact modified	Nonchondritic ultramafic to mafic
ungrouped NWA011	Melt crystallization, impact modified (?)	Mafic
Martin (SNC)		
Shergottites, Nakhlites, Chassignites, Orthopyroxenites		
Lunar		
Stony irons		
Mesosiderites	Melt crystallization, impact modified	Nonchondritic ultramafic to mafic
Pallasites		
Main group, Eagle Station, pyroxene	Melt crystallization	Fe-Ni metal & mafic
Irons		
IAB, IC, IIAB, IIC, IID, IIE, IIIAB, IIICD, IIIE, IIIF, IVA, IVB	Melt crystallization	Fe-Ni metal

1.5.2 Chondrites

The classification of chondrites is mainly based on their bulk chemistry and oxygen isotopic systematics. However, mineralogy, petrology and proportions of various chondritic components are also used to group the different kinds of chondrites. A group is generally defined when there are at least five unpaired chondrites of similar mineralogy, petrography, oxygen isotopic properties, and bulk chemical compositions in major, non-volatile elements (Krot et al., 2007). There are also ungrouped chondrites that do not fit into any existing group. Currently there are a total of 14 chondrite groups recognized, and 13 of those comprise three major classes of chondrites:

- Carbonaceous chondrites consist of eight different groups (CI, CM, CR, CO, CV, CK, CB, and CH), where the second letter is a reference to the type meteorite of that class with exception of the CH group, where the H is a reference to the high metal abundance in this group. One important feature of carbonaceous chondrites is that they contain variable amounts of refractory material, the most important of which are CAIs, the oldest dated material thought to have formed in the early Solar System (Amelin et al., 2002). Carbonaceous chondrites do not plot on the terrestrial fractionation line in three oxygen isotope space, but form a separate, mass-independent trend i.e., the carbonaceous chondrite anhydrous mineral (CCAM) line (Fig. 1.3). Oxygen isotopic variations within the carbonaceous chondrite group, especially from the CM to CR-CH-CB, are larger than the variations exhibited by the ordinary chondrites.

- Enstatite chondrites contain the groups EH and EL chondrites, which are divided mainly on their iron content, but also on mineralogy and bulk chemistry. These chondrites contain high abundances of cryptocrystalline, enstatite-rich chondrules and only rarely contain CAIs. Enstatite chondrites are the only class of chondrites

with oxygen isotopic compositions that plot on the terrestrial fractionation line, which has been used as an argument to suggest that enstatite chondrite-like material was the main building material for Earth and, perhaps, the other terrestrial planets. Enstatite chondrites contain minerals that are characteristic for formation under highly reducing conditions, such as FeO-poor enstatite, Mg and Ca-bearing sulfides, Ti and Cr-bearing troilite and Si-bearing Fe-Ni metal (e.g., Keil, 1968; Brearley and Jones, 1998) similar to the related achondrite group of aubrites and there are enstatite chondrites that have been classified as melt rocks.

- Ordinary chondrites are the by far most commonly found meteorites on Earth ($\sim$ 80% of all meteorite falls) and consist of three groups, LL, L and H, where the letters describe the metal abundance with increasing metal content from LL to H. The oxygen isotopic variations of ordinary chondrites are fairly restricted, but the oxygen isotopic composition of single chondrules from LL, L, and H chondrites do define a common fractionation line, suggesting a single common source for the chondrules from all three groups. The slight difference in the bulk isotopic composition may be related to size sorting with the mean chondrule size distribution to increase in the order: H $>$ L $>$ LL (Rubin, 1989).

The R chondrite (Rumuruti-like) group and the K (Kakangari-like) grouplet differ from the other classes of chondrites through their mineralogy, matrix abundance and their oxygen isotope composition and are thought to represent independent groups of meteorites (Krot et al., 2007).

1.5.3 Non-chondrites

Aside from non-chondrites that are considered to originate from Mars or the Moon, there are several achondrite groups that are thought to represent samples from a number of small planetesimals that formed shortly

after the collapse of the molecular cloud and formation of the Solar System. Some of these achondrites only experienced minor degrees of melting, the so called primitive achondrites, whereas others are samples that come from planetesimal bodies that experienced planetesimal-wide differentiation. A further silicate-bearing member of this group are stony irons, which are mixtures of Fe-Ni metal and silicate clasts or minerals that are likely the products of planetesimal-wide disruptions.

Howardite-Eucrite-Diogenite Association

The howardite-eucrite-diogenite (HED) suite of meteorites is the largest group of differentiated crustal rocks considered to originate from a single asteroid, presumed to be 4 Vesta (e.g., Binzel and Xu, 1993). The HED suite consists of mafic and ultramafic igneous rocks most of which are breccias that have basalt, cumulate gabbro and orthopyroxenite lithologies. *Diogenites* are mostly monomict orthopyroxenites that show a compositional range in orthopyroxene En from 66 to 84. Generally, the major element composition of orthopyroxenes are uniform, whereas minor and incompatible trace elements show considerable variation. These variations in supposedly monomict breccias can be attributed to natural variation in the trace element contents in the minerals, variations of a trapped melt component or an admixture of small amounts of basaltic eucrite contaminants. *Basaltic eucrites* are commonly fragmental breccias of fine- to medium-grained basalts that have typically experienced thermal metamorphism. There are two different compositional trends - Stannern and Nuevo Laredo - defined by bulk rock trace element contents that are considered to represent distinct magmatic evolution trends. *Cumulate eucrites* are are coarse-grained gabbros intermediate in En between diogenites and basaltic eucrites, many of which are unbrecciated. It is not clear if cumulate eucrite genesis is related to basaltic eucrites or not (Hsu and Crozaz, 1997; Treiman, 1997). *Polymict eucrites* consist of fragmental and melt-matrix breccias dominantly comprised of diogenite, basaltic eucrite and

cumulate eucrite lithologies. *Howardites* are part of this group and represent a lithified regolith of the HED (Krot et al., 2007).

A number of models have been postulated to explain the petrogenesis of HED meteorites. None so far can explain all features found in HED meteorites, which suggests that either all the HED meteorites are not from the same parent body or that some assumptions of the models are flawed (Barrat et al., 2000; Righter and Drake, 1997; Ruzicka et al., 1997; Shearer et al., 1997; Stolper, 1977; Warren, 1997; Mittlefehldt and Lindstrom, 2003).

Mesosiderites

Mesosiderites are stony iron meteorites in which the silicate material is a polymict breccia of crustal rock, including mainly basalts, gabbros and pyroxenites, but also some dunites and anorthosites. The silicate material is very similar to the HED suite of meteorites, but there are differences mainly in their mineralogy, pyroxene compositions and the range of trace element compositions (Mittlefehldt, 2007) that suggest mesosiderites may have formed on a different parent body. The metal component is presumed to be core material from an asteroid and mesosiderites are the result of impact mixing, however it is not clear if the metal and silicates are material from the same parent body (Haack et al., 1996; Scott et al., 2001; Wasson and Rubin, 1985).

Angrites

Angrites have mass-independent oxygen isotopic compositions that distinguish them from other achondrites (Greenwood et al., 2005) and they are believed to have formed as partial melts of primitive source materials under oxidizing conditions. Several distinct parent melts are required to explain the angrite suite of meteorites (Mittlefehldt, 2002). Angrites generally have basaltic compositions and consist mainly of Ca-Al-Ti-rich pyroxene, calcium-rich olivine, and anorthitic plagioclase. The petrol-

ogy of angrites is quite diverse with textures ranging from equilibrated to quenched and they are interpreted to be mafic igneous rocks from the crust of a differentiated asteroid (Mittlefehldt, 2007, and reference therein). Angrites are extremely depleted in moderately volatile elements and depleted in highly volatile elements. They are also enriched in incompatible lithophile elements as expected for basaltic rocks (Mittlefehldt, 2007). The parent body of angrites appears to have had an exceptionally low $^{204}Pb/^{238}U$ ratio that makes it possible to Pb-Pb date angrite formation very precisely (Amelin, 2008a), making this group of meteorites a useful anchor for short-lived (relative) chronometers.

Aubrites

Aubrites or enstatite achondrites are enstatite pyroxenites that are the most reduced achondrites known. Aubrites consist dominantly of FeO-free enstatite and, with the exception of the igneous Shallowater (Keil et al., 1989) and Mt. Egerton, all aubrites are brecciated. Similarities in the highly reduced nature, mineralogy and oxygen isotopic compositions suggest that aubrites are related to enstatite chondrites, but from distinct parent bodies. It has been argued that aubrites, the igneous Shallowater aubrite, and the H- and L-group enstatite chondrites represent samples from four different asteroidal parent bodies. Aubrites are depleted in a basaltic component, but their formation mechanism is poorly understood and they lack a well constrained chronology. However, it is generally considered that they are igneous rocks and, perhaps, cumulates from a magma ocean of a highly reduced planetesimal.

Ureilites

Ureilites are the second largest group of achondrites and have features of both primitive and differentiated achondrites. Ureilites are ultramafic rocks composed mainly of olivine and pyroxene, but also contain inter-

stitial material that is rich in elemental carbon. They exhibit varying degrees of shock, but most are unbrecciated or monomict. Polymict ureilites can also contain a large variety of other meteoritic material foreign to monomict ureilite assemblages that provide evidence for impact events on the ureilite parent body (Goodrich et al., 2004). Different ureilite meteorites exhibit variable oxygen isotope compositions that are parallel to the carbonaceous chondrite anhydrous mineral line (Clayton et al., 1988). There is conflicting evidence as to whether ureilites are primitive rocks or have a high-temperature origin, and there is as yet no clear understanding of the origins of these rocks, although a high-temperature origin currently seems most likely (Goodrich et al., 2004).

Pallasites

Pallasites are stony iron meteorites composed of roughly equal amounts of silicate (dominantly olivine), metal, and troilite. The 50 known pallasites are subdivided into three groups on the basis of oxygen isotopic, mineral, and metal compositions: main group pallasites (by far the most abundant group), the Eagle Station pallasites, and the pyroxene pallasites. The differences between the groups suggest that pallasites originated on at least three separate asteroidal bodies. Although mixing of olivine and metal and some features of pallasite olivine seem inconsistent with a deep-seated core-mantle boundary origin this interpretation still remains the most plausible site for the origin of pallasite meteorites (Mittlefehldt et al., 1998).

Brachinites

The brachinite group was originally classified as a suite of primitive achondrites, but more recently a cumulate origin has been preferred. Brachinites consist dominantly of olivine with some high-calcium pyroxene, and their bulk chemical composition is quite variable. Postulated modes

of origin range from metamorphism and oxidation of chondritic material to accumulation from a magma (Nehru et al., 1992, 1996; Mittlefehldt et al., 2003). The petrological heterogeneity between different brachinite meteorites suggests that they might not have all formed by the same processes, and this is quite plausible especially given that many of the meteorites in this group have not yet been exhaustively studied.

Acapulcoite-Lodranite Clan

The acapulcoite-lodranite clan is a primitive achondrite group. Acapulcoites have modal bulk compositions that are broadly chondritic and also seem to contain some relict chondrules. Lodranites on the other hand are distinctly non-chondritic and generally depleted in a basaltic component (Mittlefehldt et al., 1998). Despite the broadly chondritic compositions and presence of relict chondrules in some of the acapulcoite-lodranite clan, this group of meteorites clearly differs from ordinary chondrites given their distinct mass-independent oxygen isotopic compositions (Clayton and Mayeda, 1996). Acapulcoite-lodranite clan meteorites contain metal-sulfide veins that provide evidence for melting. The origin of meteorites from this clan is thought to be a result of extensive high-temperature metamorphism and retarded anatexis of primitive, reduced chondritic material that produced a range in final temperatures, resulting in rocks that retained their chondritic composition, but depleted in metal-sulfide system minimum melts and depleted in mafic partial melts (McCoy et al., 1996, 1997).

Winonaites

Another primitive achondrite group is formed by winonaites and silicate inclusions in some IAB iron meteorites. There is also substantial heterogeneity in the chemical and textural composition in this group, which contains members with primitive chondritic compositions similar to ordinary

chondrites, basalt-depleted lithologies, and lithologies containing mafic segregations. The unique mixture of primitive silicate material with iron provides a considerable challenge to explain the origin of the winonaite-IAB-iron silicate inclusion clan. A range of proposed models cannot satisfactorily explain the genesis of the whole clan (Benedix et al., 2000), but the most plausible involves the breakup and reassembly of a hot, partially differentiated parent body.

Northwest Africa 011

Northwest Africa 011 (NWA 011) is a unique meteorite that has been paired with NWA 2976, which has been analyzed in this study. The recrystallized texture of this meteorite has been used to suggest that NWA 011 is a recrystallized breccia (Yamaguchi et al., 2002). NWA 011 is basaltic in composition and has a cumulate eucrite-like rare earth element pattern and an oxygen isotopic composition similar to CR chondrites, which is distinctly different from other achondrites, and implies it represents the product of a previously unsampled planetesimal.

1.5.4 Sample selection

All types of meteorites contain valuable petrographic, chemical, isotopic and, potentially, chronological information as to how our Solar System formed and evolved in its first few million years. To best aid our understanding of early Solar System processes it is ideal to have high-precision chronological information for as many meteorites as possible. Unfortunately, the only long-lived, absolute chronometer with a time resolution sufficient to do this is the Pb-Pb chronometer, and the usefulness of this system is restricted to suitable meteoritic material with high U/Pb ratios and limited contamination by terrestrial Pb (e.g., Tera, 1999; Connelly et al., 2008b).

However, in addition to the long-lived absolute chronometers used

to date meteorites, as previously discussed, several short-lived, extinct chronometers that existed in sufficient abundance in the proto-planetary disk can be useful for determining the relative ages of meteorites. The short half-life of these now extinct chronometers coupled with large fractionations of the parent and daughter elements in the early Solar System allows them to be used to routinely obtain relative ages with precisions of $\leq \pm 1$ Myr (e.g., Burkhardt et al., 2008; Wadhwa et al., 2009a). A critical consideration when using short-lived chronometers however, is the requirement for the abundance of the short-lived isotope to have been homogeneously distributed throughout the proto-planetary disk. If short-lived isotopes were heterogeneously distributed these chronometric systems may be compromised. Demonstration of significant isotopic anomalies within meteorites of, for example, neutron-rich isotopes of iron-group elements (e.g., Rotaru et al., 1992; Trinquier et al., 2007, 2009) may hint that it is also possible that some short-lived isotopes were also heterogeneously distributed in the early Solar System.

In this study more than 50 different meteorites were analysed to high-precision for their Mg isotopic composition. These results were used for three purposes. First, to detect variations in ^{26}Mg isotope anomalies that resulted from ^{26}Al-^{26}Mg decay and then use these to date the formation events of these meteorites to high precision. Second, to assess the degree of homogeneity (or otherwise) of ^{26}Al and Mg isotopes on a planetesimal scale in the proto-planetary disk in the young Solar System through analysis of a range of chondrite types . Third, examining the Mg isotope composition within a group of ultramafic meteorites to search for age related Mg isotopic variations of a single parent body. The samples analysed in this study includes samples from all classes of chondrites (with the exception of R- and K-chondrites), and a wide variety of achondrites including angrites, mesosiderites, eucrites, diogenites, aubrites, ureilites, and the unique basaltic achondrite NWA 011-NWA 2976, as well as main-group pallasites.

Chapter 2

Methods

2.1 Sample preparation

All sample preparation and digestions were conducted in the state-of-the-art clean room facilities at Victoria University of Wellington, New Zealand, with the exception of the diogenite samples provided by NASA that were processed at the University of Copenhagen, Denmark. All Mg separation work was conducted in class 10 laminar flow hoods situated in a class 100 clean laboratory. Ultrapure Seastar^{TM} acids and >18.2 MΩ Millipore® water were used in New Zealand and double distilled acid and water of even higher purity was used for the separation work conducted in Denmark.

For bulk rock analysis of meteorites, small pieces weighing between 50–200 mg were cut from larger pieces using a diamond saw to ensure that all surfaces of the processed samples were fresh. To aid digestion, most meteorite samples were then powdered using an agate mortar and pestle and 5–50 mg of each powdered sample was weighed for digestion. Samples were digested in Savillex® screw-top beakers using a mixture of concentrated HF-HNO_3 (3:1) at a temperature of 110 to 130° C on a hot-plate, followed by a sequential attack using concentrated HNO_3, HCl and HNO_3. Samples were further refluxed in aqua regia to ensure complete

dissolution of the samples. Although these digestion techniques will not dissolve pre-solar carbon-rich and oxide grains contained in chondrites, given their typical abundance in chondrite meteorites, and the Mg contents and Mg isotope ratios of these grains (Zinner, 2007), they would have negligible leverage on the Mg isotopic composition, which is dominated by the silicate-hosted Mg in the meteorites.

All chemical separations were done on aliquots of digested material equivalent to $\leq$2 mg of sample to assure that no Mg was lost due to overloading any of the chromatographic separation columns.

2.2 Chemical separation of Mg

A major aspect of this study was the development of a Mg separation technique from essentially any silicate matrix resulting in very high Mg purities of $>$ 99%, while also ensuring 100% yields. A high purity of Mg is important for isotopic measurement using multi-collector inductively coupled plasma mass spectrometry (MC-ICP-MS) as any matrix introduced into the MC-ICP-MS can result in inaccurate stable Mg isotope and mass-bias corrected ^{26}Mg* data (e.g., Galy et al., 2001; Spivak-Birndorf et al., 2009). Further, ca. 100% yields are required to ensure that no fractionation of the isotopes occurs during chromatographic separation. The technique described here, produces the required $>$ 99% Mg yields of $>$99% purity, surpassing previously reported separation techniques, which do not provide an effective separation of Mg from elements such as Mn and Ni (e.g., Baker et al., 2005; Bizzarro et al., 2005; Wiechert and Halliday, 2007; Wadhwa et al., 2003a; Teng et al., 2007; Spivak-Birndorf et al., 2009; Wadhwa et al., 2009a).

Samples were processed through a maximum of five different column separation steps (Fig. 2.1), detailed in sections 2.2.1 – 2.2.5 below. After chemical separation and prior to Mg isotope analysis all samples were screened for over 20 potential contaminants and secondary cleaning steps

were applied if significant amounts of contaminant elements (>1%) were found in the sample solution. Samples were processed in essentially the same way in both New Zealand and Denmark with the only significant difference being that the cation chemistry step conducted in Denmark was optimised to recover both Cr and Mg from the same sample, whereas in New Zealand only the cut containing Mg was collected. Each separation step is aimed to separate specific matrix elements from the desired Mg. After the final separation step, the evaporated Mg was fluxed in 1 mL of aqua regia for 12 hr at 110° C to break down any residual organic material. Samples were then converted to chloride form ready for analysis. Mg procedural blanks were always $< 0.001\%$ of the processed Mg for each sample.

2.2.1 Fe removal

The first separation step uses ∼0.5 mL Bio-Rad AG®1-X4 anion exchange resin in a 1.25 mL pipette tip column to remove Fe. Columns were precleaned with three consecutive washes of 11M HCl and MQ water each. Samples in 0.1 to 1 mL 11M HCl were loaded onto the columns and Mg eluted in four column loads (approx 3 mL) of 11M HCl, with Fe retained on the resin. Removal of Fe prior to the second, Ca-removal step is critical as both Fe and Ca compete on the TODGA resin used in this column, greatly reducing the efficiency at which Ca is removed.

2.2.2 Ca removal

Calcium was found to be the matrix element that has the most profound effect on the measured Mg isotopic composition (see Chapter 3), and its quantitative removal is therefore critical to accurate Mg isotope measurements. Following the first anion column step, samples were dissolved in 0.5 mL 3M HNO_3 and loaded onto a 1.25 mL pipette tip column containing ∼0.25 mL of Eichrom® TODGA (N,N,N′,N′-tetra-n-octyldiglycolamide)

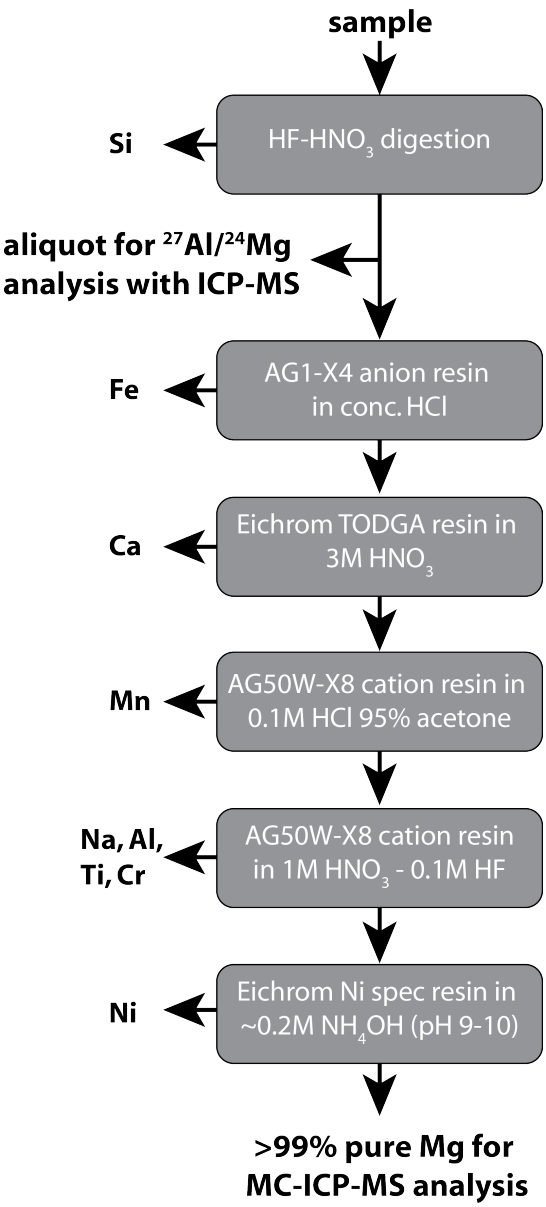

Figure 2.1: Schematic of the chemical separation procedures used to purify Mg from the samples.

resin. In weak nitric acid, calcium is retained by this resin while Mg is completely unaffected (Horwitz et al., 2005). Magnesium was eluted in 1.5 column loads (approximately 1.5 mL) of 3M HNO_3. This separation step was repeated two to three times for samples with several weight percent calcium in the original sample to ensure >99% removal of Ca.

2.2.3 Na, Al, Ti, Cr removal

Several elements, including Na, Al, Ti and Cr that remain in the matrix after the first two steps can be efficiently removed on a cation exchange column using weak nitric acid containing a trace of HF. Samples dissolved in 0.5 mL of 1M HNO_3-0.1M HF were loaded onto columns comprising ~1 mL of Bio-Rad AG®50W-X8 200-400 mesh resin, and Na, Al, Ti and Cr were eluted in 5 mL of 1M HNO_3-0.1M HF. Mg was then collected in a further 16 mL of 1M HNO_3-0.1M HF. The use of trace amounts of HF in the eluting acid has two advantages over cation exchange separation techniques based on either HNO_3 or HCl without HF. First, any remaining Fe is eluted prior to Mg. Second, and more importantly, the elution of Al and Ti is rapid and quantitative (100%) in the presence of trace amounts of HF. Without sufficient (i.e., excess) amounts of HF in the eluted solution both Al and Ti can exhibit two elution peaks - one early in the elution scheme and the second later in the elution scheme where it partially overlaps with the Mg elution (Fig. 2.2). This column step was usually repeated at the end to remove any remaining Na blank that may have been introduced in subsequent separation steps.

2.2.4 Mn removal

Manganese is difficult to separate from magnesium in either HCl or HNO_3 media on a cation exchange column. However, the distribution coefficient of Mn decreases significantly in the presence of high acetone concentrations (>90%) (Strelow et al., 1971). Taking advantage of this effect, samples

were dissolved in 200 μL 12M HCl and then diluted to a 0.5M HCl-95% acetone mixture using 2 mL of AR grade acetone. If, as observed in some cases using large samples, this results in a phase separation of HCl and acetone, up to an additional 2 mL of the 0.5M HCl-95% acetone mixture was added to produce a homogeneous solution.

The sample solution was loaded onto a column containing 1 mL of Bio-Rad AG®AG50W-X8 200-400 mesh resin and Mn eluted in 2-4 mL of 0.5M HCl-95% acetone, such that a total volume of 6 mL 0.5M HCl-95% acetone was loaded onto the column. Mg was then collected in 8 mL of 6M HCl.

2.2.5 Ni removal

Nickel is also very difficult to separate from Mg using conventional cation exchange chemistry. However, Eichrom Technologies provide a resin that is specifically designed to retain Ni in alkaline conditions on a ion exchange column. The resin essentially relies on a previously developed liquid-liquid extraction technique that uses a solution of dimethylglyoxime (DMG) onto a resin by incorporation of DMG into the pore spaces of an inert polymer support. Both methods, liquid-liquid extraction and Ni-spec chemistries, are described in Quittè and Oberli (2006). The method described by Quittè and Oberli (2006), however, uses citric acid as a buffer solution, which results in an organic residue that is hard to decompose and may cause unwanted analytical artefacts during Mg isotopic analysis. To avoid this, the chemistry applied here uses an ammonium hydroxide solution mixed with dilute HCl to adjust the pH of the sample solution.

Samples were typically first dissolved in 1 mL of 0.1M HCl and 2.5 mL of $>$18.2 MΩ Millipore® water and 0.5 mL of concentrated NH_4OH then added, resulting in a final solution with a pH of 9-10. The volume of solution used was adjusted depending on sample size to ensure the samples were fully in solution in the high-alkali conditions. The sample solution was then loaded onto a column containing $\sim$1 mL of Eichrom Ni-

spec resin and the Mg eluted using an additional 10 mL of ∼0.2M NH_4OH solution adjusted to a pH of 8-9 with HCl.

2.3 ^{27}Al/^{24}Mg ratio measurements

Aliquots of fully digested samples were taken prior to chemical separation and analysed for $^{27}Al/^{24}Mg$ using an Agilent® 7500CS ICP-MS. A helium collision cell was used to minimise interferences on Al and Mg isotopes (^{27}Al, ^{24}Mg and ^{25}Mg). Sample analyses were bracketed with analyses of gravimetrically prepared solutions (Al/Mg = 2.0 and 0.1) made from Aristar® single element ICP-MS solutions. The reproducibility for the Al/Mg measurements was taken as ± 2% (2 sd), based on repeated measurements of USGS basaltic rock standards BCR-2 and BHVO-2. Repeated analyses of these standards yielded $^{27}Al/^{24}Mg$ ratios of 3.81 ± 0.05 (2 sd; BCR-2, n = 3, Table 2.1) and 1.90 ± 0.02 (2 sd; BHVO-2, n = 6), which are within error of the recommended values for these standards: 3.76 ± 0.15 and 1.87 ± 0.08, respectively (GeoRem, 2010).

Doping tests were carried out to evaluate the veracity of the Al/Mg measurements. Addition of Ca to the Al/Mg = 2.0 solution up to Ca/Mg = 4 resulted in no measurable deviation (< 1%) in the measured Al/Mg value compared to that obtained for the pure Al/Mg = 2.0 solution, while there is a measureable offset when measuring the Al/Mg ratios with the MC-ICP-MS (Table 2.2).

$^{27}Al/^{24}Mg$ ratios of diogenite samples supplied by NASA (see Chapter 5) were measured by a different approach using a ^{27}Al-^{25}Mg spike (Al:Mg = 1:1). Samples were doped with small amounts of spike increasing the Mg concentration in the sample by less than 10%. The doped sample was measured against a pure sample using a Neptune MC-ICP-MS and the standard-sample bracketing technique. The $^{27}Al/^{24}Mg$ ratio in the undoped sample was calculated based on the change in the Mg isotopic composition and the increase in the Al/Mg ratio of the doped sample us-

Table 2.1: Summary of the $^{27}Al/^{24}Mg$ ratios of BHVO-2 and BCR-2 standards measured over the course of this study. Reference values are from GeoRem (2010).

$^{27}Al/^{24}Mg$	
BHVO-2	BCR-2
1.96	3.79
1.94	3.78
1.90	3.82
1.90	
1.90	
1.93	
1.92 ± 0.05	**3.80 ± 0.04**
reference:	
(1.87 ± 0.08)	*(3.76 ± 0.15)*

ing the AlMg_Nept data reduction scheme of the Iolite software package (Hellstrom et al., 2008).

2.4 Mg isotope measurements by Nu MC-ICP-MS

Mg isotopes were measured with a Nu Plasma high-resolution MC-ICP-MS operated in pseudo-high resolution mode. As opposed to true high resolution mode, where both the width of source entrance slit and collector defining slit are reduced, the pseudo-high resolution mode only reduces the width of the source entrance slit. Because of this the pseudo-high resolution mode can only resolve interferences that are on the same side of the peak. The purified Mg was dissolved in 0.1M HCl and solutions with concentrations of ~0.75 ppm to 3 ppm Mg were introduced into the plasma via a DSN-100 desolvating nebuliser system at an uptake rate of

Table 2.2: Summary of Ca doping tests of the Al/Mg = 2.0 standard solution with variable amounts of Ca and the resulting effect on the measured Al/Mg to the pure standard using either the ICP-MS, the MC-ICP-MS in low resolution, high sensitivity mode and the MC-ICP-MS using the pseudo-high resolution mode as used for Mg isotope analysis.

Ca/Mg ratio (wt.%)	$^{27}Al/^{24}Mg$ (% deviation)		
	ICP-MS	MC ICP-MS	
		(high sensitivity)	(high resolution)
2	+0.6	-	-
4	+0.9	-8.3	-14.6

approximately 0.12 mL/min. Sensitivity of the MC-ICP-MS was reduced to approximately 15 V per ppm total ion beam by analysing in pseudo-high-resolution mode and by reducing the transfer vacuum to ca. 2 mbar in order to increase the signal stability. Use of the pseudo-high-resolution mode allowed for an effective mass resolution of between 2000 and 2500, which enables resolution of all molecular interferences on the high mass side (e.g., $^{12}C_2^+$, $^{12}C^{14}N^+$) of Mg. The only high mass interference not fully resolved at this mass resolution is $^{24}Mg^1H^+$ on ^{25}Mg, but this interference is resolved at this resolution at the 70% level. Potential interferences of doubly charged species on the low mass side of Mg cannot be resolved using the pseudo-high-resolution method, which is one of the reasons that it was important to analyse highly pure Mg solutions. Doping tests indicated that at the level of purity of our Mg solutions, these interferences are present at much lower levels than the analytical precision (see Chapter 3).

Two different setups were used to monitor ^{24}Mg, ^{25}Mg and ^{26}Mg, either using the L5, Ax and H6 Faraday collectors equipped with 10^{11} Ohm resistors or using the L4, Ax and H5 collectors where the L4 collector was equipped with a 10^{10} Ohm resistor to allow larger ion beams of ca. 25-50,

3-6 and 3-6 V to be measured on masses 24, 25 and 26 respectively. The larger ion beams used in the second setup can under ideal circumstances improve the internal errors by a factor of $\sim$ 1.5.

Single analyses consisted of four blocks of 120 s of baseline and 400 s of data acquisition, making a total of 480 s of baseline measurements and 1600 s of data acquisition. All isotopic measurements in this study were conducted using the standard-sample bracketing technique, where the isotope ratios are expressed as per mil (‰) deviations from the mean Mg isotopic composition measured in the bracketing standards:

$$\delta^x Mg = [(^x Mg/^{24} Mg)_{sample}/(^x Mg/^{24} Mg)_{standard} - 1] \times 10^3, \quad (2.1)$$

and x is either 25 or 26. The mass-independent ^{26}Mg abundance (δ^{26}Mg*) in the samples was corrected for instrumental mass bias by normalising the measured ^{26}Mg/^{24}Mg ratios to a ^{25}Mg/^{24}Mg ratio of 0.12663 (Catanzaro et al., 1966) using the exponential law (β = 0.511). Uncertainties on sample analyses were calculated as weighted means of replicate analyses and quadratically incorporate the errors of the sample runs as well as those of the bracketing standards, resulting in an internal precision on the mass-bias-corrected ^{26}Mg/^{24}Mg (δ^{26}Mg*) that is $\pm$ 0.021 to $\pm$ 0.012‰. Typically, where sufficient Mg was available, each sample analysis reported represents the mean of 10 individual measurements preferably carried out over a continuous 14 hr period and consuming about 30-100 μg of Mg (Table 2.3). The reported errors on the δ^{26}Mg* for a single sample measured 10 times is 2 se of the 10 separate measurements combined as a weighted mean using Isoplot (Ludwig, 2003), resulting in uncertainties that are typically $\pm$0.0050 to $\pm$0.0060‰ (2 se). These errors are internal errors. However the external reproducibility of δ^{26}Mg* is estimated to be less than a factor of 1.5 larger than the 2 se based on repeated measurements of samples and terrestrial standards standards with gravimetrically prepared excesses in ^{26}Mg (see Chapter C:basalt).

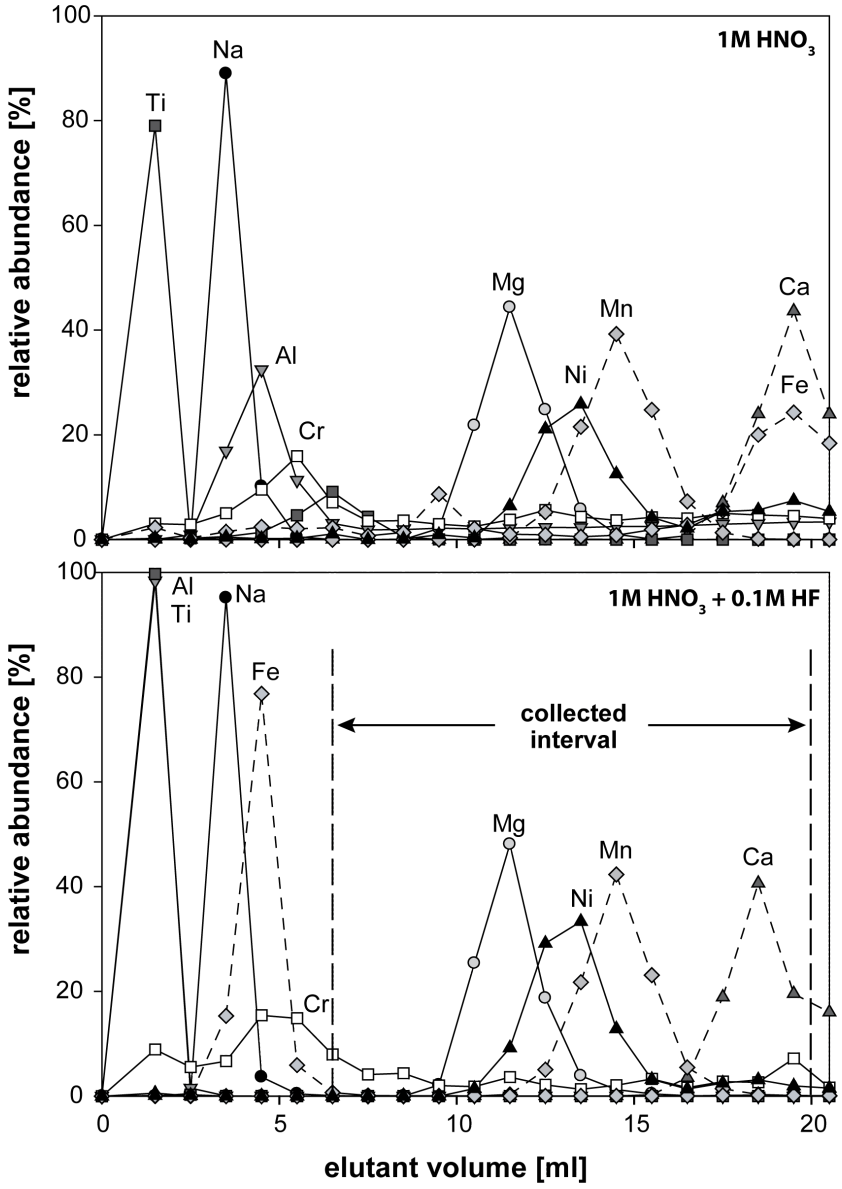

Figure 2.2: Elution curves for Na, Mg, Al, Ca, Ti, Cr, Mn, Fe and Ni through a 1 mL cation exchange column of Bio-Rad AG50W-X8 200-400 mesh resin loaded in 1M HNO_3 and 1M HNO_3-0.1M HF for the basalt standard BCR-2. Each sample was loaded in 0.5 mL and cuts collected in 1 mL intervals. Dotted lines highlight elements that are removed in other chemical separation steps prior to the final cation exchange separation step.

Table 2.3: An example of a typical Mg isotope analysis using the Nu Plasma MC-ICP-MS. Ten single analyses of the sample (NWA 1877), bracketed by the Mg standard DSM-3, are combined as a weighted mean in the reported δ^{26}Mg*, δ^{26}Mg and δ^{25}Mg. Uncertainties in the $\frac{^{x}Mg}{^{24}Mg}$ ratios are shown in brackets and incorporate the error on the bracketing standards. fc = fractionation corrected using the exponential law, raw = ratio as measured.

Sample	$\frac{^{26}Mg}{^{24}Mg}_{fc}$	δ^{26}Mg* (‰)	$\frac{^{26}Mg}{^{24}Mg}_{raw}$	δ^{26}Mg (‰)	$\frac{^{25}Mg}{^{24}Mg}_{raw}$	δ^{25}Mg (‰)
DSM-3	0.1395065(11)		0.1557185(10)		0.1339478(7)	
NWA 1877	0.1395079(10)	+0.0140 ± 0.0204	0.1556945(12)	-0.122 ± 0.017	0.1339369(7)	-0.067 ± 0.014
DSM-3	0.1395054(10)		0.1557086(8)		0.1339440(6)	
NWA 1877	0.1395093(10)	+0.0143 ± 0.0206	0.1556858(9)	-0.163 ± 0.018	0.1339320(6)	-0.091 ± 0.014
DSM-3	0.1395092(11)		0.1557137(13)		0.1339444(8)	
NWA 1877	0.1395076(11)	-0.0050 ± 0.0216	0.1556902(11)	-0.240 ± 0.021	0.1339341(7)	-0.123 ± 0.015
DSM-3	0.1395074(10)		0.1557413(10)		0.1339567(6)	
NWA 1877	0.1395089(9)	+0.0219 ± 0.0197	0.1557462(11)	-0.145 ± 0.019	0.1339586(6)	-0.087 ± 0.013
DSM-3	0.1395043(11)		0.1557962(9)		0.1339837(6)	
NWA 1877	0.1395073(10)	+0.0086 ± 0.0202	0.1557744(9)	-0.287 ± 0.016	0.1339719(6)	-0.152 ± 0.012
DSM-3	0.1395079(10)		0.1558421(8)		0.1340007(5)	
NWA 1877	0.1395066(10)	-0.0043 ± 0.0207	0.1557741(12)	-0.290 ± 0.020	0.1339724(6)	-0.142 ± 0.014
DSM-3	0.1395065(11)		0.1557965(12)		0.1339822(7)	
DSM-3	0.1395073(9)		0.1557414(9)		0.1339567(6)	
NWA 1877	0.1395060(10)	-0.0054 ± 0.0206	0.1557466(14)	-0.196 ± 0.022	0.1339606(8)	-0.092 ± 0.015
DSM-3	0.1395062(11)		0.1558128(9)		0.1339892(6)	
NWA 1877	0.1395052(12)	-0.0014 ± 0.0225	0.1556895(24)	-0.536 ± 0.032	0.1339338(11)	-0.287 ± 0.019
DSM-3	0.1395046(11)		0.1557332(8)		0.1339553(6)	
NWA 1877	0.1395066(10)	+0.0125 ± 0.0202	0.1556992(9)	-0.215 ± 0.019	0.1339390(6)	-0.118 ± 0.014
DSM-3	0.1395051(10)		0.1557322(14)		0.1339542(8)	
NWA 1877	0.1395078(10)	+0.0143 ± 0.0205	0.1556886(10)	-0.346 ± 0.020	0.1339342(6)	-0.179 ± 0.014
DSM-3	0.1395065(10)		0.1557529(9)		0.1339622(6)	
DSM-3	0.1395018(10)		0.1554214(9)		0.1338190(6)	
NWA 1877	0.1395042(10)	+0.0082 ± 0.0203	0.1554792(7)	+0.326 ± 0.014	0.1338433(6)	+0.161 ± 0.012
DSM-3	0.1395043(10)		0.1554356(8)		0.1338245(6)	
NWA 1877	0.1395031(10)	-0.0072 ± 0.0196	0.1553837(7)	-0.461 ± 0.015	0.1338020(6)	-0.230 ± 0.012
DSM-3	0.1395039(10)		0.1554752(9)		0.1338410(6)	
NWA 1877	0.1395051(10)	-0.0011 ± 0.0207	0.1554203(8)	-0.237 ± 0.014	0.1338172(5)	-0.117 ± 0.012
DSM-3	0.1395066(11)		0.1554390(7)		0.1338248(6)	
NWA 1877	0.1395045(10)	-0.0065 ± 0.0201	0.1554137(7)	-0.229 ± 0.013	0.1338148(5)	-0.113 ± 0.012
DSM-3	0.1395042(10)		0.1554597(9)		0.1338350(6)	
DSM-3	0.1395038(10)		0.1555607(7)		0.1338795(6)	
NWA 1877	0.1395026(10)	-0.0061 ± 0.0209	0.1555366(7)	-0.164 ± 0.012	0.1338697(5)	-0.080 ± 0.012
DSM-3	0.1395031(10)		0.1555636(6)		0.1338812(6)	
NWA 1877	(n = 15)	+0.0040 ± 0.0052		-0.259 ± 0.069		-0.134 ± 0.035

2.5 Mg isotope measurements by Neptune MC-ICP-MS

Mg isotope data presented in Chapter 5 were measured with a Thermo Finnigan Neptune MC-ICP-MS operated in medium resolution mode. Following chemical separation, Mg was dissolved in 2.5% HNO_3 and solutions with concentrations of 4 to 5 ppm Mg were introduced into the plasma using a spray chamber with an uptake rate of approximately 60 μL/min. Machine sensitivity was increased through use of an X-cone, resulting in a 20 - 25 V signal per ppm Mg. The medium resolution mode allowed for an effective mass resolution of around 2500, which allows all molecular interferences on the high mass side (e.g., $^{12}C_2^+$, $^{12}C^{14}N^+$) of Mg to be resolved, with the exception of Mg-hydrides. ^{24}Mg, ^{25}Mg and ^{26}Mg were monitored with the L3, Ax and H3 Faraday collectors. The L3 collector was equipped with a 10^{10} Ohm resistor allowing ion beams of ca. 100, 14 and 14 V to be measured on masses 24, 25 and 26 respectively. Single analyses consisted of one block of 300 s of baseline and 100 16 s integrations. All isotopic measurements in this study were conducted using the standard-sample bracketing technique, with a peak center conducted prior to each standard analysis. Each sample was measured 10 times, with internal errors on the mass-bias corrected δ^{26}Mg* of single analysis of 0.0030 to 0.0050‰ (Table 2.4). All isotope calculations were made off line using the 'Mg_Neptune' data reduction scheme in the Iolite software package (see appendix and Bizzarro et al., 2010) with a 3 sd outlier rejection for single integrations and the spline_smooth_auto function to fit the spline. Reported Mg isotope ratios are weighted means of the 10 analyses with 2 se values that incorporate the error on the spline fit though the standard analyses. The final reported error on the δ^{26}Mg* for a single sample is typically $\pm$0.0010 to $\pm$0.0020‰ (2 se), and although these errors are internal errors, the external reproducibility on δ^{26}Mg* is estimated to be 0.0025‰ for the described analytical conditions on the basis of repeated analysis of

various standards that will be presented in Bizzarro et al. (2010).

Table 2.4: An example of the Mg isotope analysis of a sample (diogenite NWA 1877) using the Thermo Finnigan Neptune MC-ICP-MS. Ten single analyses of the sample, bracketed by the Mg standard DSM-3, are shown in chronological order. δ^{26}Mg*, δ^{26}Mg and δ^{25}Mg shown are the difference from the spline fit through the standard analyses. The final δ^{26}Mg*, δ^{26}Mg and δ^{25}Mg of the sample are the weighted average with the 2 se including the uncertainty on the spline fit through the standards. Uncertainties in the $\frac{^{x}Mg}{^{24}Mg}$ ratios are shown in brackets, raw = ratio as measured, fc = fractionation corrected using the exponential law, std cor = corrected to the known standard composition of DSM-3.

Sample	$\frac{^{25}Mg}{^{24}Mg}_{raw}$	$\frac{^{26}Mg}{^{24}Mg}_{raw}$	$\frac{^{26}Mg}{^{24}Mg}_{fc}$	δ^{26}Mg* (‰)	$\frac{^{26}Mg}{^{24}Mg}_{stdcor}$	δ^{26}Mg (‰)	$\frac{^{25}Mg}{^{24}Mg}_{stdcor}$	δ^{25}Mg (‰)
DSM-3 (1)	0.1345918(5)	0.1570667(9)	0.1393750(6)	-0.0002 ± 0.0043	0.1393751(8)	+0.0009 ± 0.0057	0.1266301(5)	+0.0006 ± 0.0037
DSM-3 (2)	0.1345917(8)	0.1570672(16)	0.1393750(6)	-0.0002 ± 0.0041	0.1393750(14)	0.0000 ± 0.0099	0.1266300(7)	0.0000 ± 0.0057
DSM-3 (3)	0.1345904(7)	0.1570647(13)	0.1393753(6)	+0.0018 ± 0.0042	0.1393749(12)	-0.0006 ± 0.0085	0.1266299(6)	-0.0004 ± 0.0050
DSM-3 (4)	0.1345909(7)	0.1570658(13)	0.1393749(6)	-0.0007 ± 0.0041	0.1393751(11)	+0.0010 ± 0.0082	0.1266301(6)	+0.0005 ± 0.0049
DSM-3 (5)	0.1345901(7)	0.1570642(14)	0.1393746(6)	-0.0026 ± 0.0044	0.1393748(13)	-0.0017 ± 0.0092	0.1266299(7)	-0.0009 ± 0.0051
DSM-3 (6)	0.1345928(7)	0.1570719(13)	0.1393753(6)	+0.0020 ± 0.0042	0.1393752(13)	+0.0016 ± 0.0090	0.1266301(6)	+0.0007 ± 0.0051
DSM-3 (7)	0.1345922(7)	0.1570698(12)	0.1393748(6)	-0.0015 ± 0.0046	0.1393749(10)	-0.0008 ± 0.0075	0.1266300(6)	-0.0003 ± 0.0050
DSM-3 (8)	0.1345923(5)	0.1570711(7)	0.1393752(6)	+0.0011 ± 0.0040	0.1393750(7)	0.0000 ± 0.0047	0.1266300(4)	-0.0001 ± 0.0035
DSM-3 (9)	0.1345931(6)	0.1570728(12	0.1393748(6)	-0.0014 ± 0.0041	0.1393751(11)	+0.0004 ± 0.0076	0.1266300(6)	+0.0003 ± 0.0045
DSM-3 (10)	0.1345928(5)	0.1570728(9)	0.1393751(5)	+0.0006 ± 0.0039	0.1393749(9)	-0.0007 ± 0.0062	0.1266299(5)	-0.0005 ± 0.0039
DSM-3 (11)	0.1345949(7)	0.157078(15)	0.1393751(7)	+0.0007 ± 0.0048	0.1393752(14)	+0.0011 ± 0.0098	0.1266301(6)	+0.0006 ± 0.0051
NWA 1877 (1)	0.1345725(7)	0.1570228(13)	0.1393750(6)	0.0000 ± 0.0043	0.1393348(12)	-0.2884 ± 0.0083	0.1266114(6)	-0.1472 ± 0.0048
NWA 1877 (2)	0.1345713(6)	0.1570209(12	0.1393751(6)	+0.0004 ± 0.0041	0.1393352(10)	-0.2853 ± 0.0072	0.1266116(5)	-0.1454 ± 0.0043
NWA 1877 (3)	0.1345694(7)	0.1570163(14)	0.1393746(5)	-0.0029 ± 0.0038	0.1393315(13)	-0.3125 ± 0.0094	0.1266100(7)	-0.1576 ± 0.0054
NWA 1877 (4)	0.1345701(7)	0.1570189(15)	0.1393748(5)	-0.0016 ± 0.0035	0.1393346(13)	-0.2901 ± 0.0092	0.1266110(6)	-0.1500± 0.0048
NWA 1877 (5)	0.1345702(6)	0.157019(11)	0.1393746(6)	-0.0026 ± 0.0042	0.1393316(11)	-0.3115 ± 0.0081	0.1266101(6)	-0.1574 ± 0.0046
NWA 1877 (6)	0.1345702(6)	0.1570195(11)	0.1393747(6)	-0.0023 ± 0.0042	0.1393288(10)	-0.3317 ± 0.0068	0.1266087(5)	-0.1681 ± 0.0043
NWA 1877 (7)	0.1345719(8)	0.1570238(17)	0.1393747(6)	-0.0023 ± 0.0040	0.1393341(16)	-0.2934 ± 0.0111	0.1266111(7)	-0.1496 ± 0.0057
NWA 1877 (8)	0.1345724(6)	0.1570258(14)	0.1393752(6)	+0.0014 ± 0.0040	0.1393338(12)	-0.2955 ± 0.0089	0.1266109(6)	-0.1511 ± 0.0049
NWA 1877 (9)	0.1345720(6)	0.1570247(11)	0.1393747(6)	-0.0019 ± 0.0041	0.1393327(10)	-0.3035 ± 0.0070	0.1266104(5)	-0.1549 ± 0.0042
NWA 1877 (10)	0.1345737(6)	0.1570288(12)	0.1393745(5)	-0.0038 ± 0.0037	0.1393338(12)	-0.2960 ± 0.0084	0.1266111(6)	-0.1492 ± 0.0048
		NWA 1877	(n = 10)	-0.0016 ± 0.0010		-0.3008 ± 0.0093		-0.1530 ± 0.0043

2.6 Choice of Mg standard

For precise and accurate δ^{26}Mg* measurements it is crucial to use a magnesium standard that is not only widely available but also has a stable isotopic composition that is representative of Earth and closely matches the Solar System Mg isotopic composition. This is because instrumental mass-bias in the MC-ICP-MS is corrected for using the kinetic (= exponential) fractionation law. However, the difference in slope between equilibrium and kinetic fractionation could result in artificial δ^{26}Mg* anomalies if either the standard or the sample have experienced equilibrium fractionation. For example, a 0.100‰ difference in the δ^{25}Mg composition resulting from pure equilibrium fractionation produces an erroneous, negatively correlated ~0.004‰ difference per between sample and standard. The isotopic measurements conducted to determine δ^{26}Mg* in the various materials analysed here were bracketed using DSM-3 (Galy et al., 2003) and/or Mg separated from J11 mantle olivine ($\delta^{25}Mg_{DSM-3}$ = -0.110 ± 0.006‰; Handler et al., 2009), an in-house standard subjected to the same Mg separation procedure as the analysed samples. The J11 olivine has a stable Mg isotopic composition that more closely represents the Mg isotopic composition of the Earth (Handler et al., 2009; Bizzarro et al., 2010). If the slight isotopic difference between DSM-3 and J11 (or bulk Earth) is the result of equilibrium fractionation processes (Young and Galy, 2004; Tipper et al., 2008) results could potentially be biased by up to +0.004‰. However, the data in this study cannot resolve such a potential offset and hence, even though DSM-3 is not representative of the Earth's Mg isotopic composition, it is generally preferred over J11 olivine, which has to be processed through chemical separation and is not as widely available as DSM-3.

2.7 Major and trace element determinations for diogenites

Major and trace element compositions for the diogenites analysed in Chapter 5 were determined at Victoria University of Wellington using a JEOL JXA-8230 Superprobe electronprobe microanalyser (EPMA) (major elements) and an Agilent 7500CS ICP-MS coupled to a New Wave deep UV laser (trace elements). Analyses were conducted on polished half-mounts of small pieces of diogenite. EPMA measurements were made using an accelerating voltage of 15 kV, a beam current of 12 nA and a focused beam (spot $<$0.5 μm). X-ray intensities were calibrated against concentrations using Johnstown hypersthene (Cr, Mg, Si, Al, Fe), Kakanui augite (Ti, Na, Ca) and synthetic MnO (Mn). Three secondary standards, Johnstown hypersthene (USNM 746), Kakanui augite (NMNH 122142) and Natural Bridge diopside (NMNH 117733), were used throughout the sessions (Table 2.5; Jarosewich et al., 1980).

Trace elements were measured on the same mount close to the electron microprobe pits (Table 2.6). Each sample was analysed 5 to 11 times. Each analysis consisted of approximately 60 seconds background measurement and 60 seconds ($\sim$ 55 scans) of data acquisition with an ablating laser beam. Sample analyses were typically bracketed every five analysis with a measurement of the calibration standard (BCR-2G).

Iolite software with the 'trace element IS' data reduction scheme was used for all data treatment (Hellstrom et al., 2008; Woodhead et al., 2008). Standards were interpolated using the 'spline smooth auto' function. Baselines and all integrations were treated with a 3 sd outlier rejection. The background corrected data was converted to absolute element concentrations using the element concentrations in the BCR-2 glass standard and the silicon concentration in the glass shards measured with the EPMA using ^{29}Si for internal normalisation as schemacticaly shown in equation 2.2 and 2.3:

Table 2.5: Summary of the EPMA analysis of Johnstown diogenite hypersthene (USNM 746), Kakanui augite (NMNH 122142) and Natural Bridge diopside (NMNH 117733) used as secondary reference standards for analysis of orthopyroxene in diogenites, and their relative difference from the recommended compositions (Jarosewich et al., 1980).

	Hypersthene Johnstown meteorite n = 77		Diopside Natural Bridge, NY n = 60		Augite Kakanui, NZ n = 25	
	av. (2 sd)	% diff.	av. (2 sd)	% diff.	av. (2 sd)	% diff.
SiO_2	54.06(59)	0	54.48(2.05)	-1	49.78(72)	-2
TiO_2	0.09(3)	-46	0.00(1)	-	0.73(4)	-1
Al_2O_3	1.15(22)	-6	0.08(15)	-27	8.41(87)	-4
Cr_2O_3	0.50(6)	-34	0.04(4)	-	0.16(9)	7
FeO	14.90(87)	-2	0.15(18)	-39	6.31(24)	17
MnO	0.49(5)	0	0.02(3)	-61	0.10(11)	-23
MgO	26.79(42)	0	18.33(1.05)	0	16.30(81)	-2
CaO	1.39(29)	-8	25.59(1.02)	0	15.91(27)	1
Na_2O	0.01(2)	-	0.05(11)	-84	1.29(9)	2
Total	99.39(1.59)	-1	97.35(2.76)	-2	98.98(1.82)	-2

$$X_{CPS_{av.}} = \sum \left(\frac{Si_{CPS_{av.}} - Si_{CPS_{bg.}}}{Si_{CPS_{scan}} - Si_{CPS_{bg.}}} * (X_{CPS_{scan}} - X_{CPS_{bg.}}) \right) * \frac{1}{\sum scan} \quad (2.2)$$

$$X_{ppm} = \frac{X_{ppm_{std.}}}{X_{CPS_{std.}}} * X_{CPS_{av.}} * \frac{Si_{ppm}}{Si_{CPS_{av.}}}, \quad (2.3)$$

where X is an element. Absolute concentrations were obtained by correcting the counts per second (cps) for each element relative to the known concentration of Si in the samples. This procedure takes into account the different locations of the sample and standard in the ablation chamber and different ablation efficiencies of different types of material, which result in different gains. To assess accuracy and reproducibility, BHVO-2 glass was also analysed in a session with the diogenites (Table 2.7). This test shows that, using the BCR-2 glass as standard, very accurate and reproducible results can be achieved for BHVO-2 glass. However, it cannot assess the effects of the different matrices of the standard glass and the sample. Furthermore, it should be noted that trace element concentrations in the diogenites orthopyroxenes are significantly lower than in either BCR-2 or BHVO-2. Consequently, although absolute trace element concentrations should be treated with caution, one can be confident when comparing relative trace element differences among the various diogenite samples.

Table 2.6: Typical tuning and analytical parameters for the LA-ICP-MS.

Plasma condition			**Ion lenses**		
RF power	:	1500 W	Extract 1	:	4.8 V
Smpl. Depth	:	7 mm	Extract 2	:	-120 V
Torch - H	:	0.2 mm	Omega Bias-cs	:	-40 V
Torch - V	:	-0.2 mm	Omega Lens-cs	:	9.4 V
Carrier Gas (Ar)	:	0.82 L/min	Cell Entrance	:	-40 V
Optional Gas (He)	:	89 %	QP Focus	:	2 V
			Cell exit	:	-40 V
Octopole parameters			**Detector parameters**		
OctP RF	:	180 V	Discriminator	:	8 mV
OctP Bias	:	-6 V	Analog HV	:	1660 V
			Pulse HV	:	1370 V
Q-pole parameters			**Reaction cell**		
AMU Gain	:	122	Reaction mode	:	OFF
AMU Offset	:	124			
Axis Gain	:	0.9991			
Axis Offset	:	-0.08			
QP Bias	:	-3 V			

Dwell times

10 ms	:	^{29}Si, ^{25}Mg, ^{47}Ti, ^{53}Cr, ^{55}Mn, ^{88}Sr
20 ms	:	^{7}Li, ^{43}Ca, ^{45}Sc, ^{51}V, ^{59}Co, ^{60}Ni, ^{63}Cu, ^{66}Zn, ^{71}Ga, ^{85}Rb, ^{88}Sr, ^{89}Y, ^{90}Zr, ^{93}Nb, ^{95}Mo, ^{133}Cs, ^{138}Ba, ^{139}La, ^{140}Ce, ^{141}Pr, ^{146}Nd, ^{147}Sm, ^{153}Eu, ^{157}Gd, ^{159}Tb, ^{163}Dy, ^{165}Ho, ^{166}Er, ^{172}Yb, ^{175}Lu, ^{178}Hf, ^{181}Ta, ^{182}W, ^{208}Pb, ^{232}Th, ^{238}U

Number of scans

background	:	20-40
elements	:	55-60

Laser setting

wavelength	:	193 nm
frequency	:	5 Hz
output	:	65 %
mode: spot	:	75 μm

Table 2.7: Mean trace element data for five repeated BHVO-2G analyses measured using a 75 μm laser spot diameter with BHVO-2G reference values taken from the literature (GeoRem, 2010) shown for comparison.

isotope	**mean**±2 sd **ppm**	± 2 sd %	**ref. values ppm**	**diff.** %
^{7}Li	**4.40**±0.24	5.4	**4.4**[1]	0.0
^{25}Mg	**7.14**±0.14*	2.0	**7.13**[2]	0.1
^{43}Ca	**11.4**±0.2*	2.1	**11.4**[2]	0.1
^{45}Sc	**33**±1	3.0	**33**[1]	0.0
^{47}Ti	**16778**±625	3.7	**16300**[1]	2.9
^{51}V	**309**±14	4.4	**308**[1]	0.4
^{53}Cr	**294**±17	5.8	**293**[1]	0.4
^{55}Mn	**0.17**±0.01*	5.6	**0.17**[2]	0.5
^{59}Co	**44.2**±2.3	5.1	**44**[1]	0.4
^{60}Ni	**116**±6	5.3	**116**[1]	0.3
^{63}Cu	**127**±7	5.2	**127**[1]	0.3
^{66}Zn	**102**±6	5.8	**102**[1]	0.5
^{71}Ga	**22**±1	5.5	**22**[1]	0.3
^{85}Rb	**9.2**±0.6	6.1	**9.2**[1]	0.2
^{88}Sr	**397**±23	5.7	**396**[1]	0.4
^{89}Y	**26.0**±1.6	6.1	**26**[1]	0.2
^{90}Zr	**170**±10	5.9	**170**[1]	0.2
^{93}Nb	**18.4**±1.1	5.8	**18.3**[1]	0.4
^{95}Mo	**3.8**±0.37	9.6	**3.8**[2]	0.9
^{133}Cs	**0.1**±0.0	19.2	**0.1**[1]	2.0
^{137}Ba	**132**±8	6.3	**131**[2]	0.5
^{139}La	**15.3**±1.0	6.8	**15.2**[2]	0.4
^{140}Ce	**37.8**±2.4	6.4	**37.6**[2]	0.5
^{141}Pr	**5.37**±0.36	6.8	**5.35**[1]	0.4
^{146}Nd	**24.7**±1.9	7.9	**24.5**[2]	0.8
^{147}Sm	**6.2**±0.6	9.7	**6.1**[2]	1.0
^{153}Eu	**2.09**±0.21	10.1	**2.07**[2]	0.9
^{157}Gd	**6.19**±0.61	9.9	**6.16**[2]	0.4
^{159}Tb	**0.93**±0.08	9.1	**0.92**[1]	0.6
^{163}Dy	**5.31**±0.50	9.3	**5.28**[2]	0.6
^{165}Ho	**0.99**±0.10	10.2	**0.98**[1]	0.9
^{166}Er	**2.57**±0.27	10.4	**2.56**[2]	0.5
^{169}Tm	**0.34**±0.05	14.8	**0.34**[1]	0.9
^{172}Yb	**2.02**±0.25	12.1	**2.01**[2]	0.7
^{175}Lu	**0.282**±0.043	15.2	**0.279**[2]	1.1
^{178}Hf	**4.36**±0.42	9.6	**4.32**[1]	0.9
^{181}Ta	**1.16**±0.12	10.1	**1.15**[1]	0.6
^{182}W	**0.23**±0.05	21.2	**0.23**[2]	1.5
^{208}Pb	**1.7**±0.2	10.5	**1.7**[1]	0.5
^{232}Th	**1.23**±0.13	10.4	**1.22**[1]	0.8
^{238}U	**0.408**±0.055	13.4	**0.403**[3]	1.2

* in oxide wt.%, [1]pref. GeoRem values, [2]Jochum et al. (2005), [3]Willbold and Jochum (2005)

Chapter 3

^{26}Al-^{26}Mg dating of asteroidal magmatism in the young Solar System

Abstract

We present high precision Mg isotope data for most classes of basaltic meteorites including eucrites, mesosiderite silicate clasts, angrites and the ungrouped Northwest Africa (NWA) 2976 measured by pseudo-high-resolution multiple-collector inductively coupled plasma mass spectrometry and utilising improved techniques for chemical purification of Mg. With the exception of the angrites Angra dos Reis, Lewis Cliff (LEW) 86010, NWA 1296 and NWA 2999 and the diogenite Bilanga, which have either been shown to have young ages by other dating techniques or have low Al/Mg ratios, all bulk samples of basaltic meteorites have ^{26}Mg excesses (δ^{26}Mg* = +0.0135 to +0.0392‰). The ^{26}Mg excesses cannot be explained by analytical artefacts, cosmogenic effects or heterogeneity of initial ^{26}Al/^{27}Al, Al/Mg ratios or Mg isotopes in asteroidal parent bodies as compared to Earth or chondrites. The ^{26}Mg excesses record asteroidal melting and formation of basaltic magmas with super-chondritic Al/Mg and confirm that radioactive decay of short-lived ^{26}Al was the primary

heat source that melted planetesimals. Model ^{26}Al-^{26}Mg ages for magmatism on the eucrite/mesosiderite, angrite and NWA 2976 parent bodies are 2.6-3.2, 3.9-4.1 and 3.5 Myr, respectively, after formation of calcium-aluminium-rich inclusions (CAIs). However, the validity of these model ages depends on whether the elevated Al/Mg ratios of basaltic meteorites result from magma ocean evolution on asteroids through fractional crystallisation or directly during partial melting. Mineral isochrons for the angrites Sahara (Sah) 99555 and D'Orbigny, and NWA 2976, yield ages of $5.06^{+0.06}_{-0.05}$ Myr and $4.86^{+0.10}_{-0.09}$ Myr, respectively, after CAI formation. Both isochrons have elevated initial δ^{26}Mg* values. Given the brecciated and equilibrated texture of NWA 2976 it is probable that its isochron age and elevated initial δ^{26}Mg* ($+0.0175 \pm 0.0034$‰) reflects thermal resetting during an impact event and slow cooling on its parent body. However, in the case of the angrites the marginally elevated initial δ^{26}Mg* ($+0.0068 \pm 0.0058$‰) may reflect either δ^{26}Mg* ingrowth in a magma ocean prior to eruption and crystallisation or in an older igneous protolith with super-chondritic Al/Mg prior to impact melting and crystallisation of these angrites, or partial internal re-equilibration of Mg isotopes after crystallisation. ^{26}Al-^{26}Mg model ages and a olivine+pyroxene+whole rock isochron for the angrites Sah 99555 and D'Orbigny are in good agreement with age constraints from ^{53}Mn-^{53}Cr and ^{182}Hf-^{182}W short-lived chronometers, suggesting that the ^{26}Al-^{26}Mg feldspar-controlled isochron ages for these angrites may be compromised by the partial resetting of feldspar Mg isotope systematics. Even when age constraints from the ^{26}Al-^{26}Mg angrite model ages or the mafic mineral+whole rock isochron are considered, the relative time difference between Sah 99555/D'Orbigny crystallisation and CAI formation cannot be reconciled with Pb-Pb ages for Sah 99555/D'Orbigny and CAIs, which are ca. 1.0 Myr too old (angrites) or too young (CAIs) for reasons that are not clear. This discrepancy might indicate that ^{26}Al was markedly lower (ca. 40%) in the planetesimal- and planet-forming regions of the proto-planetary disc as compared to CAIs, or that CAI Pb-Pb ages may not

accurately date CAI formation, which might be better dated by the ^{182}Hf-^{182}W and ^{26}Al-^{26}Mg chronometers as 4568.3 $\pm$ 0.7 (Burkhardt et al., GCA **72** (2008), 24) and 4568.5 $\pm$ 0.3 Ma (herein), respectively, when mapped onto an absolute timescale using Pb-Pb ages for angrites.

3.1 Introduction

The short-lived ^{26}Al-^{26}Mg chronometer is based on the decay of ^{26}Al to ^{26}Mg with a half-life of 0.73 Myr. Unequivocal evidence for the former presence of ^{26}Al in the Solar System's oldest solids (Amelin et al., 2002) - calcium-aluminium-rich inclusions (CAIs) - in the form of ^{26}Mg excesses correlated with the Al/Mg ratio of mineral phases in CAIs was first presented in Lee et al. (1977). The ^{26}Al-^{26}Mg chronometer has since become one of the most useful relative chronometers to precisely date silicate melting and crystallisation events in the first few million years of the Solar System (e.g., Srinivasan et al., 1999).

The timing of magmatism on planetesimals in the Solar System is important as it constrains the timescales of planetary accretion, melting and differentiation around the young Sun. The timing of magmatism also has a bearing on the likely heat source or physical mechanisms responsible for planetesimal melting and differentiation, as the radioactive decay of ^{26}Al can only have melted planetesimals if the precursor material initially contained CAI-like levels of ^{26}Al and planetesimals accreted within 1.5-2.0 Myr of CAI formation (Sanders and Taylor, 2005; Sahijpal et al., 2007). Moreover, concordance or otherwise between different chronometers with parent nuclides produced by different nucleosynthetic processes when applied to the same meteorites also has the potential to shed light on the astrophysical setting of Solar System formation and mixing timescales within the proto-planetary disc.

There are four groups of basaltic meteorites that do not originate from Mars or the Moon that represent samples of at least three differ-

ent asteroidal parent bodies. These groups are distinguished on the basis of their chemistry and mass-independent oxygen isotopic composition (Δ^{17}O) - angrites, eucrites from the howardite-eucrite-diogenite (HED) parent body, silicate clasts from mesosiderite stony-iron meteorites, and the unique NWA 011/NWA 2976 meteorite (Yamaguchi et al., 2002; Greenwood et al., 2005, 2006). In early models of Solar System formation, chondrites from undifferentiated planetesimals were thought to be representative of the precursor material from which differentiated planetesimals and the larger planets accreted. Chondrites were thus considered to be older than achondrites, including basaltic meteorites, which originate from differentiated planetesimals, as early ^{26}Al-^{26}Mg investigations of high Al/Mg material such as feldspar in basaltic meteorites could not identify resolvable ^{26}Mg excesses (MacPherson et al., 1995). The absence of ^{26}Mg excesses was consistent at that time with the relatively young Pb-Pb ages that had been obtained for both eucrites and angrites (Manhes et al., 1984; Lugmair and Galer, 1992; Tera et al., 1997).

Subsequently, ^{53}Mn-^{53}Cr dating showed that the HED parent body formed and differentiated within the first three million years of the Solar System (Lugmair and Shukolyukov, 1998). The first compelling ^{26}Al-^{26}Mg evidence for very early basaltic volcanism on planetesimals was presented by the studies of Srinivasan et al. (1999) and Nyquist et al. (2003) who measured ^{26}Mg excesses in high Al/Mg feldspars, which demonstrated that basaltic volcanism occurred within 4 Myr of CAI formation. However, most basaltic meteorites lacked evidence for the former presence of live ^{26}Al. Possible reasons for this were: (a) the large analytical uncertainties of the techniques used in these studies ($>\pm 0.1‰$), or (b) the ease with which Mg diffuses in feldspar at relatively low temperatures, which can lead to internal re-equilibration of Mg isotopes amongst minerals after ^{26}Al extinction (LaTourrette and Wasserburg, 1998) through slow cooling, later thermal metamorphism or shock of the meteorites, or (c) that most basaltic meteorites actually did form after extinction of ^{26}Al. The latter

possibility is problematic as radioactive decay of ^{26}Al is considered the most likely heat source to have driven melting of early formed planetesimals (Urey, 1954).

The application of multiple-collector inductively coupled plasma mass spectrometry (MC-ICP-MS) to Mg isotope studies has allowed ^{26}Mg anomalies to be measured with precisions $<\pm 0.02‰$ (2 se). Application of this method to basaltic meteorites from the HED, mesosiderite and angrite parent bodies revealed a Mg isotope fingerprint suggestive of the former presence of live ^{26}Al in all groups of basaltic meteorites studied thus far (Baker et al., 2005; Bizzarro et al., 2005). Small ^{26}Mg excesses were used to calculate model ages for formation of basaltic magmas on differentiated planetesimals that range from 2.5 to 4.0 Myr after CAI formation. Pb-Pb dating of some angrites (Sah 99555 and D'Orbigny) has also yielded apparent dates of 4566.2 to 4564.4 Myr (Baker et al., 2005; Amelin, 2008b,a; Connelly et al., 2008b), with the youngest dates currently thought to best represent the age of these meteorites, supporting the antiquity of at least some basaltic meteorites. These ages combined with numerical models for predicting the timing of accretion of their parent bodies require very early accretion of differentiated planetesimals, prior to accretion of chondritic parent bodies (Baker et al., 2005; Bizzarro et al., 2005; Sahijpal et al., 2007). These early timescales for accretion and melting of differentiated planetesimals are also consistent with ^{53}Mn-^{53}Cr and ^{182}Hf-^{182}W chronological studies of bulk samples of eucrites (Lugmair and Shukolyukov, 1998; Kleine et al., 2004) and ^{182}Hf-^{182}W studies of iron meteorites (Kleine et al., 2005a; Schersten et al., 2006; Markowski et al., 2006a).

However, aspects of the studies of Baker et al. (2005) and Bizzarro et al. (2005) remain controversial. The model ^{26}Al-^{26}Mg whole rock age for the angrite Sah 99555 is considerably older than the age obtained from feldspar ^{26}Al-^{26}Mg data (Baker et al., 2005; Spivak-Birndorf et al., 2005) and a whole rock - mineral isochron for angrites Sah 99555 and D'Orbigny (Spivak-Birndorf et al., 2009). Furthermore, other MC-ICP-MS studies of

bulk basaltic meteorite samples from the HED parent body (Wadhwa et al., 2003a; Wiechert and Halliday, 2007) have been unable to detect the small ^{26}Mg excesses reported by Baker et al. (2005) and Bizzarro et al. (2005).

We have developed improved Mg chemical separation techniques for meteorites that yield Mg with a purity >99% and have measured ^{26}Mg abundances, for the first time, in pseudo-high resolution mode by MC-ICP-MS to high precision in a range of basaltic meteorites from the angrite, HED and mesosiderite parent bodies. We also report the first high-precision Mg isotope data for minerals and bulk samples of the ungrouped achondrite NWA 2976 (paired with NWA 011). NWA 2976/NWA 011 has a distinctive Δ^{17}O (Yamaguchi et al., 2002) and excesses in neutron-rich isotopes of Cr and Ti as compared to all other basaltic meteorites, which have deficits in neutron-rich isotopes of Cr and Ti (Bogdanovski and Lugmair, 2004; Trinquier et al., 2007, 2009) requiring it to come from a different parent body to those of the other classes of basaltic meteorites.

3.2 Materials and methods

3.2.1 Samples and sample preparation

The studied meteorites are, in most cases, well documented meteorites for which detailed descriptions are available elsewhere (Mittlefehldt, 2007, and reference therein). However, the two mesosiderite clasts 1991.304 and 1991.305 are a gabbro and polymict basalt clast from the Vaca Muerta meteorite, respectively. The diogenite Bilanga and the eucrites Juvinas, Millibillillie, Dhofar 007 and Camel Donga are from the HED parent body. HED meteorites and mesosiderite silicate clasts share a common and unique Δ^{17}O (Greenwood et al., 2006) suggesting they may originate from the same parent body.

Angrites have a common Δ^{17}O that is distinct from the HED meteorites (Greenwood et al., 2005). Angrites mainly comprise aluminan-titanian-

diopside + calcium-rich olivine + kirschsteinite ± anorthite. The angrites analysed in this study have different textures. Sah 99555, D'Orbigny and NWA 1296 have quenched textures with strongly zoned mineral phases indicating that all three meteorites cooled rapidly. In contrast, LEW 86010 has a hypidiomorphic-granular texture, Angra dos Reis (ADOR) has an equilibrated texture, and NWA 2999 has a polygonal-granular texture. Minerals in LEW 86010 and ADOR are unzoned.

The ungrouped achondrite NWA 2976 comprises coarse anhedral pigeonite and augite set in fine-grained plagioclase. This meteorite has a texture indicating it has experienced a complex thermal history involving brecciation, recrystallisation and thermal annealing (Yamaguchi et al., 2002).

Three chondrites were also included in this study. NWA 530 is a primitive chondrite of the CR2 type that exhibits signs of mild aqueous alteration but escaped thermal metamorphism (Krot et al., 2002). Sah 97096 is an EH3 enstatite chondrite and Bovedy is an L3 ordinary chondrite that contains multistage compound chondrules (Sanders and Hill, 1994).

Small fragments of bulk basaltic meteorites (ca. 50 mg) were hand-picked for analysis. Some whole rock fragments of Sah 99555, D'Orbigny and NWA 2976 were lightly crushed in an agate mortar and mineral separates were then prepared by hand-picking from the lightly crushed material under a binocular microscope or by magnetic separation (feldspar). Chondrite samples of 100-200 mg were powdered and homogenised in an agate mortar.

3.2.2 Chemical separation of Mg

Separation of Mg from other elements in silicate rocks is important for Mg isotope analyses as the presence of other elements can impart matrix effects (Albarede and Beard, 2004) that result in inaccurate stable Mg isotope data (e.g., Galy et al., 2001) and, potentially, the ^{26}Mg excess, which is

used to calculate meteorite ages. We developed a new chemical separation procedure that produces >99% Mg yields of >99% purity, as conventional cation exchange separation procedures used to separate Mg from silicate matrices in the studies of Baker et al. (2005), Bizzarro et al. (2005), Wiechert and Halliday (2007), Wadhwa et al. (2003a), Teng et al. (2007) and Spivak-Birndorf et al. (2009) do not provide an effective separation of Mg from elements like Mn and Ni (Fig. 3.1).

All procedures were carried out in class 10 laminar flow hoods situated in a class 100 clean laboratory using ultrapure Seastar^{TM} acids and >18.2 MΩ Millipore® water. Samples were digested in Savillex® screw-top beakers in a mixture of concentrated HF-HNO_3 (3:1) at a temperature of 110° C on a hotplate followed by sequential attack with concentrated HNO_3, HCl and HNO_3. Aliquots of digested material equivalent to ≤2 mg of sample were then processed through either 4 or 5 steps:

1. The sample in 11M HCl was passed through a 1.25 mL pipette tip column loaded with ∼0.5 mL Bio-Rad AG®1-X4 anion exchange resin. Mg was eluted from the column with 4 column loads of 11M HCl while Fe was retained on the column.

2. The Mg cut from (1) was dissolved in 0.5 mL of 1M HNO_3-0.1M HF. Na, Al, Ti, Cr and, to some extent, Ca were then separated from Mg on a cation exchange column containing ∼1 mL of Bio-Rad AG®50W-X8 200-400 mesh resin (Fig. 3.1). Use of trace amounts of HF in the eluting acid has two advantages over cation exchange separation techniques based on either HNO_3 or HCl without HF. Firstly, Fe is eluted prior to Mg. Secondly, and more importantly, the elution of Al and Ti is more rapid and quantitative (100%) in the presence of trace amounts of HF. Without sufficient (i.e., excess) amounts of HF in the eluted solution both Al and Ti can exhibit two elution peaks - one early in the elution scheme and the second later in the elution scheme where it partially overlaps with the Mg elution.

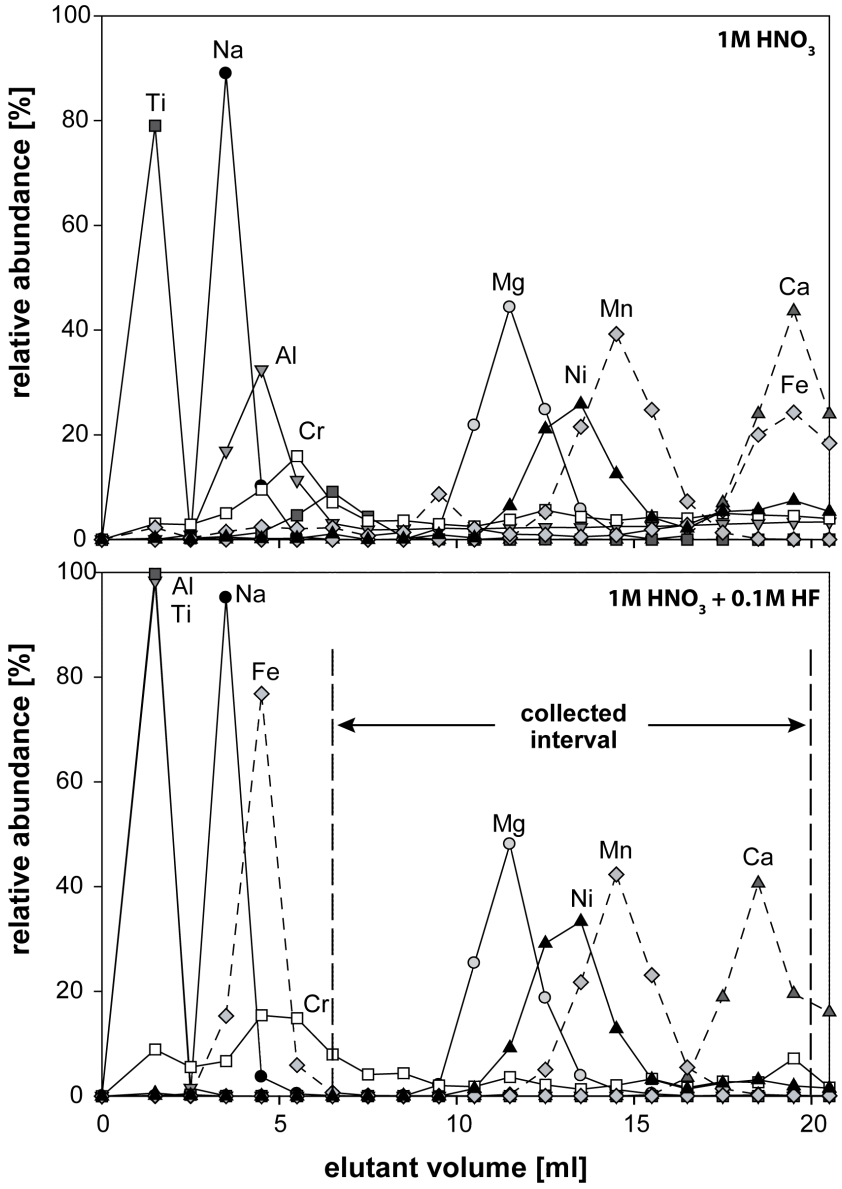

Figure 3.1: Comparison of the elemental elution curves of the basalt standard BCR-2 in 1M HNO_3 and 1M HNO_3-0.1M HF for Na, Mg, Al, Ca, Ti, Cr, Mn, Fe and Ni through a 1 mL cation exchange column loaded with Bio-Rad AG50W-X8 200-400 mesh resin. Each sample was loaded in 0.5 mL and cuts collected in 1 mL intervals. Dotted lines highlight elements that are removed in other chemical separation steps prior to the final cation exchange separation step.

3. The Mg cut from (2) was dissolved in 3M HNO_3 and loaded onto a 1.25 mL pipette tip column containing ~0.25 mL of Eichrom® DGA resin (Horwitz et al., 2005). Mg was eluted from the column with 1.5 column loads of 3M HNO_3, with the DGA resin retaining Ca. This separation step was repeated to ensure >99% removal of Ca remaining from step (2).

4. The Mg cut from (3) was dissolved in 2 mL of 0.5M HCl-95% acetone. This solution was loaded on a column containing ~1 mL of Bio-Rad AG®AG50W-X8 200-400 mesh resin. The high acetone concentration significantly decreases the distribution coefficient of Mn on the resin (Strelow et al., 1971) allowing elution of Mn from the column in 4 mL of 0.5M HCl-95% acetone. Mg was then collected from the column in 8 mL of 6M HCl. This solution was then evaporated, converted to nitrates, and taken up in 250 μL 1M HNO_3-0.1M HF to repeat step 2 in order to remove any Na that might have been introduced as blank during steps (2), (3) and (4).

5. Only the Ni-rich chondrite samples were then passed through an additional Ni separation as a last step. The method used is similar to that described by Quittè and Oberli (2006) using Eichrom Ni-spec resin. The dry sample containing only Mg and Ni was dissolved in 1 mL of 0.1M HCl and then 2.5 mL of >18.2 MΩ Millipore® water and 0.5 mL of concentrated NH_4OH are added, resulting in a final solution with pH of 9-10. The solution was loaded onto a column containing ~1 mL of Eichrom Ni-spec resin and the Mg was eluted from the column with additional 10 mL of ~0.2M NH_4OH solution adjusted to a pH of 8-9 with HCl. The advantage of using an ammonium hydroxide solution instead of the more commonly used ammonium citrate buffer solution is the lack of organic residue in the collected Mg cut that may cause unwanted analytical artefacts during the Mg isotopic analysis.

Table 3.1: Comparison of the initial abundance of selected elements relative to Mg in BCR-2 (GeoRem, 2010) and chondrites (Palme and Jones, 2003) before and after chemical separation. DGA stands for diglycolamide and DMG for dimethylglyoxime chemistries.

	initial element/Mg ratio		*ratio after chemistry*		*removing step*
	BCR-2	chondrites	BCR-2	chondrites	
Al/Mg	3.30	0.088	0.0011	0.001	cation
Ca/Mg	2.35	0.097	0.0004	<0.0001	DGA
Cr/Mg	0.008	0.028	0.0004	0.0005	cation
Fe/Mg	4.46	1.92	0.0004	<0.0001	anion + cation
Mn/Mg	0.070	0.020	0.0023	0.0003	acetone
Na/Mg	1.08	0.052	0.0032	0.006	cation
Ni/Mg	0.0008	0.11	0.0008	<0.0001	DMG
P/Mg	0.071	0.010	<0.0001	<0.0001	cation
Si/Mg	11.68	1.11	<0.0001	<0.0001	HF-digestion
Ti/Mg	6.24	0.005	<0.0001	<0.0001	cation
Zn/Mg	0.006	0.003	0.0016	0.0004	anion

After the final step (4. or 5.), the evaporated Mg is fluxed for 12 hr at 110°C in 1 mL of aqua regia and then converted to chloride form. The final Mg cut is typically $\geq$ 99% pure with typical element/Mg ratios prior to and after separation shown in Table 3.1.

3.2.3 ^{27}Al/^{24}Mg ratio measurements by ICP-MS

Al/Mg ratios were measured on aliquots of fully digested samples with an Agilent® 7500CS ICP-MS using He in a collision cell to minimize interferences on Al and Mg isotopes (^{27}Al, ^{24}Mg and ^{25}Mg). Sample analyses were bracketed with analyses of a gravimetrically prepared Al/Mg = 2.0 solution made from Aristar® single element ICP-MS solutions. The error assigned to the Al/Mg ratio is $\pm$ 2% (2 sd) based on repeated measurements of USGS basaltic rock standards BCR-2 and BHVO-2. Repeated analyses of

these standards yielded $^{27}Al/^{24}Mg$ ratios of 3.81 $\pm$ 0.05 (2 sd; BCR-2) and 1.90 $\pm$ 0.02 (2 sd; BHVO-2), which are within error of the recommended values for these standards i.e, 3.76 $\pm$ 0.15 and 1.87 $\pm$ 0.08, respectively (GeoRem, 2010). Doping tests were carried out to evaluate the veracity of the Al/Mg measurements by ICP-MS. Addition of Ca to the Al/Mg = 2.0 solution up to Ca/Mg = 4 resulted in no deviation ($<$ 1%) in measured Al/Mg from the value obtained on the pure Al/Mg = 2.0 solution.

3.2.4 Mg isotope measurements by MC-ICP-MS

All Mg isotope analyses were conducted on a Nu Plasma^{TM} high resolution MC-ICP-MS. Mg dissolved in 0.1M HCl is introduced to the argon plasma via a DSN-100 desolvating nebulizer. ^{24}Mg, ^{25}Mg and ^{26}Mg are monitored by the L5, Ax and H6 Faraday collectors equipped with 10^{11} Ohm resistors. Magnesium concentrations of $\sim$0.75 ppm in the solutions and an uptake rate of approximately 0.12 mL/min resulted in 8-9 V signals on ^{24}Mg. The relatively low sensitivity of the MC-ICP-MS was a combined result of analysing in pseudo-high-resolution mode and also a low transfer vacuum (ca. 2 mbar) in order to increase the signal stability. The pseudo-high-resolution mode allowed for an effective mass resolution between 2000 and 2500, which enables resolution of all molecular interferences on the high mass side (e.g., $^{12}C_2^+$, $^{12}C^{14}N^+$) from Mg. The only high mass interference not fully resolved at this mass resolution is $^{24}Mg^1H^+$ on ^{25}Mg, but this interference is resolved at this resolution at the 70% level. Interferences of potential doubly charged species on the low mass side of Mg cannot be resolved by the pseudo-high-resolution method. However, doping tests have shown that, at the level of purity of our Mg solutions, the levels of these interferences are much lower than the analytical precision (Tables 3.1 and 3.2).

Each analysis comprises a total of 480 s of baseline measurements and 1600 s of data acquisition in four blocks. Sample analyses are bracketed

Table 3.2: δ^{26}Mg* and δ^{25}Mg data for Aristar® Mg doped with 2 wt.% of different contaminant elements measured against a pure Aristar® Mg solution. The effect of calcium is also shown at the 20% and 200% level.

Sample	δ^{26}Mg* $\pm$ 2 se (‰)	δ^{25}Mg $\pm$ 2 se (‰)	n
Ca/Mg	+0.0102 $\pm$ 0.0080	+0.67 $\pm$ 0.15	4
Ca/Mg (= 0.2)	+0.0294 $\pm$ 0.0142	+0.80 $\pm$ 0.13	1
Ca/Mg (= 2.0)	+0.2425 $\pm$ 0.0240	+0.76 $\pm$ 0.18	1
Mn/Mg	-0.0022 $\pm$ 0.0089	+0.64 $\pm$ 0.05	3
Ti/Mg	+0.0074 $\pm$ 0.0094	+0.30 $\pm$ 0.01	3
Ni/Mg	-0.0008 $\pm$ 0.0074	+0.16 $\pm$ 0.03	5
Fe/Mg	+0.0095 $\pm$ 0.0081	+0.24 $\pm$ 0.05	4
Cr/Mg	-0.0036 $\pm$ 0.0096	+0.35 $\pm$ 0.20	3
Al/Mg	-0.0072 $\pm$ 0.0083	+0.27 $\pm$ 0.01	3
Na/Mg	-0.0002 $\pm$ 0.0120	+0.05 $\pm$ 0.01	2

by analyses of the DSM-3 standard (Galy et al., 2003). The ^{26}Mg excess (δ^{26}Mg*) was calculated by internally normalising the ^{26}Mg/^{24}Mg to ^{25}Mg/^{24}Mg = 0.12663 using the exponential mass fractionation law (β = 0.511) and calculating the difference between this value for the sample and the average value of the bracketing standards in the per mil notation (‰). All stable Mg isotope data are also reported in the per mil notation as the difference between the sample and the average value of the bracketing standards. Uncertainties on the analysis of a sample are calculated as weighted means of replicate analyses of the sample and quadratically incorporate the errors of the sample runs as well as those of the bracketing standards. Single Mg isotope analyses have uncertainties (2 se) on mass-bias-corrected δ^{26}Mg* that are $\pm$0.021‰ to $\pm$0.017‰ when the uncertainties on the bracketing standards are incorporated into the error. Multiple analysis of samples (n = 8 to 47), with the exception of the low-Mg feldspars, results in weighted means with uncertainties (2 se) that are $\pm$0.0029 to $\pm$0.0068‰. Typically, where sufficient Mg is available each

"analysis" of a sample would represent the mean of 8-10 individual measurements carried out over a 12-14 hr period. In a number of cases, this type of analysis would be repeated on either remaining Mg left over from the first 8-10 analyses in another analytical session, or on Mg separated in a new chemical separation chemistry from remaining digested material of the sample, or of Mg separated from the same sample in a new chemical separation chemistry where new material was digested a second (or even a third) time.

3.3 Results

3.3.1 Verifying the accuracy and reproducibility of high precision Mg isotope measurements

The small δ^{26}Mg* variations previously reported for basaltic meteorites necessitates an evaluation of whether analytical artefacts can generate inaccurate Mg isotope data. We tested whether different elements that occur in a basaltic matrix might generate inaccurate data when present at an element/Mg ratio of 2 wt.% (Table 3.2). Such levels of contaminants are typically $>10\times$ higher than those measured in the Mg cuts after chemical separation (Table 3.1). As these effects are close to linear at low concentration levels (<10-15 wt.%; Galy et al., 2001), effects on measured δ^{26}Mg* of samples are likely to be at least $10\times$ less than in the tests i.e., much smaller than the analytical uncertainty on the measured δ^{26}Mg* values for the meteorites.

Obvious effects on the Mg isotope measurements due to the presence of contaminant elements were restricted to the stable isotope composition, which was variably biased to heavier ratios. Ca was the element that had the most significant influence on δ^{26}Mg*, and the presence of Ca (and Mn) also produced the most marked shift to heavier stable isotope ratios. More detailed tests with Ca doping at increased Ca/Mg ratios (Table 3.2)

showed that each 1% of Ca added resulted in an increase in δ^{26}Mg* of ca. 0.001 to 0.002‰. This level of Ca is >20× higher than observed in the Mg cuts analysed in this study (Table 3.1).

In a further test, 1000 μg of Aristar Mg standard was processed through the entire chemical procedure alongside the basaltic meteorites and then analysed against unprocessed Aristar Mg. The δ^{25}Mg of the column processed Aristar Mg is within 0.1‰ of zero, which is the estimated analytical reproducibility of our δ^{25}Mg values using the long analysis times utilised in this study. More significantly, the δ^{26}Mg* is also within analytical uncertainty (2 se) of zero (Table 3.3). This suggests that the Mg chemical separation techniques introduce no undesirable analytical artefacts.

Two terrestrial basalt standards (BCR-2 and BHVO-2) were also processed through the entire chemical procedure alongside the basaltic meteorites. Two digestions of BCR-2 resulted in an average δ^{26}Mg* = +0.0017 $\pm$ 0.0044‰ and five processed aliquots of two digestions of BHVO-2 yielded an average δ^{26}Mg* = -0.0017 $\pm$ 0.0034‰ (Table 3.3), demonstrating the veracity of the Mg separation techniques and precision and accuracy of the δ^{26}Mg* measurements on material similar in composition to the basaltic meteorites. Multiple analyses of basalt standards and some meteorite samples in different sessions and/or of different digestions and Mg separations typically yield external reproducibilities (2 sd) that are $\leq$ 1.5 times the 2 se obtained on any analysis from each individual session (Fig. 3.2). Thus, throughout this paper we calculate model and isochron ages using this conservative estimate of data reproducibility i.e. 1.5 times the final 2 se obtained for each sample. It is necessary to define the relationship between 2 se and external reproducibility of each analysis in this manner to account for the fact that not all meteoritic samples were analysed the same number of times. For example, the external reproducibility of samples that could only be measured a small number of times (e.g., the low-Mg feldspars) will necessarily be characterised by a larger external reproducibility than other samples (Mg-rich mafic minerals or bulk rocks)

Table 3.3: Al/Mg and Mg isotope data for synthetic and terrestrial standards, chondrites, and meteorites from the HED and mesosiderite parent body or bodies.

	δ^{26}Mg* $\pm$ 2 se (‰)	δ^{25}Mg $\pm$ 2 se (‰)	δ^{26}Mg $\pm$ 2 se (‰)	n	^{27}Al/^{24}Mg
Earth					
Aristar$_{vs.Aristar}$	-0.0011 $\pm$ 0.0036	+0.085 $\pm$ 0.057	+0.170 $\pm$ 0.110	28	-
Aristar$_{vs.Aristar}$ +0.010‰	+0.0138 $\pm$ 0.0045	-0.021 $\pm$ 0.029	-0.032 $\pm$ 0.057	20	-
Aristar$_{vs.Aristar}$ +0.020‰	+0.0225 $\pm$ 0.0065	+0.090 $\pm$ 0.140	+0.190 $\pm$ 0.270	10	-
Aristar$_{vs.Aristar}$ +0.030‰	+0.0313 $\pm$ 0.0062	-0.022 $\pm$ 0.042	-0.011 $\pm$ 0.083	10	-
Aristar$_{vs.Aristar}$ +1.000‰	+1.0221 $\pm$ 0.0202	-0.013 $\pm$ 0.012	+0.991 $\pm$ 0.015	1	-
BCR-2	+0.0017 $\pm$ 0.0044	-0.017 $\pm$ 0.095	-0.030 $\pm$ 0.190	18	3.81
BHVO-2	-0.0017 $\pm$ 0.0034	-0.153 $\pm$ 0.049	-0.300 $\pm$ 0.095	42	1.90
BHVO-2 +0.010‰	+0.0126 $\pm$ 0.0043	-0.088 $\pm$ 0.043	-0.159 $\pm$ 0.084	20	-
BHVO-2 +0.020‰	+0.0238 $\pm$ 0.0061	-0.052 $\pm$ 0.041	-0.086 $\pm$ 0.076	10	-
BHVO-2 +0.030‰	+0.0338 $\pm$ 0.0060	-0.119 $\pm$ 0.042	-0.203 $\pm$ 0.080	10	-
chondrites					
NWA 530 (CR2)	-0.0004 $\pm$ 0.0065	-0.110 $\pm$ 0.100	-0.220 $\pm$ 0.210	10	0.097
Bovedy (L3)	-0.0029 $\pm$ 0.0052	-0.099 $\pm$ 0.077	-0.200 $\pm$ 0.150	13	0.088
Sah 97096 (EH3)	+0.0010 $\pm$ 0.0061	-0.125 $\pm$ 0.029	-0.243 $\pm$ 0.061	10	0.073
diogenites					
Bilanga	-0.0018 $\pm$ 0.0038	-0.087 $\pm$ 0.041	-0.168 $\pm$ 0.079	27	0.032
eucrites					
Dhofar 007	+0.0212 $\pm$ 0.0062	-0.072 $\pm$ 0.077	-0.120 $\pm$ 0.150	10	0.99
Juvinas	+0.0303 $\pm$ 0.0033	-0.082 $\pm$ 0.056	-0.170 $\pm$ 0.130	34	1.71
Millibillillie	+0.0324 $\pm$ 0.0065	-0.078 $\pm$ 0.064	-0.120 $\pm$ 0.120	10	2.00
Camel Donga	+0.0411 $\pm$ 0.0058	-0.090 $\pm$ 0.110	-0.140 $\pm$ 0.220	10	2.03
mesosiderites					
Vaca Muerta 1991.304	+0.0385 $\pm$ 0.0046	-0.103 $\pm$ 0.057	-0.160 $\pm$ 0.110	18	1.42
Vaca Muerta 1991.305	+0.0392 $\pm$ 0.0047	+0.005 $\pm$ 0.027	+0.043 $\pm$ 0.056	17	1.69
Vaca Muerta 1991.305	+0.0448 $\pm$ 0.0085	-0.080 $\pm$ 0.140	-0.110 $\pm$ 0.270	6	2.03

where the sample could be measured many times.

In order to further assess the reliability of the δ^{26}Mg* measurements unprocessed Aristar Mg standard solutions were gravimetrically doped with a ^{26}Mg spike (97.6% purity) to generate δ^{26}Mg* anomalies of 1.000, 0.030, 0.020 and 0.010‰, respectively, that were then measured against undoped Aristar Mg standard. In addition, three aliquots of BHVO-2 powder were also gravimetrically doped with the ^{26}Mg spike to generate δ^{26}Mg* anomalies of 0.030, 0.020 and 0.010‰ and were subsequently digested and processed through the Mg chemical separation scheme. The purified Mg solutions from these spiked BHVO-2 standards were then measured against DSM-3 (Fig. 3.3). All these doped synthetic and natural standards yield δ^{26}Mg* values within 2 se of the calculated anomalies (Fig. 3.3 and Table 3.3).

3.3.2 High precision Mg isotope data for basaltic meteorites and chondrites

Mg isotope data for meteorites are reported in Tables 3.3 and 3.4. The diogenite Bilanga has sub-chondritic ^{27}Al/^{24}Mg = 0.032, and a δ^{26}Mg* of -0.0018 $\pm$ 0.0038‰. The basaltic eucrites have super-chondritic ^{27}Al/^{24}Mg of 0.99 to 2.03 and resolvable δ^{26}Mg* excesses of +0.0212 $\pm$ 0.0062‰ to +0.0411 $\pm$ 0.0058‰. Two mesosiderite silicate clasts with super-chondritic Al/Mg ratios yielded δ^{26}Mg* values of +0.0385 $\pm$ 0.0046‰ (1991.304) and +0.0405 $\pm$ 0.0041‰ (1991.305). The data reported in this study for Bilanga, eucrites and mesosiderite silicate clasts are in excellent agreement with those of Bizzarro et al. (2005) (Fig. 3.4).

Two groups of angrites were analysed for Mg isotopes. ADOR and LEW 86010 have relatively young Pb-Pb ages of 4557-4559 Ma (Amelin, 2008a), whereas Sah 99555 and D'Orbigny have yielded Pb-Pb ages that range from 4566.2 to 4564.4 Ma, with the younger age currently considered to represent the best Pb-Pb age for this group of angrites (Baker et al.,

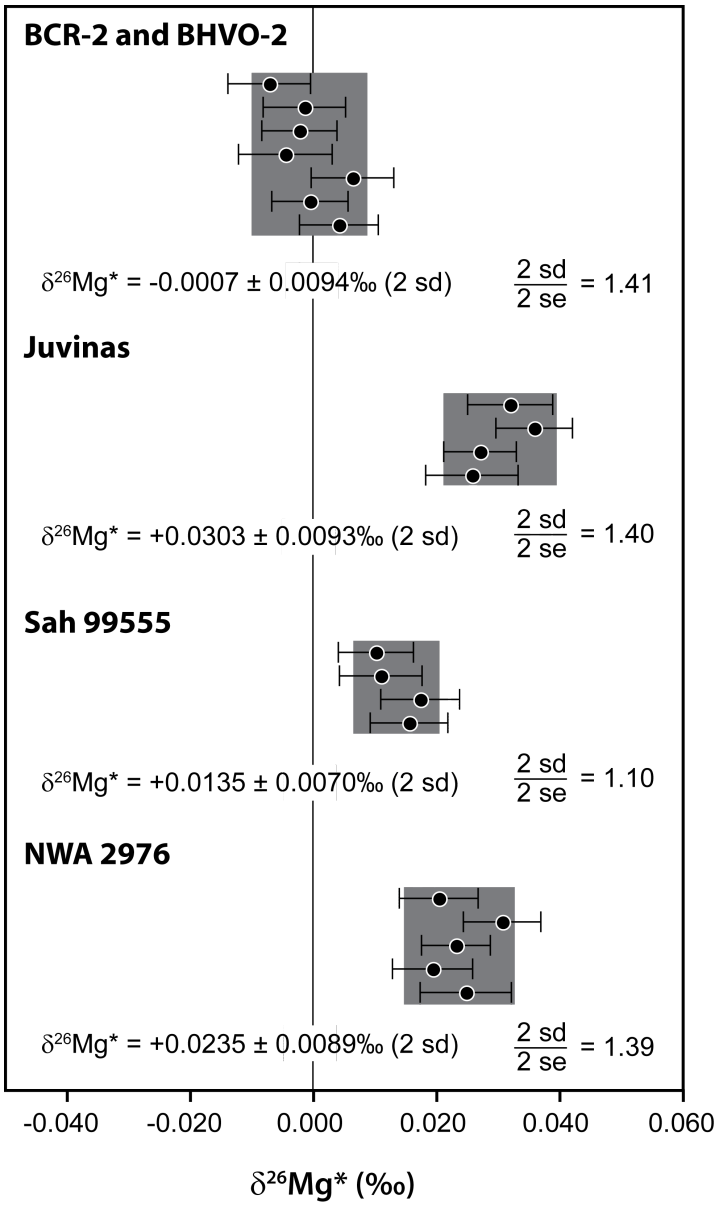

Figure 3.2: External reproducibility of multiple analyses of Mg isotope measurements (δ^{26}Mg*) on terrestrial basalts and three different basaltic meteorites. Dark grey fields represent the 2 sd calculated from multiple results obtained for each sample.

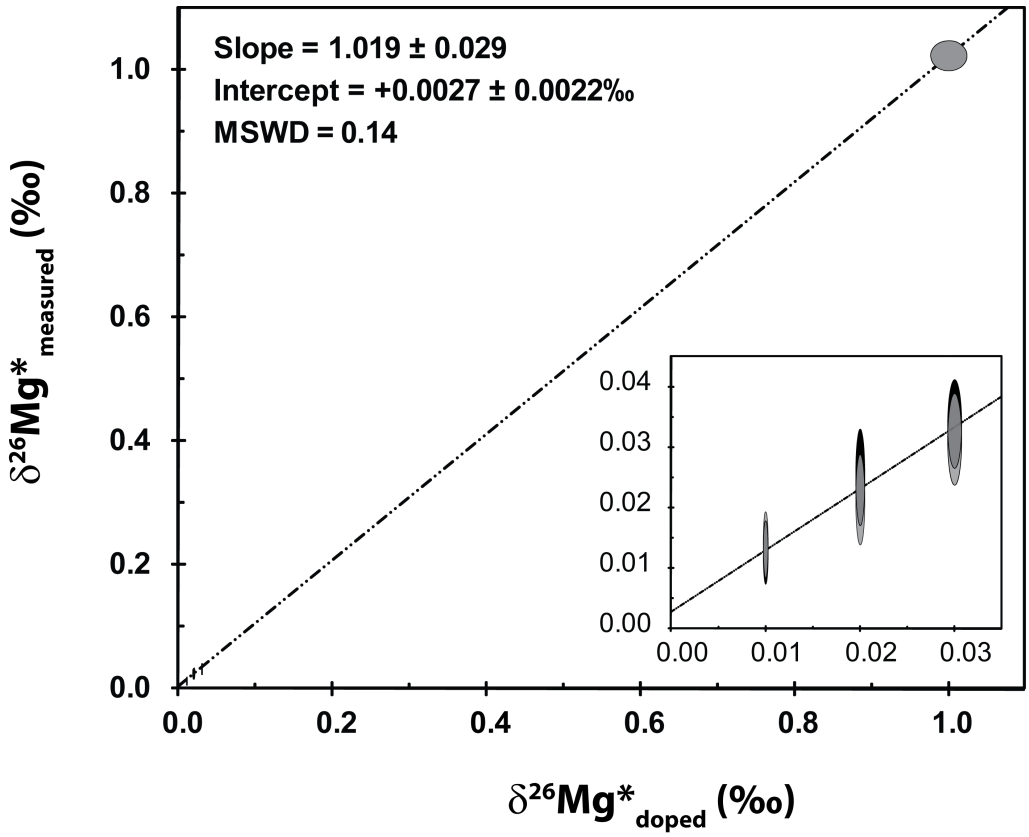

Figure 3.3: Correlation of the doped δ^{26}Mg* anomalies based on ^{26}Mg isotope doping of BHVO-2 powder (black error ellipse) and Aristar Mg standard solution (grey error ellipse) on a weight basis at the 0.010, 0.020, 0.030 and 1.000‰ level with anomalies that were measured by MC-ICP-MS. The errors shown are 2 se for the measured δ^{26}Mg* anomalies and $\pm$2% for the doped anomalies based on the analysis of the 1.000‰ doped Aristar Mg solution, which was used to calibrate the spike concentration.

Table 3.4: Al/Mg and Mg isotope data for meteorites from the angrite and NWA 011/NWA 2976 parent bodies. Abbreviations are ol = olivine, px = pyroxene, fsp = feldspar, wr = whole rock.

	δ^{26}Mg* $\pm$ 2 se (‰)	δ^{25}Mg $\pm$ 2 se (‰)	δ^{26}Mg $\pm$ 2 se (‰)	n	^{27}Al/^{24}Mg
angrite parent body					
LEW 86010	-0.0003 $\pm$ 0.0066	-0.075 $\pm$ 0.092	-0.160 $\pm$ 0.190	9	1.62
Angra dos Reis	-0.0026 $\pm$ 0.0048	-0.214 $\pm$ 0.029	-0.431 $\pm$ 0.052	17	0.98
Angra dos Reis	-0.0052 $\pm$ 0.0070	+0.190 $\pm$ 0.170	+0.360 $\pm$ 0.320	8	1.00
NWA 2999	-0.0064 $\pm$ 0.0046	-0.021 $\pm$ 0.034	-0.047 $\pm$ 0.067	20	0.21
NWA 1296	+0.0088 $\pm$ 0.0068	-0.171 $\pm$ 0.072	-0.330 $\pm$ 0.140	10	1.87
Sah 99555 ol	+0.0022 $\pm$ 0.0060	-0.252 $\pm$ 0.073	-0.490 $\pm$ 0.150	10	0.063
Sah 99555 px	+0.0088 $\pm$ 0.0068	+0.032 $\pm$ 0.050	+0.064 $\pm$ 0.092	8	1.36
Sah 99555 px	+0.0007 $\pm$ 0.0061	+0.042 $\pm$ 0.050	+0.080 $\pm$ 0.110	10	1.42
Sah 99555 px	+0.0101 $\pm$ 0.0059	-0.036 $\pm$ 0.059	-0.060 $\pm$ 0.110	10	1.48
Sah 99555 wr	+0.0135 $\pm$ 0.0032	-0.085 $\pm$ 0.035	-0.153 $\pm$ 0.068	37	2.00
Sah 99555 wr	+0.0167 $\pm$ 0.0068	-0.003 $\pm$ 0.086	-0.010 $\pm$ 0.170	10	2.35
Sah 99555 fsp	+0.0677 $\pm$ 0.0130	-0.017 $\pm$ 0.106	+0.030 $\pm$ 0.215	6	17.4
Sah 99555 fsp	+0.2752 $\pm$ 0.0244	-0.067 $\pm$ 0.052	+0.121 $\pm$ 0.103	2	86.9
D'Orbigny ol	+0.0049 $\pm$ 0.0061	-0.180 $\pm$ 0.210	-0.340 $\pm$ 0.420	10	0.070
D'Orbigny px	+0.0073 $\pm$ 0.0052	+0.164 $\pm$ 0.064	+0.330 $\pm$ 0.130	15	1.23
D'Orbigny wr	+0.0208 $\pm$ 0.0040	+0.073 $\pm$ 0.049	+0.163 $\pm$ 0.099	24	2.45
D'Orbigny fsp	+0.0928 $\pm$ 0.0110	+0.140 $\pm$ 0.210	+0.370 $\pm$ 0.410	4	28.7
D'Orbigny fsp	+0.3126 $\pm$ 0.0155	+0.290 $\pm$ 0.170	+1.240 $\pm$ 0.460	4	110.0
ungrouped achondrite					
NWA 2976 px	+0.0191 $\pm$ 0.0044	-0.103 $\pm$ 0.077	-0.180 $\pm$ 0.150	19	0.27
NWA 2976 px	+0.0205 $\pm$ 0.0065	-0.075 $\pm$ 0.055	-0.102 $\pm$ 0.099	8	0.35
NWA 2976 wr	+0.0235 $\pm$ 0.0029	-0.056 $\pm$ 0.041	-0.081 $\pm$ 0.089	47	1.90
NWA 2976 fsp	+0.5820 $\pm$ 0.0769	-0.144 $\pm$ 0.065	+0.203 $\pm$ 0.117	1	143.7
NWA 2976 fsp	+0.9050 $\pm$ 0.0627	-0.444 $\pm$ 0.056	-0.092 $\pm$ 0.107	1	258.1

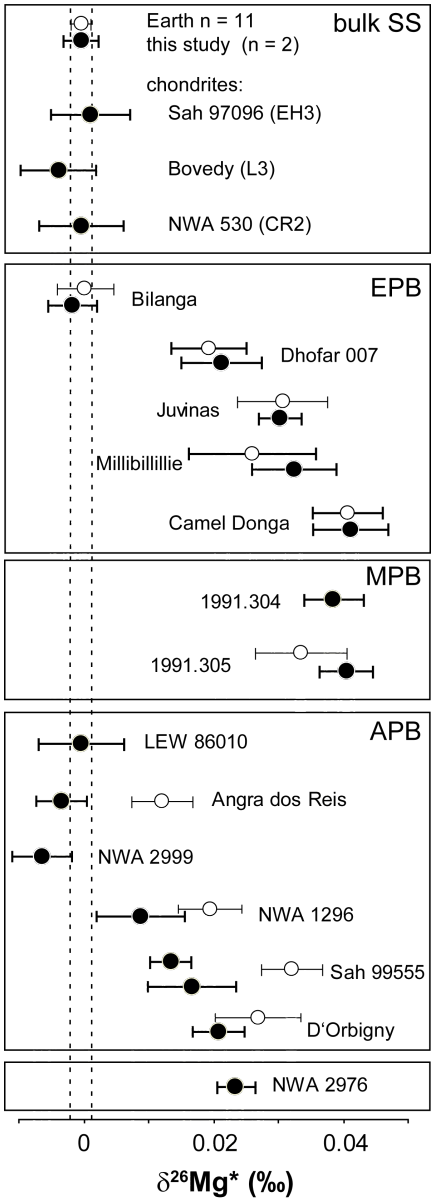

Figure 3.4: Previously published high precision δ^{26}Mg* data for meteorites from Baker et al. (2005) and Bizzarro et al. (2005) (open symbols) compared with the new data reported here (solid symbols); error bars are 2 se. Abbreviations refer to: bulk SS: bulk Solar System, EPB: eucrite parent body, MPB: mesosiderite parent body, APB: angrite parent body.

2005; Amelin, 2008b,a; Connelly et al., 2008b). ADOR and LEW 86010 do not show any resolvable δ^{26}Mg* anomaly, despite the fact that they have super-chondritic ^{27}Al/^{24}Mg ratios and NWA 2999, which has a near chondritic ^{27}Al/^{24}Mg ratio, also shows no δ^{26}Mg* excess (Table 3.4). These three angrites have a mean δ^{26}Mg* = -0.0039 $\pm$ 0.0027‰, which, considering their young Pb-Pb ages, may represent the Mg isotopic composition of the bulk angrite parent body after complete ^{26}Al decay.

However, five aliquots of two digestions of bulk fragments of Sah 99555 all have resolvable δ^{26}Mg* anomalies as does analysis of a bulk fragment of D'Orbigny (Fig. 3.4; Table 3.4). The high precision δ^{26}Mg* data reported for the bulk angrites Sah 99555, D'Orbigny, NWA 1296 and ADOR differ from Baker et al. (2005), who reported bulk rock δ^{26}Mg* values for these angrites that were slightly more positive than those of this study, but within error for D'Orbigny and NWA 1296 (Fig. 3.4). However, more recent data from Spivak-Birndorf et al. (2009) for Sah 99555 and D'Orbigny do generally agree with the data presented here, although the bulk angrite data from the study of Spivak-Birndorf et al. (2009) are an order of magnitude less precise than the results presented here. NWA 1296 yields a small positive δ^{26}Mg* anomaly but, given our estimated external reproducibility, we cannot with certainty distinguish this from the terrestrial standard.

δ^{26}Mg* data for the bulk samples and mineral separates of Sah 99555 and D'Orbigny each define separate isochrons and an combined isochron (n = 13) with an initial ^{26}Al/^{27}Al of (4.07 $\pm$ 0.21) $\times$ 10^{-7} (Fig. 3.5). The initial δ^{26}Mg* of the combined isochron is slightly elevated compared to the terrestrial standard i.e., +0.0068 $\pm$ 0.0058‰ and distinct from the average δ^{26}Mg* of the bulk analyses of ADOR, LEW 86010 and NWA 2999.

Five aliquots of three digestions of NWA 2976 show super-chondritic Al/Mg typical of basaltic meteorites and a resolvable δ^{26}Mg* anomaly of +0.0235 $\pm$ 0.0029‰. Despite the low Al/Mg of pyroxene in this rock, it also has a resolvable δ^{26}Mg* anomaly of +0.0195 $\pm$ 0.0036‰ determined from the average of two different separates. Al/Mg and δ^{26}Mg* data for

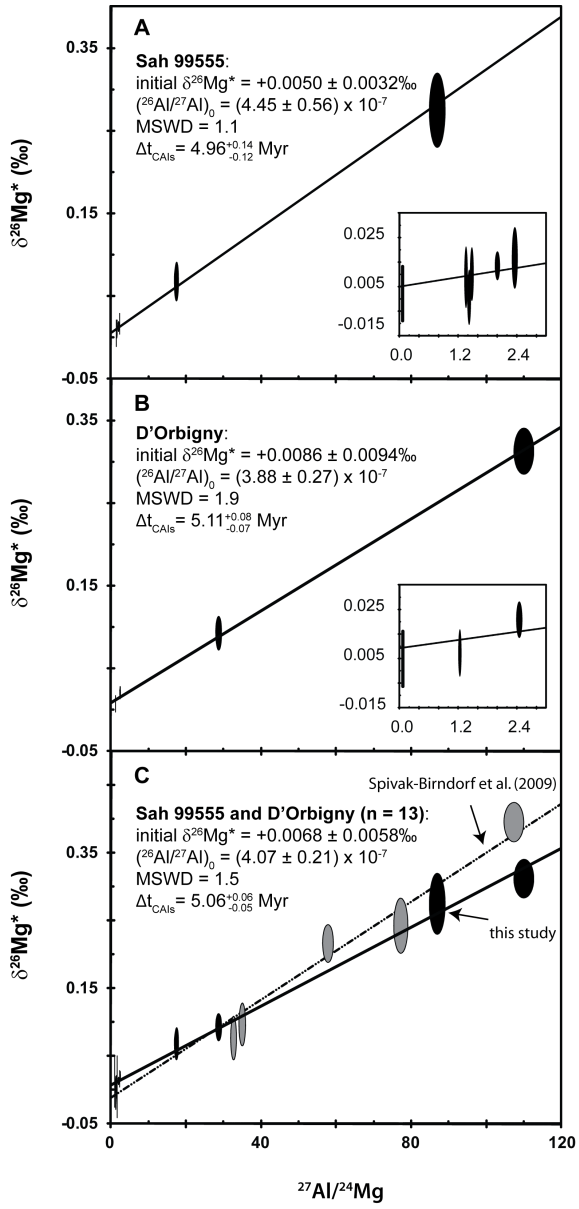

Figure 3.5: ^{26}Al-^{26}Mg isochrons for the angrites Sah 99555 (A), D'Orbigny (B) and a combined isochron for both angrites (C). Shown for comparison in (C) is also the Mg isotope data reported for Sah 99555 and D'Orbigny by Spivak-Birndorf et al. (2009) (grey ellipses). Errors used to calculate the isochrons are 1.5 times the 2 se for δ^{26}Mg* and 2% for ^{27}Al^{24}Mg ratios.

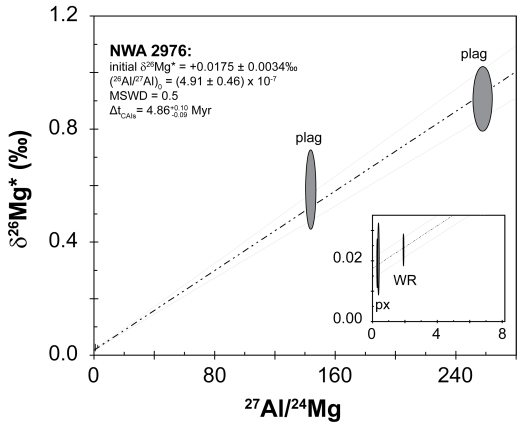

Figure 3.6: ^{26}Al-^{26}Mg isochron for NWA 2976.

the bulk rock and pyroxene combined with two feldspar analyses form an isochron with an initial ^{26}Al/^{27}Al of (4.91 $\pm$ 0.46) $\times$ 10^{-7} (Fig. 3.6). The initial δ^{26}Mg* is significantly elevated compared to the terrestrial standard i.e., +0.0175 $\pm$ 0.0034‰, and also clearly different from the δ^{26}Mg* measured in the CR2 chondrite NWA530 (-0.0004 $\pm$ 0.0065‰), which shares a similar nucleosynthetic fingerprint as NWA 2976 for elements like Cr and Ti (Trinquier et al., 2007, 2009).

Three chondrites all have δ^{26}Mg* within uncertainties of Earth, even though ^{54}Cr anomalies for these types of chondrites have been reported to range from -0.4 (L3) to +1.3 (CR2) epsilon units (Trinquier et al., 2007) i.e., more than an order of magnitude greater than their potential range in δ^{26}Mg*.

Stable Mg isotope variations of the studied achondrites are limited and generally consistent with previously published data for terrestrial igneous and mantle rocks and basaltic meteorites (Baker et al., 2005; Bizzarro et al., 2005; Wiechert and Halliday, 2007; Wadhwa et al., 2003a; Teng et al., 2007; Handler et al., 2009). δ^{25}Mg values of the three chondrites are slightly lighter than DSM-3, but within the range observed for the basalts.

3.4 Discussion

3.4.1 Data accuracy and reproducibility

Given the small size of the δ^{26}Mg* anomalies reported here for basaltic meteorites, it is important to assess the nature of the approach taken to measure these to the final quoted precisions. This is important because the final precision for each meteorite is achieved by combining or 'pooling' a number of separate analyses of the same sample each with a standard error that is similar in size to the anomalies ($\sim 0.020‰$) into a final result with a significantly better quoted precision. This is an approach that is common practise in the application of short-lived chronometers to meteorites and in resolving fine time differences in the early Solar System. For example, pooling of analyses to derive more accurate (and precise) isotopic data has been routinely used in ^{26}Al-^{26}Mg, ^{53}Mn-^{53}Cr and ^{182}Hf-^{182}W isotopic studies of solid formation, planetary differentiation and magmatism in the young Solar System (e.g., Lugmair and Shukolyukov, 1998; Kleine et al., 2005b,a; Markowski et al., 2006b,a; Schersten et al., 2006; Markowski et al., 2007; Jacobsen et al., 2008; Spivak-Birndorf et al., 2009). The accuracy and reproducibility of this approach can be demonstrated through analysing synthetic or natural terrestrial samples that will have no anomalies compared to the terrestrial standard, or through analysis of standards with artificial anomalies prepared by gravimetric doping with an enriched isotopic tracer (Fig. 3.3). We tested the accuracy of the pooling approach by analysing two materials (Aristar Mg standard solution and BHVO-2 basaltic rock standard) variably doped with a ^{26}Mg isotope spike to produce anomalies similar in size to the expected anomalies (δ^{26}Mg* = 0.010, 0.020, 0.030‰) in the basaltic meteorites (Table 3.3). Measurements of these doped standards resulted in δ^{26}Mg* values that were within 2 standard errors of the values anticipated from the gravimetrically prepared values. These results show that the pooling approach utilizing the chemical separation and mass spectrometric procedures used in this study generates

final results that are both accurate and precise to the quoted uncertainties. A pooled analysis of n = 20 or n =10 individual measurements can readily resolve δ^{26}Mg* anomalies smaller than 0.010 and 0.020‰, respectively.

3.4.2 Comparison with previously published ^{26}Al-^{26}Mg data for basaltic meteorites

For most of the analysed meteorites, ^{26}Al-^{26}Mg data has been previously published by Bizzarro et al. (2005), Baker et al. (2005) and Spivak-Birndorf et al. (2009). However, none of these previous studies utilised as rigorous techniques for chemical separation of Mg as this study. The analytical methods used in this study are also unique as they are the only high precision Mg isotope data obtained for these meteorites by pseudo-high-resolution mass spectrometry to ensure potential isobaric interferences are minimised. Furthermore, the reported meteorite data result from combining a greater number of pooled analyses than in the other studies, including analyses repeated in different analytical sessions, on Mg separated from the same sample digestion subjected to different chemistries and also on Mg separated from different digestions of the same samples. Twelve different basaltic meteorites including bulk rock samples and the mineral separates from the angrite Sah 99555 have been analysed to high precision in both this study and those of Bizzarro et al. (2005) and Baker et al. (2005). Ten out of twelve of these analyses show excellent agreement between these previously published studies and the data presented here i.e., within the quoted 2 se of the measurements (Fig. 3.4). However, the data previously published for the bulk samples of ADOR and Sah 99555 show slightly higher δ^{26}Mg* values than the data presented here. While it can not be definitively shown what is responsible for the difference between the results of Baker et al. (2005) for Sah 99555 and Angra dos Reis and this study, we suggest that these two samples might have experienced matrix effects that have produced artificially elevated δ^{26}Mg* excesses in

the study of Baker et al. (2005). In particular, it is possible that the presence of minor amounts of Ca in the Mg analysed by Baker et al. (2005) may have been responsible for the erroneous δ^{26}Mg* excesses as the presence of Ca leads to anomalously heavy stable Mg isotope compositions and small δ^{26}Mg* excesses (Table 3.2).

Given the more extensive assessment of analytical accuracy and reproducibility carried out in this study, and use of improved chemical separation techniques, as well as high resolution mass spectrometry, we consider that the data presented here should be considered the currently best available Mg isotope data for angrite meteorites and focus the discussion of the angrite ^{26}Al-^{26}Mg data and its chronological significance to the data presented in this paper and Spivak-Birndorf et al. (2009). We note that the Mg isotope data presented by Spivak-Birndorf et al. (2009) for bulk samples and mineral separates of the angrites Sah 99555 and D'Orbigny are generally consistent with the data presented here, although the uncertainties of the Mg isotope data of Spivak-Birndorf et al. (2009) for their low Al/Mg material (bulk samples, olivine and pyroxene) are somewhat larger than for the equivalent samples presented here. Data for three of the five feldspar separates presented by Spivak-Birndorf et al. (2009) also fall on the whole rock - mineral isochron shown in (Figure 3.5). Data for two other feldspar separates presented by Spivak-Birndorf et al. (2009) fall above the isochron in Figure 3.5 and also prevent the data of Spivak-Birndorf et al. (2009) from defining a statistically valid isochron sensu stricto. The reason for this is considered further in section 4.6, but is considered to reflect real heterogeneity and complexity within these angrite samples rather than analytical biases between and within these aforementioned studies.

3.4.3 Do small δ^{26}Mg* excesses in bulk basaltic meteorites have chronological significance?

It is pertinent to consider if the small δ^{26}Mg* excesses measured in bulk basaltic meteorites have chronological significance related to ^{26}Al decay as other explanations might be invoked to explain the excesses:

1. Cosmogenic effects: Meteorites with long cosmic ray exposure ages can experience burnout of isotopes that compromises dating with some short-lived isotopic systems, e.g., W isotopes in some iron meteorites (e.g., Schersten et al., 2006). However, the short exposure times of the studied meteorites (<100 Myr; Herzog, 2003), coupled with the small thermal neutron capture cross-sections of Mg isotopes ($\sigma(^{24}\text{Mg}) = 0.054$ barns; $\sigma(^{25}\text{Mg}) = 0.200$ barns; $\sigma(^{26}\text{Mg}) = 0.039$ barns; Walkiewicz et al., 1992) and low Na/Mg ($\sigma(^{23}\text{Na}) = 0.54$ barns) in the analysed samples means that it is unlikely that burnout of Mg isotopes (^{i}Mg(n,γ)$\rightarrow^{i+1}$Mg; ^{27}Mg(β^-)$\rightarrow^{27}$Al) or ^{24}Mg production from ^{23}Na (^{23}Na(n,γ,β^-)$\rightarrow^{24}$Mg) by interaction with galactic cosmic rays is responsible for the observed Mg isotope variations. Furthermore, calculation of the spallation burnout of Mg and Si isotopes based on production rates for ^{3}He (and ^{21}Ne) deduced from ^{81}Kr/Kr exposure ages (Herzog, 2003; Eugster, 2003) shows that production of these cosmogenic nuclides by interaction with higher energy particles over 100 Myr is orders of magnitude smaller than the observed ^{26}Mg excesses.

2. Parent body ^{26}Al isotope, Mg isotope or Al/Mg heterogeneity: The different δ^{26}Mg* values in basaltic meteorites as compared to Earth might be explained by the parent bodies of the basaltic meteorites having accreted from material with higher ^{26}Al or Al/Mg as compared to Earth (i.e., the terrestrial standards). Alternatively, nucleosynthetic Mg isotope heterogeneity might characterise the different parent bodies of the basaltic meteorites. These possibilities can

be ruled out. Firstly, three different classes of chondrites (EH3, L3 and CR2) that exhibit variable nucleosynthetic isotopic anomalies in, for example, ^{54}Cr (Trinquier et al., 2007) do not show any resolvable δ^{26}Mg* variations that would hint at ^{26}Al or Mg isotope heterogeneity on a planetesimal scale in the Solar System. Secondly, the diogenite Bilanga with sub-chondritic Al/Mg, which has an identical Δ^{17}O as the eucrites and mesosiderites and suggests these meteorites all originate from the same parent body (Greenwood et al., 2005, 2006), lacks the δ^{26}Mg* excesses of the eucrites and the mesosiderite clasts. Thirdly, all bulk samples of the 'old' angrites (Sah 99555, D'Orbigny) have positive δ^{26}Mg* anomalies that lie on a mineral isochron (Fig. 3.5), while other bulk angrites which other dating techniques have established to be considerably younger (Lugmair and Galer, 1992; Amelin, 2008b,a) do not have resolvable δ^{26}Mg* excesses.

3. Analytical artefacts: The small δ^{26}Mg* excesses in bulk basaltic meteorites are unlikely to be analytical artefacts as matrix-matched terrestrial standards do not show comparable δ^{26}Mg* excesses and, again, as the small δ^{26}Mg* excesses for the 'old' angrites lie on a mineral isochron. The method used to calculate δ^{26}Mg* excesses in this study uses the implicit assumption that any stable isotope fractionation between the sample and standard (DSM-3) is controlled by a kinetic rather than an equilibrium process. Given the limited stable Mg isotope fractionation observed between the samples and DSM-3 this is unlikely to generate any significant analytical artefacts. The small δ^{26}Mg* excesses also do not result from the relatively small samples analysed in this study fortuitously sampling feldspar-rich, high Al/Mg fragments, e.g. the measured ^{27}Al/^{24}Mg ratio of D'Orbigny that has a resolvable δ^{26}Mg* excess is within 1% of bulk major element analyses carried out on a much larger sample (0.2 g; Mittlefehldt et al., 2002).

In summary, all the available evidence suggests that the variable δ^{26}Mg* excesses measured in bulk basaltic meteorites result from ^{26}Al decay during the lifetime of ^{26}Al and have some chronological significance. We now consider exactly what process(es) and chronological significance the δ^{26}Mg* excesses in bulk basaltic meteorites might actually record.

3.4.4 What do ^{26}Al-^{26}Mg model ages of basaltic meteorites date?

The initial ^{26}Al/^{27}Al obtained from each of the three mineral isochrons (Sah 99555, D'Orbigny and NWA 2976) and the respective model initial ^{26}Al/^{27}Al values that can be obtained for the same samples by regressing the ^{26}Al-^{26}Mg data for the bulk rocks with the chondritic composition do not yield statistically identical initial ^{26}Al/^{27}Al values using the two different approaches. In all cases, the model initial ^{26}Al/^{27}Al obtained for the bulk rock is significantly higher by a factor of 2-4 than that obtained from the mineral isochron (Tables 3.5 and 3.6) meaning that the ^{26}Al-^{26}Mg model ages of the basaltic meteorites are 0.8 to 1.4 Myr (i.e., 1 to 2 half-lives of ^{26}Al) older than the mineral isochron ages. Two mechanisms can be invoked to explain this discrepancy. The first and most straightforward possibility is that complete or partial resetting of the ^{26}Al-^{26}Mg system in the rocks after crystallisation has redistributed Mg isotopes amongst the different minerals, which lowers the slope of the isochron and results in a positive intercept. This is a plausible scenario for NWA 2976, where the petrology suggests that the meteorite has experienced brecciation and thermal metamorphism (Yamaguchi et al., 2002). However, this is less likely to be the case for the two angrites Sah 99555 and D'Orbigny, which given the presence of strongly zoned mineral phases are thought to have cooled rapidly and to have experienced a simple thermal history (Mittlefehldt, 2007).

Table 3.5: Comparison of ages available for Sah 99555 and D'Orbigny and the angrite parent body. ^{26}Al-^{26}Mg isochron and model ages are calculated as described in Section 3.4.5. ^{182}Hf-^{182}W relative ages are calculated using $(^{182}Hf/^{180}Hf)_0 = (9.72 \pm 0.44) \times 10^{-5}$ for CAIs (Burkhardt et al., 2008) and these relative ages are anchored onto an absolute timescale using the Pb-Pb age of CAI AJEF. ^{53}Mn-^{53}Cr ages are anchored to the angrite NWA 4801 with a Pb-Pb age of 4558.0 ± 0.13 Ma (Amelin and Irving, 2007) and an initial $(^{53}Mn/^{53}Cr)_0 = (0.96 \pm 0.04) \times 10^{-6}$ (Shukolyukov et al., 2009).

Sample	Method & Source	$(^{26}Al/^{27}Al)_0$ (10^{-7})	t ± $2\sigma^1$ (Ma)	t ± $2\sigma^2$ (Ma)	t ± $2\sigma^3$ (Ma)	Δt^1 (Myr)	Δt^2 (Myr)	Δt^3 (Myr)
Angrites D'Orbigny and Sah 99555 combined								
(isochron)	^{26}Al-^{26}Mg	4.07 ± 0.21	4562.5 ± 0.4	4562.6 ± 0.2		$5.06^{+0.06}_{-0.05}$	$4.52^{+0.06}_{-0.05}$	
without fsp's	^{26}Al-^{26}Mg	9.63 ± 4.46	$4563.4^{+0.5}_{-0.7}$	$4563.5^{+0.4}_{-0.7}$	$4565.4^{+0.4}_{-0.7}$	$4.15^{+0.66}_{-0.40}$	$3.62^{+0.66}_{-0.40}$	$-0.96^{+0.66}_{-0.40}$
D'Orbigny								
(model)	^{26}Al-^{26}Mg	12.4 ± 3.5	$4563.7^{+0.4}_{-0.5}$	$4563.8^{+0.3}_{-0.4}$	$4565.6^{+0.3}_{-0.4}$	$3.88^{+0.35}_{-0.26}$	$3.35^{+0.35}_{-0.26}$	$-1.22^{+0.35}_{-0.26}$
(isochron)	^{26}Al-^{26}Mg	3.88 ± 0.27	4562.5 ± 0.4	4562.5 ± 0.2		$5.11^{+0.08}_{-0.07}$	$4.57^{+0.08}_{-0.07}$	
	^{26}Al-^{26}Mg[4]	5.06 ± 0.92	4562.8 ± 0.4			$4.83^{+0.21}_{-0.18}$		
	^{182}Hf-^{182}W[5]		4563.7 ± 1.0					
	^{53}Mn-^{53}Cr[6]		4563.8 ± 0.7					
	^{53}Mn-^{53}Cr[7]		4564.6 ± 0.3					
	^{207}Pb-^{206}Pb[8]		4564.42 ± 0.12					
Sah 99555								
(model)	^{26}Al-^{26}Mg	10.0 ± 3.1	4563.5 ± 0.5	$4563.5^{+0.4}_{-0.3}$	$4565.4^{+0.4}_{-0.3}$	$4.11^{+0.38}_{-0.28}$	$3.57^{+0.38}_{-0.28}$	$-1.00^{+0.38}_{-0.28}$
(isochron)	^{26}Al-^{26}Mg	4.45 ± 0.56	4562.6 ± 0.4	4562.7 ± 0.2	4564.6 ± 0.2	$4.96^{+0.14}_{-0.12}$	$4.43^{+0.14}_{-0.12}$	$-0.14^{+0.14}_{-0.12}$
	^{26}Al-^{26}Mg[4]	5.13 ± 1.90	$4562.8^{+0.5}_{-0.6}$			$4.81^{+0.49}_{-0.33}$		
	^{182}Hf-^{182}W[5]		4563.3 ± 1.0					
	^{53}Mn-^{53}Cr[6]		$4563.8^{+0.9}_{-1.1}$					
	^{207}Pb-^{206}Pb[9]		4564.58 ± 0.14					
APB	^{53}Mn-^{53}Cr[10]		4564.8 ± 0.5					

[1] wrt CAIs (Jacobsen et al., 2008), [2] wrt CAIs (Amelin et al., 2006; Wadhwa et al., 2009b), [3] wrt D'Orbigny herein and Amelin (2008a), [4] Spivak-Birndorf et al. (2009), [5] Markowski et al. (2007), [6] Sugiura et al. (2005), [7] Glavin et al. (2004), [8] Amelin (2008a), [9] Connelly et al. (2008b), [10] Shukolyukov and Lugmair (2007).

Table 3.6: Comparison of ages available for eucrites, mesosiderites, NWA 2976 and their parent bodies. All ages are calculated in the same manner as described in Table 3.5.

Sample	Method & Source	$(^{26}Al/^{27}Al)_0$ (10^{-7})	t $\pm 2\sigma^1$ (Ma)	t $\pm 2\sigma^2$ (Ma)	t $\pm 2\sigma^3$ (Ma)	Δt^1 (Myr)	Δt^2 (Myr)	Δt^3 (Myr)
Dhofar 007	^{26}Al-^{26}Mg	33.2 ± 14.0	$4564.8^{+0.5}_{-0.7}$	$4564.8^{+0.4}_{-0.6}$	$4566.7^{+0.4}_{-0.6}$	$2.96^{+0.57}_{-0.37}$	$2.31^{+0.57}_{-0.37}$	$-2.26^{+0.57}_{-0.37}$
	^{26}Al-^{26}Mg[4]		4564.6 ± 0.4					
Juvinas	^{26}Al-^{26}Mg	26.2 ± 4.2	4564.5 ± 0.4	4564.6 ± 0.2	4566.4 ± 0.2	$3.10^{+0.18}_{-0.16}$	$2.56^{+0.18}_{-0.16}$	$-2.01^{+0.18}_{-0.16}$
	^{26}Al-^{26}Mg[4]		4564.6 ± 0.4					
	^{53}Mn-^{53}Cr[5]		$4564.2^{+1.1}_{-1.2}$					
Millibillillie	^{26}Al-^{26}Mg	23.9 ± 7.0	4564.4 ± 0.5	$4564.5^{+0.3}_{-0.4}$	$4566.3^{+0.3}_{-0.4}$	$3.20^{+0.36}_{-0.27}$	$2.66^{+0.36}_{-0.27}$	$-1.91^{+0.36}_{-0.27}$
	^{26}Al-^{26}Mg[4]		$4564.0\ ^{+0.5}_{-0.6}$					
Camel Donga	^{26}Al-^{26}Mg	29.7 ± 6.1	4564.6 ± 0.4	4564.7 ± 0.3	$4566.6^{+0.2}_{-0.3}$	$2.96^{+0.24}_{-0.20}$	$2.43^{+0.24}_{-0.20}$	$-2.14^{+0.24}_{-0.20}$
	^{26}Al-^{26}Mg[4]		4564.7 ± 0.4					
1991.304	^{26}Al-^{26}Mg	40.7 ± 7.1	4565.0 ± 0.4	$4565.0^{+0.2}_{-0.3}$	4566.9 ± 0.2	$2.63^{+0.21}_{-0.17}$	$2.10^{+0.21}_{-0.17}$	$-2.48^{+0.21}_{-0.17}$
1991.305	^{26}Al-^{26}Mg	33.8 ± 5.0	4564.8 ± 0.4	4564.8 ± 0.2	4566.7 ± 0.2	$2.83^{+0.17}_{-0.15}$	$2.29^{+0.17}_{-0.15}$	$-2.28^{+0.17}_{-0.15}$
	^{26}Al-^{26}Mg[4]		4564.7 ± 0.4					
HED	^{53}Mn-^{53}Cr[5]		4566.6 ± 0.8					
E/MPB	^{53}Mn-^{53}Cr[6]		4566.0 ± 0.3					
MPB	^{53}Mn-^{53}Cr[7]		$4564.7\ ^{+1.3}_{-1.1}$					
NWA 2976	^{26}Al-^{26}Mg	18.1 ± 3.3	4564.1 ± 0.4	$4564.2^{+0.2}_{-0.3}$	4566.0 ± 0.2	$3.48^{+0.21}_{-0.18}$	$2.95^{+0.21}_{-0.18}$	$-1.62^{+0.21}_{-0.18}$
(isochron)	^{26}Al-^{26}Mg	4.91 ± 0.46	4562.7 ± 0.4	4562.8 ± 0.2	4564.7 ± 0.2	$4.86^{+0.10}_{-0.09}$	$4.32^{+0.10}_{-0.09}$	$-2.48^{+0.10}_{-0.09}$
	^{26}Al-^{26}Mg[8]		4563.1 ± 0.5					
	^{53}Mn-^{53}Cr[8]		$4564.0^{+2.2}_{-3.5}$					
	^{53}Mn-^{53}Cr[9]		~ 4565					

[1] wrt CAIs (Jacobsen et al., 2008), [2] wrt CAIs (Amelin et al., 2006; Wadhwa et al., 2009b),
[3] wrt D'Orbigny herein and Amelin (2008a), [4] Bizzarro et al. (2005), [5] Lugmair and Shukolyukov (1998),
[6] Trinquier et al. (2008), [7] Wadhwa et al. (2003b), [8] Sugiura and Yamaguchi (2007), [9] Bogdanovski and Lugmair (2004).

Here we describe a second scenario that might account for the different initial $^{26}Al/^{27}Al$ values obtained for the angrites from minerals isochrons as compared to the model age approach that has potential implications for interpretation of all ^{26}Al-^{26}Mg model ages for basaltic meteorites. Primitive meteorites or chondrites have $^{27}Al/^{24}Mg \sim 0.1$ (Krot et al., 2007), while the basaltic meteorites have $^{27}Al/^{24}Mg$ ratios that are much higher (~ 2). What is central to interpreting ^{26}Al-^{26}Mg model ages of basaltic meteorites is the nature of the process(es) that produced the elevated $^{27}Al/^{24}Mg$ ratios in the basaltic meteorites. In particular, whether the elevated $^{27}Al/^{24}Mg$ ratios reflects partial melting of chondritic (mantle) material of a planetesimal with $^{27}Al/^{24}Mg \sim 0.1$ to produce a basalt with a $^{27}Al/^{24}Mg \sim 2$ or whether extensive planetesimal melting produced a magma with an a $^{27}Al/^{24}Mg$ ratio much lower than that of the basaltic meteorites and that subsequent magmatic differentiation drove $^{27}Al/^{24}Mg$ ratios to the final values recorded by the basaltic meteorites.

Oxygen isotope evidence (Greenwood et al., 2005) suggests that small planetesimals like the HED and angrite parent bodies underwent complete or near complete melting leading to formation of magma oceans in the first few million years of the Solar System while there was enough heat supplied through radiogenic decay of ^{26}Al. It is unknown for how long these magma oceans might have persisted, but in the case of near complete melting, these magma oceans must have initially had chondritic $^{27}Al/^{24}Mg$ ratios that with time and declining radiogenic heat production cooled, differentiated due to crystallisation of olivine, spinel and pyroxene and changed composition. Depending on the timing of the onset of differentiation of the magma ocean and the time interval it then took to produce basaltic magmas with $^{27}Al/^{24}Mg$ ratios comparable to the basaltic meteorites, live ^{26}Al would have produced a certain amount of in-growth of ^{26}Mg in the magma ocean given its evolving and super-chondritic $^{27}Al/^{24}Mg$ ratio. As a result of this, basaltic magmas that erupted from differentiating magma oceans will today yield: (a) $\delta^{26}Mg^*$ excesses in bulk

samples that reflect a contribution from ^{26}Al decay in the magma ocean and, if eruption and crystallisation took place prior to extinction of ^{26}Al, also after solidification of the magma; (b) positive δ^{26}Mg* intercepts on ^{26}Al-^{26}Mg mineral isochron plots; (c) discrepant bulk rock model ages and mineral isochron ages, with the mineral isochron ages (if undisturbed by later events) representing crystallisation ages and the model ages representing a time that post-dates formation of the magma ocean (i.e., planetesimal melting) but pre-dates the crystallisation age of the magma.

To illustrate this, Figure 3.7 shows the possible, hypothetical, combinations of onset of magma ocean differentiation and timing of final crystallisation that can produce a basaltic sample with a δ^{26}Mg* anomaly and ^{27}Al/^{24}Mg ratio the same as measured in Juvinas in this study. As an example, if melting of the parent body was so extensive that the magma ocean initially had near-chondritic Al/Mg, then the δ^{26}Mg* excess of Juvinas can be produced in a magma ocean that had formed *prior* to 2.4 Myr (after CAI formation), began to evolve at 2.4 Myr, and underwent a ca. 1.7 Myr period of crystallisation producing a residual magma with an Al/Mg ratio like Juvinas that solidified 4.1 Myr after CAI formation yielding a crystallisation age consistent with the ^{53}Mn-^{53}Cr internal isochron for Juvinas (Fig. 3.7; Lugmair and Shukolyukov, 1998). Planetesimal melting is likely to have occurred significantly prior to 2.4 Myr after CAI formation as this time just reflects the onset of differentiation and Al/Mg evolution of the magma ocean. Very early crystallisation and differentiation of the magma ocean would have been retarded by heating due to the radioactive decay of ^{26}Al, while $\sim$ 2.3 Myr after CAI formation heating solely driven by radioactive decay of ^{26}Al would have been insufficient to induce melting (Sanders and Taylor, 2005). Other models where the degree of melting of the parent body is not as extensive and produces a magma ocean with higher than chondritic Al/Mg ratios require later differentiation of the magma ocean that would only pre-date the model ages by ca. 0.1 to 0.2 Myr. In general, the model age will always significantly post-date the

formation age of the magma ocean and slightly post-date the onset of differentiation of the magma ocean and potentially significantly pre-date the crystallisation age of the magma. Based on this modeling it is clear that ^{26}Al-^{26}Mg model ages do not necessarily date formation and crystallisation of basaltic magmas unless partial melting of the planetesimal directly produced magmas of basaltic composition and highlights that caution is necessary in extracting chronological information from ^{26}Al-^{26}Mg model ages, unless these are consistent with other chronological information.

3.4.5 Time anchors for mapping ^{26}Al-^{26}Mg data on to relative and absolute time scales

We calculate ^{26}Al-^{26}Mg ages either as isochron ages from mineral isochrons (Figs. 3.5 and 3.6) or model ages for bulk basaltic meteorites anchored to the chondritic composition of ^{27}Al/^{24}Mg = 0.1 and δ^{26}Mg* = 0 (Tables 3.5 and 3.6). Model ages calculated using either EH3 Sah 97096 or L3 Bovedy as representative for a chondritic composition change the calculated ages by less than 0.1 Myr.

Relative and absolute ages are calculated with a ^{26}Al decay constant of $\lambda_{^{26}Al}$ = 9.4952 $\times$ 10^{-7} yr^{-1} and using either: (1) the initial ^{26}Al/^{27}Al for the Allende CAI AJEF of (^{26}Al/^{27}Al)$_0$ = (4.96 $\pm$ 0.25) $\times$ 10^{-5} and its respective Pb-Pb age of 4567.60 $\pm$ 0.36 Ma (Jacobsen et al., 2008), or (2) the initial ^{26}Al/^{27}Al for the Efremovka CAI E60 of (^{26}Al/^{27}Al)$_0$ = (2.98 $\pm$ 0.27) $\times$ 10^{-5} (Wadhwa et al., 2009b) and its Pb-Pb age of 4567.11 $\pm$ 0.16 Ma (Amelin et al., 2002, 2006), or (3) the initial ^{26}Al/^{27}Al abundance in D'Orbigny obtained from the feldspar-controlled mineral - whole rock isochron in this study (^{26}Al/^{27}Al)$_0$ = (3.88 $\pm$ 0.27) $\times$ 10^{-7} and a Pb-Pb age of 4564.42 $\pm$ 0.12 Ma (Amelin, 2008a, Fig. 3.5). Relative and absolute ages referred to in the following sections are always anchored relative to AJEF if not stated otherwise, although absolute ages relative to all three anchors are shown in Tables 3.5 and 3.6 and the discrepancies between these different

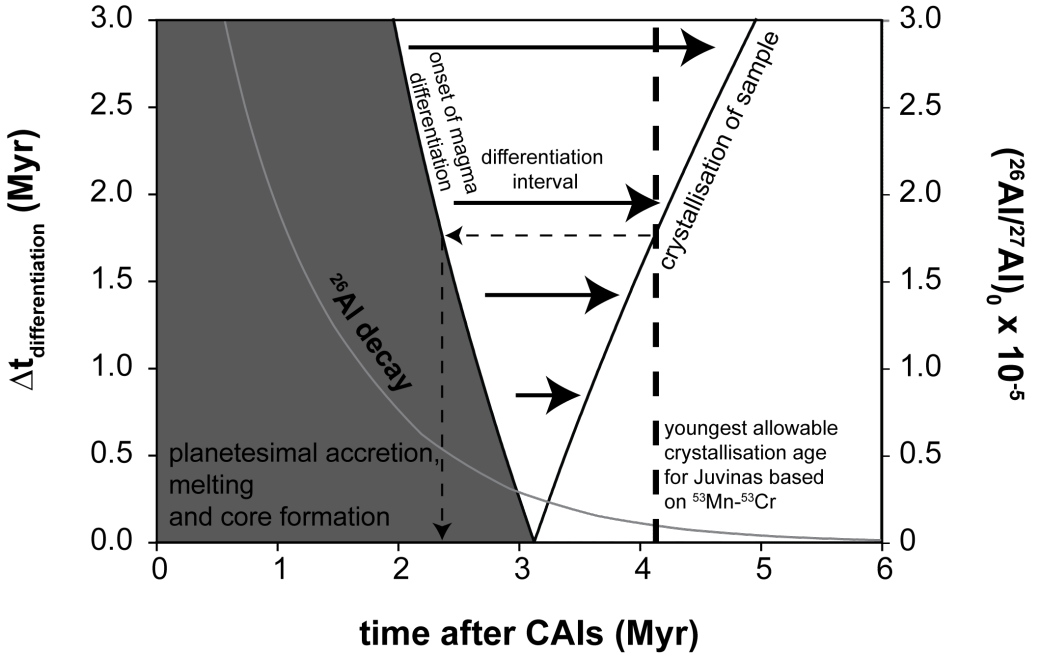

Figure 3.7: Modelled Mg isotope evolution of a differentiating magma ocean undergoing fractional crystallisation that produces a δ^{26}Mg* excess of 0.0303‰ (solid line marked as 'crystallisation of sample') as measured in Juvinas (^{27}Al/^{24}Mg = 1.71). The model demonstrates different ways that the same δ^{26}Mg* excess as in a bulk basaltic meteorite like Juvinas can be produced from a near completely molten planetesimal with a variable time for the onset of magma ocean differentiation and different time intervals for differentiation of the magma ocean. Evolution of the ^{27}Al/^{24}Mg ratio in the magma ocean resulting from fractional crystallisation is taken to be linear with time starting from an initially chondritic ratio (0.1) and finishing with the ^{27}Al/^{24}Mg ratio as recorded in the basaltic meteorite (Juvinas = 1.71). Exponential and logarithmic evolution of the ^{27}Al/^{24}Mg ratio in the magma ocean have also been modelled but do not deviate significantly from the linear evolution and for the sake of clarity are not shown. Also shown is the ^{26}Al/^{27}Al evolution over the same time period indicating the rapid decrease of radiogenic heat production that initially generates melting and prevents magma ocean differentiation on planetesimals. ^{53}Mn-^{53}Cr crystallisation age limit from (Lugmair and Shukolyukov, 1998).

approaches are explored further in section 4.7.

Recent high-precision measurements of uranium isotope ratios ($^{235}U/^{238}U$) in both CAIs (Brennecka et al., 2010b) and the angrite D'Orbigny (Brennecka et al., 2010a) have apparently revealed measurable deviations from the terrestrial value of 1/137.88 as a result of decay of short-lived ^{247}Cm in the early Solar System. These will result in the absolute ages for CAIs being ca. 0.5-1.0 Myr younger than the values used here, as only small differences in $^{235}U/^{238}U$ ratios have been reported for the large, coarse-grained, Type B CAIs that have been precisely Pb-Pb dated (Amelin et al., 2006; Jacobsen et al., 2008). Similarly, the $^{235}U/^{238}U$ ratio reported for pyroxene from the angrite D'Orbigny will also result in this angrite having a Pb-Pb age 0.6 Myr younger (Amelin, 2008a) than the value used here. Thus while the absolute ages quoted in Tables 3.5 and 3.6 may be too young by 0.5 to 1.0 Myr, any discrepancies in the ages obtained from different chronometers can not be readily explained by inaccuracies in Pb-Pb ages due to uranium isotope variations in meteorites.

3.4.6 ^{26}Al-^{26}Mg ages for asteroidal silicate melting

HED parent body: The small $\delta^{26}Mg^*$ excesses for Dhofar 007, Juvinas, Millibillillie and Camel Donga yield relative ages of $2.96^{+0.57}_{-0.37}$ Myr (Dhofar 007), $3.10^{+0.18}_{-0.16}$ Myr (Juvinas), $3.20^{+0.36}_{-0.27}$ Myr (Millibillillie) and $2.96^{+0.24}_{-0.20}$ Myr (Camel Donga) after formation of the CAI AJEF or $2.26^{+0.57}_{-0.37}$ Myr (Dhofar 007), $2.01^{+0.18}_{-0.16}$ Myr (Juvinas), $1.91^{+0.36}_{-0.27}$ Myr (Millibillillie) and $2.14^{+0.24}_{-0.20}$ Myr (Camel Donga) before crystallisation of D'Orbigny. Absolute ages obtained from the relative model ages anchored to CAIs and the D'Orbigny isochron are shown in Table 3.6 and range from 4564.4-4564.8 (CAIs) or 4566.3-4566.7 (D'Orbigny, Fig. 3.8). The absolute ages calculated for the basaltic meteorites are identical irrespective of whether the Allende CAI AJEF or Efremovka CAI E60 are used as the time anchors.

However, as discussed in section 4.4, these model ages may partly re-

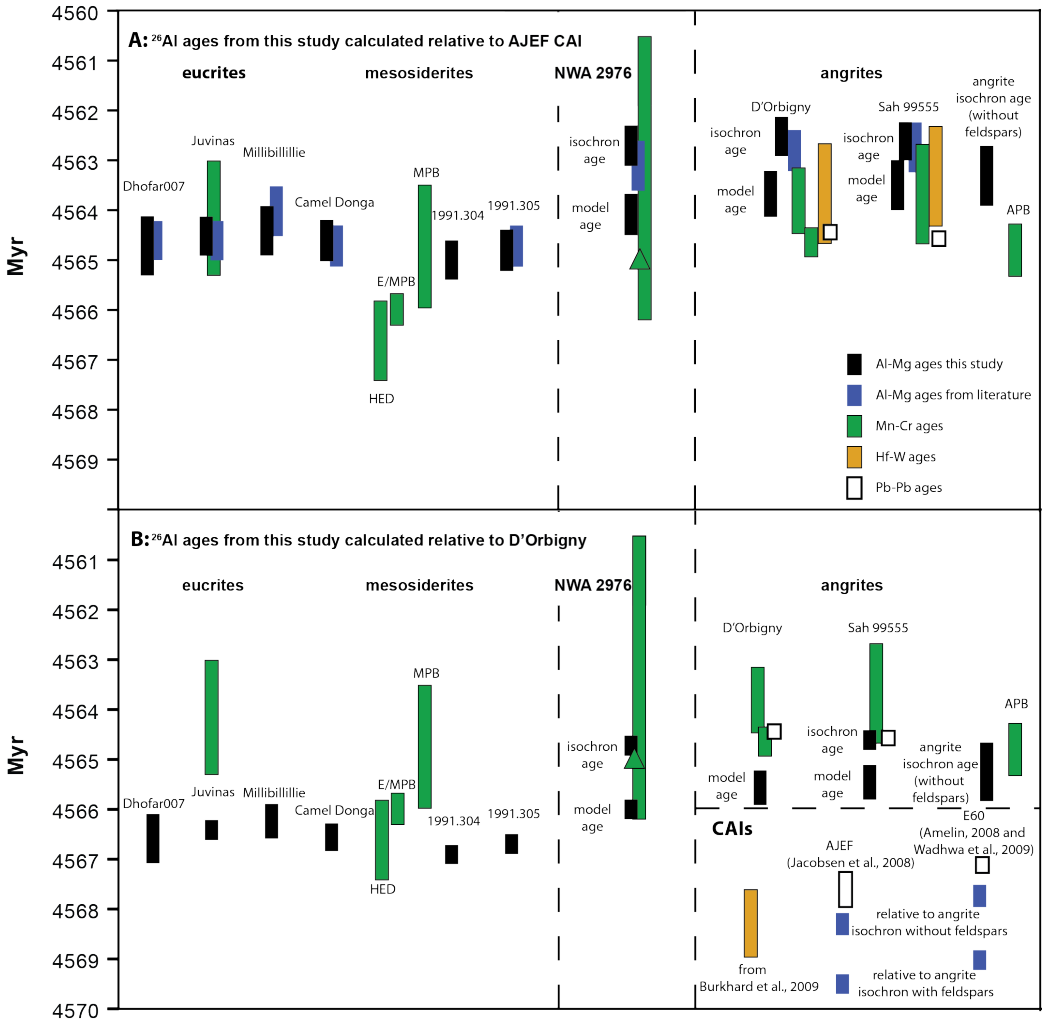

Figure 3.8: Comparison of absolute ages for basaltic meteorites obtained from absolute Pb-Pb and relative ^{182}Hf-^{182}W, ^{53}Mn-^{53}Cr and ^{26}Al-^{26}Mg ages anchored either to the Pb-Pb age of CAIs or D'Orbigny. In (A) Al-Mg ages are referenced relative to the Pb-Pb age of AJEF CAI, while in (B) Al-Mg relative ages are converted to absolute ages using the D'Orbigny feldspar-controlled mineral isochron as an anchor. For absolute ages shown in the figure please refer to Tables 3.5 and 3.6. Additionally, in (B) CAI ages are also shown when anchored to angrites relative to their absolute Pb-Pb ages.

flect the Al/Mg increase associated with formation (melting and differentiation) of basaltic magmas rather than the final crystallisation of the magmas. The model ages can only be realistic crystallisation ages if partial melting of a solid source produced magmas with a composition close to that of the basaltic meteorites and if this magma was erupted and solidified rapidly thereafter. If extensive melting initially produced an ultramafic magma ocean with much lower Al/Mg than the basaltic meteorites and this magma ocean then underwent fractional crystallisation over a period of several hundred thousands of years (or longer) to produce magmas akin to the basaltic meteorites then the model ages must be significantly younger than the timing of planetesimal melting and older than the crystallisation ages.

Mesosiderite parent body: The model ages for the two clasts from Vaca Muerta have similar relative ages of $2.63^{+0.21}_{-0.17}$ (1991.304) and $2.83^{+0.17}_{-0.15}$ Myr (1991.305) relative to CAI AJEF and $2.48^{+0.21}_{-0.17}$ (1991.304) and $2.28^{+0.17}_{-0.15}$ Myr (1991.305) before crystallisation of D'Orbigny that are within error of the model ages for the eucrites. Anchored to the CAIs AJEF or E60 these relative ages correspond to absolute ages of 4564.8-4565.0 Ma (Fig. 3.8). The absolute ages are ca. 2 Myr older when mapped onto an absolute timescale using the D'Orbigny feldspar-controlled mineral isochron.

Angrite parent body: The bulk rock analyses of Sah 99555 and D'Orbigny from this study can be used to calculate relative model ages of $4.11^{+0.38}_{-0.28}$ Myr and $3.88^{+0.35}_{-0.26}$ Myr after formation of CAI AJEF formation, which correspond to absolute ages of 4563.5 ± 0.5 Ma and $4563.7^{+0.4}_{-0.5}$ Ma, respectively (Fig. 3.8). The absolute age of Sah 99555 is ca. 2 Myr older when mapped onto an absolute timescale using the D'Orbigny feldspar-controlled mineral isochron.

However, the δ^{26}Mg* values of Sah 99555 and D'Orbigny can also be explained by the model presented in section 4.4, through formation of an extensive magma ocean on the angrite parent body within 3.0-3.5 Myr of CAI formation followed by $\sim$ 1.5-2.0 Myr of evolution of the magma ocean

before eruption and crystallisation 5.1 Myr after CAI formation. This age corresponds to that from a mineral-whole rock isochron using mineral and bulk rock data from Sah 99555 and D'Orbigny, which yields an isochron with an age of $5.06^{+0.06}_{-0.05}$ Myr after CAI formation, corresponding to an absolute age of 4562.5 $\pm$ 0.4 Ma, with no resolvable age difference between the different isochrons for Sah 99555 and D'Orbigny. The isochron has a non-zero intercept which might be explained by δ^{26}Mg* in-growth in an evolving magma ocean prior to crystallisation or impact melting of precursor material with an elevated Al/Mg that already carried elevated δ^{26}Mg* at 4562.5 Ma, or partial internal re-equilibration of Mg isotopes on a mineral scale after (earlier) crystallisation of these angrites. The isochron ages for D'Orbigny and Sah 99555 are both slightly younger but within uncertainties of isochron ages published by Spivak-Birndorf et al. (2009) for these angrites. The angrites LEW 86010 and ADOR have no resolvable δ^{26}Mg* excesses which is consistent with their young Pb-Pb ages (Amelin, 2008a). NWA 2999 also has no δ^{26}Mg* excess and is within error of the terrestrial standard, which is unsurprising given its low and near chondritic ^{27}Al/^{24}Mg ratio (0.21). While NWA 1296 appears to have a small positive δ^{26}Mg* anomaly, which is consistent with its similar age to Sah 99555 and D'Orbigny (Baker et al., 2005) and its super-chondritic ^{27}Al/^{24}Mg ratio (1.87), the precision of this study means that the anomaly is not clearly resolved from the terrestrial standard and hence no age constraints for this angrite are possible.

NWA 2976/NWA 011 parent body: The bulk rock analysis of NWA 2976 can be used to calculate a model age of $3.48^{+0.21}_{-0.18}$ Myr after formation of CAI AJEF, which corresponds to an absolute age of 4564.1 $\pm$ 0.4 Ma when anchored to this CAI. The absolute age is ca. 2 Myr older when mapped onto an absolute timescale using the D'Orbigny feldspar-controlled mineral isochron (Fig. 3.8). A mineral-whole rock isochron for NWA 2976 yields a significantly younger age of $4.86^{+0.10}_{-0.09}$ Myr after formation of CAI AJEF. The isochron has a significant positive δ^{26}Mg* intercept

that most likely reflects internal re-equilibration of Mg isotopes during brecciation and later thermal resetting of NWA 2976 (Yamaguchi et al., 2002) during the lifetime of ^{26}Al.

3.4.7 Comparisons with other long- and short-lived chronometers

HED parent body: Precise absolute age determinations on eucrites generally record much younger ages than the ^{26}Al-^{26}Mg model ages presented here that reflects, for example, the sensitivity of the Pb-Pb system (age range: 4.31 - 4.52 Gyr) to brecciation events (Tera et al., 1997; Galer and Lugmair, 1996). However, ^{53}Mn-^{53}Cr ages for the HED meteorites are consistent with ^{26}Al-^{26}Mg model ages for the eucrites (Table 3.6). Juvinas has a ^{53}Mn-^{53}Cr isochron age of $4564.2^{+1.1}_{-1.2}$ Ma and analyses of bulk HED meteorites define ages of ca. 4566 Ma (Lugmair and Shukolyukov, 1998; Trinquier et al., 2008) that are interpreted to represent global differentiation of the eucrite parent body. This age is slightly older than the ^{26}Al-^{26}Mg model ages (and modelled estimate for onset of differentiation of a magma ocean) anchored to CAIs. However, Mn/Cr ratios are likely to have been considerably more sensitive to crystal fractionation during magma ocean differentiation than Al/Mg ratios in (ultra)mafic magmas due to sequestering of the trace element Cr in large quantities in pyroxene and chromite. This may account for the ^{53}Mn-^{53}Cr differentiation age being slightly older than modelled estimate of the oldest ^{26}Al-^{26}Mg differentiation age (4564.7 Myr) of the magma ocean, based on a combination of the ^{53}Mn-^{53}Cr internal isochron and the ^{26}Al-^{26}Mg model age for Juvinas. ^{182}Hf-^{182}W data for basaltic eucrites have recently been reinterpreted to reflect core formation on the HED parent 2.5 $\pm$ 1.2 Myr after CAI formation (Touboul et al., 2008), which is in general agreement with the ^{26}Al-^{26}Mg model and differentiation ages.

Mesosiderite parent body: ^{53}Mn-^{53}Cr data for mesosiderite silicate

clasts (Wadhwa et al., 2003b) defined an apparent differentiation age that is 2 Myr younger than the HED parent body and is apparently at odds with the slightly older ^{26}Al-^{26}Mg model ages obtained for mesosiderite silicate clasts in this study as compared to Juvinas. This discrepancy most likely reflects either partial resetting of the ^{53}Mn-^{53}Cr system in the mesosiderite silicates during the catastrophic impact that produced the mesosiderites or a sampling phenomena due to the relatively small number of samples studied herein and Wadhwa et al. (2003b) whereby the mesosiderite silicate clasts analysed in this study are fortuitously older than those studied by Wadhwa et al. (2003b). This latter possibility is consistent with the fact that newly published analyses of mesosiderite clasts lie on the HED isochron (Trinquier et al., 2008), although the near-chondritic Mn/Cr ratios of the mesosiderite clasts analysed by Trinquier et al. (2008) mean that it is inevitable that these analyses will lie close to the HED ^{53}Mn-^{53}Cr isochron.

Angrite parent body: The ^{26}Al-^{26}Mg model ages for Sah 99555 and D'Orbigny are in excellent agreement with recently published age constraints from other short-lived chronometers (Table 3.5) including both the ^{53}Mn-^{53}Cr and the ^{182}Hf-^{182}W systems. However, the ^{26}Al-^{26}Mg isochron age for angrites is significantly younger than the ^{26}Al-^{26}Mg model ages and ^{53}Mn-^{53}Cr and ^{182}Hf-^{182}W isochron ages. The reason for this is not clear, but might reflect internal redistribution of Mg isotopes between feldspar and the mafic minerals it is intergrown with after crystallisation. While feldspar has a relatively low diffusion temperature for Mg (LaTourrette and Wasserburg, 1998), the textures of Sah 99555 and D'Orbigny do not hint at such internal re-equilibration through diffusion or brecciation. However, an isochron calculation utilising just analyses of mafic minerals (olivine+pyroxene) and bulk rock samples of Sah 99555 and D'Orbigny yields an initial ^{26}Al/^{27}Al value and age that is identical to the ^{26}Al-^{26}Mg model ages lending credence to the hypothesis that feldspar Mg isotope systematics in these angrites are partially reset and do not, in detail, ac-

tually record the crystallisation ages of these rocks. While the errors on such a mafic mineral (olivine+pyroxene) and bulk rock isochron are still large and should be tested with higher precision analysis, the difference between isochrons with and without feldspars may also explain why some of the feldspar ^{26}Al-^{26}Mg data reported by Spivak-Birndorf et al. (2009) do not define a true isochron. We thus consider the ^{26}Al-^{26}Mg model ages for the angrites Sah 99555 and D'Orbigny along with the mafic mineral - whole rock isochron to best date the crystallisation of these angrites. This interpretation implies that the feldspar-controlled mineral isochron(s) for the angrites should not be used to map the ^{26}Al-^{26}Mg ages onto an absolute timescale.

However, in detail, the preferred absolute age (4563.6 $\pm$ 0.3 Ma; mean model ages for Sah 99555 and D'Orbigny) for these angrites calculated from the ^{26}Al-^{26}Mg data anchored to CAIs still appear to be ca. 1 Myr younger than the high precision Pb-Pb ages of these angrites (Table 3.5). This suggests either that the Pb-Pb ages of Sah 99555 and D'Orbigny are compromised and too old due to the presence of a small amount of highly radiogenic initial Pb inherited from the precursor material (e.g., Connelly et al., 2008b) in these meteorites or that the Pb-Pb ages for CAIs, which are used as the absolute time anchors for the ^{26}Al-^{26}Mg (and ^{182}Hf-^{182}W) systems in Table 3.5, are erroneous and slightly too young for reasons that are currently not clear. A recent study of ^{182}Hf-^{182}W systematics of CAIs (Burkhardt et al., 2008) integrated with a ^{182}Hf-^{182}W study of angrites (Markowski et al., 2007) also came to a similar conclusion that CAIs were, in fact, 4568.3 $\pm$ 0.7 Ma in age and that CAI Pb-Pb ages were slightly too young for as yet unknown reasons. Utilising ^{26}Al-^{26}Mg bulk-rock model ages and the mafic mineral - whole rock isochron age for Sah 99555 and D'Orbigny yields a formation age for CAIs and minimum age of the Solar System of 4568.5 $\pm$ 0.3 Myr, which is identical to that of Burkhardt et al. (2008).

While the possibility that Pb-Pb ages of CAIs do not accurately date

their formation is the simplest explanation, a more speculative explanation for the discrepancies that emerges when ages for angrites and CAIs are compared is that the precursor material from which the angrite parent body accreted contained only ca. 40% of the ^{26}Al inventory of CAIs, hinting at possible heterogeneous distribution of this short-lived nuclide in the proto-planetary disc. Such a ^{26}Al deficit would make the angrites 1.0 Myr older removing the apparent offset between Pb-Pb and ^{26}Al-^{26}Mg model ages. However, given the similar δ^{26}Mg* of terrestrial material, chondrites, Bilanga and the initial δ^{26}Mg* of the angrite isochron it also implies that all bodies in the planet-forming region would have accreted from material with lower ^{26}Al as compared to the initial abundance in CAIs. This would then also require the ^{26}Al-^{26}Mg ages of eucrites and mesosiderites when mapped onto an absolute timescale to actually be ca. 1.0 Myr older than shown in Table 6. Another implication of such low levels of ^{26}Al in the planetesimal- and planet-forming region of the proto-planetary disc is that ^{26}Al would have only been the primary heat source for melting planetesimals in the young Solar System if these bodies accreted at the same time as CAI formation.

NWA 2976/NWA 011 parent body: Existing age constraints for NWA 2976 or NWA 011 are scarce. However, available ^{53}Mn-^{53}Cr and ion probe ^{26}Al-^{26}Mg data yield age estimates which are broadly consistent with the ^{26}Al-^{26}Mg model and isochron ages for NWA 2976 presented here (Table 3.6).

3.4.8 Timing of accretion of achondrite parent bodies and mechanisms for planetesimal melting

With the exception of the 'young' angrites all basaltic meteorites have small δ^{26}Mg* excesses that are consistent with asteroidal melting and formation of basaltic magmas having taken place whilst ^{26}Al was extant in the young Solar System and their parent bodies. Basaltic magmatism and

asteroidal melting on the eucrite/mesosiderite parent body dates to within 2.6 to 3.2 Myr of CAI formation (Table 3.6) and the available data allows magma ocean formation considerably earlier than this. Simple thermal models of accreting asteroids heated by the radioactive decay of ^{26}Al (Bizzarro et al., 2005; Sanders and Taylor, 2005; Sahijpal et al., 2007) show that planetesimals tens of kilometres in size that accreted in the first million years of the Solar System would have undergone almost complete melting due to the radioactive decay of ^{26}Al. Melting of the planetesimals takes place rapidly i.e., within a few hundred thousand years of accretion. The significant time delay that is apparent between melting and the model and isochron ages for basaltic meteorites obtained in this study are not unexpected as continued radioactive heating by ^{26}Al delays the onset of significant cooling, crystallisation and differentiation of the magma ocean for a further 1-2 Myr (e.g., Sanders and Taylor, 2005). This may also explain the significant time gap (2 Myr) between ^{182}Hf-^{182}W age constraints of metal-silicate segregation as recorded by iron meteorites (Kleine et al., 2005a; Schersten et al., 2006; Markowski et al., 2006a) and ^{26}Al-^{26}Mg age constraints for silicate differentiation and crystallisation on planetesimals presented here.

The angrite parent body appears to be different to the eucrite/mesosiderite parent body in two respects. Firstly, assuming an identical initial abundances of ^{26}Al in the material both these parent bodies accreted from, the oldest model ages of angrites are ca. 1.5 Myr younger than for basaltic meteorites from the eucrite/mesosiderite parent body. Secondly, some samples from the angrite parent body formed significantly later than Sah 99555 and D'Orbigny. However, initial ^{87}Sr/^{86}Sr ratios can be used to argue that the angrite parent body (or the material it accreted from) experienced volatile depletion very shortly after CAI formation and that this predated volatile depletion on the eucrite/mesosiderite parent body by ca. 1 Myr (Halliday and Porcelli, 2001). It is unlikely that this early Rb volatile depletion event shortly after CAI formation also pro-

duced the extreme U/Pb ratios throughout the entire angrite parent body and, specifically, the source(s) of LEW 86010 and ADOR. If this were the case then Pb-Pb model ages for the young angrites LEW 86010 and ADOR (4557-4559 Myr) would be erroneous (too old) because of several million years of radiogenic in-growth of Pb in an extreme U/Pb planetesimal (Lugmair and Galer, 1992). This would be inconsistent with the mounting evidence that the Pb-Pb ages of the young angrites are in general agreement with short-lived chronometers (Markowski et al., 2007; Kleine et al., 2007; Burkhardt et al., 2008), specifically their ^{182}Hf-^{182}W systematics, and in general terms with the ^{26}Al-^{26}Mg age constraints from this work.

Thus, we speculate that if all the angrites originate from the same parent body that two further, secondary, phases of more extreme volatile depletion are required on the angrite parent body that occurred at ca. 4557 - 4559 Ma and 4564 Ma, which post-date the early, modest, volatile depletion associated with accretion. The most plausible explanation to produce these later extreme volatile depletion events separated by several million years are large impact events. Such impact events between planetesimals have been suggested to have produced material from which the CB chondrite parent body accreted (Krot et al., 2005). The collisional events on the angrite parent body would need to have involved significant impactors to account for the extreme Pb depletion, but not sufficiently energetic to completely destroy the impacted parent body as was apparently the case for the CB chondrite body. Finally, we note that the absence of δ^{26}Mg* excesses in the young angrites coupled with their varied petrography and range of Al/Mg ratios suggests that the impact event must have been large enough to create a significant body of magma from part of the angrite parent body with a near chondritic Al/Mg ratio and did not simply involve remelting of pre-existing basaltic crust with elevated Al/Mg of comparable age to the other (older) angrites.

3.5 Conclusions

A high-precision Mg isotope study of basaltic meteorites by pseudo-high-resolution MC-ICP-MS utilising improved chemical separation techniques for Mg has shown:

1. Bulk samples of basaltic meteorites from at least three parent bodies have δ^{26}Mg* excesses that cannot be explained by cosmogenic effects, or parent body ^{26}Al, Mg isotope or Al/Mg heterogeneity, or analytical artefacts and confirm the studies of Baker et al. (2005) and Bizzarro et al. (2005) that radioactive decay of ^{26}Al was responsible for planetesimal melting in the young Solar System.

2. ^{26}Al-^{26}Mg model ages for the basaltic meteorites constrain asteroidal melting and magmatism to 2.6-3.2 (eucrite/mesosiderite parent body), 3.9-4.1 (angrite parent body) and 3.5 Myr (NWA 2976/NWA 011 parent body) after CAI formation. However, these ages may record Al/Mg fractionation associated with differentiation of asteroidal magma oceans and formation of basaltic magmas rather than the timing of basalt crystallisation. Given evidence for widespread magma oceans on planetesimals it is likely these ages are younger than asteroidal melting which will predate the model ages by a period of time until levels of ^{26}Al had decayed sufficiently to allow cooling and differentiation of the magma oceans.

3. Bulk rock and mineral separate data of the angrites (Sah 99555 and D'Orbigny) and NWA 2976 yield isochron ages of $5.06^{+0.06}_{-0.05}$ Myr and $4.86^{+0.10}_{-0.09}$ Myr, respectively, after CAI formation. The combined angrite isochron has a slightly positive δ^{26}Mg* that either reflects in-growth of δ^{26}Mg* in an evolving magma ocean prior to crystallisation of these angrites or impact melting of a precursor with super-chondritic Al/Mg that already carried elevated δ^{26}Mg*, or most likely partial internal re-equilibration of Mg isotopes after crys-

tallisation. The data suggests that the feldspar-controlled mineral isochron for the angrites Sah 99555 and D'Orbigny is not ideal to map ^{26}Al-^{26}Mg age information onto an absolute timescale. NWA 2976 has a larger positive initial δ^{26}Mg* that probably reflects internal re-equilibration of Mg isotopes during brecciation and thermal resetting after crystallisation of this rock.

4. ^{26}Al-^{26}Mg model and mafic mineral - whole rock isochron ages and ^{53}Mn-^{53}Cr and ^{182}Hf-^{182}W ages for Sah 99555 and D'Orbigny are concordant mapped onto an absolute timescale using the Pb-Pb ages for CAIs [^{26}Al-^{26}Mg, ^{182}Hf-^{182}W] and NWA 4801 [^{53}Mn-^{53}Cr]. However, the precise relative age constraints from ^{26}Al-^{26}Mg data are uniformly younger ($\sim$ 1 Myr) than precise Pb-Pb ages for Sah 99555 and D'Orbigny. This can either be explained through the Pb-Pb ages for the angrites being too old or those for CAIs too young for reasons that are not as yet well understood. While this discrepancy may hint that ^{26}Al was markedly heterogeneously distributed between the CAI- and planetesimal- and planet-forming regions of the protoplanetary disc, the simplest explanation is that the Pb-Pb ages for CAIs do not accurately date their formation and that the age of CAI formation is best constrained by the relative ^{182}Hf-^{182}W and ^{26}Al-^{26}Mg clocks anchored to the Pb-Pb ages of angrites as being 4568.3 $\pm$ 0.7 and 4568.5 $\pm$ 0.3 Ma, respectively.

5. Two generations of angrites are evident from long- and short-lived chronometry that formed at ca. 4557-4559 Ma (LEW 86010 and ADOR) and 4564 Ma (Sah 99555 and D'Orbigny). The extreme U/Pb ratios of both the 'young' and 'old' angrites can not have been a feature of the entire angrite parent body since the time of the volatile depletion event that established the low initial ^{87}Sr/^{86}Sr ratios of the angrites 1 - 2 Myr after CAI formation. The two generations of angrites may have been produced by large impact melting events on

the angrite parent body which resulted in Pb loss and production of extreme U/Pb.

Chapter 4

High precision Mg isotopic systematics of bulk chondrites

Abstract

Variations of the mass-independent abundance of ^{26}Mg (δ^{26}Mg*) and stable Mg (δ^{25}Mg) isotope composition of chondrites are important because they constrain the homogeneity of ^{26}Al and Mg isotopes in the protoplanetary disk and the validity of the short-lived ^{26}Al-to-^{26}Mg chronometer applied to meteorites. We present high-precision Mg isotope data and Al/Mg ratios of chondrites representing nearly all major chondrite classes, including a step-leaching experiment on the CM2 chondrite Murchison. δ^{26}Mg* variations in leachates of Murchison representing acid soluble material are $\leq$ 30 times smaller than reported for neutron-rich isotopes of Ti and Cr and do not reveal resolvable deficits in δ^{26}Mg* (-0.002 to +0.118‰). Very small variations in δ^{26}Mg* anomalies in bulk chondrites (-0.006 to +0.019‰) correlate with increasing ^{27}Al/^{24}Mg ratios and δ^{50}Ti, reflecting the variable presence of calcium-aluminium-rich inclusions (CAIs) in some types of carbonaceous chondrites. Similarly, release of radiogenic ^{26}Mg produced by ^{26}Al decay from CAI material in the step-leaching of Murchison best explains the high δ^{26}Mg* observed in the last, aggressive, leaching steps of this experiment. Overall, the observed variations in

δ^{26}Mg* are small and potential differences beyond that which result from the presence of CAI-like material cannot be detected within the analytical uncertainties of this study. The results do not allow radical heterogeneity of ^{26}Al ($\geq \pm$ 30%) or measurable Mg nucleosynthetic heterogeneity ($\geq \pm$ 0.005‰) to have existed on a planetesimal scale in the protoplanetary disk. Combined with published δ^{26}Mg* data for CAIs, the bulk chondrite data yield a precise initial $(^{26}Al/^{27}Al)_0$ = (5.21 $\pm$ 0.06) $\times$ 10^{-5} and δ^{26}Mg* = -0.0340 $\pm$ 0.0016‰ for the Solar System. However, it is not possible with the currently available data to determine with certainty whether CAIs and the material from which planetesimals accreted had precisely the same initial levels of ^{26}Al, although planetesimals (i.e., chondrite parent bodies) and planets appear to have accreted from material with a mean initial $(^{26}Al/^{27}Al)_0$ in the range of 2.1 to 6.7 $\times$ 10^{-5}. The average stable Mg isotope composition of all analysed chondrites, with the exception of a chondrule from the CBa chondrite Gujba ($\delta^{25}Mg_{DSM-3}$ = -0.032 $\pm$ 0.035‰), is $\delta^{25}Mg_{DSM-3}$ = -0.152 $\pm$ 0.079‰ (2 sd) and is indistinguishable from that of Earth's mantle.

4.1 Introduction

Magnesium (Mg) is the most abundant non-gaseous element on an atomic basis in the Solar System and is characterised by a moderately refractory nature ($T_{c(Mg_2SiO_4)}$ = 1430°; Lattimer et al., 1978). Mg has three stable isotopes (^{24}Mg, ^{25}Mg, ^{26}Mg) that are produced in stellar environments through explosive hydrogen burning (^{24}Mg) and neon burning in the α-process, carbon burning, and explosive nucleosynthesis (^{25}Mg and ^{26}Mg; Anders and Grevesse, 1989). In addition to the potentially different presolar stellar nucleosynthetic Mg isotope contributions to meteorites, the abundance of ^{26}Mg in meteorites can also be affected by the decay of now-extinct ^{26}Al ($t_{1/2}$ = (7.08 $\pm$ 0.17) $\times$ 10^5 yr; Nishiizumi, 2004). This short-lived isotope and the Mg isotope system form the basis of an important

short-lived chronometer for dating meteorites and their constituents and, thus, solid formation and planetesimal accretion and differentiation in the young Solar System (e.g., Russell et al., 1996; Srinivasan et al., 1999). It has been known for sometime that the short-lived isotope ^{26}Al was probably heterogeneously carried into the proto-Solar System given that sub-micron sized pre-solar grains in chondrite meteorites preserve a wide range of inferred ^{26}Al values encompassing five orders of magnitude from 10^{-5} to almost 10^{0} (e.g., Zinner et al., 2005). However, it is currently unclear to what level ^{26}Al was homogeneously distributed in the Solar System on both a scale of mm- to cm-sized solids such as in calcium-aluminium-rich inclusions (CAIs) and chondrules, and on a much larger km-sized scale of planetesimals as represented by chondrite and achondrite meteorites and Earth and the terrestrial planets. However, a recent study of the Mg isotope systematics of chondrules from the unequilibrated LL3.0 ordinary chondrite Semarkona concluded that these data were consistent with ^{26}Al and Mg isotopes having been homogeneously ($\pm$ 10%) distributed in the material that chondrules in this chondrite formed from, as well as Earth and CAIs (Villeneuve et al., 2009).

Recent studies have identified significant mass-independent variations (e.g., δ^{50}Ti $\sim 0.7‰$) in the abundance of neutron-rich isotopes of iron-peak elements (Ti, Cr and Ni; Trinquier et al., 2007, 2009; Regelous et al., 2008) in chondritic and achondritic meteorites, which reflect imperfectly mixed pre-solar nucleosynthetic contributions to the proto-planetary disk on a planetesimal scale in the Solar System. While the stellar processes responsible for these variations are not necessarily coupled to ^{26}Al or Mg isotope nucleosynthesis, these variations highlight the need for a careful evaluation of the degree of ^{26}Al and Mg isotope heterogeneity in meteorites. This is particularly important as improvements in analytical techniques are increasingly being utilised to measure and use very small Mg isotope variations ($\leq 0.01‰$) to date early Solar System processes with uncertainties of $\leq \pm$ 0.1 Myr. However, such information derived from the ^{26}Al-

^{26}Mg clock might be erroneous if either ^{26}Al or Mg isotopes were heterogeneously distributed in the proto-planetary disk around the young Sun. For example, model ^{26}Al-^{26}Mg ages inferred for asteroidal silicate magmatism from small positive ^{26}Mg anomalies in bulk basaltic meteorites (Baker et al., 2005; Bizzarro et al., 2005; Schiller et al., 2010a) as compared to Earth may have no, or inaccurate, age significance if Mg nucleosynthetic variations exist on a planetesimal scale in the Solar System or if ^{26}Al was heterogeneously distributed amongst different planetesimals and planets. Furthermore, all relative ^{26}Al-^{26}Mg ages of meteoritic material and their absolute ages when mapped onto the absolute timescale with anchoring Pb-Pb ages could be compromised if ^{26}Al was heterogeneously distributed in the proto-planetary disk.

In addition to the potential mass-independent variations in Mg isotopes in the proto-planetary disk, mass-dependent variations in Mg isotopes are also important in understanding the nature of material from, and processes by which, solids formed and planetesimals and planets accreted around the young Sun. Mg stable isotopes are most likely to have been fractionated in the proto-planetary disk by thermal processing and evaporation and condensation processes. For example, the Solar System's oldest solids (CAIs) have both heavy and light stable Mg isotope compositions indicating that they experienced multi-stage evaporation and condensation events (Clayton et al., 1988; Young et al., 2005). Currently, debate exists as to whether the Earth has the same stable Mg isotopic composition as undifferentiated chondritic meteorites (Wiechert and Halliday, 2007; Teng et al., 2007; Handler et al., 2009; Yang et al., 2009).

In this paper we investigate the magnitude of mass-independent (n = 17) and mass-dependent (n = 19) Mg isotope variations in all major classes of chondrite meteorites determined by improved chemical separation and mass spectrometric techniques (Schiller et al., 2010a). This data set also includes a progressive acid step-leaching experiment on the CM2 chondrite Murchison. These are the first high-precision Mg isotope data de-

termined on chondrites after complete removal of matrix elements such as Mn and Ni and measured by high-resolution mass spectrometry. These data demonstrate that at the current levels of analytical reproducibility (ca. $\pm$ 0.005‰) ^{26}Al and mass-independent abundances of Mg isotopes were distributed homogeneously in chondrite parent bodies, although some bulk chondrites exhibit minor variability in the mass-independent abundance of ^{26}Mg due to the presence of CAIs. The average stable Mg isotope composition of chondrites is also shown not to be significantly different to Earth.

4.2 Samples and Methods

4.2.1 Samples

We analysed a wide range of chondrites including two LL3 chondrites (Begaa, a LL3.2 and Talbachat n'aït Isfoul a LL3.7), one H6 chondrite (Portales Valley, which is an unusual H6 chondrite; Ruzicka and Hutson, 2005), one L3 chondrite (Bovedy) and one enstatite chondrite, Sahara 97096 (Sah 97096; Weisberg and Prinz, 1998). Eleven carbonaceous chondrites were analysed including the CI chondrite Orgueil, two CM2 chondrites (Murchison and provisionally named Northwest Africa (NWA) 4428), two CO3 chondrites (NWA 763 and NWA 1232 of which the lesser metamorphosed phase was analysed; Kiriishi and Tomeoka, 2008), two CV3 chondrites (Allende and NWA 2364), three CR2 chondrites (NWA 1180, NWA 530 and NWA 801), one CH3 chondrite (Sayh Al Uhaymir 290, hereafter called SAU 290), one chondrule from the CBa chondrite Gujba and two CK chondrites (the CK3 NWA 1559 and the CK5 NWA 1563).

4.2.2 Sample preparation

Between 50-200 mg of each meteorite was powdered with an agate mortar and pestle. Larger and representative fragments of the most petrograph-

ically diverse chondrites (e.g., CV and CK) were crushed to ensure that samples were representative of each chondrite type. In the case of the CBa chondrite Gujba, approximately half of a single large (ca. 5 mm) chondrule was crushed. 5-10 mg of each powdered sample was digested in a mixture of concentrated HF-HNO_3 (3:1) on a hotplate at 130°C. Samples were also refluxed in aqua regia to ensure complete dissolution of samples. While our digestion techniques will not dissolve carbon-rich and oxide pre-solar grains, given typical Mg isotope ratios of these grains (Zinner, 2007) and their Mg contents and abundances in chondritic meteorites, these have no leverage on our results, which are dominated by the Mg isotopic composition of silicate-hosted Mg in the meteorites. These digestion procedures are essentially identical to those used for studies of Cr and Ti nucleosynthetic variations in meteorites (Trinquier et al., 2007, 2009) and make our results directly comparable with those studies. Solution aliquots equivalent to $\sim$ 2 mg of digested sample were then processed through several chemical separation steps in order to purify Mg.

A detailed description of the analytical procedures used for Mg separation is given in Schiller et al. (2010a) and a schematic of this procedure is shown in Figure 4.1. After the last separation step, the Mg is fluxed for 12 h at 110° C in 1 mL of aqua regia and then converted to chloride form. Prior to analysis, all samples were screened for potential contaminant elements to ensure the purity of each sample. The final Mg cut of the chondrite samples is typically >99.5% pure Mg.

4.2.3 Mg isotope measurements

Mg isotope ratios were analysed with a Nu Plasma high-resolution multi-collector inductively coupled plasma mass spectrometer (MC-ICP-MS) operated in pseudo-high resolution mode. Mg solutions were introduced using a desolvating nebulizer (DSN-100). All isotopic measurements in this study were conducted using the standard-sample bracketing technique,

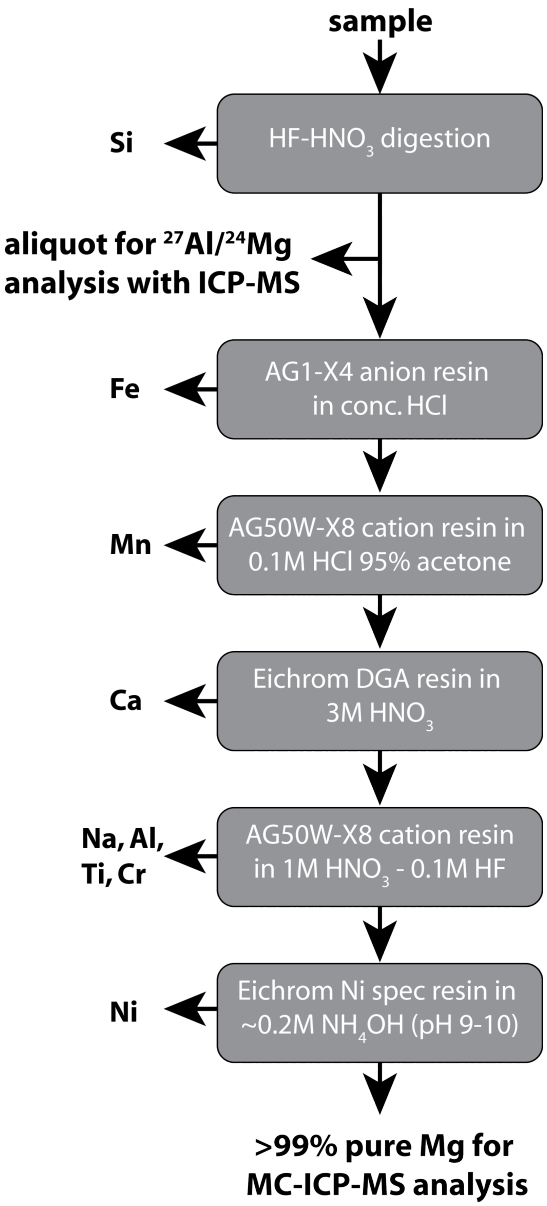

Figure 4.1: Schematic of the chemical separation procedures used to purify Mg. A detailed description of these procedures can be found in Schiller et al. (2010a).

where the isotope ratios are expressed as per mil (‰) deviations from the mean Mg isotopic composition measured in the bracketing standards $\delta^x Mg = [(^xMg/^{24}Mg)_{sample}/(^xMg/^{24}Mg)_{standard} - 1] \times 10^3$, and x is either 25 or 26. The mass-independent ^{26}Mg abundance (δ^{26}Mg*) in the samples was corrected for instrumental mass bias by normalising the measured ^{26}Mg/^{24}Mg ratios to a ^{25}Mg/^{24}Mg ratio of 0.12663 (Catanzaro et al., 1966) using the exponential law (β = 0.511).

The isotopic measurements to determine δ^{26}Mg* in the various materials analysed here were bracketed against DSM-3 (Galy et al., 2003) and/or Mg separated from J11 mantle olivine, an in house standard ($\delta^{25}Mg_{DSM-3}$ = -0.110 $\pm$ 0.006‰; Handler et al., 2009) subjected to the same Mg separation procedure as the analysed samples. J11 olivine has a stable Mg isotopic composition which more closely represents the Mg isotopic composition of the Earth than DSM-3 (Handler et al., 2009). The reason for using J11 is that it is possible that the slight isotopic difference between DSM-3 and Earth is a result of equilibrium fractionation processes (Young and Galy, 2004; Tipper et al., 2008). If so, pure equilibrium fractionation could result in slightly erroneous mass-bias-corrected δ^{26}Mg* anomalies when calculated using the kinetic (= exponential) fractionation law by ~0.004‰ per 0.100‰ difference in the δ^{25}Mg between sample and standard. The errors for high-precision data presented here are internal errors, while the external reproducibility on δ^{26}Mg* is estimated to be less than a factor of 1.5 worse than the 2 se based on repeated measurements of samples (see Schiller et al., 2010a).

Single analyses consisted of four blocks of 120 s of baseline and 400 s of data acquisition resulting in an internal precision on the mass-bias-corrected ^{26}Mg/^{24}Mg (δ^{26}Mg*) that is $\leq$0.020‰, including the error contribution from the bracketing standards. Because there is no resolvable difference between δ^{26}Mg* data obtained on the same meteorite when both J11 and DSM-3 were used as bracketing standards, and in order to improve the precision on anomalies, the data is reported both separately and

combined in Table 4.1. The reported errors on the δ^{26}Mg* for a single sample is the 2 se of 10 to 42 separate analyses of the same sample that have been combined as a weighted mean using Isoplot (Ludwig, 2003).

To improve precision on the stable Mg isotope data for the chondrites that is hampered by instrumental drift during the long analyses required to achieve high precision on the δ^{26}Mg* analyses (Schiller et al., 2010a), each chondrite sample was also analysed again in the same manner as described in Handler et al. (2009).

4.2.4 Al/Mg ratio measurements

Al/Mg ratios were measured on aliquots of fully digested samples with an Agilent 7500 ICP-MS using He in a collision cell to minimise interferences on Al and Mg. Sample analyses were bracketed with analyses of gravimetrically prepared Al/Mg = 2.0 and 0.1 solutions made from Aristar® single element ICP-MS solutions. The error assigned to the Al/Mg ratio is $\pm$ 2% (2 sd) based on repeated measurements of the USGS basaltic rock standard BHVO-2. Analyses of this standard in the same session as the samples yielded an ^{27}Al/^{24}Mg ratio of 1.897, which is within error of the recommended values for this standard (1.87 $\pm$ 0.08; GeoRem, 2010).

4.2.5 Stepwise leaching experiment on the CM2 chondrite Murchison

It has been shown that different leachates of some chondrites have large variations in the isotopic abundance of δ^{54}Cr (10‰; Rotaru et al., 1992; Trinquier et al., 2007) that reveal different nucleosynthetic contributions to chondritic meteorites. In this study, we repeated the stepwise acid leaching experiments used by Trinquier et al. (2007) on a powdered sample of Murchison ($\sim$ 200 mg) and analysed the Mg isotopic composition of the different leaching steps to ascertain the nature of δ^{26}Mg* anomalies in each step. The steps applied were: (1) a 30 min leach in cold 2.5% acetic acid,

(2) a 24 h leach in cold 50% acetic acid, (3) a 7 day leach in cold 7M HNO_3, (4) a 4 day leach in a 1:1 mix of 6M HCl and 27M HF, and (5) a 4 day leach in a 1:1 mix of 16M HNO_3 and 27M HF. Each single step was carried out in a acid volume of 5 mL and after each step the sample was centrifuged and 4.5 mL of the supernatant removed for Mg separation and isotopic analysis. After each step, the remaining undigested sample was then washed twice with 5 mL of MQ water and the wash was discarded before proceeding with the next leaching step. The Mg leachates were evaporated and taken up in 12M HCl and Mg was separated using the same methods as for the bulk chondrites.

4.3 Results

Resolving very small δ^{26}Mg* anomalies in meteorites requires careful evaluation of analytical methods to ensure that the Mg separation and mass spectrometry procedures do not introduce analytical artifacts that produce inaccurate Mg isotope measurements. To evaluate this, Aristar Mg ICP-MS standard was processed through the entire Mg chemical separation procedure and measured against unprocessed Aristar Mg in the same analytical sessions as the chondrites (δ^{26}Mg* = -0.0007 $\pm$ 0.0042‰; Table 4.1) suggesting that the Mg separation procedure does not affect the Mg isotopic composition of the samples. Furthermore, Mg separated from mantle clinopyroxene and mantle orthopyroxene from J11 (an anhydrous spinel peridotite from Jordan) was analysed against DSM-3 and Mg separated from J11 olivine and yields average δ^{26}Mg* values that are within two standard errors of zero i.e., -0.0022 $\pm$ 0.0043‰ (clinopyroxene) and +0.0022 $\pm$ 0.0031‰ (orthopyroxene), respectively (Table 4.1). These results are consistent with those of Schiller et al. (2010a) who showed through analysis of synthetic and terrestrial rocks standards with gravimetrically prepared δ^{26}Mg* anomalies that it is possible to resolve very small δ^{26}Mg* anomalies ($\leq$ 0.005‰) in meteorites.

Table 4.1: $^{27}Al/^{24}Mg$ and high-precision Mg isotope data for samples from Earth and chondrites. Data were measured versus DSM-3 or Mg separated from J11 olivine (analyses marked with an asterisk).

Sample	$\delta^{26}Mg^*_{all} \pm 2\sigma$ (‰)	$\delta^{26}Mg^* \pm 2\sigma$ (‰)	$\delta^{25}Mg \pm 2\sigma$ (‰)	$\delta^{26}Mg \pm 2\sigma$ (‰)	n	$^{27}Al/^{24}Mg$
Aristar Mg standard		-0.0007 ± 0.0042	-0.060 ± 0.110	-0.120 ± 0.200	23	-
BHVO-2		not determined				1.897
J11 clinopyroxene (1)	-0.0022 ± 0.0043	+0.0005 ± 0.0062	-0.051 ± 0.026	-0.097 ± 0.051	10	-
J11 clinopyroxene (2)*		-0.0048 ± 0.0061	+0.036 ± 0.039	+0.063 ± 0.074	10	-
J11 orthopyroxene (1)*	+0.0022 ± 0.0031	+0.0022 ± 0.0031	+0.087 ± 0.034	+0.172 ± 0.072	42	-
ordinary chondrites						
Bovedy (L3)	-0.0017 ± 0.0038	-0.0029 ± 0.0052	-0.099 ± 0.077	-0.200 ± 0.150	13	0.088
Bovedy*		-0.0002 ± 0.0059	+0.085 ± 0.033	+0.167 ± 0.070	10	″
Talbachat (LL3)	-0.0033 ± 0.0040	-0.0032 ± 0.0055	-0.014 ± 0.091	-0.040 ± 0.170	14	0.086
Talbachat*		-0.0035 ± 0.0061	+0.060 ± 0.060	+0.120 ± 0.120	10	″
Begaa (LL3)	-0.0014 ± 0.0039	+0.0018 ± 0.0048	-0.080 ± 0.110	-0.170 ± 0.220	17	0.089
Begaa*		-0.0072 ± 0.0065	+0.100 ± 0.090	+0.190 ± 0.180	10	″
Portales Valley (H6)	+0.0001 ± 0.0042	+0.0051 ± 0.0056	-0.115 ± 0.059	-0.220 ± 0.120	13	0.087
Portales Valley*		-0.0066 ± 0.0064	+0.060 ± 0.130	+0.120 ± 0.260	10	″
enstatite chondrites						
Sah 97096 (EH3)	-0.0010 ± 0.0042	+0.0010 ± 0.0061	-0.125 ± 0.029	-0.243 ± 0.061	10	0.081
Sah 97096*		-0.0030 ± 0.0061	+0.050 ± 0.070	+0.080 ± 0.130	10	″
carbonaceous chondrites						
Orgueil (CI1)	+0.0017 ± 0.0063	+0.0017 ± 0.0063	-0.086 ± 0.072	-0.160 ± 0.140	10	0.113
Murchison (CM2)	+0.0057 ± 0.0036	+0.0066 ± 0.0049	-0.164 ± 0.072	-0.320 ± 0.140	16	0.115
Murchison*		+0.0045 ± 0.0057	+0.051 ± 0.062	+0.100 ± 0.130	11	″
NWA 4428* (CM2)	+0.0131 ± 0.0041	+0.0131 ± 0.0041	+0.043 ± 0.045	+0.092 ± 0.090	24	0.115
NWA 763 (CO3)	+0.0082 ± 0.0038	+0.0092 ± 0.0052	-0.084 ± 0.070	-0.150 ± 0.140	18	0.110

Continued on next page

Table 4.1 – continued from previous page

Sample	δ^{26}Mg*$_{all} \pm 2\sigma$ (‰)	δ^{26}Mg* $\pm 2\sigma$ (‰)	δ^{25}Mg $\pm 2\sigma$ (‰)	δ^{26}Mg $\pm 2\sigma$ (‰)	n	^{27}Al/^{24}Mg
NWA 763*		+0.0070 ± 0.0057	+0.100 ± 0.100	+0.200 ± 0.210	11	″
NWA 1232 (CO3)	+0.0050 ± 0.0054	+0.0050 ± 0.0054	-0.180 ± 0.047	-0.345 ± 0.091	15	0.102
Allende (CV3)		+0.0202 ± 0.0060	-0.190 ± 0.071	-0.350 ± 0.130	13	0.131
Allende*		+0.0117 ± 0.0060	+0.009 ± 0.066	+0.030 ± 0.130	10	0.124
NWA 2364 (CV3)	+0.0189 ± 0.0033	+0.0206 ± 0.0039	-0.105 ± 0.057	-0.180 ± 0.110	29	0.130
NWA 2364*		+0.0143 ± 0.0063	+0.100 ± 0.170	+0.200 ± 0.340	11	″
NWA 530 (CR2)	+0.0034 ± 0.0042	+0.0080 ± 0.0059	+0.042 ± 0.074	+0.090 ± 0.140	13	0.097
NWA 530*		-0.0013 ± 0.0059	+0.080 ± 0.010	+0.153 ± 0.026	10	″
NWA 1180 (CR2)	-0.0018 ± 0.0038	+0.0002 ± 0.0048	-0.130 ± 0.110	-0.260 ± 0.220	21	0.094
NWA 1180*		-0.0051 ± 0.0061	+0.042 ± 0.034	+0.077 ± 0.068	11	″
SAU 290 (CH3)	-0.0063 ± 0.0040	-0.0100 ± 0.0054	+0.046 ± 0.077	+0.080 ± 0.150	14	0.094
SAU 290*		-0.0021 ± 0.0058	+0.180 ± 0.130	+0.340 ± 0.250	10	″
Gujba (CBa)	-0.0027 ± 0.0046	-0.0001 ± 0.0065	+0.131 ± 0.086	+0.260 ± 0.160	10	0.098
Gujba*		-0.0052 ± 0.0065	+0.192 ± 0.026	+0.386 ± 0.031	10	″
NWA 1559 (CK3)	+0.0173 ± 0.0043	+0.0200 ± 0.0059	-0.116 ± 0.058	-0.200 ± 0.110	12	0.131
NWA 1559*		+0.0143 ± 0.0063	+0.040 ± 0.040	+0.090 ± 0.077	10	″

Table 4.2: Al/Mg and high-precision δ^{26}Mg* data obtained in a leaching experiment on a ~200 mg sample of the CM2 chondrite Murchison using a procedure following Trinquier et al. (2007). Mg isotope data were measured versus Mg separated from J11 olivine.

	δ^{26}Mg* ± 2 se (‰)	δ^{25}Mg ± 2 se (‰)	δ^{26}Mg ± 2 se (‰)	n	^{27}Al/^{24}Mg	Mg μg
leach 1	+0.0060 ± 0.0059	-0.326 ± 0.068	-0.630 ± 0.130	10	0.033	530
leach 2	-0.0016 ± 0.0063	+0.089 ± 0.066	+0.170 ± 0.140	10	0.242	1038
leach 3	+0.0161 ± 0.0060	-0.153 ± 0.032	-0.284 ± 0.065	10	0.123	2663
leach 4	+0.0826 ± 0.0068	+0.017 ± 0.078	+0.120 ± 0.150	9	0.249	78
leach 5	+0.1176 ± 0.0210	+0.403 ± 0.017	+0.916 ± 0.023	1	0.744	4.4
combined	+0.0118 ± 0.0280	-0.103 ± 0.163	-0.263 ± 0.304	-	0.148	5678
single digestion:						
vs. J11 ol.	+0.0045 ± 0.0057	+0.051 ± 0.062	+0.100 ± 0.130	11	0.115	-
vs. DSM-3	+0.0066 ± 0.0049	-0.164 ± 0.072	-0.320 ± 0.140	16	″	-

4.3.1 Stepwise leaching of the CM2 chondrite Murchison

The five increasingly aggressive acid leaching steps that are inferred to progressively digest carbonate/sulphide/sulphate, metal, silicate and refractory phases have variable δ^{26}Mg* values (Table 4.2). δ^{26}Mg* ranges from -0.0016 ± 0.0063‰ in the second leaching step up to +0.118 ± 0.021‰ in the final leaching step. The combined δ^{26}Mg* anomaly of all five digestions is +0.0118 ± 0.0280‰, when the amount of Mg released in each step is taken into account, and within error of the bulk analysis of Murchison that has an average composition of +0.0057 ± 0.0036‰. Both the stable Mg isotopic composition (δ^{25}Mg) and the Al/Mg ratio in the leachates show broad trends to isotopically heavier Mg and higher Al/Mg ratios in the more aggressive leaching steps (Fig. 4.2).

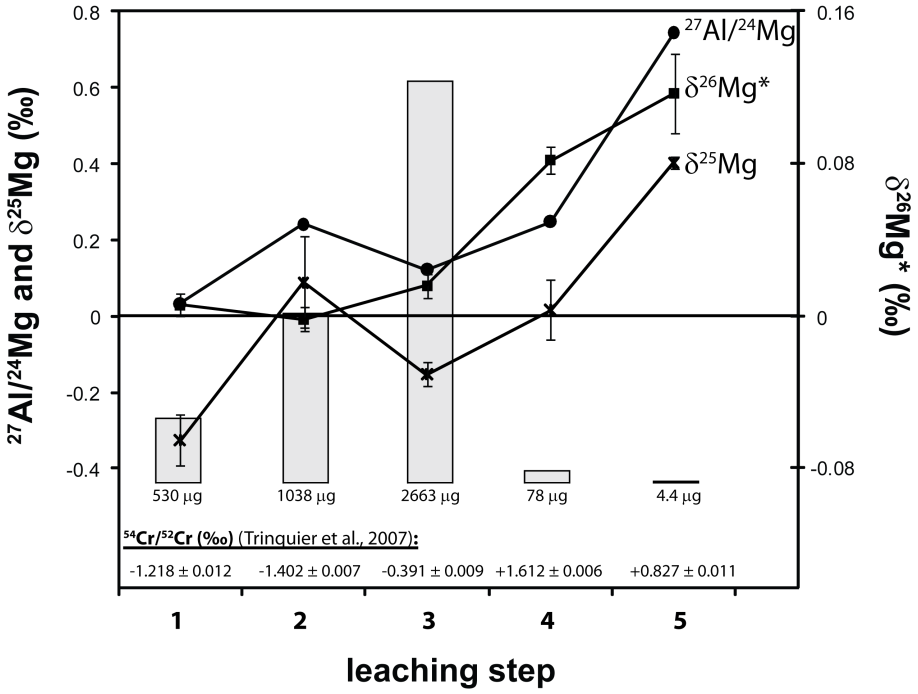

Figure 4.2: Variation of the δ^{25}Mg, δ^{26}Mg*, ^{27}Al/^{24}Mg and the Mg yield in five stepwise leaching steps of $\sim$ 200 mg of the CM2 chondrite Murchison following the leaching procedure described in Trinquier et al. (2007). The steps applied were (1) a 30 min leach in cold 2.5% acetic acid, (2) a 24 h leach in cold 50% acetic acid, (3) a 7 day cold leach in 7M HNO_3, (4) a 4 day leach in a 1:1 mix of 6M HCl and 27M HF, and (5) a 4 day leach in a 1:1 mix of 16M HNO_3 and 27M HF. ^{54}Cr/^{52}Cr data for Murchison reported in Trinquier et al. (2007) is shown for comparison.

4.3.2 Mg isotopic composition of bulk chondrites

$^{27}Al/^{24}Mg$ and Mg isotope ratios were determined to high precision in bulk samples of chondrites comprising examples of all the major classes of ordinary (L3, LL3, H6), enstatite (EH3) and carbonaceous chondrites (CI1, CM2, CO3, CV3, CR2, CH3, CBa, CK3, CK5). Two different sets of data are presented in Tables 4.1 and 4.3, with Table 4.1 presenting high precision data for δ^{26}Mg* obtained using long analysis times and Table 4.3 presenting high precision data for the stable Mg isotope composition using shorter analysis times which yields better stable isotope data given that drifts in instrumental mass bias are less significant over short time periods. The combined stable δ^{25}Mg isotope data from both Tables 4.1 and 4.3 are plotted on Figure 4.3. δ^{26}Mg* data shown on Figure 4.4 are (in most cases) the combined average of data for each meteorite measured against both DSM-3 and Mg separated from J11 olivine (Table 4.1).

δ^{26}Mg* values for the bulk chondrites show small variations that exceed analytical uncertainties i.e., δ^{26}Mg* = -0.0063 $\pm$ 0.0040‰ (CH3 SAU 290) to +0.0189 $\pm$ 0.0033‰ (CV3 NWA 2364; Table 4.1). However, apart from the CM, CO, CV and CK chondrites, all the other carbonaceous chondrites and ordinary and enstatite chondrites have δ^{26}Mg* values that are within estimated external reproducibilities (i.e., 1.5 $\times$ the internal error) of the terrestrial standards and Earth. These chondrites have an average δ^{26}Mg* = -0.0015 $\pm$ 0.0013‰ (2 se). It is notable that the carbonaceous chondrites with elevated δ^{26}Mg* have the highest $^{27}Al/^{24}Mg$ ratios and Figure 4.3 shows that $^{27}Al/^{24}Mg$ and δ^{26}Mg* exhibit a general correlation with a slope ([6.32 $\pm$ 1.26] x 10^{-5}) that is within error of the initial ^{26}Al abundance of CAIs.

With the exception of the chondrule from the CBa chondrite Gujba, all the chondrites show very limited stable Mg isotope variations i.e., δ^{25}Mg = -0.089 $\pm$ 0.042‰ (CV3 NWA 2364) to -0.220 $\pm$ 0.049‰ (CV3 Allende; Table 4.3). No systematic variation of δ^{25}Mg is evident with any particular chondrite group. The mean δ^{25}Mg is -0.152 $\pm$ 0.079‰ (2 sd) and is

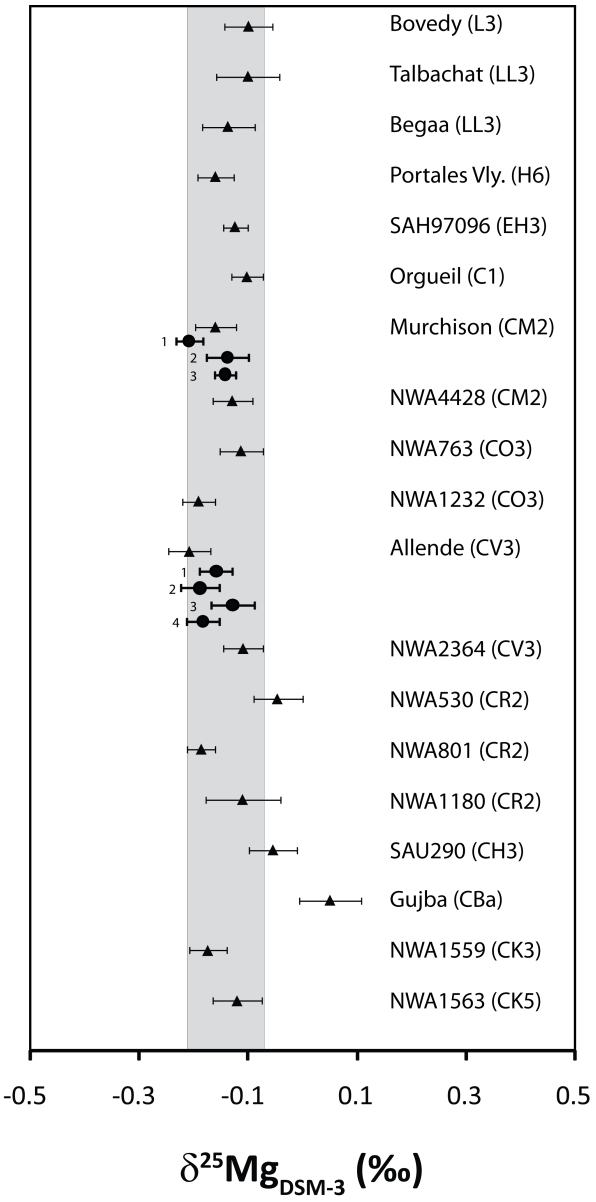

Figure 4.3: Stable Mg isotope (δ^{25}Mg) data for chondrites from this study compared with previously published data for Murchison and Allende [round symbols; 1: Teng et al. (2007), 2: Wiechert and Halliday (2007), 3: Baker et al. (2005), 4: Young and Galy (2004)]. Error bars represent 2 se uncertainties and the grey shaded area is the average upper mantle composition reported in Handler et al. (2009). All data in this figure were measured versus DSM-3.

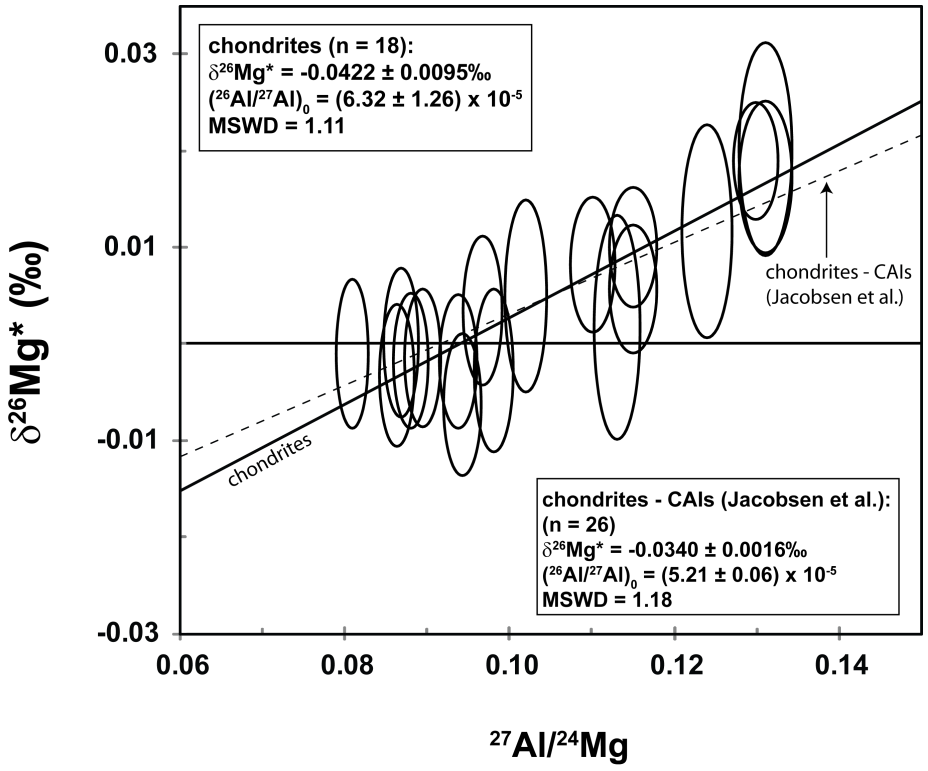

Figure 4.4: High-precision δ^{26}Mg* data for chondrites plotted versus ^{27}Al/^{24}Mg ratio. A regression is shown for all analysed chondrites and also a separate regression for the chondrites combined with previously published high-precision data for CAIs (Jacobsen et al., 2008). The error ellipse comprises a 2% error for the ^{27}Al/^{24}Mg ratio and, for δ^{26}Mg*, errors are expanded by 1.5 times the 2 se, which is the estimated external reproducibility of the Mg isotope data (Schiller et al., 2010a). Regressions have been calculated using Isoplot (Ludwig, 2003).

Table 4.3: Stable Mg isotope data for samples from Earth and chondrites. Mg isotope data were measured versus DSM-3. Each analysis comprises the mean of 8 - 25 measurements involving a 60 s baseline and 200 s of data acquisition bracketed by analyses of DSM-3.

Sample	δ^{26}Mg* $\pm 2\sigma$ (‰)	δ^{25}Mg $\pm 2\sigma$ (‰)	δ^{26}Mg $\pm 2\sigma$ (‰)	n
Earth				
Aristar Mg standard	+0.006 ± 0.024	+0.016 ± 0.070	+0.040 ± 0.140	10
Aristar Mg standard (2)	+0.014 ± 0.020	-0.038 ± 0.051	-0.064 ± 0.098	8
J11 olivine (1)	-0.009 ± 0.022	-0.108 ± 0.051	-0.200 ± 0.100	10
J11 olivine (2)	-0.002 ± 0.020	-0.096 ± 0.058	-0.190 ± 0.100	10
J11 olivine (3)	+0.001 ± 0.019	-0.088 ± 0.085	-0.180 ± 0.170	10
J11 orthopyroxene	+0.009 ± 0.020	-0.136 ± 0.036	-0.253 ± 0.081	10
ordinary chondrites				
Bovedy (L3)	+0.021 ± 0.025	-0.098 ± 0.051	-0.174 ± 0.098	10
Talbachat (LL3)	+0.002 ± 0.014	-0.174 ± 0.072	-0.340 ± 0.140	20
Begaa (LL3)	-0.004 ± 0.015	-0.140 ± 0.041	-0.273 ± 0.082	15
Portales Valley (H6)	+0.008 ± 0.014	-0.202 ± 0.026	-0.391 ± 0.054	15
enstatite chondrites				
Sah 97096 (EH3)	+0.007 ± 0.018	-0.123 ± 0.042	-0.235 ± 0.087	10
carbonaceous chondrites				
Orgueil (CI1)	+0.015 ± 0.013	-0.123 ± 0.032	-0.231 ± 0.067	20
Murchison (CM2)	-0.001 ± 0.014	-0.156 ± 0.030	-0.309 ± 0.056	15
NWA 4428 (CM2)	+0.008 ± 0.016	-0.129 ± 0.023	-0.260 ± 0.045	10
NWA 763 (CO3)	-0.010 ± 0.017	-0.165 ± 0.019	-0.330 ± 0.042	10
NWA 1232 (CO3)	+0.010 ± 0.029	-0.208 ± 0.033	-0.394 ± 0.057	10
Allende (CV3)	-0.007 ± 0.014	-0.220 ± 0.049	-0.431 ± 0.097	20
NWA 2364 (CV3)	+0.024 ± 0.022	-0.089 ± 0.042	-0.148 ± 0.074	10
NWA 530 (CR2)	+0.020 ± 0.018	-0.118 ± 0.032	-0.210 ± 0.070	11
NWA 801 (CR2)	+0.025 ± 0.018	-0.186 ± 0.026	-0.332 ± 0.065	10
NWA 1180 (CR2)	+0.011 ± 0.019	-0.158 ± 0.034	-0.288 ± 0.067	10
SAU 290 (CH3)	-0.009 ± 0.016	-0.129 ± 0.036	-0.264 ± 0.058	15
Gujba (CBa)	-0.005 ± 0.019	-0.032 ± 0.035	-0.075 ± 0.063	10
NWA 1559 (CK3)	+0.014 ± 0.015	-0.203 ± 0.041	-0.380 ± 0.088	17
NWA 1563 (CK5)	+0.021 ± 0.015	-0.120 ± 0.045	-0.204 ± 0.092	15

indistinguishable from analyses of Earth's upper mantle and our data are generally consistent with that previously published for a limited range of chondrite types (Fig. 4.3). The chondrule from the CBa chondrite Gujba has a slightly heavier stable Mg isotope composition (δ^{25}Mg = -0.032 $\pm$ 0.035‰) than all the other bulk chondrite analyses.

4.4 Discussion

4.4.1 δ^{26}Mg* anomalies in leachates of the CM2 chondrite Murchison

In general, the δ^{26}Mg* anomalies in leachates of Murchison follow a similar trend as Cr isotopes in leachates of the same meteorite (Fig. 4.2). However, three aspects of the Mg isotope variations differ from those observed for Cr isotopes. Firstly, the observed variations for δ^{26}Mg* (0.1‰) are more than an order of magnitude smaller than those observed for δ^{54}Cr (3.0‰). Secondly, no resolvable deficits in δ^{26}Mg* are measured in any of the leachate steps, which contrasts with Cr isotopes where large δ^{54}Cr deficits of up to -1.4‰ were measured in early leachate steps (Trinquier et al., 2007). Finally, the small positive δ^{26}Mg* anomalies in the final two leaching steps are also accompanied by significant correlated increases in Al/Mg ratios of these leachate steps (^{27}Al/^{24}Mg = 0.25-0.74), whereas δ^{54}Cr values in leachates of chondrite meteorites are uncorrelated with Mn/Cr ratios.

In contrast to Cr isotopes, the mass-independent variations in δ^{26}Mg* of the Murchison leachates provide no evidence for significant Mg isotope nucleosynthetic heterogeneity within the acid soluble components of this meteorite. Rather, the small δ^{26}Mg* variations are most readily attributed to progressive attack and dissolution of the small amounts of refractory inclusions or CAIs that make up ca. 5% of CM chondrites (Scott and Krot, 2007). Digestion of CAI material in the latter stages of the step leaching

experiment results in elevated Al/Mg ratios in the leachate and elevated δ^{26}Mg* given that CAIs contain radiogenic ^{26}Mg due to the former decay of ^{26}Al. The two leachate steps with elevated δ^{26}Mg* yield apparent initial $(^{26}\text{Al}/^{27}\text{Al})_0$ of 7.7 and 2.6 $\times$ 10^{-5}, which are similar, but not identical, to the values measured in CAIs (Jacobsen et al., 2008) or hibonites in Murchison (Liu et al., 2009). The difference between the values obtained for these leachate steps and the initial ^{26}Al value measured directly in CAIs can be explained by elemental fractionation of Al and Mg during the acid leaching procedure. The heavy stable Mg isotope composition measured in the final leachate step is also consistent with release of Mg from CAIs in this step as many CAIs have highly fractionated and heavy stable Mg isotopic compositions due to evaporative loss of Mg during transient heating events around the young Sun (Young et al., 2005).

In general, the leaching experiment showed the expected trend for digestion of a CAI-bearing chondrite, where the δ^{26}Mg* anomalies reflect a variable mixture of Mg released from readily acid-soluble matrix material with δ^{26}Mg* $\sim$ 0.000‰ with acid-resistant CAI-like material with elevated δ^{26}Mg* due to the former decay of ^{26}Al.

4.4.2 Mass-independent abundance of Mg isotopes in bulk chondrites

The chondrites have a range of $^{27}\text{Al}/^{24}\text{Mg}$ ratios from 0.081 to 0.131 and these data are generally consistent (Fig. 4.5) with previous studies of chondrites (Wasson and Kallemeyn, 1988; Scott and Krot, 2007), which is notable given that the samples in this study ranged from 50 to 200 mg in size and the macroscopic petrographic heterogeneity observed in some chondrites. This observation is important as the Mg isotopic composition of CAI- and large chondrule-bearing chondrites might be biased through non-representative sampling of the meteorite, yet Figure 4.5 suggests that our analyses are broadly representative of each class of chondrite. The

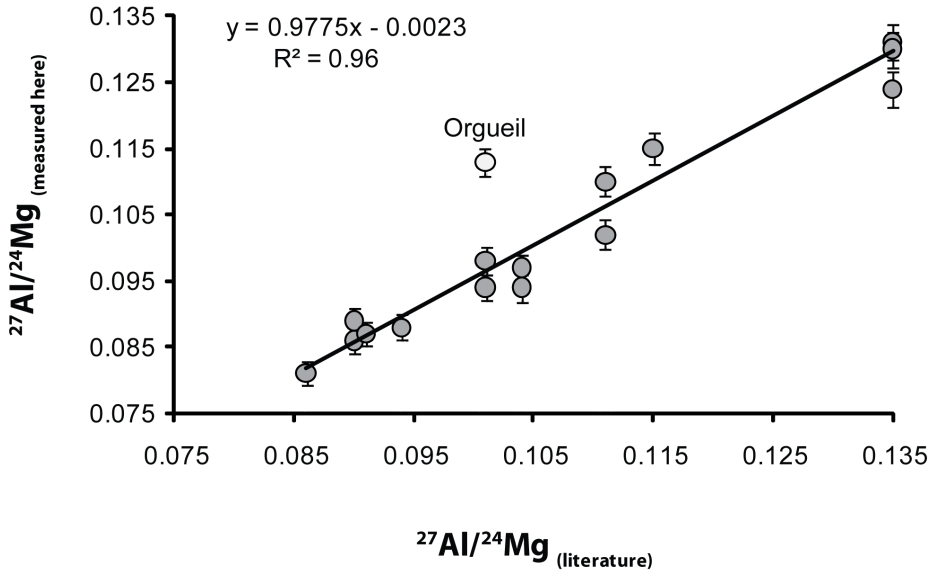

Figure 4.5: Correlation of the $^{27}Al/^{24}Mg$ ratios measured for each chondrite sample analysed in this study compared with $^{27}Al/^{24}Mg$ ratios typical for each respective class of chondrites from the literature (Wasson and Kallemeyn, 1988; Scott and Krot, 2007).

only sample that has an $^{27}Al/^{24}Mg$ ratio that is significantly different to the expected value from the literature is the CI chondrite Orgueil (0.113), while CI chondrites should have the solar ratio of 0.101 (Scott and Krot, 2007). The most likely explanation for this difference is the very small sample of this meteorite that was digested for analysis.

In general, a broad correlation between $^{27}Al/^{24}Mg$ and $\delta^{26}Mg^*$ anomalies is observed (Fig. 4.4). Chondrites documented to contain $< 0.5\%$ CAIs (i.e., not CM, CO, CV and CK carbonaceous chondrites) have an average $^{27}Al/^{24}Mg$ ratio of 0.091 and $\delta^{26}Mg^*$ of -0.0015 $\pm$ 0.0013‰ (2 se), and no resolvable trend with the Al/Mg ratio is evident for these chondrites. This value is within estimated analytical reproducibility ($\leq$ 1.5 times the 2 se) of the terrestrial standard and provides no evidence for significant Mg nucleosynthetic variations or ^{26}Al heterogeneity amongst these bulk

chondrite types or compared to Earth, despite the fact that they exhibit significant variations in δ^{54}Cr and δ^{50}Ti of 0.204 $\pm$ 0.009‰ and 0.278 $\pm$ 0.021‰, respectively. In the case of the ordinary chondrites (δ^{26}Mg* = -0.0016 $\pm$ 0.0019‰, n = 4), if the low Al/Mg ratio of these chondrites (and their constituents) as compared to the solar value was produced at the same time as CAI formation, and Earth and chondrites had the same initial $(^{26}Al/^{27}Al)_0$ as CAIs, then the chondrites would be expected to have δ^{26}Mg* deficits of -0.0036‰. However, given evidence that chondrule formation began shortly after CAI formation and persisted for several million years after this (Amelin and Krot, 2007), the δ^{26}Mg* is consistent with the prediction that the δ^{26}Mg* deficit of these chondrites lies between this minimum value and that of the terrestrial standard i.e., between -0.0036 and 0.0000‰.

The small positive δ^{26}Mg* anomalies in the chondrites with elevated $^{27}Al/^{24}Mg$ ratios (i.e., CM, CO, CV and CK carbonaceous chondrites) can potentially be explained by the small amounts of CAI and other refractory material in these chondrites that have δ^{26}Mg* anomalies that are related to ^{26}Al decay. This explanation can be tested by comparison of the δ^{26}Mg* data with δ^{50}Ti and δ^{54}Cr data previously reported for chondrites (Fig. 4.6). While the reported variations for both δ^{50}Ti and δ^{54}Cr are more than an order of magnitude larger than the δ^{26}Mg* variations in chondrites, the correlations with δ^{26}Mg* are consistent with contributions from a CAI-like component in carbonaceous chondrites controlling the δ^{26}Mg* variations. A marked positive co-variation between δ^{26}Mg* and δ^{50}Ti for CAI-bearing carbonaceous chondrites can be modelled as mixing of a chondrite with a broadly CI-like composition with up to ca. 3-4% of CAI-like material with typical δ^{26}Mg* excesses (1.0‰) and δ^{50}Ti = +0.6 to 0.9‰ (Trinquier et al., 2009) of CAIs. This correlation is clear on Fig. 4.6 as CAIs are enriched in Ti and are also characterised by extreme δ^{26}Mg* anomalies resulting from ^{26}Al decay, as compared to chondrites, and only a few percent of CAI-like material will result in measurable changes in the bulk Mg and Ti

isotopic composition of these carbonaceous chondrites. Given these mixing calculations are based on the δ^{50}Ti isotopic composition of CI chondrites, which may overestimate the δ^{50}Ti isotopic anomaly of the matrix and chondrules of other groups of carbonaceous chondrites (i.e., CO, CM, CV and CK) (Trinquier et al., 2009), these calculations result in minimum estimates of the contribution of CAI-like material in the mixing calculations. Because CAIs are depleted in Cr compared to chondrites the addition of 3-4% of CAI-like material does not significantly change the δ^{54}Cr of the CAI-bearing carbonaceous chondrites and, hence, there is no clear correlation between δ^{54}Cr and δ^{26}Mg*.

4.4.3 Homogeneity of the initial ^{26}Al abundance in chondrites, the planet-forming region, and CAIs?

The chondrite data define a coherent regression whereby most samples have δ^{26}Mg* values within analytical uncertainty of the terrestrial standard and CAI-bearing samples have slightly elevated Al/Mg and δ^{26}Mg* as compared to the non-CAI-bearing chondrites. Using the "canonical" initial ^{26}Al value for CAIs (Jacobsen et al., 2008) it can be calculated that planetesimals that accreted from material with initially "canonical" ^{26}Al values would have a δ^{26}Mg* value 0.036‰ higher than a planetesimal which accreted from material with no ^{26}Al, if all planetesimals initially had a solar Al/Mg ratio. This calculation constrains the scale of potential present-day δ^{26}Mg* heterogeneity possible if different planetesimals formed with radically variable levels of ^{26}Al due to heterogeneity of ^{26}Al in the protoplanetary disk. Given the uncertainties on the δ^{26}Mg* data presented here, the coherent regression through the chondrite data and also the fact that Earth (i.e., the terrestrial standard) shares a similar δ^{26}Mg* as the regression through the non-CAI-bearing chondrites at a near-solar Al/Mg ratio the following three observations can be made:

(1) These data provide no evidence for radical ^{26}Al heterogeneity ($\geq$

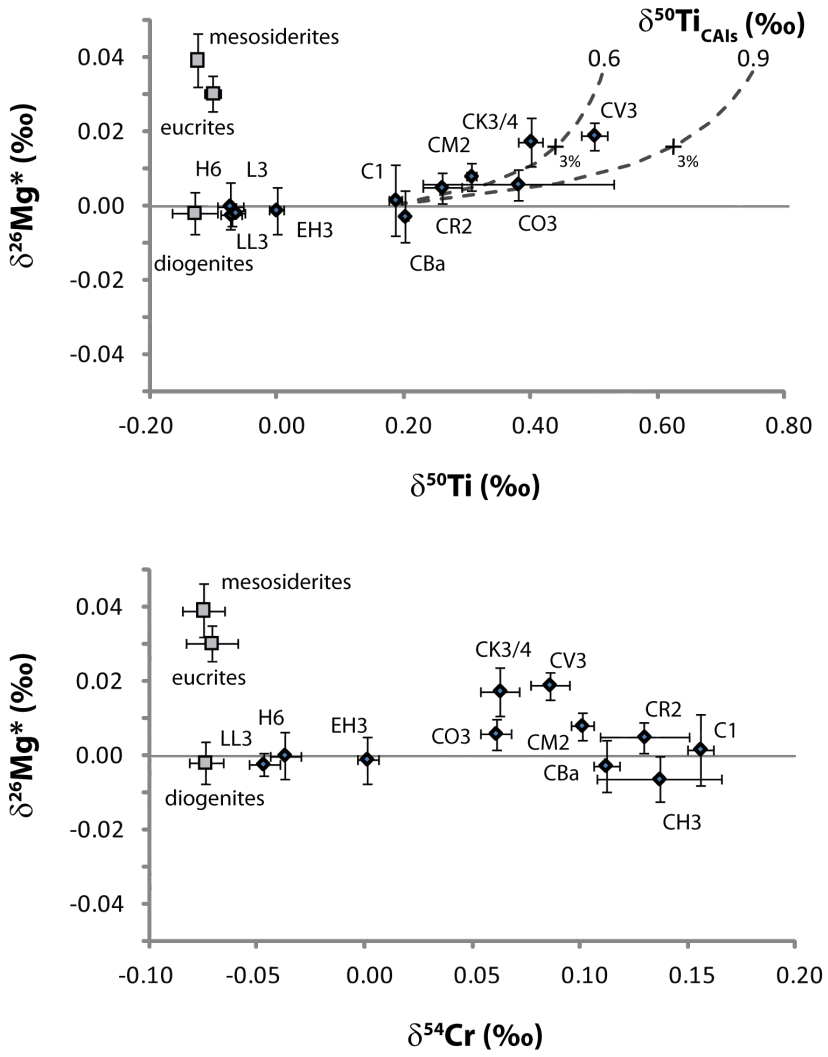

Figure 4.6: Co-variation of δ^{26}Mg* with δ^{54}Cr (Trinquier et al., 2007) and δ^{50}Ti (Trinquier et al., 2009) in different classes of chondrites. Mg isotope data for eucrites, basaltic mesosiderite clasts and diogenites are taken from Schiller et al. (2010a) and the modelled chondrite-CAI mixing lines are based on bulk compositions for CAIs (Kimura et al., 1993) and CI chondrites (Palme and Jones, 2003), and Mg isotope data reported in Jacobsen et al. (2008) i.e., CAIs - Ti = 2.46 wt.%, δ^{50}Ti = 0.6 and 0.9‰, Mg = 5.05 wt.%, δ^{26}Mg* = 1.0‰; CI chondrite - Ti = 458 ppm, δ^{50}Ti = 0.19‰, Mg = 9.61 wt.%, δ^{26}Mg* = 0.0‰.

30%) amongst different chondrite parent bodies, or compared to differentiated planetesimals like the angrite and howard-eucrite-diogenite (HED) parent bodies, given that young angrites have a mean δ^{26}Mg* = -0.0039 $\pm$ 0.0027‰ and diogenites like Bilanga have δ^{26}Mg* values within error of the terrestrial standard (Schiller et al., 2010a).

(2) Any Mg nucleosynthetic variations on a planetesimal scale, apart from those resultant from the presence of CAIs and the former decay of ^{26}Al, are extremely muted in nature and below the levels of our analytical uncertainties i.e. $\leq$ 0.005‰. (3) Earth accreted from material with broadly similar levels of ^{26}Al as undifferentiated (chondrites) and differentiated (angrites, HED) planetesimals given that the chondrite regression crosses the δ^{26}Mg* value (0.000‰) of the terrestrial standard at a near-solar Al/Mg ratio. However, analyses of upper mantle samples indicate that the Earth has an ^{27}Al/^{24}Mg ratio of 0.122 (Palme and O'Neill, 2007), which is significantly higher than the average of non-CAI bearing chondrites in this study (0.091) or estimates of the solar composition (0.101 $\pm$ 0.004; Palme and Jones, 2003). The observation that terrestrial samples have identical δ^{26}Mg* as non-CAI-bearing chondrites implies that either Earth accreted from material containing ca. 30% less ^{26}Al than chondrites or that the Bulk Earth's inferred Al/Mg ratio is not correct and that a significant part of Earth's mantle has significantly lower abundances of refractory elements relative to Mg than the small selection of samples currently available from the Earth's uppermost upper mantle in the form of volcanic-hosted xenolith samples and exhumed peridotite massifs.

Our results and conclusions are broadly consistent with those of Villeneuve et al. (2009) who, based on a high precision Mg isotope study of chondrules from the LL3.0 ordinary chondrite Semarkona, showed that ^{26}Al was homogeneously ($\pm$ 10%) distributed in the material from which Semarkona chondrules formed, as well Earth and CAIs. However, the data presented here do not make it possible to ascertain whether the material planetesimals and planets accreted from initially had precisely the same

levels of ^{26}Al as CAIs. High precision Mg isotope studies of CAIs (Bizzarro et al., 2004; Thrane et al., 2006; Jacobsen et al., 2008) do not clearly show whether the CAI initial δ^{26}Mg* and δ^{26}Mg* at a solar Al/Mg are significantly different from the hypothetical Solar System initial δ^{26}Mg* with respect to Earth (-0.036‰) or the mean δ^{26}Mg* of non-CAI bearing chondrites, respectively. The chondrite data presented in this paper can be regressed with published δ^{26}Mg* data for CAIs (Jacobsen et al., 2008) and yield a statistically significant Model 1 isochron with an apparently precise initial $(^{26}Al/^{27}Al)_0 = (5.21 \pm 0.06) \times 10^{-5}$ for the Solar System. However, systematically offsetting the δ^{26}Mg* values for CAIs (as compared to the chondrites) still results in statistically significant isochrons over a range of offsets from -0.012 to +0.036‰, which implies that the material from which planets and planetesimals accreted from can have had initial ^{26}Al abundances that ranged from essentially zero to ca. 30% greater than CAIs. However, given that angrites and eucrites preserve clear evidence for the former presence of ^{26}Al and the comparison of ^{26}Al-^{26}Mg ages with other relative and absolute chronometers (Spivak-Birndorf et al., 2009; Schiller et al., 2010a), the material that planetesimals and planets accreted from would have to have had $(^{26}Al/^{27}Al)_0$ in the range of 2.1 to 6.7 $\times$ 10^{-5}. Clearly, even higher precision Mg isotope studies of CAIs are necessary to more precisely constrain whether planetesimals and planets accreted from material that initially had very similar, CAI-like, levels of ^{26}Al.

4.4.4 Implications for the ^{26}Al - ^{26}Mg chronometer

One important implication of the distribution of ^{26}Al and mass-independent abundance of Mg isotopes in the proto-planetary disk relates to the use of small δ^{26}Mg* excesses in samples of bulk basaltic meteorites with super-chondritic $^{27}Al/^{24}Mg$ ratios to calculate model ages for asteroidal basaltic magmatism (Baker et al., 2005; Bizzarro et al., 2005; Schiller et al., 2010a). Given the size of δ^{26}Mg* excesses present in bulk samples

of basaltic eucrites and mesosiderite clasts (up to 0.041‰; Schiller et al., 2010a), there is little doubt that these excesses reflect ^{26}Al decay. However, the chronological interpretation of these excesses is not straightforward and depends on the mechanism by which basaltic magmas were produced on planetesimals in the early Solar System (Schiller et al., 2010a). The possibility that the δ^{26}Mg* excesses in asteroidal basalts reflected melting of a planetesimal that accreted with 5-10% CAI material can be ruled out as basaltic eucrites and mesosiderite clasts should then be characterised by δ^{50}Ti excesses, which is precisely the opposite of what is observed (Trinquier et al., 2009). The absence of significant Mg isotope heterogeneity amongst a wide range of chondrite groups, the young angrites (e.g., LEW 86010 and Angra do Reis), and meteorites with low Al/Mg (i.e., diogenites) from the HED parent body also precludes the δ^{26}Mg* excesses in these basaltic meteorites reflecting Mg nucleosynthetic variations in different planetesimals as compared to Earth.

The results presented here also imply that it might be possible to use δ^{26}Mg* deficits to date meteoritic material (e.g., olivine from pallasite meteorites) with Al/Mg = 0 that formed very early in the Solar System. Such material would be characterised by a δ^{26}Mg* deficit equal to the initial of the regression presented in Fig. 4.4, if it formed at the same time as CAIs and, given analytical uncertainties that can be obtained with current techniques ($\pm$0.005‰), may allow dating of such material provided it formed in the first 1-2 million years of the Solar System. However, given the potential heterogeneous distribution of ^{26}Al in the early Solar System as allowed here, δ^{26}Mg* anomalies can only produce meaningful age constraints if the precise initial abundance of ^{26}Al of the respective parent body is known. If lower levels of ^{26}Al characterised the part of the protoplanetary disk from which planetesimals and planets formed, then δ^{26}Mg* deficit ages calculated with respect to CAIs will reflect minimum age estimates.

4.4.5 Stable Mg isotopic composition of chondrites

Excluding the silicate chondrule from the CBa chondrite Gujba, there are no clear systematic differences in the stable Mg isotopic composition between different types of chondrites. The average stable Mg isotopic composition of 18 analysed chondrites is $\delta^{25}Mg_{DSM-3}$ = -0.152 ± 0.079‰ (2 sd, Fig. 4.3). This stable Mg isotopic composition is generally consistent with average compositions reported for the Earth's mantle, eucrites, pallasite olivine, mesosiderites and angrites (Baker et al., 2005; Bizzarro et al., 2005; Wiechert and Halliday, 2007; Teng et al., 2007; Tipper et al., 2008; Young et al., 2008; Handler et al., 2009). In particular, the average stable Mg isotopic composition of chondrites presented here and Earth's mantle ($\delta^{25}Mg_{DSM-3}$ = -0.14 ± 0.07‰, 2 sd) appear to be almost identical (Handler et al., 2009). Accurate determination of the stable Mg isotopic composition of chondrites has been hampered by the complex matrices of these rocks. Despite this, the measured stable Mg isotopic compositions of the CI chondrite Orgueil, CM chondrite Murchison and the CV3 chondrite Allende are in agreement with those reported in previous studies that used different chemical separation and analytical procedures (Fig. 4.3; Galy et al., 2003; Young and Galy, 2004; Baker et al., 2005; Thrane et al., 2006; Wiechert and Halliday, 2007; Teng et al., 2007; Young et al., 2008). However, the silicate chondrule from Gujba has the heaviest Mg isotopic composition measured in this study ($\delta^{25}Mg_{DSM-3}$ = +0.051 ± 0.057‰), which is consistent with the formation of chondrules in CBa chondrites by condensation after impact melting and evaporation of their precursor material during a collision between two Mars-sized planetary embryos (Krot et al., 2005).

4.5 Conclusions

A high-precision study of the mass-independent abundance of ^{26}Mg ($\delta^{26}Mg^*$) and stable Mg ($\delta^{25}Mg$) isotope composition of chondrites has

shown that:

(1) Variations of δ^{26}Mg* in stepwise acid leaching steps of the Murchison CM2 chondrite and bulk analyses of chondrites are much smaller than for neutron-rich isotopes of iron-peak elements such as Cr or Ti. δ^{26}Mg* values are typically within analytical uncertainty of the terrestrial standard or are slightly positive. The small positive δ^{26}Mg* anomalies in carbonaceous chondrites are correlated with δ^{50}Ti anomalies, increasing ^{27}Al/^{24}Mg and the presence of CAIs, suggesting that in these carbonaceous chondrites they reflect the presence of small amounts of CAIs with radiogenic δ^{26}Mg* produced by the former decay of ^{26}Al.

(2) High-precision Mg isotope data of chondrites suggests that there is no radical ^{26}Al heterogeneity ($\geq \pm$ 30%) or measurable Mg isotope nucleosynthetic variations ($\geq \pm$ 0.005‰) between different planetesimals and planets. However, it cannot yet be precisely demonstrated that the planet-forming region of the protoplanetary disk had the same ^{26}Al abundance as CAIs

(3) The stable Mg isotopic composition of all the analysed chondrites is relatively uniform with a mean $\delta^{25}Mg_{DSM-3}$ = -0.152 $\pm$ 0.079‰ (2 sd), which is indistinguishable from the mean value determined for Earth's upper mantle.

Chapter 5

Timing and mechanisms of the evolution of the magma ocean on the HED parent body

Abstract

Diogenites are ultramafic pyroxene and olivine rocks that are presumed to be cumulates that resulted from magmatic differentiation on the howardite-eucrite-diogenite (HED) parent body. There are, however, no precise and independent age constraints on the formation of diogenites and, in particular, their age relationships with the basaltic eucrites. Here we report a mineralogical (major and trace elements) and high-precision Mg isotope study of 24 diogenite meteorites that cover the known range of orthopyroxene and olivine compositions (En = 65.4 to 85.3 and Fo = 70.1 to 91.0) present in this group of meteorites. Despite having significant sub-chondritic $^{27}Al/^{24}Mg$ the diogenites exhibit significant variations in the mass-independent abundance of ^{26}Mg ($\delta^{26}Mg^*$) from -0.0108 $\pm$ 0.0018 to +0.0128 $\pm$ 0.0018‰. $\delta^{26}Mg^*$ correlates with orthopyroxene major and trace element chemistry, and can only be explained through active decay of live ^{26}Al ($t_{1/2}$ = 0.73 Myr) throughout the formation history of the diogenites. These observations suggest that large scale magmatic differentia-

tion driven by decay energy of ^{26}Al decay on the HED parent body during the lifetime of ^{26}Al resulted in the cumulate minerals capturing the chemical and isotopic evolution of large scale magma bodies or a magma ocean on the HED parent body. Calculated ^{27}Al/^{24}Mg ratios of the diogenite parent melts inverted from orthopyroxene major element chemistry positively correlate with increasing δ^{26}Mg* and suggest an initial degree of melting of 20 to 25%. The largest δ^{26}Mg* deficits appear to date the onset of diogenite formation to just 0.7 to 1.3 Myr after CAIs considering the uncertainty in the initial $(^{26}Al/^{27}Al)_0$ abundance of the HED parent body. Thus diogenite formation significantly pre-dates the formation of basaltic eucrites. The period of magmatic differentiation responsible for forming the full suite of diogenites might have been as short as ca. 0.2 Myr, but could have lasted longer depending on the initial $(^{26}Al/^{27}Al)_0$ of the HED parent body and uncertainties in the model calculations. The increase in heavy REE concentrations from the oldest to the youngest diogenites produced in this interval require up to 85 to 90% fractional crystallization of a common parent magma.

5.1 Introduction

Isotopic anomalies in meteorites that result from decay of short-lived radioactive isotopes are used to date and trace processes that shaped the early Solar System (e.g., Lugmair and Shukolyukov, 1998; Kleine et al., 2002; Bizzarro et al., 2005). One such short-lived isotope system, the ^{26}Al-to-^{26}Mg chronometer ($t_{1/2}$ = 0.73 Myr), is ideally suited to investigating crust-mantle differentiation that occurred during the lifetime of ^{26}Al because of the large fractionation of Al and Mg between different minerals and during partial melting and fractional crystallization processes in silicate melts. Meteorites from the howardite-eucrite-diogenite association (HED) include a wide range of magmatic products that represent the silicate differentiation of a planetesimal (Drake, 2001). To-date there is no con-

sensus on how the HED parent body differentiated and whether diogenites formed as partial melts of a semi-molten parent body or crystallized from a large magma ocean, as each genetic model proposed so far appears to be unable to explain all the aspects of HED meteorite chemistry (Mittlefehldt and Lindstrom, 2003). However, there is a growing consensus that magmatism on the HED parent body occurred shortly (2-3 Myr) after CAI formation (Lugmair and Shukolyukov, 1998; Smoliar, 1993; Bizzarro et al., 2005; Schiller et al., 2010a).

Diogenites are ultramafic rocks that are generally monomict but fragmental breccias of originally coarse-grained igenous rock comprising 90% orthopyroxene with minor chromite and olivine. Diogenites are presumed to be the igneous product of the HED parent body evolution. No precise and indendent age constraints on diogenite formation exist apart from the fact that diogenites plot on the HED whole rock ^{53}Mn-^{53}Cr isochron (Lugmair and Shukolyukov, 1998; Trinquier et al., 2008). This reflects the fact that diogenites are not easily dateable with most chronometric techniques as these rocks do not have high parent/daughter ratios that would make them amenable to dating with most absolute and relative chronometers. Furthermore, later thermal metamorphism has also affected the diogenites, which has homogenised the major element compositions of diogenite minerals and major elements seem to be decoupled from minor and trace element concentrations among diogenites (Mittlefehldt and Lindstrom, 2003). The genesis and chronology of eucrite and diogenite formation is not well understood and it has been variably proposed that diogenites may be the products of partial melting residues of a primitive body, total melting followed by fractional crystallization or equilibrium crystallisation or in situ magma ocean crystallisation or remelting of cumulates (Stolper, 1977; Warren, 1997; Shearer et al., 1997; Ruzicka et al., 1997; Righter and Drake, 1997; Barrat et al., 2000, 2008).

Recently it has been demonstrated that it is possible to ^{26}Al-^{26}Mg date material with very low ^{27}Al/^{24}Mg that has ^{26}Mg deficits related to its

very early formation during the lifetime of ^{26}Al (Fig. 5.1; Baker and Schiller, 2010). Because of their ultramafic composition, diogenites also have significantly sub-chondritic ^{27}Al/^{24}Mg ratios (0.01 - 0.05) and thus potentially preserve the δ^{26}Mg* composition of their parent magma at the time of their formation, which makes them potentially an ideal target for ^{26}Al-^{26}Mg deficit dating. However, the mass-independent ^{26}Mg anomaly only provides accurate age information on the time of diogenite formation, if they formed as cumulates from partial melts of a chondritic source very shortly after partial melting. In the case that their parental magma (with elevated ^{27}Al/^{24}Mg) experienced a long term chemical and Mg isotopic evolution in a magma ocean, the mass-independent ^{26}Mg signature will contain a mixed signature that is a result of the initial melt and the ^{26}Mg ingrowth in the magma ocean, which is a function of initial ^{26}Al/^{27}Al abundance and ^{27}Al/^{24}Mg ratio in the melt over time (Schiller et al., 2010a). In this case, the ^{26}Mg isotopic composition still provides general chronological constraints on diogenite formation and, provided ^{26}Al was still alive, the combination of evolving ^{26}Mg isotopic composition and information about the chemical composition of the parent magma produces snapshots of the chemical evolution of the parent magma over time. Such a scenario might potentially result in systematic changes in the major and trace element chemistry of diogenite cumulus minerals with evolving ^{26}Mg isotopic composition and offer new insights into the mechanisms and timescales of magmatic evolution on the HED parent body. To this end, we have measured the Mg isotopic composition and the major and trace elements of orthopyroxene and olivine of a representative suite of 24 monomict diogenites with orthopyroxene and olivine compositions ranging from En = 65.4 to 85.3 and Fo = 70.1 to 91.0, respectively, covering the known compositional range of mineralogical variability in diogenites.

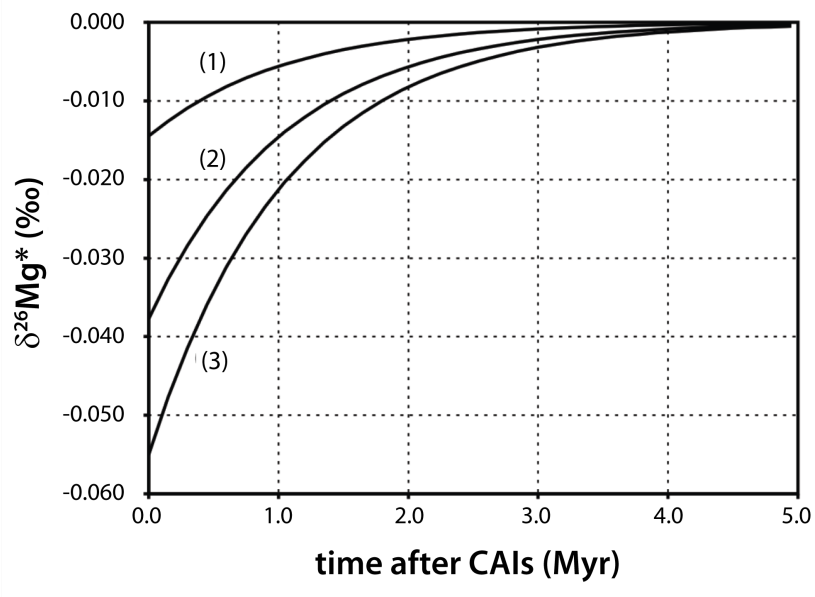

Figure 5.1: δ^{26}Mg* isotopic evolution of the Solar System in the first five million years after CAI formation. Meteorites or meteoritic material characterised by sub-chondritic Al/Mg (^{27}Al/^{24}Mg < 0.101) will be characterised by δ^{26}Mg* deficits if they formed within two million years of CAIs. Three different isotopic evolution curves are shown representing different initial ^{26}Al/^{27}Al values for the Solar System and its proto-planetary disk. Curve 2 shows the δ^{26}Mg* evolution if the proto-planetary disc has the same initial ^{26}Al/^{27}Al as indicated by a regression through Mg isotope data for chondrites and CAIs (Schiller et al., 2010a; Jacobsen et al., 2008). Curves 1 and 3 represent the minimum (2×10^{-5}) and maximum (7.6×10^{-5}) initial ^{26}Al/^{27}Al of the proto-planetary disc as estimated from the range of ^{26}Al/^{27}Al values over which bulk Mg isotopic analyses of chondrites and CAIs will produce coherent, statistically significant, regressions (Schiller et al., 2010b).

5.2 Methods

5.2.1 Major and trace element measurements

Major and trace element compositions of minerals from the diogenites were determined at Victoria University of Wellington using a JEOL JXA-8230 Superprobe electron microprobe (major elements) and an Agilent 7500CS ICP-MS coupled to a New Wave deep (193 nm) UV laser (trace elements). Analyses were conducted on polished half-mounts of small fragments of diogenites. Electron microprobe analyses were carried out using an accelerating voltage of 15 kV, a beam current of 12 nA and a focused beam (spot $<$0.5 μm). X-ray intensities were calibrated against elemental concentrations by analysis of the standards Johnstown hypersthene (Cr, Mg, Si, Al, Fe), Kakanui augite (Ti, Na, Ca) and synthetic MnO (Mn). Three secondary standards - Johnstown hypersthene (USNM 746), Kakanui augite (NMNH 122142) and Natural Bridge diopside (NMNH 117733) were repeatedly analysed throughout the sessions as secondary standards (Jarosewich et al., 1980).

Trace elements were measured on the same mount close to the electron microprobe pits. Each sample was analysed 5 to 11 times and consisted of a ca. 60 s background measurement and 60 s (around 50 scans) of data acquisition whilst ablating the sample. Sample analyses were bracketed every five analyses by a measurement on the calibration standard (BCR-2G). All data treatment was performed using the 'trace element IS' data reduction scheme of Iolite software (Hellstrom et al., 2008). Standard interpolation was done using the 'spline smooth auto' function. Baselines and all integrations were treated with a 3 sd outlier rejection. The background-corrected data were converted to absolute element concentrations using the element concentrations in the BCR-2 glass standard (GeoRem, 2010) and the silicon concentration in the diogenites measured with the electron microprobe using ^{29}Si for internal normalization.

5.2.2 Mg isotope and $^{27}Al/^{24}Mg$ ratio determinations

Mg isotopes were measured with a Thermo Finnigan Neptune multiple collector inductively coupled plasma mass spectrometer (MC-ICP-MS) in Copenhagen, Denmark, operated in medium resolution mode with an effective mass resolution of ca. 2500, which resolves all molecular interferences on the high mass side (e.g., $^{12}C_2^+$, $^{12}C^{14}N^+$) from Mg with the exception of Mg hydrides. Mg solutions of 4-5 ppm in 2.5% HNO_3 were introduced into the system as a 'wet' plasma using a spray chamber with an uptake rate of approximately 60 μL/min. Sensitivity of the mass spectrometer was increased by using an X-cone resulting in a 20-25 V signal per ppm Mg. ^{24}Mg, ^{25}Mg and ^{26}Mg were monitored with the L3, Ax and H3 Faraday collectors where the L3 collector was equipped with a 10^{10} Ohm resistor allowing larger ion beams of ca. 100, 14 and 14 V to be measured on masses 24, 25 and 26, respectively. Single analyses consisted of one block of 300 s of baseline and 100 $\times$ 16 s integrations. In addition to these measurements, Mg solutions of 13 diogenites analyzed on the Neptune were also measured using a Nu Plasma MC-ICP-MS using the approach described in Chapter 2.

All isotopic measurements were conducted using the standard-sample bracketing technique using DSM-3 as Mg standard (Galy et al., 2003), where the isotope ratios are expressed as per mil (‰) deviations from the mean Mg isotopic composition measured on the bracketing standards (Nu Plasma) or spline fit through all standards measured in the same session (Neptune): $\delta^x Mg = [(^xMg/^{24}Mg)_{sample}/(^xMg/^{24}Mg)_{standard} - 1] \times 10^3$, and x is either 25 or 26. The mass-independent ^{26}Mg abundance (δ^{26}Mg*) in the samples was corrected for instrumental mass bias by normalising the measured $^{26}Mg/^{24}Mg$ ratios to a $^{25}Mg/^{24}Mg$ ratio of 0.12663 (Catanzaro et al., 1966) using the exponential law (β = 0.511). Stable Mg isotope data (δ^{25}Mg and δ^{26}Mg) are reported in the per mil notation as the difference between the sample and the average value of the bracketing standards.

On the Neptune each sample was measured 10 times with internal er-

rors of the mass-bias-corrected δ^{26}Mg*$_{Neptune}$ = ± 0.0030 to 0.0050‰. All isotope calculations for data produced with the Neptune were done off line using the 'Mg_Neptune' data reduction scheme in the Iolite software package (Bizzarro et al., 2010) with a 3 sd outlier rejection for single integrations and the spline_smooth_auto function for the spline fit. Reported Mg isotope ratios are weighted means of the 10 analyses with 2 se errors that incorporate the error on the spline fit through the standard analyses. The final reported errors on the δ^{26}Mg*$_{Neptune}$ for a single sample are typically ± 0.0010 to 0.0020‰ (2 se), and while these errors are internal errors, the external reproducibility on δ^{26}Mg*$_{Neptune}$ is estimated to be ± 0.0025‰ using the described analytical conditions based on repeated analysis of various standards (Bizzarro et al., 2010).

Uncertainties on the analysis of a sample measured with the Nu Plasma are calculated as weighted means of replicate analyses of the sample and quadratically incorporate the errors of the sample runs as well as those of the bracketing standards resulting in an internal precision on δ^{26}Mg*$_{NuPlasma}$ that is ∼ ± 0.020‰, including the error contribution from the bracketing standards. The final reported errors on the δ^{26}Mg*$_{NuPlasma}$ for a single sample is the 2 se of the separate analysis (n = 15 - 20) that have been combined as a weighted mean resulting typically in uncertainties that are ± 0.0050 (2 se) and the external reproducibility on δ^{26}Mg*$_{NuPlasma}$ is estimated to be 1.5 times the 2 se based on repeated analysis of various standards (Schiller et al., 2010a).

The ^{27}Al/^{24}Mg ratios for Bilanga, Tatahouine, Ibbenbueren and all Northwest Africa (NWA) samples were measured on aliquots of completely digested samples taken before chemical separation of Mg with an Agilent 7500CS ICP-MS using He in a collision cell to minimise interferences on Al and Mg isotopes (^{27}Al, ^{24}Mg and ^{25}Mg). Sample analyses were bracketed with analyses of gravimetrically prepared Al/Mg = 2.0 and 0.1 solutions made from Aristar single element ICP-MS solutions. The error assigned to the ^{27}Al/^{24}Mg ratio is ± 2% (2 sd) based on repeated measure-

ments of USGS basaltic rock standards BCR-2 and BHVO-2 (Schiller et al., 2010a). $^{27}Al/^{24}Mg$ ratios for diogenite samples supplied by NASA (MET, LAP, GRO, and PCA named samples) were measured with the Neptune MC-ICP-MS applying a different approach that is described in detail in Bizzarro et al. (2010) using an Al-Mg spike and the AlMg_Nept data reduction scheme of the Iolite software package (Bizzarro et al., 2010; Hellstrom et al., 2008) to determine the $^{27}Al/^{24}Mg$ in the samples. In this study the error assigned to these samples is also $\pm$ 2% (2 sd), but expected to be $>$ 10 times smaller (Bizzarro et al., 2010).

5.2.3 Calculation of $^{27}Al/^{24}Mg$ in parental magmas

Magnesium concentrations in the parental magma were calculated from orthopyroxene compositions assuming a constant K_D (Mg) = 3, which was also used to determine a K_D (Ca) = 0.1258 using equation 39 in Beattie et al. (1991). Ti concentrations in the melt were calculated using equation 10a in Bèdard (2007) using the Wo content in the pyroxene. The Ca/Al ratio in primitive magmas is close to 1, but as Stolper (1977) noted there is a linear correlation between the Ca/Al ratio and Ti concentrations in the melt, which was used to convert Ca into Al concentrations. The $^{27}Al/^{24}Mg$ was calculated correcting the Mg concentration for an ^{26}Mg abundance of 0.7899.

5.3 Results

5.3.1 Olivine and orthopyroxene major and trace element chemistry

Major and trace element data measured on polished mounts of 23 diogenites that contain orthopyroxene or olivine are tabulated in Tables 5.1, 5.2 and 5.3, respectively. One sample (NWA 5480) could not be analyzed

for its mineral composition as it was only available as homogenized powder. In 19 of the analyzed sample mounts, orthopyroxene was the only major mafic mineral phase and in the remaining 4 samples only olivine was present. The calculated Mg-Fe mineral end-members from the major element compositions in orthopyroxene and olivine range from Fs = 13.8 (NWA 1461) to 30.6 (LEW 88008) and Fa = 8.8 (NWA 3329) to 29.2 (NWA 4223; Table 5.4).

With decreasing Mg concentration in orthopyroxene, Fe and Ca concentrations increase. Calcium concentrations in orthopyroxene are also positively correlated with Al and Ti concentrations, while Cr and Mn concentrations are similar in all orthopyroxene. There is a strong correlation of Ca with trace elements like Sc, Y, Hf and the heavy rare earth elements (REE; Figs. 5.2 and 5.3). With the exception of the two orthopyroxene-bearing diogenites (NWA 1461 and MET 00425), the REE patterns of the remaining 17 orthopyroxene-bearing diogenites are similar showing light REE depletion and negative Eu anomalies (Fig. 5.3a). NWA 1461 and MET 00425 have the lowest heavy REE concentrations of the analyzed diogenites and relative flat patterns that do not show the light REE depletion (relative to heavy REE) found in the other diogenites.

5.3.2 Magnesium isotopic composition of the diogenites

The diogenites measured with the Neptune MC-ICP-MS have δ^{26}Mg* anomalies that vary from -0.0108 $\pm$ 0.0018 to +0.0128 $\pm$ 0.0018‰ (Table 5.4). The group of diogenites analyzed with the Nu Plasma MC ICP-MS have a similar range from -0.0076 $\pm$ 0.0050 to +0.0153 $\pm$ 0.0051‰ albeit with larger errors (Table 5.5) and the determined δ^{26}Mg* anomalies agree well with results obtained on the Neptune (Fig. 5.4). Olivine and orthopyroxene samples both show a similar range in their δ^{26}Mg* of 0.0209‰ and 0.0232‰, respectively. The weighted average δ^{25}Mg compositions of all 24 diogenites is -0.124 $\pm$ 0.009‰ (2 se) with two samples that have slightly

Table 5.1: Major (wt.%) and trace element (ppm) data for diogenite orthopyroxene (part 1/2).

	NWA 1461	**MET 425**	**MET 436**	**Bilanga**	**NWA 5484**	**MET 855**	**Tatahouine**	**LAP 91900**	**MET 422**
SiO_2	56.01	55.84	53.57	54.91	54.84	53.42	53.15	53.63	53.92
TiO_2	0.031	0.026	0.025	0.068	0.036	0.024	0.065	0.054	0.039
Al_2O_3	0.31	0.41	0.28	0.53	0.52	0.31	0.80	0.63	0.47
Cr_2O_3	0.69	0.62	0.18	0.60	0.43	0.18	0.71	0.67	0.70
FeO	9.43	10.83	18.77	14.81	14.74	18.94	12.80	15.44	16.95
MnO	0.35	0.36	0.68	0.42	0.55	0.68	0.48	0.55	0.59
MgO	32.78	28.93	23.61	28.25	29.08	23.39	26.34	25.50	24.67
CaO	0.47	0.36	0.65	0.67	0.68	0.67	0.75	0.95	0.73
Sc	12.1	12.7	17.8	18.4	19.9	17.0	18.9	15.5	12.7
V	76.5	73.9	82.9	89.5	95.5	82.2	103.3	100.7	105.9
Co	10.0	11.5	3.5	16.1	11.5	5.1	11.6	10.7	15.2
Ni	5.07	5.25	0.10	2.64	0.36	0.13	7.41	4.00	9.77
Cu	n.d.	0.240	0.042	0.301	0.721	0.468	0.245	0.170	1.267
Zn	1.098	1.286	1.070	1.030	1.207	1.114	0.778	0.906	1.348
Sr	0.988	0.258	0.223	0.119	0.452	0.198	0.018	0.154	0.124
Y	0.237	0.167	0.150	0.757	0.376	0.226	0.247	0.447	0.176
Zr	0.266	0.633	0.205	0.724	0.194	0.304	0.025	0.386	0.168
Nb	0.018	0.052	0.004	0.203	0.016	0.006	0.016	0.022	0.019
La	0.017	0.022	0.000	0.011	0.006	0.006	0.000	0.004	0.007
Ce	0.114	0.092	0.011	0.037	0.007	0.020	0.002	0.018	0.027
Pr	0.016	0.015	0.002	0.006	0.002	0.004	0.001	0.005	0.004
Nd	0.099	0.077	0.020	0.040	0.010	0.027	n.d.	0.029	0.016
Sm	0.021	0.033	0.017	0.030	0.002	0.012	n.d.	0.012	0.006
Eu	0.009	0.004	0.001	0.006	0.000	0.002	n.d.	0.000	0.001
Gd	0.028	0.039	0.021	0.070	0.019	0.021	0.001	0.030	0.015
Tb	0.001	0.005	0.002	0.012	0.007	0.004	0.004	0.008	0.002
Dy	0.021	0.031	0.020	0.124	0.056	0.032	0.030	0.054	0.025
Ho	0.005	0.005	0.004	0.027	0.009	0.007	0.009	0.015	0.005
Er	0.033	0.016	0.014	0.082	0.039	0.024	0.046	0.053	0.023
Tm	0.004	0.003	0.002	0.015	0.010	0.004	0.012	0.010	0.006
Yb	0.033	0.019	0.019	0.112	0.051	0.023	0.072	0.076	0.028
Lu	0.011	0.005	0.003	0.020	0.010	0.005	0.013	0.014	0.006
Hf	0.009	0.012	0.006	0.023	0.022	0.006	0.001	0.011	0.006

Table 5.2: Major (wt.%) and trace element (ppm) data for diogenite orthopyroxene (part 2/2).

	LAP 3630	**NWA 2286**	**NWA 5600**	**MET 1060**	**NWA 1877**	**GRO 95555**	**Ibben-bueren**	**PCA 91077**	**NWA 1821**	**LEW 88008**
SiO_2	53.50	54.07	55.83	55.23	54.23	53.44	53.02	53.97	53.41	52.24
TiO_2	0.059	0.034	0.143	0.045	0.054	0.082	0.101	0.082	0.117	0.138
Al_2O_3	0.68	0.78	0.83	0.39	0.39	1.12	0.32	0.74	1.13	1.25
Cr_2O_3	0.63	0.28	0.65	0.29	0.40	0.82	0.32	0.69	0.74	0.89
FeO	15.57	15.95	14.07	13.35	16.78	14.91	14.94	16.35	16.92	18.48
MnO	0.54	0.57	0.45	0.54	0.60	0.55	0.51	0.59	0.63	0.59
MgO	25.17	26.93	28.64	27.85	26.03	25.00	26.40	24.69	22.29	24.46
CaO	1.00	0.64	1.31	0.54	0.96	1.15	1.22	1.17	1.68	1.67
Sc	15.7	18.5	19.9	14.2	21.0	14.8	19.7	16.0	20.2	26.6
V	97.9	112.7	85.8	97.8	141.3	123.2	82.8	102.0	114.4	152.4
Co	10.8	7.5	11.3	2.5	5.7	8.6	16.9	13.0	11.3	11.5
Ni	1.72	0.64	16.11	0.55	0.27	0.64	12.96	9.28	7.43	1.54
Cu	0.056	0.687	0.273	0.103	0.081	n.d.	n.d.	0.420	0.543	0.040
Zn	1.145	0.932	1.379	1.227	1.144	1.209	1.284	0.968	1.369	0.801
Sr	0.131	0.262	0.498	0.079	0.214	0.249	0.142	0.214	0.356	0.027
Y	0.551	0.119	2.061	0.120	0.338	0.986	1.203	0.890	1.397	1.628
Zr	0.363	0.038	3.895	0.018	0.727	2.415	0.703	0.617	1.120	0.469
Nb	0.012	0.012	0.164	0.014	0.016	0.025	0.017	0.017	0.020	0.018
La	0.003	0.001	0.026	0.002	0.004	0.023	n.d.	0.006	0.021	0.005
Ce	0.016	0.011	0.094	0.015	0.020	0.166	0.017	0.033	0.154	0.008
Pr	0.004	0.005	0.019	0.002	0.008	0.035	0.004	0.006	0.014	0.002
Nd	0.023	0.019	0.120	0.017	0.050	0.264	0.043	0.049	0.094	0.021
Sm	0.024	n.d.	0.076	0.003	0.031	0.075	0.025	0.020	0.051	0.014
Eu	0.002	n.d.	0.023	n.d.	0.008	0.011	n.d.	0.007	0.003	0.002
Gd	0.026	n.d.	0.146	0.003	0.040	0.114	0.085	0.057	0.113	0.071
Tb	0.006	0.002	0.036	0.000	0.010	0.021	0.020	0.015	0.024	0.018
Dy	0.074	0.018	0.291	0.011	0.043	0.153	0.171	0.121	0.205	0.181
Ho	0.019	0.005	0.079	0.004	0.011	0.037	0.050	0.030	0.050	0.050
Er	0.069	0.020	0.293	0.022	0.047	0.122	0.139	0.108	0.167	0.210
Tm	0.011	0.005	0.044	0.003	0.005	0.019	0.028	0.020	0.030	0.033
Yb	0.098	0.034	0.313	0.039	0.074	0.138	0.171	0.143	0.227	0.265
Lu	0.017	0.004	0.053	0.008	0.010	0.022	0.035	0.024	0.041	0.047
Hf	0.010	n.d.	0.110	0.003	0.041	0.070	0.026	0.022	0.039	0.020

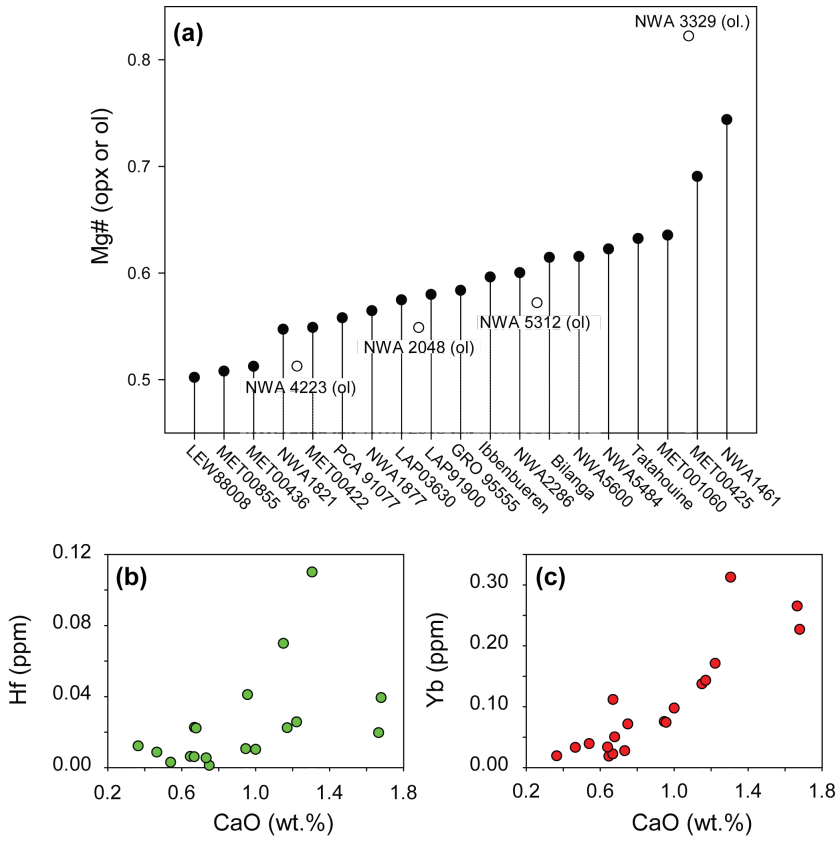

Figure 5.2: (a) A plot of the Mg# in diogenite orthopyroxene and olivine, (b) and (c) concentrations of Hf and Yb versus CaO measured in diogenite orthopyroxene. In (a) black circles represent orthopyroxene analyses and white circles olivine analyses.

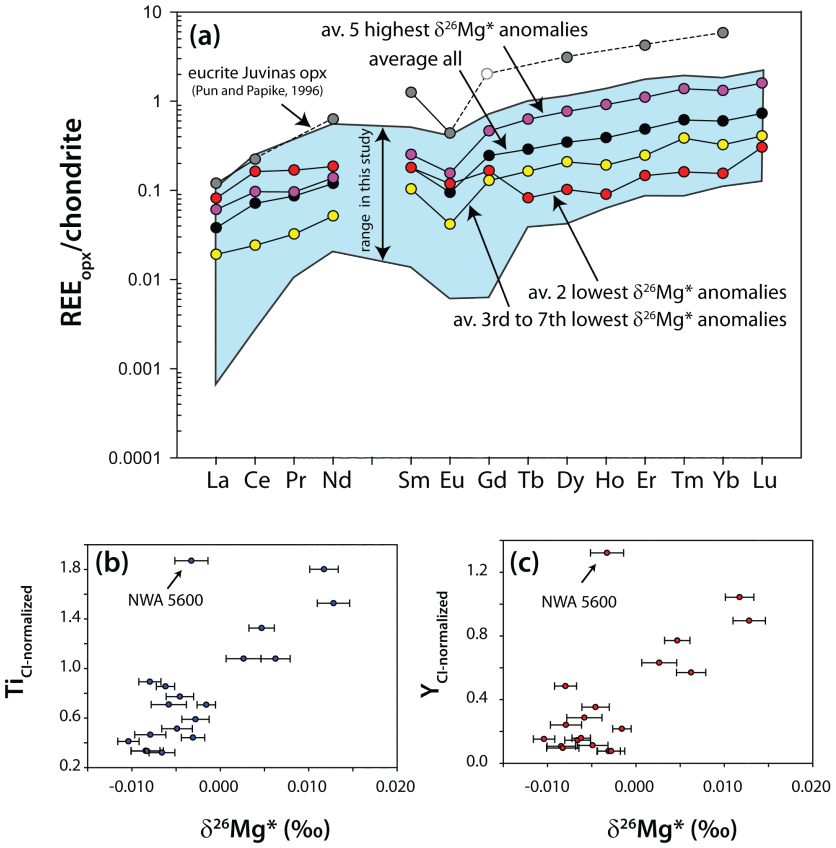

Figure 5.3: Part (a) shows the rare earth element patterns of analysed diogenite orthopyroxene as the range of measured concentrations and average of all diogenites as well as the average patterns of the 2 samples with the most negative δ^{26}Mg* (NWA 1461 and MET 00425), the 3rd to 7th most negative δ^{26}Mg* (MET 00436, Bilanga, NWA 5484, MET 00855 and Tatahouine) and the 5 samples with the most positive δ^{26}Mg* anomalies (GRO 95555, Ibbenbueren, PCA 91077, NWA 1821, LEW 88008). Part (b) and (c) show CI-normalized Ti and Y concentrations, respectively, in diogenite pyroxene versus δ^{26}Mg*. CI concentrations from (Anders and Grevesse, 1989).

Table 5.3: Major (wt.%) and trace element (ppm) data for diogenite olivine.

	NWA 3329	**NWA 5312**	**NWA 2048**	**NWA 4223**
SiO_2	40.6	38.3	37.1	37.4
FeO	8.57	22.84	24.39	26.48
MnO	0.26	0.51	0.65	0.60
MgO	47.7	36.6	35.6	33.4
CaO	0.06	0.02	0.03	0.22
Sc	5.15	3.97	4.00	4.73
V	22.0	6.04	12.2	20.1
Co	12.9	7.26	31.9	26.5
Ni	112	27.7	31.8	29.2
Cu	0.43	n.d.	0.98	3.37
Zn	2.51	1.37	1.91	1.15
Zr	0.061	0.202	0.044	0.083

heavier δ^{25}Mg isotopic compositions (MET 001060 and NWA 5312; Table 5.4).

$^{27}Al/^{24}Mg$ ratios measured in the digested sample solutions are on average 0.026 and show no trend with δ^{26}Mg* anomalies, while the only sample with significantly higher, but still sub-chondritic $^{27}Al/^{24}Mg$ ratio is LEW 88008 (0.091). The slightly elevated $^{27}Al/^{24}Mg$ ratio for this sample might be related to small amounts of terrestrial Al contamination of the $^{27}Al/^{24}Mg$ aliquot, considering that the $^{27}Al/^{24}Mg$ ratio of the in situ analysis of pyroxene of this same sample is much lower and indistinguishable from pyroxene analysis of the other diogenites.

Table 5.4: Magnesium isotope data determined with the Neptune MC-ICP-MS in Copenhagen, Denmark. In addition, the $^{27}Al/^{24}Mg$ ratios of the digested diogenite samples, orthopyroxene and calculated ratios in the parent melts are also shown. In addition, the mineral composition of orthopyroxene and olivine are shown where determined.

	δ^{26}Mg* (‰)	± 2 se	δ^{25}Mg (‰)	± 2 se	δ^{26}Mg (‰)	± 2 se	n	$^{27}Al/^{24}Mg$ sample	opx	melt	pyroxene/olivine Wo	Fs
J11 opx	-0.0022	0.0026	-0.1544	0.0065	-0.3032	0.0137	10					
Aristar + 5ppm	+0.0040	0.0015	-0.0075	0.0085	-0.0091	0.0165	10					
NWA 1461	-0.0104	0.0012	-0.1206	0.0063	-0.2471	0.0122	10	0.014	0.007	0.49	0.87	13.8
MET 00425	-0.0084	0.0016	-0.1524	0.0076	-0.3072	0.0156	10	0.014	0.009	0.45	0.76	15.4
MET 00436	-0.0083	0.0018	-0.1277	0.0118	-0.2587	0.0233	10	0.015	0.008	0.99	1.54	20.2
Bilanga	-0.0080	0.0013	-0.1170	0.0060	-0.2385	0.0107	10	0.029	0.013	0.69	1.30	22.4
NWA 5484	-0.0079	0.0018	-0.1433	0.0080	-0.2881	0.0158	10	0.023	0.012	0.79	1.28	22.0
MET 00855	-0.0066	0.0015	-0.0962	0.0119	-0.1948	0.0226	10	0.015	0.008	1.04	1.39	30.8
Tatahouine	-0.0062	0.0010	-0.1147	0.0033	-0.2300	0.0062	10	0.008	0.019	0.86	1.59	21.1
LAP 91900	-0.0058	0.0020	-0.1296	0.0083	-0.2576	0.0197	10	0.023	0.017	1.18	1.96	24.9
MET 00422	-0.0049	0.0017	-0.1108	0.0086	-0.2221	0.0165	10	0.019	0.012	1.01	1.53	27.4
LAP 03630	-0.0046	0.0016	-0.1544	0.0074	-0.3072	0.0163	10	0.024	0.018	1.22	2.06	25.2
NWA 2286	-0.0031	0.0013	-0.0983	0.0095	-0.1951	0.0191	10	0.033	0.020	1.06	2.50	21.1
NWA 5600	-0.0033	0.0019	-0.1102	0.0053	-0.2193	0.0105	10	0.016	0.020	0.81	1.25	24.5
MET 001060	-0.0028	0.0015	-0.0496	0.0076	-0.1006	0.0163	10	0.012	0.009	0.63	1.09	21.0
NWA 1877	-0.0016	0.0010	-0.1530	0.0043	-0.3008	0.0093	10	0.018	0.011	1.17	1.92	26.0
GRO 95555	0.0026	0.0020	-0.1259	0.0194	-0.2416	0.0401	10	0.044	0.030	1.32	2.42	24.5
Ibbenbueren	0.0047	0.0014	-0.1095	0.0054	-0.2103	0.0103	10	0.030	0.008	1.24	2.45	23.5
PCA 91077	0.0063	0.0017	-0.1420	0.0057	-0.2697	0.0113	10	0.029	0.020	1.36	2.42	26.4
NWA 1821	0.0117	0.0016	-0.1110	0.0075	-0.2055	0.0143	10	0.028	0.031	1.70	3.41	27.1
LEW 88008	0.0128	0.0018	-0.1621	0.0055	-0.3045	0.0101	10	0.091	0.038	2.00	3.56	30.6
NWA 5480	0.0007	0.0021	-0.1100	0.0032	-0.2153	0.0063	10	0.024			**Fo**	**Fa**
NWA 3329	-0.0108	0.0018	-0.1193	0.0082	-0.2435	0.0164	10	0.007			91.0	8.79
NWA 5312	-0.0070	0.0020	-0.0588	0.0123	-0.1225	0.0234	10	0.053			74.8	24.7
NWA 2048	0.0001	0.0017	-0.0990	0.0043	-0.1942	0.0091	10	0.024			72.4	27.0
NWA 4223	0.0101	0.0010	-0.1147	0.0033	-0.2300	0.0062	10	0.013			70.1	29.2

REE concentrations and, in particular, those of the heavy REE that are less likely to be affected by terrestrial alteration than light REE (Barrat et al., 1999; Mittlefehldt and Lindstrom, 1991) generally increase with increasing δ^{26}Mg*. The only clear exception from this is NWA 5600, which has the highest REE concentrations of all analyzed samples and is also anomalous rich in Ti and Y (Fig. 5.3b and c). Apart from NWA 5600, concentrations in the incompatible minor element Ti and trace element Y also show a trend of increasing concentrations with increasing δ^{26}Mg*. There is also a positive correlation between δ^{26}Mg* and the calculated ^{27}Al/^{24}Mg ratios of the melt that can partly be explained because the ^{27}Al component of these ^{27}Al/^{24}Mg ratios is calculated based on the calcium and titantium concentrations in the pyroxene, which show a similar correlation (Figs. 5.3b and 5.5). Trace element concentrations in the four olivine samples are very low and apart from the correlation in the major element composition and the δ^{26}Mg* anomaly the number of samples is too small to identify clear trends. However, it should be noted that NWA 3329, with the lowest δ^{26}Mg* anomaly has nearly 4 times higher Ni concentration as the other three samples.

5.4 Discussion

5.4.1 Data accuracy and significance of δ^{26}Mg* anomalies

In order to demonstrate that it is possible to measure δ^{26}Mg* anomalies that are much smaller than 0.0100‰ accurately and precisely, we measured an orthopyroxene separate from a mantle peridotite from Jordan (J11 opx) processed through the Mg chemical separation scheme and an Aristar ICP-MS Mg solution that was gravimetrically doped with a pure ^{26}Mg spike to have an δ^{26}Mg* excess of 0.0050‰ with the Neptune MC-ICP-MS (Aristar +5ppm; Table 5.4). Both the mantle orthopyroxene (-0.0022 $\pm$ 0.0026‰) and the doped Mg standard solution (+0.0040 $\pm$ 0.0015‰) have δ^{26}Mg*

Table 5.5: Magnesium isotope data of diogenite samples measured with the Nu MC-ICP-MS in Wellington, New Zealand.

	δ^{26}Mg* ± 2 se (‰)		δ^{25}Mg ± 2 se (‰)		δ^{26}Mg ± 2 se (‰)		n
J11 opx	-0.0002	0.0049	-0.138	0.057	-0.270	0.110	15
NWA 1461	-0.0076	0.0050	0.001	0.080	-0.010	0.160	15
Bilanga	-0.0072	0.0049	-0.057	0.037	-0.120	0.073	15
NWA 5484	-0.0051	0.0049	-0.105	0.058	-0.210	0.110	15
Tatahouine	-0.0057	0.0046	-0.067	0.040	-0.134	0.081	18
NWA 2286	0.0006	0.0048	-0.080	0.027	-0.145	0.045	20
NWA 5600	-0.0015	0.0050	-0.029	0.042	-0.054	0.081	16
NWA 1877	0.0040	0.0052	-0.134	0.035	-0.259	0.069	15
Ibbenbueren	0.0049	0.0045	-0.053	0.038	-0.101	0.077	20
NWA 1821	0.0155	0.0054	-0.065	0.029	-0.112	0.054	15
NWA 5480	0.0003	0.0051	-0.037	0.032	-0.072	0.059	15
NWA 3329	-0.0066	0.0051	-0.077	0.030	-0.157	0.060	15
NWA 2048	0.0080	0.0051	-0.008	0.059	-0.010	0.120	15
NWA 4223	0.0153	0.0051	0.020	0.047	0.053	0.094	15

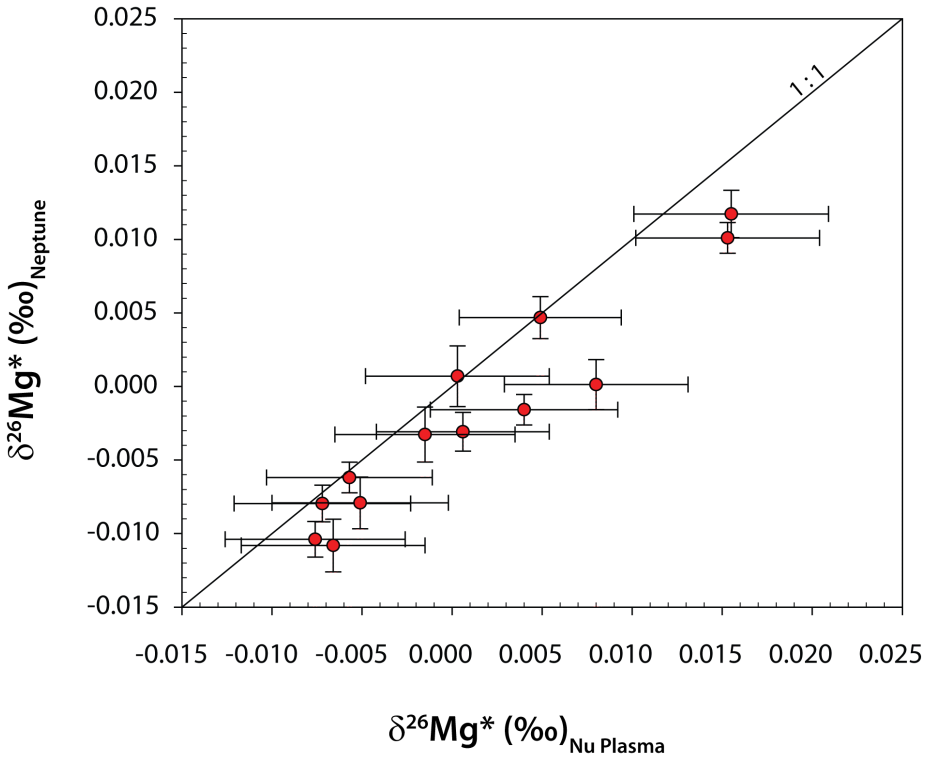

Figure 5.4: Comparison of δ^{26}Mg* values determined on the same diogenite with the Nu Plasma MC-ICP-MS in Wellington, New Zealand and the Neptune MC-ICP-MS in Copenhagen, Denmark. Also shown is a 1-to-1 correlation line for comparison.

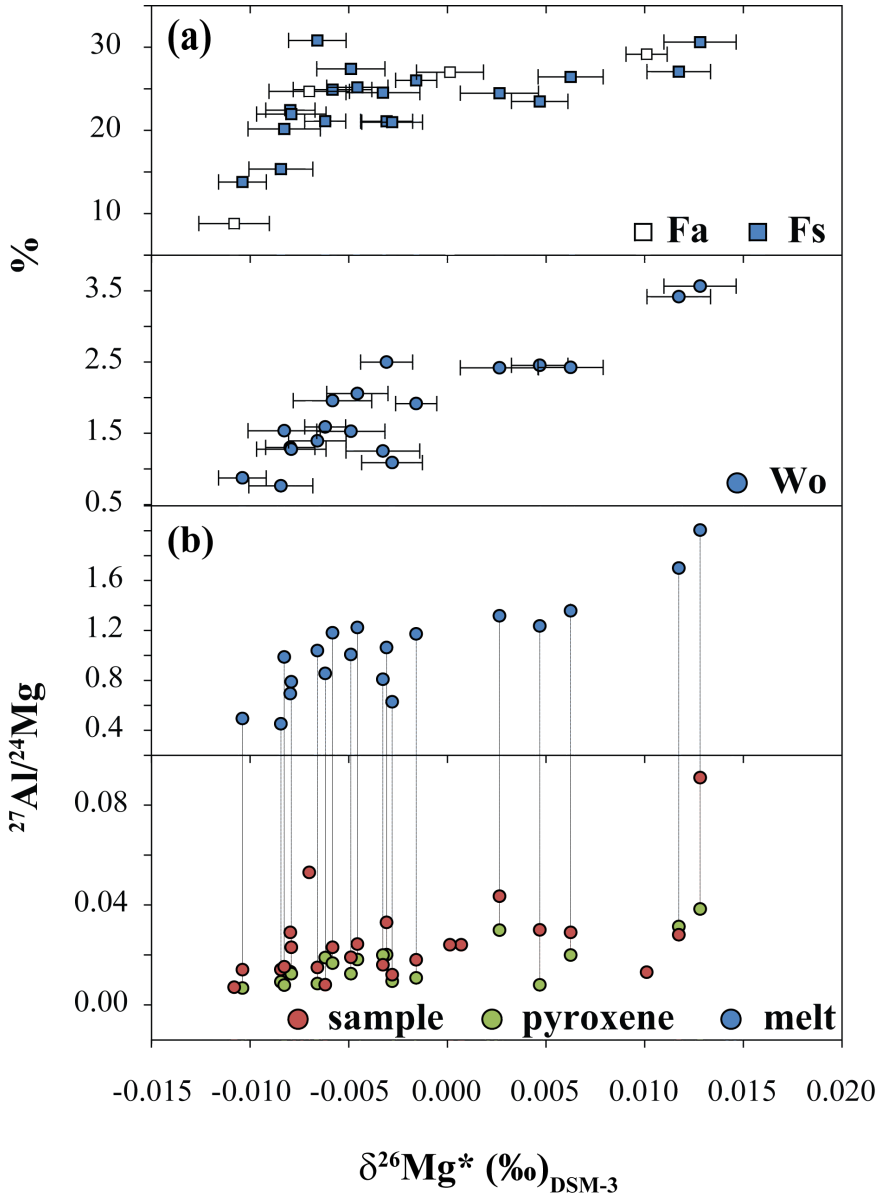

Figure 5.5: (a) The percent abundance of the measured fayalite (Fa), wollastonite (Wo) and ferrosillite (Fs) component in the olivine and orthopyroxene, respectively, of the diogenites is shown versus δ^{26}Mg* measured with the Neptune MC-ICP-MS. (b) The ^{27}Al/^{24}Mg ratios measured in an aliquot of the sample solution used for δ^{26}Mg* analysis and the ^{27}Al/^{24}Mg ratios measured in situ in orthopyroxene by EPMA and the ^{27}Al/^{24}Mg ratios calculated for the parental magma of the orthopyroxene for each sample plotted versus δ^{26}Mg* of each diogenite.

that are within errors (2 se) of the expected anomalies (0.0000 and 0.0050‰, respectively). Measured δ^{26}Mg* anomalies in diogenites have a total range of 0.0232‰ that cannot be explained through variable exposure ages and cosmogenic effects because the δ^{26}Mg* anomalies are independent of the exposure ages of the diogenites. Large cosmogenic effects of Mg isotopes in diogenites are also unlikely because of the small thermal neutron capture cross-sections of Mg isotopes and the short exposure ages of diogenites ($<$ 50 Myr) (Welten et al., 1997; Walkiewicz et al., 1992).

Samples that have also been measured with the Nu Plasma MC-ICP-MS do, despite their larger errors ($\sim$ 0.0050‰), in general correlate well with the results from the Neptune (Fig. 5.4 and Table 5.5). The correlation in δ^{26}Mg* seems to be possibly slightly biased to more positive δ^{26}Mg* anomalies when measured with the Nu Plasma, although this offset is barely significant considering the analytical uncertainties on the Nu Plasma δ^{26}Mg* measurements. Importantly, however, results from both mass spectrometers show a resolvable range in δ^{26}Mg* values from clearly negative to clearly positive δ^{26}Mg* values.

The variations in δ^{26}Mg* can also not be explained through variable amounts of uncorrected stable isotope fractionation and the nature of the mass fractionation laws used to correct for instrumental mass bias, as the measured range of stable isotopic compositions is very restricted and much smaller than required to produce such effects (e.g., Young and Galy, 2004). The consistent results from two different mass spectrometers and the demonstration of the analytical precision through measurements of a doped standard and tests reported in Bizzarro et al. (2010) demonstrate that the analytical techniques applied in this study make it possible to resolve mass-independent variations in δ^{26}Mg* that are as small as 0.0025‰. The existence of this range of δ^{26}Mg* values suggests that they are related to changes in ^{27}Al/^{24}Mg and ^{26}Al/^{27}Al in the parent melt of diogenites and demonstrates the evolution of δ^{26}Mg* anomalies in the HED parent body over a period of time very early in the Solar System when ^{26}Al was

still extant.

5.4.2 Age constraints on the onset of diogenite formation

Genetic models for eucrite and diogenite formation and silicate differentiation of the HED parent body can potentially be tested by examining the relative chronology of eucrite and diogenite formation. However, so far there are no precise age constraints on the relative chronology of eucrite and diogenite formation as absolute Pb-Pb ages of eucrites seem to be disturbed (Manhes et al., 1984; Tera et al., 1997) and diogenites are also not suited to dating with such techniques. ^{53}Mn-^{53}Cr data for bulk eucrites and diogenites form a single isochron suggesting the HED parent body differentiated within 1 to 3 Myr of calcium-aluminum-rich inclusions (CAIs), but given the uncertainties on this data and limited range in Mn/Cr ratios exhibited by diogenites, it is difficult to discern age differences between eucrites and diogenites the using ^{53}Mn-^{53}Cr chronometer (Lugmair and Shukolyukov, 1998; Trinquier et al., 2008). Model ages based on δ^{26}Mg* values of eucrites suggest that eucrites formed ca. 3 Myr after CAIs (Srinivasan et al., 1999; Bizzarro et al., 2005; Schiller et al., 2010a).

The former existence of live ^{26}Al in the early Solar System has long been demonstrated (Lee et al., 1977) and it is well established that most CAIs contained a so-called 'canonical' $(^{26}\mathrm{Al}/^{27}\mathrm{Al})_0$ abundance of 5.21×10^{-5} (MacPherson et al., 1995; Jacobsen et al., 2008). Planestesimals with CAI-like ^{26}Al abundances and a chondritic $^{27}\mathrm{Al}/^{24}\mathrm{Mg}$ ratio (0.104 ± 0.004; Palme and Jones, 2003) forming at the same time as CAIs would have initially had a δ^{26}Mg* deficit of $\sim 0.0373‰$ relative to their present-day δ^{26}Mg* value after complete ^{26}Al decay. This initial $(^{26}\mathrm{Al}/^{27}\mathrm{Al})_0$ abundance has been inferred to be homogeneous throughout the Solar System and used to date basaltic (Srinivasan et al., 1999; Baker et al., 2005; Bizzarro et al., 2005; Spivak-Birndorf et al., 2009; Schiller et al., 2010a) and ultramafic (Baker and Schiller, 2010) achondrites.

The initial Solar System $(^{26}Al/^{27}Al)_0$ abundance and the negative anomalies in the most magnesian diogenites [NWA 1461: -0.0104 $\pm$ 0.0012‰ (En = 85.3) and NWA 3329: -0.00108 $\pm$ 0.0018‰, where NWA3329 is an olivine diogenite with Fo = 91.9 (Table 5.4)] can be used to place model age constraints on the onset of initial cumulate diogenite formation. These two most negative δ^{26}Mg* values measured in the analyzed diogenites are within error of the δ^{26}Mg* deficits reported in pallasite olivine (Baker and Schiller, 2010) and are likely to reflect the earlymost stages of magmatic differentiation of substantive bodies of magma on the HED parent body. Using the same approach as Baker and Schiller (2010) to calculate the initial $(^{26}Al/^{27}Al)_0$ abundances for these two diogenites by regressing the $^{27}Al/^{24}Mg$ - δ^{26}Mg* diogenite data with the average composition of non-CAI-bearing chondrites ($^{27}Al/^{24}Mg$ = 0.091; δ^{26}Mg* = -0.0015 $\pm$ 0.0013‰; Schiller et al., 2010a) defines lines with slopes and initial $(^{26}Al/^{27}Al)_0 = 1.6 \pm 0.4 \times 10^{-5}$ for each of the two diogenites (Fig. 5.6). With respect to the initial $(^{26}Al/^{27}Al)_0$ abundance of CAIs (Jacobsen et al., 2008), NWA 1461 and NWA 3329 yield relative ages of $1.2^{+0.3}_{-0.2}$ and $1.3^{+0.3}_{-0.2}$ Myr, respectively. These model ages are maximum ages (i.e. the ages could be older) that ignore potential δ^{26}Mg* in-growth resulting from a superchondritic $^{27}Al/^{24}Mg$ ratio in the parent magma prior to crystallization and diffusive closure of the diogenite minerals and in situ in-growth in the diogenite minerals that results from the non-zero $^{27}Al/^{24}Mg$ ratio in the minerals, where both effects allow the true formation ages to be slightly closer to CAI formation. Because the relative ages for eucrites (Bizzarro et al., 2005; Schiller et al., 2010a) and diogenites are based on the same short-lived chronometer and the same assumptions of initial $(^{26}Al/^{27}Al)_0$ abundance and a chondritic $^{27}Al/^{24}Mg$ ratio, these diogenite ages demonstrate that the initial formation of diogenites pre-dates the formation of eucrites on the HED parent body by ca. 1.5 Myr.

However, it has not yet been clearly demonstrated that achondrite parent bodies, Earth and CAIs all formed from a homogeneous reservoir with

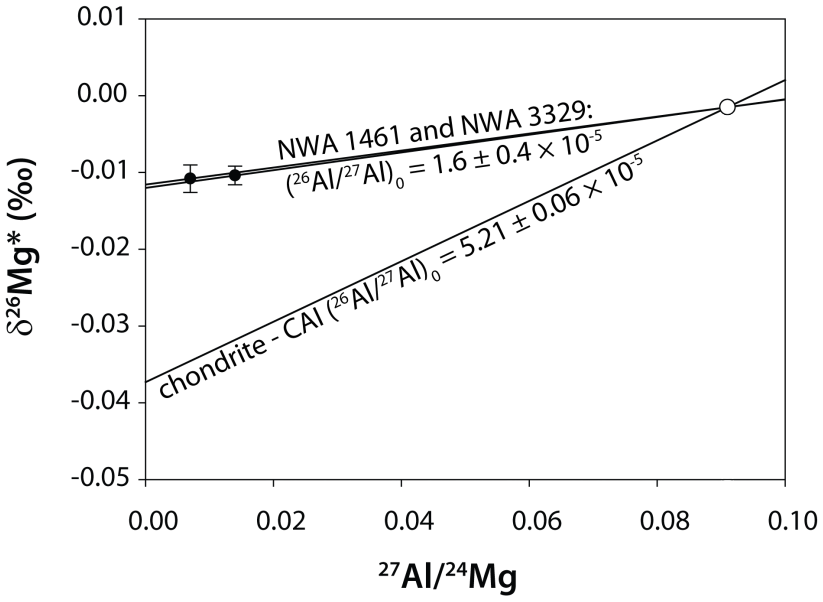

Figure 5.6: Chondrite - diogenite isochrons for NWA 1461 and NWA 3329 and the chondrite - CAI isochron using the $(^{26}Al/^{27}Al)_0$ from Jacobsen et al. (2008). The chondrite composition was taken from (Schiller et al., 2010a).

the same initial $(^{26}Al/^{27}Al)_0$ abundance (5.21×10^{-5}). Schiller et al. (2010a) suggested that it was allowable for the planetesimal region to have formed with an $(^{26}Al/^{27}Al)_0$ as low as 2.1×10^{-5}. If planetesimals and planets indeed accreted from material with a low initial $(^{26}Al/^{27}Al)_0$ abundance and one assumes that Earth and the HED parent body accreted from material with similar $(^{26}Al/^{27}Al)_0$ abundances, NWA 1461 and NWA 3329 could have formed as early as 0.3 Myr after CAI formation. In such a case it is likely that the HED had a lower initial $(^{26}Al/^{27}Al)_0$ abundance than Earth that places the age of diogenite formation relative to CAIs somewhere in between 0.3 and 1.3 Myr depending on the relative abundances of $(^{26}Al/^{27}Al)_0$ in the HED parent body, Earth and CAIs. Irrespective of these various scenarios, an unescapable conclusion is that diogenite formation on the HED parent body occurred very early in the Solar System, post-dating formation of CAIs by less than 1.5 Myr.

5.4.3 Heat source for HED parent body melting

There are a number of different mechanisms that can potentially explain planetesimal melting early in the Solar System. However, heating by radioactive decay of short-lived radionuclides in general, and specifically ^{26}Al-decay, is considered to be the most viable heat source (Urey, 1955).

The evidence of significant negative δ^{26}Mg* anomalies in NWA 1461 and NWA 3329 can be used to examine if ^{26}Al-decay could have been the major heat source responsible for the early melting and differentiation of the HED parent body. Assuming minimal heat loss from the planetesimal body and only minor heat contribution from ^{60}Fe decay, it can be calculated that an abundance of $^{26}Al/^{27}Al \sim 1.15 \times 10^{-5}$, which equals -0.0082‰ change in the δ^{26}Mg* composition, is theoretically sufficient to heat and completely melt dry, CI-like, dust from ambient temperatures (Castillo-Rogez et al., 2009; Hevey and Sanders, 2006). This provides a conservative estimate of the minimal amount of ^{26}Al decay that is required to melt a

planetesimal providing ^{26}Al decay is the major heat source. If the HED parent body had an initial $(^{26}Al/^{27}Al)_0$ = 5.21 $\times$ 10^{-5}, the original δ^{26}Mg* deficit in the HED precursor material was -0.0373‰ and from the difference of this initial deficit to the δ^{26}Mg* deficits in NWA 1461 and NWA 3329 it can be calculated that $\sim$ 3.7 $\times$ 10^{-5} of the original $(^{26}Al/^{27}Al)_0$ had decayed, which produced 3 $\times$ the minimal amount of energy required to heat and melt the HED parent body and demonstrates that ^{26}Al is the most likely heat source responsible for early planetesimal melting.

In the case that the initial $(^{26}Al/^{27}Al)_0$ of Earth and HED was only ca. 2.1 $\times$ 10^{-5}, ^{26}Al decay could have only contributed around 50% of the required energy to heat and melt the HED parent body until NWA 1461 and NWA 3329 were formed. However, considering δ^{26}Mg* anomalies are measured with respect to Earth, an initial heterogeneity between Earth and HED parent body equivalent to a HED parent body δ^{26}Mg* deficit of $\sim$ 0.005‰ could allow for ^{26}Al decay to have produced the required energy to melt the HED parent body at the time of formation of NWA 1461 and NWA 3329. In order to produce the minimum amount of energy to melt the HED parent body in such a extreme scenario it is required that at least half of the initial ^{26}Al abundance in the HED parent body decayed, placing a minimum age of $\sim$ 0.7 Myr on the formation of NWA 1461 and NWA 3329. Considering this, the requirement to heat and melt the HED parent body constrains the initial formation of diogenites in combination with the lack of an independent precise estimate of the initial $(^{26}Al/^{27}Al)_0$ abundance of the HED parent body to within 0.7 to 1.3 Myr after CAI formation, while at the same time the HED parent body accretion must also have occurred either simultaneously or within one half-life of ^{26}Al after CAI formation.

5.4.4 Magma ocean versus partial melting models

In order to understand the evolution of the δ^{26}Mg* anomalies in the magma body (or ocean) that diogenites crystallized from over time it is crucial to constrain the ^{27}Al/^{24}Mg ratio(s) of the evolving magma. This is complicated by the fact that the incorporation of aluminum in pyroxene is not particularly sensitive to the magma composition (Bèdard, 2007). To overcome this problem a proxy approach was taken and this method produces realistic ^{27}Al/^{24}Mg ratios of the magma that are consistent with regards to the range in ^{27}Al/^{24}Mg ratios expected from a chondritic parent body that produced basaltic eucrites with ^{27}Al/^{24}Mg ratios $\sim$ 2.

Given that the calculated lowest initial ^{27}Al/^{24}Mg ratios of the parent melt are not chondritic, but are about four to five times higher than the chondritic value (Table 5.4), it can be deduced that the initial magma on the HED parent body from which the oldest diogenites (NWA 1461 and MET 00425) formed represented a degree of melting between 20 and 25 % (assuming Al essentially behaves incompatibly during partial melting). It is not clear if these diogenites represent the earliest cumulates that crystallized from the original partial melt. However, considering the low Fs component in the orthopyroxene in these two diogenites (13.8 and 15.4, respectively) and the relatively flat REE patterns in the orthopyroxene that distinguish these two meteorites from the other diogenites it is likely these diogenites represent the earliest stage in the magmatic evolution of the HED parent body. This interpretation is also supported by the δ^{26}Mg* deficit in NWA 3329, which contains olivine with very high Fo = 90.96 and the highest Ni content of the analyzed olivines, as well as δ^{26}Mg* deficits in pallasite olivines (Baker and Schiller, 2010) that all have δ^{26}Mg* deficits indistinguishable from NWA 1461. Furthermore , because the REE patterns of NWA 1461 and MET 00425 contrast with the other diogenites, we suggest that these two samples are cumulates resulting during the earliest magma formation on the HED parent body. This scenario implies that NWA 1461 and MET 00425 are samples that represent the onset of melt

formation and silicate differentiation on the HED parent body.

Apart for some potential impact-impregnated Fe-Ni metal, diogenites lack a metal component and suggest they formed after complete removal of the metal phase into the core. The calculated degree of the initial silicate melting is in agreement with experimental studies of silicate - metal segregation (Larimer, 1995; Terasaki et al., 2008) core formation on the HED parent body occurred at relative low degrees of melting. The calculated degree of silicate melting and core formation at a low degree of melting also argues against models of complete melting of the HED parent body (e.g., Righter and Drake, 1997). However, because all the analysed diogenites, with the exception of the NWA 5600, show a consistent trend of enrichment in incompatible elements it is likely that the diogenites that formed after NWA 1461 and MET 00425 are cumulates that crystallized from a common or closely related magma source.

However, depending on the initial $(^{26}Al/^{27}Al)_0$ abundance in the material the HED parent body accreted from NWA 1461, NWA 3329 and MET 00425 are either representative of the initial degree of melting on the HED parent body. If the initial $(^{26}Al/^{27}Al)_0$ abundance in the HED parent body was low, or, if the initial $(^{26}Al/^{27}Al)_0$ abundance of HED was essentially the same as CAIs and the HED parent body accretion was early, there was potentially a much larger degree of melting. In the latter case, assuming the estimated degree of melting is correct, and because the analyzed samples in this study cover the complete range of known orthopyroxene and olivine compositions of HED cumulates, the cumulates that formed from such an initial and much larger melt are not represented by the HED meteorite collection thus far.

5.4.5 δ^{26}Mg* and melt evolution on the HED parent body

While in the previous section the focus was mainly on the information that can be gained from the samples with the most negative anoma-

lies, the complete range of δ^{26}Mg* and their correlated mineral chemistry holds valuable information on the processes that occurred after the initial magma formation. The anomalies in the diogenites broadly correlate with their respective orthopyroxene composition from the most magnesian (En = 85.3; -0.0104‰) to the most ferroan sample (En = 65.4; +0.0128‰), while the correlation is even more prominent with the wollastonite content (Fig. 5.5a), but can also be seen for some minor and trace elements as well as the heavy REE (Fig. 5.3). There is also a positive correlation between the fayalite content in the four analysed olivine samples and their respective δ^{26}Mg* anomalies that cover the same range as the orthopyroxene diogenites (Table 5.4). These correlations suggest that δ^{26}Mg* anomalies evolved alongside the magmatic differentiation on the HED parent body while ^{26}Al was alive and decaying and supports the interpretation that diogenites are cumulates crystallized from a magma body and record the cooling history and change of the magmatic composition. To estimate the amount of fractional crystallization that produced the range of diogenites one can use the change in relative concentration of incompatible elements. Concentrations of REE elements in orthopyroxene increase from NWA 1461 to LEW 88008 roughly by a factor of 8 to 12 (Fig. 5.3). Because the increase is quite consistent between all diogenites (with the exception of NWA 5600) and can also be seen for incompatible elements like Y and Ti it can be assumed all diogenites formed at different stages from a common parental magma and were separated from the magma body at different stages of the fractional crystallization. In order to achieve such an increase in the relative element concentrations from NWA 1461 to LEW 88008 requires a large amount of fractional crystallization (80-95% assuming these elements are perfectly incompatible). This large change supports the assumption that the range of analyzed diogenites does in fact represent most of the magmatic evolution on the HED parent body and this fractionation trend also shows that it is theoretically possible to produce REE element concentrations in eucrite orthopyroxene as measured in Juvinas from the corresponding par-

ent magma of the most evolved diogenites in this study by continuing the fractional crystallization trend that is responsible for the range of diogenites (Fig. 5.3).

In a closed system, increasing δ^{26}Mg* anomalies do indicate time evolution, but it is much more difficult to extract an accurate absolute chronology. To understand the timescale of magma evolution on the HED parent body it is crucial to extract the history of ^{27}Al/^{24}Mg evolution in the magma that produced diogenites. This is because magma differentiation and fractional crystallization of olivine and pyroxene is removing significantly more Mg than Al from the magma increasing the ^{27}Al/^{24}Mg ratio, which is recorded in eucrites, the basaltic products from the HED parent body that have ^{27}Al/^{24}Mg ratios $\sim$ 2 and are marked by ^{26}Mg* excesses of 0.030 - 0.040‰ (Bizzarro et al., 2005; Schiller et al., 2010a). Unfortunately it is not possible to de-convolute the precise evolution path of the ^{27}Al/^{24}Mg ratios and the δ^{26}Mg* anomaly over time because both, time of formation of single diogenites that provide snapshot of their parent magma and the precise ratio and rate of change of ^{27}Al/^{24}Mg in the parent magma, are unknown. However, assuming that the most ferroan diogenites samples NWA 1821 and LEW 88008 with the most positive δ^{26}Mg* anomalies and the highest calculated ^{27}Al/^{24}Mg ratios of $\sim$ 2.0 represent ultramafic cumulates that are closely related to the formation of eucrite-like rocks, the anomalies in the diogenites then approximately represent the existing δ^{26}Mg* anomaly in the magma producing these eucrite-like rocks.

5.4.6 ^{27}Al/^{24}Mg evolution in the magma

One can model the evolution of the δ^{26}Mg* anomaly in a magma with changing ^{27}Al/^{24}Mg ratios over time based on the assumptions that the initial ^{26}Al/^{27}Al and ^{27}Al/^{24}Mg ratios and the initial δ^{26}Mg* and final δ^{26}Mg* as well as the final ^{27}Al/^{24}Mg ratio of the evolving magma are known. Using these two endpoints different rates of change in the

$^{27}Al/^{24}Mg$ ratio will result in variable rates of increase of $\delta^{26}Mg^*$ in the magma over time. Two approaches, linear and double exponential rates of change that represent a rapid change of $^{27}Al/^{24}Mg$ and hence a rapid increase in $\delta^{26}Mg^*$ and slow increase of $^{27}Al/^{24}Mg$ and hence a more delayed and slower increase of $\delta^{26}Mg^*$ in the magma over time have been modeled (Fig. 5.7). The model starts with an initial $\delta^{26}Mg^*$ deficit and $^{27}Al/^{24}Mg$ ratio in the melt like the one calculated from NWA 1461 and finishes with the $\delta^{26}Mg^*$ anomaly and $^{27}Al/^{24}Mg$ ratio in the melt as calculated from LEW 88008. In general this model is independent of the initial $(^{26}Al/^{27}Al)_0$ abundance as this only influences the absolute time each model runs, which is not taken into account for the comparison of the resulting $^{27}Al/^{24}Mg$ ratios. When plotting the predicted $^{27}Al/^{24}Mg$ ratios from both models with the calculated $^{27}Al/^{24}Mg$ ratios from the orthopyroxene composition there is a good 1-to-1 correlation ($R^2 = 0.75$) using a linear evolution model, while the double exponential model fails to produce any correlation of the modeled $^{27}Al/^{24}Mg$ with the calculated $^{27}Al/^{24}Mg$ ratios. The remaining scatter in the linear model might be due to the uncertainties in the calculated $^{27}Al/^{24}Mg$ ratios for each sample, a non-perfect linear behavior of the $^{27}Al/^{24}Mg$ evolution, which can not be resolved considering the accuracy of the data, or indicates that especially the samples with lower $^{27}Al/^{24}Mg$ ratios evolved from reservoirs that evolved at the same time and similar rate but preserved local heterogeneities. Small local differences are also generally supported by the scatter in the REE pattern of single samples underlying the general trend of the REE enrichment correlated with increasing $\delta^{26}Mg^*$ anomalies. The linear correlation of model and calculated $^{27}Al/^{24}Mg$ ratios suggests that such a rapid and continuous evolution of the $^{27}Al/^{24}Mg$ is likely an accurate representation of the rate of change of $^{27}Al/^{24}Mg$ ratio in the parent magma of the HED parent body.

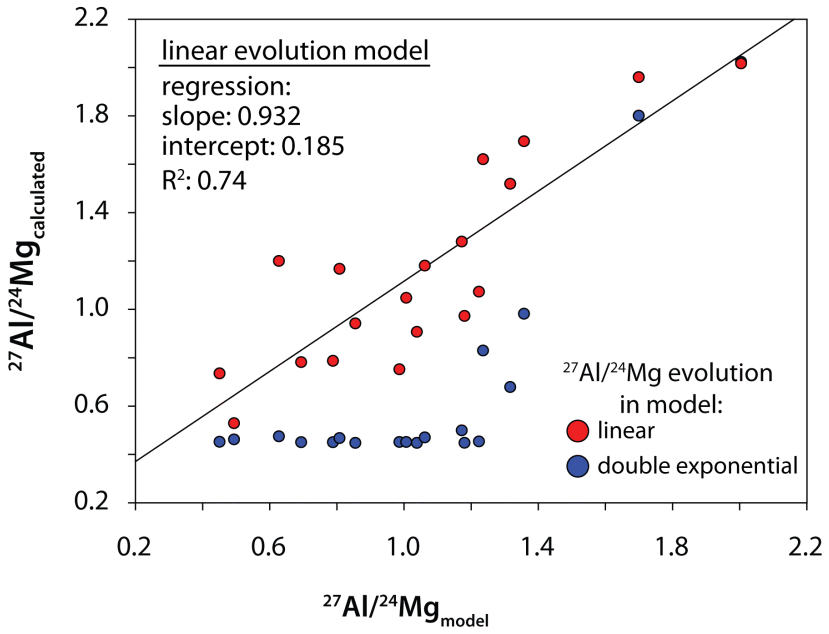

Figure 5.7: Plot of the calculated $^{27}Al/^{24}Mg$ of the parent melt based on the orthopyroxene composition versus modeled $^{27}Al/^{24}Mg$ of the parent melt using a linear and a double exponential approach of $^{27}Al/^{24}Mg$ change over time. Model settings were a change of $^{27}Al/^{24}Mg$ from 0.45 to 2.0 and a parent body $\delta^{26}Mg^*$ = -0.0109 to +0.0128‰ with an $(^{26}Al/^{27}Al)_0$ at time of initial differentiation of 1.52 $\times$ 10^{-5}. Time of magma evolution was adjusted to fit the start and end point and is mainly dependent on the choice of initial $(^{26}Al/^{27}Al)_0$ and is not the same for each model. Double exponential function used was: y = $^{27}Al/^{24}Mg_{initial}$ + a*exp(b*x) with a = 0.00154, b = 6.914 and x = 0 to 1. $^{27}Al/^{24}Mg$ ratios from the model were calculated using a function based on an polynomial fit of the model data.

5.4.7 Timescale of magma evolution on the HED parent body

Based on the observation that a linear rate of change of the $^{27}Al/^{24}Mg$ ratio in the diogenite parent magma is a good approximation of the calculated $^{27}Al/^{24}Mg$ ratio with respect to their $\delta^{26}Mg^*$ anomalies this linear approach can be used to model the $\delta^{26}Mg^*$ evolution over time and retrieve relative age information for each diogenite from this model.

The relative age calculations for diogenite formation are relative straightforward if Earth, the HED parent body and CAIs have the same initial $(^{26}Al/^{27}Al)_0$. In this case the initial $^{26}Al/^{27}Al$ abundance at the onset of diogenite formation is governed by the relative $\delta^{26}Mg^*$ deficit of NWA 1461 and NWA 3329 of -0.0104 $\pm$ 0.0012 and -0.0108 $\pm$ 0.0018‰, respectively, with respect to Earth and can be calculated to be $\sim 1.5 \times 10^{-5}$.

Based on an initial $^{27}Al/^{24}Mg$ ratio of 0.45 that evolves in the magma to a ratio of 2.0 in a linear fashion over time the magma will produce diogenites with anomalies of +0.0128‰, as measured in LEW 88008, after only $\sim$ 0.21 Myr of magmatic evolution (Fig. 5.8). Considering that it is possible that the calculated $^{27}Al/^{24}Mg$ ratios are strongly overestimating the true $^{27}Al/^{24}Mg$ ratio in the parent magma, the same model is shown with an evolving $^{27}Al/^{24}Mg$ ratio in the magma starting from 0.23 and increasing to 1.0. This scenario is considered as very conservative and as expected the $\delta^{26}Mg^*$ evolves slightly slower and a positive anomaly as observed in LEW 88008 is reached after ca. 0.5 Myr of magmatic evolution. However, assuming the remaining magma would crystallize with the final $^{27}Al/^{24}Mg$ ratio and the remaining $^{26}Al/^{27}Al$ abundance in the melt, both scenarios result in $\delta^{26}Mg^*$ anomalies that are 0.202 and 0.092‰, respectively, which are by a factor of 5 and 2 larger than the largest $\delta^{26}Mg^*$ anomalies measured in eucrites thus far (Bizzarro et al., 2005; Schiller et al., 2010a).

The discrepancy of observed and predicted $\delta^{26}Mg^*$ anomalies in eucrites can be explained in several ways. One possibility is that the method

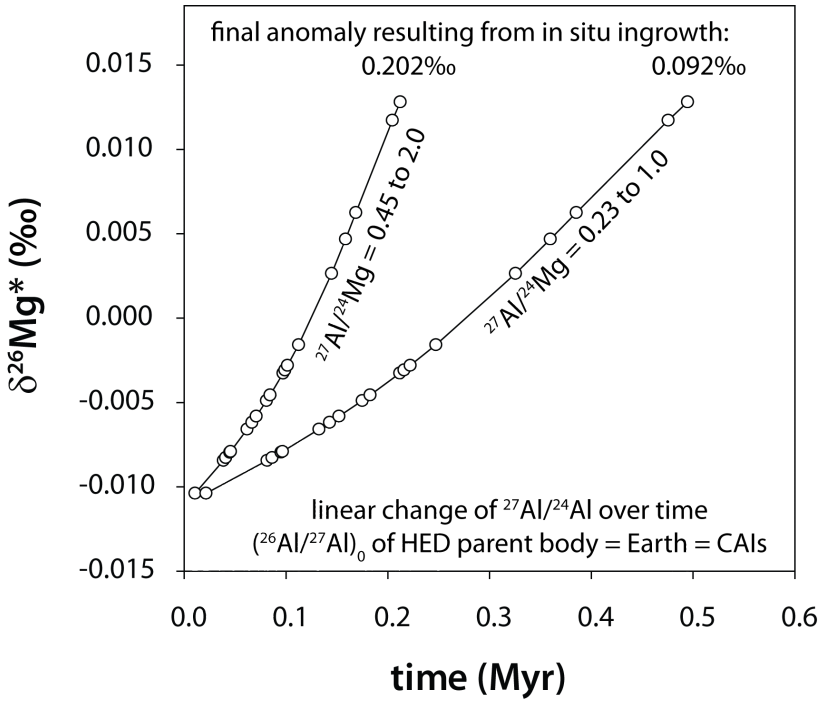

Figure 5.8: Age model for the analysed orthopyroxene-bearing diogenites. The model is based on a homogeneous distribution of $(^{26}Al/^{27}Al)_0$ in the proto-planetary disc and a linear evolution of the $^{27}Al/^{24}Mg$ in the parent magma over time. Two models are shown with $^{27}Al/^{24}Mg$ evolving from 0.45 to 2.0, based on the calculated range of $^{27}Al/^{24}Mg$ in the melt, and from 0.23 to 1.0 to show the effect on the calculated ages in the case that the proxy approach heavily overestimates the $^{27}Al/^{24}Mg$ ratios in the melt.

to calculate the $^{27}Al/^{24}Mg$ ratios if completely flawed even though the calculated $^{27}Al/^{24}Mg$ ratios seem reasonable and are in the range of expected ratios. However, because even halving the initial and final $^{27}Al/^{24}Mg$ ratios is not sufficient it seems unlikely that a radically incorrect assumption of $^{27}Al/^{24}Mg$ ratios is the cause of this discrepancy. Another possibility is that the corresponding eucrite-like basalts that originated from the parent magma of diogenites are not present in the HED suite of meteorites. This is seems also unlikely, as the analysed suite of diogenites suggest that melting on the HED parent body was a widespread, if not global event and thus far none of the analysed eucrites has shown such a large positive $\delta^{26}Mg^*$ anomaly (Srinivasan et al., 1999; Bizzarro et al., 2005; Schiller et al., 2010a). A third and more speculative possibility is that $(^{26}Al/^{27}Al)_0$ of CAIs, Earth and the HED parent body are different, and Earth and HED parent body had a much lower initial abundance (ca. 40%). In such a scenario the HED parent body would also have to have a lower initial abundance relative to Earth in order to still satisfy the requirement to heat and melt the HED parent body, which would be in agreement with the distribution of other neutron-rich isotopes (Trinquier et al., 2007, 2009). This setting allows for a much lower $(^{26}Al/^{27}Al)_0$ in the HED parent body at the time of the formation of NWA 1461 and NWA 3329, which significantly reduces the remaining $\delta^{26}Mg^*$ ingrowth in the remaining magma after production of the range of observed diogenites.

While the possibility of a heterogeneous $(^{26}Al/^{27}Al)_0$ distribution combined with a slight overestimation of the calculated $^{27}Al/^{24}Mg$ ratios of the parent magmas is the best way to reconcile the measured range of $\delta^{26}Mg^*$ in the diogenites, such a heterogeneous distribution remains to be proven and would require a precise, but yet unknown, initial $(^{26}Al/^{27}Al)_0$ abundance of the HED parent body and Earth to calculate precise relative ages for the diogenites.

5.5 Conclusions

A combined Mg isotope and mineral chemistry study of 23 diogenite meteorites from the HED parent body that cover the known range of orthopyroxene and olivine compositions has shown:

1. There is a sinificant variability in δ^{26}Mg* anomalies within these diogenites that range from -0.0108 $\pm$ 0.0018 to +0.0128 $\pm$ 0.0018‰.

2. The δ^{26}Mg* anomalies generally correlate with the mineral major element chemistry, incompatible minor and trace elements and demonstrate active ^{26}Al decay occurred during magmatic differentiation and suggest that diogenites are products of fractional crystallization from a large scale magmatic system.

3. Calculated ^{27}Al/^{24}Mg ratios of the diogenite parent melt are positively correlated with increasing δ^{26}Mg* and suggest an initial degree of melting of 20 to 25% of the HED parent body.

4. Heating and melting of the HED parent body was driven by ^{26}Al decay and led to diogenite formation 0.7 to 1.3 Myr after CAIs depending on whether a heterogeneous or homogeneous ^{26}Al/^{27}Al distribution is assumed between the proto-planetary disk and CAIs. These data provide the first independent and precise age constraints relative to CAIs for diogenites and show that their formation pre-dates the formation of eucrites on the HED by up to 2 Myr and indicate HED parent body accretion and core formation occurred within one half-life of ^{26}Al.

5. The magmatic process could have formed the range of diogenites in just $\sim$ 0.2 Myr after initial diogenite formation, but could have lasted longer ($\sim$ 1 Myr) considering the uncertainties in the model calculations and a potentially lower initial (^{26}Al/^{27}Al)$_0$ for the HED parent body relative to CAIs.

Chapter 6

Conclusions and suggestions for future work

This thesis has presented high-precision Mg isotope data for mineral separates (angrites, NWA 2976), leachates (CM2 chondrite Murchison) and bulk samples (angrites, NWA 2976, eucrites, silicate mesosiderite clasts, most classes of chondrite meteorites, diogenites) of a range of meteoritic material encompassing undifferentiated chondrites through to basaltic and ultramafic achondrites representing the products of silicate planetesimal differentiation in the early Solar System. Several aspects of the ^{26}Al-^{26}Mg chronometer have been studied in detail leading to the following main conclusions:

6.1 ^{26}Al in basaltic achondrites

Chapter 3 verified the presence of small δ^{26}Mg* ($\leq$ 0.050‰) anomalies in four groups of basaltic achondrites (angrites, eucrites, mesosiderites, and the ungrouped NWA 011-NWA 2976) and discussed their meaning. These findings confirmed earlier results by other workers (Bizzarro et al., 2005; Baker et al., 2005) and show that ^{26}Al was extant during the genesis of these asteroidal basalts. Based on an initial canonical Solar System

$(^{26}Al/^{27}Al)_0$ this silicate differentiation must have occurred on the respective parent bodies within 2-5 Myr of CAI formation. However, in detail, mineral isochron data for the angrites D'Orbigny, Sahara 99555 and NWA 2976 reveal subtle discrepancies with ^{26}Al-^{26}Mg model ages hinting at a more complex crystallisation history, evident as resolvable positive intercepts of the mineral isochrons as well as an offset between model and isochron ages of $\sim$ 1 Myr. A simple model was developed to potentially explain this discrepancy, assuming the mineral isochron ages are not partially reset by secondary events. In this model, ^{26}Al-^{26}Mg model ages are shown to potentially record different events depending on whether the asteroidal basalts were produced with basaltic Al/Mg ratios through protracted magma differentiation in a magma ocean or directly by partially melting of the silicate mantle of a planetesimal with chondritic Al/Mg. For samples where thermal resetting of the isochron can be excluded, the positive intercept of the isochron can be used to constrain the time interval of magma ocean evolution by assuming a rate of change of the $^{27}Al/^{24}Mg$ ratio of the parent magma over time. While this model is plausible, the crystallisation ages derived from the angrite and NWA 2976 mineral isochrons appear to have been partially disturbed by resetting of feldspar Mg isotope systematics. In particular, the isochron ages of the angrites are younger than age constraints from other short-lived chronometers.

6.2 High-precision Mg isotope systematics of chondrites

In Chapter 4 high-precision Mg isotope data were presented for a wide range of chondrite meteorites to examine the general distribution of $^{26}Al/^{27}Al$ and Mg isotopes in the early Solar System. The distribution, more explicitly, the homogeneity of $^{26}Al/^{27}Al$ and Mg isotopes in the early Solar System is a critical requirement for using the ^{26}Al-^{26}Mg chronome-

ter to relatively date early Solar System processes. Conversely, if there is isotopic heterogeneity in the early Solar System it is necessary to evaluate its magnitude and establish relative initial $^{26}Al/^{27}Al$ abundances for the various meteorite parent bodies. A step-leaching experiment on the CM2 chondrite Murchison was also conducted to examine the relationship between Mg isotope anomalies in different components of the meteorite and reported anomalies of the neutron-rich isotopes of Ti and Cr for the same meteorite (Trinquier et al., 2007, 2009). Overall, the results show that, within analytical precision, small ^{26}Mg anomalies within the group of carbonaceous chondrites can be primarily explained through the variable presence of CAI-material and that these anomalies correlate with their respective $^{27}Al/^{24}Mg$ ratios. The data also suggests that there was no large scale heterogeneity of ^{26}Al or Mg isotopes on a planetesimal scale in the planet forming region of the proto-planetary disk and shows that the stable Mg isotopic composition of chondrites is indistinguishable from Earth. These data do not, however, make it possible to ascertain if there was a large difference between the CAI and terrestrial planet forming region in the initial $^{26}Al/^{27}Al$ abundance.

6.3 Magma ocean evolution on the HED parent body

Chapter 5 examined variations in the mass-independent ^{26}Mg isotope abundance of diogenites in conjunction with the chemical composition of orthopyroxene and olivine, the main phases present in diogenites. Diogenites are ultramafic rocks with sub-chondritic $^{27}Al/^{24}Mg$ ratios that allow only very minor ^{26}Mg in-growth from ^{26}Al decay after their initial formation and hence record the Mg isotopic composition of their parental magma at the time of their diffusive separation from the parent magma. Diogenites provide a good record of the magmatic history of the HED par-

ent body given that there is a large collection of diogenites spanning a range of pyroxene compositions from Fs = 13.8 to 30.6. The detection of mass-independent abundances of ^{26}Mg (δ^{26}Mg*) within the group of diogenites establishes that diogenites formed while ^{26}Al was decaying and makes it possible to place constraints on the onset of diogenite formation on the HED parent body. This chronological information further establishes a relative chronology between the diogenites and eucrites, showing for the first time that diogenite formation pre-dated eucrite formation. The correlation of δ^{26}Mg* anomalies and major (Fs and Wo content) and trace element (e.g., Ti, Y) concentrations in pyroxene demonstrates that most diogenites formed as cumulates by fractional crystallisation from a common parental melt, which through continued fractional crystallisation potentially evolved to produce basaltic eucrites.

6.4 Suggestions for future work

Based on the findings of this thesis and the analytical improvements that occurred during this study, several aspects of ^{26}Al-^{26}Mg dating in the early Solar System should be investigated or re-examined.

In-depth studies of the diogenite and eucrite δ^{26}Mg* evolution. The Mg isotope study of bulk diogenites made it possible to establish a relative chronology within the diogenite group of meteorites. It would be useful to reexamine the crystallisation history of diogenites and measure orthopyroxene and spinel compositions to determine magma temperatures (e.g., Mukherjee et al., 1990). This integrated approach of chronology and thermometry might allow a better understanding of the thermal evolution of the original diogenite parent magma and perhaps of the whole HED parent body.

Taking advantage of the improvements in sensitivity using the new Thermo Neptune Plus system, which allows an increase in sensitivity by a factor of 10 during Mg isotope analysis as compared to the techniques

used in this study, chromites ($^{27}Al/^{24}Mg > 1$) separated from large diogenite samples could be measured to a similar precision as the whole rock samples of this study. It is likely that these chromites have not been thermally reset during later metamorphism as their original chemical zoning is still preserved (Mukherjee et al., 1990). Such an approach on samples with the largest bulk rock $\delta^{26}Mg^*$ deficits would make it possible to investigate the relationship between the initial $(^{26}Al/^{27}Al)_0$ of the diogenite precursor material and that of Earth, using the intercept of the two-point whole rock and chromite correlation from the diogenites. Additionally, such two-point 'isochrons' could potentially significantly improve the relative age constraints for diogenite formation.

The chronological order of diogenite and eucrite genesis has now been established, however, it is not entirely clear if eucrites and diogenites are products of a common parental magma. Extending the ultra-precise Mg isotope study to the suite of eucrites, for which only few $\delta^{26}Mg^*$ anomalies have been measured so far, could make it possible to decisively establish, or refute a genetic connection between eucrites and diogenites and improve our understanding of the magmatic evolution on the HED parent body.

High-precision ^{26}Al-^{26}Mg study of ureilites. Ureilites are thought to be partial (s)melting residues (Krot et al., 2007) but their formation mechanism(s) is also poorly understood. A combined study of Mg isotopes and mineral chemistry similar to the one presented in Chapter 5 for the group of ureilites, which consists of over 100 meteorites, may help to better understand the timing, chronology and mechanism of ureilite formation. This will be of particular interest if the initial $(^{26}Al/^{27}Al)_0$ abundance of their precursor material could be determined precisely.

Improve age constraints of Pallasite formation. Considering that Baker and Schiller (2010) shows for the first time resolvable $\delta^{26}Mg^*$ deficits in pallasite olivine, the age constraints from Baker and Schiller (2010) could be further improved by analysing corresponding Fe-Ni pallasite

metal, taking advantage of the improved sensitivity that is offered by the Neptune Plus upgrade. Pallasite metal has $^{27}Al/^{24}Mg > 1$-2 that should have produced large positive $\delta^{26}Mg^*$ anomalies that could now potentially be analysed precisely even considering the very low abundance of Mg in Fe-Ni metal.

High-precision ^{26}Al-^{26}Mg mafic mineral isochron of D'Orbigny. Given the high precision Pb-Pb age available for D'Orbigny (Amelin, 2008a), this angrite has been considered a potential common time anchor for both the ^{26}Al-^{26}Mg and the ^{53}Mn-^{53}Cr chronometers (e.g., Spivak-Birndorf et al., 2009). However, the ^{26}Al-^{26}Mg isochron ages are only accurate if the feldspar in this rock, which largely controls the slope of the isochrons reported so far, have not experienced minor and variable resetting. Taking advantage of precision ($\sim 0.0025‰$) available using the Neptune MC-ICP-MS, it should be possible to construct an olivine - pyroxene – bulk rock isochron with a similar or better precision than the reported (feldspar-controlled) isochrons for D'Orbigny and SAH 99555 (see Chapter 3 or Spivak-Birndorf et al., 2009) to test for the validity of these isochrons . Pyroxene and olivine are much less susceptible to Mg diffusion than feldspar and therefore would have experienced less resetting. Hence, an isochron based on ultra-precise analyses of these mineral separates would make it possible to definitively establish whether or not feldpsar-controlled isochrons for these meteorites are (partially) reset and if the initial $(^{26}Al/^{27}Al)_0$ is an appropriate time anchor for the ^{26}Al-^{26}Mg dating system.

High-precision ^{26}Al-^{26}Mg study of CAIs and chondrites. Use of the ^{26}Al-^{26}Mg decay system as a dating tool is based on the implicit but as yet unproven assumption that $(^{26}Al/^{27}Al)_0$ abundances in CAIs are representative of the entire proto-planetary disk. It is thus important to improve our understanding of the initial $(^{26}Al/^{27}Al)_0$ in the proto-planetary disk as compared to CAIs. The new and ultra-precise analytical methods for measuring Mg isotope and $^{27}Al/^{24}Mg$ ratios, as described in Bizzarro et al.

(2010) and applied in Chapter 5, now offer the necessary resolution to be able to resolve differences in the Mg isotopic composition of chondrites and primitive achondrites as well as allowing even small (age related?) differences in internal CAI isochrons to be resolved. Further, the technique now allows precise initial δ^{26}Mg* to be defined from bulk CAI isochrons that record CAI formation within a few kyr of each other. A precise knowledge of the initial δ^{26}Mg* with respect to Earth and chondrites could allow resolution of the potential $(^{26}Al/^{27}Al)_0$ heterogeneity between CAIs and the proto-planetary disk.

References

Albarede, F., Beard, B., 2004. Analytical Methods for Non-Traditional Isotopes. Reviews in Mineralogy and Geochemistry 55, 113–152.

Amelin, Y., 2008a. U-Pb ages of angrites. Geochimica et Cosmochimica Acta 72, 221–232.

Amelin, Y., 2008b. The U-Pb systematics of angrite Sahara 99555. Geochimica et Cosmochimica Acta 72, 4874–4885.

Amelin, Y., Irving, A. J., 2007. Seven million years of evolution on the angrite parent body from Pb-isotopic data. Workshop on Chronology of Meteorites, 4061.pdf.

Amelin, Y., Krot, A., 2007. Pb isotopic age of the Allende chondrules. Meteoritics and Planetary Science 42, 1321–1335.

Amelin, Y., Krot, A. N., Hutcheon, I. D., Ulyanov, A. A., 2002. Lead isotopic ages of chondrules and calcium-aluminum-rich inclusions. Science 297, 1678–1683.

Amelin, Y., Wadhwa, M., Lugmair, G., 2006. Pb-isotopic dating of meteorites using ^{202}Pb-^{205}Pb double-spike: comparison with other high-resolution chronometers. Lunar and Planetary Science Conference Abstracts 37, 1970.pdf.

Anders, E., Grevesse, N., 1989. Abundances of the elements: Meteoritic and solar. Geochimica et Cosmochimica Acta 53, 197–214.

Andrews, K. T., 2009. Seaching for a supernova trigger for Solar System formation using high precision nickel isotope measurements of Fe-Ni metal in meteorites. Master's thesis, Victoria University of Wellington.

Baker, J., Bizzarro, M., Wittig, N., Connelly, J., Haack, H., 2005. Early planetesimal melting from an age of 4.5662 Gyr for differentiated meteorites. Nature 436, 1127–1131.

Baker, J. A., Schiller, M., 2010. ^{26}Mg deficit dating ultramafic meteorites and silicate planetesimal differentiation in the early Solar System. Earth and Planetary Science Letters, in review.

Barrat, J., Blichert-Toft, J., Gillet, P., Keller, F., 2000. The differentiation of eucrites: the role of in situ crystallization. Meteoritics and Planetary Science 35, 1087–1100.

Barrat, J. A., Gillet, P., Lesourd, M., Blichert-Toft, J., Poupeau, G. R., 1999. The Tatahouine diogenite: Mineralogical and chemical effects of sixty-three years of terrestrial residence. Meteoritics and Planetary Science 34, 91–97.

Barrat, J. A., Yamaguchi, A., Greenwood, R. C., Benoit, M., Cotten, J., Bohn, M., Franchi, I. A., 2008. Geochemistry of diogenites: Still more diversity in their parental melts. Meteoritics and Planetary Science 43, 1759–1775.

Beattie, P. B., Ford, C. B., Russell, D. C., 1991. Partition coefficients for olivine-melt and orthopyroxene-melt systems. Contributions to Mineralogy and Petrology 109, 212–224.

Bèdard, J., 2007. Trace element partitioning coefficients between silicate melts and orthopyroxene: Parameterizations of D variations. Chemical Geology 244, 263–303.

Benedix, G., McCoy, T., Keil, K., Love, S., 2000. A petrologic study of the IAB iron meteorites: Constraints on the formation of the IAB-winonaite parent body. Meteoritics and Planetary Science 35, 1127–1142.

Binzel, R. P., Xu, S., 1993. Chips off of Asteroid 4 Vesta: Evidence for the Parent Body of Basaltic Achondrite Meteorites. Science 260, 186–191.

Bizzarro, M., Baker, J., Haack, H., Lundgaard, K., 2005. Rapid timescales for accretion and melting of differentiated planetesimals inferred from ^{26}Al-^{26}Mg chronometry. The Astrophysical Journal 632, L42 – L44.

Bizzarro, M., Baker, J. A., Haack, H., 2004. Mg isotope evidence for contemporaneous formation of chondrules and refractory inclusions. Nature 431, 275–278.

Bizzarro, M., Larsen, K., Patton, C., Ulfbeck, D., Trinquier, A., Schiller, M., 2010. High precision Mg isotope and Al/Mg ratio measurements, in preparation.

Bizzarro, M., Ulfbeck, D., Trinquier, A., Thrane, K., Connelly, J. N., Meyer, B. S., 2007. Evidence for a late supernova injection of Fe-60 into the protoplanetary disk. Science 316, 1178–1181.

Bogdanovski, O., Lugmair, G. W., 2004. Manganese-chromium isotope systematics of basaltic achondrite Northwest Africa 011. Lunar and Planetary Science Conference Abstracts 35, 1715.pdf.

Boss, A. P., 1990. Origin of the Earth. Oxford Univ. Press, Ch. 3D solar nebula models: implications for Earth origin, pp. 3–15.

Boss, A. P., Keiser, S. A., Ipatov, S. I., Myhill, E. A., Vanhala, H. A. T., 2010. Triggering collapse of the presolar dense cloud core and injecting short-lived radioisotopes with a shock wave. I. Varied shock speeds. The Astrophysical Journal 708, 1268–1280.

Brazzle, R. H., Pravdivtseva, O. V., Meshik, A. P., Hohenberg, C. M., 1999. Verification and interpretation of the I-Xe chronometer. Geochimica et Cosmochimica Acta 63, 739–760.

Brearley, A., Jones, R., 1998. Chondritic meteorites. Reviews in Mineralogy and Geochemistry 36, XV–XVI.

Brennecka, G., Wadhwa, M., Janney, P., Anbar, A., 2010a. Towards reconciling early Solar System chronometers: The $^{238}U/^{235}U$ ratios of chondrites and D'Orbigny pyroxenes. Lunar and Planetary Science Conference Abstracts 41, 2117.pdf.

Brennecka, G., Weyer, S., Wadhwa, M., Janney, P., Zipfel, J., Anbar, A., 2010b. $^{238}U/^{235}U$ variations in meteorites: Extant ^{247}Cm and implications for Pb-Pb dating. Science 327, 449.

Burbidge, E., Burbidge, G., Fowler, W., Hoyle, F., 1957. Synthesis of the elements in stars. Reviews of Modern Physics 29, 547 – 650.

Burkhardt, C., Kleine, T., Bourdon, B., Palme, H., Zipfel, J., Friedrich, J. M., Ebel, D. S., 2008. Hf-W mineral isochron for Ca,Al-rich inclusions: Age of the solar system and the timing of core formation in planetesimals. Geochimica et Cosmochimica Acta 72, 6177 – 6197.

Cameron, A. G. W., 1978. Physics of the primitive solar accretion disk. Moon and Planets 18, 5–40.

Cameron, A. G. W., Truran, J. W., 1977. The supernova trigger for formation of the solar system. Icarus 30, 447–461.

Cassen, P., 2001. Nebular thermal evolution and the properties of primitive planetary materials. Meteoritics and Planetary Science 36, 671–700.

Castillo-Rogez, J., Johnson, T. V., Lee, M. H., Turner, N. J., Matson, D. L., Lunine, J., 2009. ^{26}Al decay: Heat production and a revised age for Iapetus. Icarus 204, 658 – 662.

Catanzaro, E. J., Murphy, T. J., Garner, E. L., Shields, W. R., 1966. Absolute isotopic abundance ratios and atomic weights of magnesium. Journal of Research at the National Bureau of Standards 70a, 456–458.

Chambers, J., 2007. Planet formation. In: Holland, H. D., Turekian, K. K. (Eds.), Treatise on Geochemistry. Pergamon, Oxford, pp. 1 – 17.

Chaussidon, M., Robert, F., McKeegan, K. D., 2006. Li and B isotopic variations in an Allende CAI: Evidence for the in situ decay of short-lived ^{10}Be and for the possible presence of the short-lived nuclide ^{7}Be in the early solar system. Geochimica et Cosmochimica Acta 70, 224 – 245.

Chen, J., Wasserburg, G., 1990. The isotopic composition of Ag in meteorites and the presence of ^{107}Pd in protoplanets. Geochimica et Cosmochimica Acta 54, 1729–1743.

Clayton, R., 2003. Oxygen Isotopes in Meteorites. In: Holland, H. D., Turekian, K. K. (Eds.), Treatise on Geochemistry. Pergamon, Oxford, pp. 129–142.

Clayton, R. N., 1993. Oxygen isotopes in meteorites. Annual Review of Earth and Planetary Sciences 21, 115–149.

Clayton, R. N., Hinton, R. W., Davis, A. M., 1988. Isotopic Variations in the Rock-forming Elements in Meteorites. Philosophical Transactions of the Royal Society of London. Series A. Physical Sciences and Engineering 325, 483–501.

Clayton, R. N., Mayeda, T. K., 1996. Oxygen isotope studies of achondrites. Geochimica et Cosmochimica Acta 60 (11), 1999–2017.

Colgan, S. W. J., Haas, M. R., Erickson, E. F., Lord, S. D., Hollenbach, D. J., 1994. Day 640 infrared line and continuum measurements: Dust formation in SN 1987A. The Astrophysical Journal 427, 874–888.

Connelly, J. N., Amelin, Y., Krot, A. N., Bizzarro, M., 2008a. Chronology of the solar system's oldest solids. The Astrophysical Journal Letters 675, L121–L124.

Connelly, J., Bizzarro, M., Thrane, K., Baker, J., 2008b. The Pb-Pb age of angrite SAH99555 revisited. Geochimica et Cosmochimica Acta 72, 4813–4824.

Connolly, H., Jones, B., Hewins, R., 1998. The flash melting of chondrules: An experimental investigation into melting history and physical nature of chondrule precursors. Geochimica et Cosmochimica Acta 62, 2725–2735.

Cook, D. L., Wadhwa, M., Janney, P. E., Dauphas, N., Clayton, R. N., Davis, A. M., 2006. High precision measurements of non-mass-dependent effects in nickel isotopes in meteoritic metal via multicollector ICPMS. Analytical Chemistry 78, 8477–8484.

Dauphas, N., Cook, D. L., Sacarabany, A., Frohlich, C., Davis, A. M., Wadhwa, M., Pourmand, A., Rauscher, T., Gallino, R., 2008. Iron 60 evidence for early injection and efficient mixing of stellar debris in the protosolar nebula. The Astrophysical Journal 686, 560–569.

Dauphas, N., Foley, C., Wadhwa, M., Davis, A., Janney, P., Qin, L., Göpel, C., Birck, J., 2005. Protracted Core Differentiation in Asteroids from ^{182}Hf-^{182}W Systematics in the Eagle Station Pallasite. Lunar and Planetary Science Conference Abstracts 36, 1100.

Desch, S. J., Connolly, H. C., Srinivasan, G., 2004. An interstellar origin for the beryllium 10 in calcium-rich, aluminium-rich inclusions. The Astrophysical Journal 602, 528–642.

Drake, M. J., 2001. The eucrite/Vesta story. Meteoritics and Planetary Science 36, 501–513.

Eugster, O., 2003. Cosmic-ray exposure ages of meteorites and lunar rocks and their significance. Chemie der Erde - Geochemistry 63, 3–30.

Feigelson, E., Broos, P., Gaffney III, J., Garmire, G., Hillenbrand, L., Pravdo, S., Townsley, L., Tsuboi, Y., 2002a. X-ray-emitting young stars in the Orion nebula. The Astrophysical Journal 574, 258–292.

Feigelson, E., Garmire, G., Pravdo, S., 2002b. Magnetic flaring in the pre-main-sequence Sun and implications for the early solar system. The Astrophysical Journal 572, 335–349.

Gaidos, E., Krot, A. N., Williams, J. P., Raymond, S. N., 2009. ^{26}Al and the formation of the Solar System from a molecular cloud contaminated by Wolf-Rayet winds. The Astrophysical Journal 696, 1854–1863.

Galer, S. J. G., Lugmair, G. W., 1996. Lead isotope systematics of noncumulate eucrites. Meteoritics and Planetary Science 31, A47.

Galy, A., Belshaw, N. S., Halicz, L., O'Nions, R. K., 2001. High-precision measurement of magnesium isotopes by multiple-collector inductively coupled plasma mass spectrometry. International Journal of Mass Spectrometry 208, 89–98.

Galy, A., Yoffe, O., Janney, P. E., Williams, R. W., Cloquet, C., Alard, O., Halicz, L., Wadhwa, M., Hutcheon, I. D., Ramon, E., Carignan, J., 2003. Magnesium isotope heterogeneity of the isotopic standard SRM980 and new reference materials for magnesium-isotope-ratio measurements. Journal of Analytical Atomic Spectrometry 18, 1352–1356.

GeoRem, 2010.
URL http://georem.mpch-mainz.gwdg.de/

Glavin, D., Kubny, A., Jagoutz, E., Lugmair, G., 2004. Mn-Cr isotope systematics of the D'Orbigny angrite. Meteoritics and Planetary Science 39, 693–700.

Goodrich, C., Scott, E., Fioretti, A., 2004. Ureilitic breccias: clues to the petrologic structure and impact disruption of the ureilite parent asteroid. Chemie der Erde-Geochemistry 64 (4), 283–327.

Gounelle, M., Meibom, A., 2007. The Oxygen Isotopic Composition of the Sun as a Test of the Supernova Origin of ^{26}Al and ^{41}Ca. The Astrophysical Journal Letters 664, L123–L125.

Gounelle, M., Meibom, A., 2008. The origin of short-lived radionuclides and the astrophysical environment of solar system formation. The Astrophysical Journal 680, 781–792.

Gounelle, M., Meibom, A., Hennebelle, P., Inutsuka, S., 2009. Supernova propagation and cloud enrichment: A new model for the origin of Fe-60 in the early Solar System. The Astrophysical Journal Letters 694, L1–L5.

Gounelle, M., Shu, F., Shang, H., Glassgold, A., Rehm, K., Lee, T., 2001. Extinct radioactivities and protosolar cosmic rays: Self-shielding and light elements. The Astrophysical Journal 548, 1051–1070.

Greenwood, R. C., Franchi, I. A., Jambon, A., Barrat, J. A., Burbine, T. H., 2006. Oxygen isotope variation in stony-iron meteorites. Science 313, 1763–1765.

Greenwood, R. C., Franchi, I. A., Jambon, A., Buchanan, P. C., 2005. Widespread magma oceans on asteroidal bodies in the early Solar System. Nature 435, 916–918.

Guan, Y., McKeegan, K., MacPherson, G., 2000. Oxygen isotopes in calcium-aluminum-rich inclusions from enstatite chondrites: New evidence for a single CAI source in the solar nebula. Earth and Planetary Science Letters 181, 271–277.

Haack, H., McCoy, T., 2007. Iron and Stony-Iron Meteorites. In: Holland, H. D., Turekian, K. K. (Eds.), Treatise on Geochemistry. Pergamon, Oxford, pp. 1 – 22.

Haack, H., Scott, E., Rasmussen, K., 1996. Thermal and shock history of mesosiderites and their large parent asteroid. Geochimica et Cosmochimica Acta 60, 2609–2619.

Halliday, A., 2003. The Origin and Earliest History of the Earth. In: Holland, H. D., Turekian, K. K. (Eds.), Treatise on Geochemistry. Pergamon, Oxford, pp. 509 – 557.

Halliday, A. N., Porcelli, D., 2001. In search of lost planets - the paleocosmochemistry of the inner solar system. Earth and Planetary Science Letters 192, 545–559.

Handler, M. R., Baker, J. A., Schiller, M., Bennett, V. C., Yaxley, G. M., 2009. Magnesium stable isotopic composition of the Earth's upper mantle. Earth and Planetary Science Letters 282, 306–313.

Hartmann, L., 2000. Observational constraints on transport (and mixing) in pre-main sequence disks. Space Science Reviews 92, 55–68.

Hartmann, L., Ballesteros-Paredes, J., Bergin, E. A., 2001. Rapid formation of molecular clouds and stars in the solar neighborhood. The Astrophysical Journal 562, 852–868.

Hartmann, L., Burkert, A., 2007. On the structure of the Orion A Cloud and the formation of the Orion Nebula Cluster. The Astrophysical Journal 654, 988–997.

Hayashi, C., Nakazawa, K., Mizuno, H., 1979. Earth's melting due to the blanketing effect of the primordial dense atmosphere. Earth and Planetary Science Letters 43, 22–28.

Hellstrom, J., Paton, C., Woodhead, J., Hergt, J., 2008. Iolite: software for spatially resolved LA-(quad and MC) ICPMS analysis. In: Sylvester, P. (Ed.), Laser Ablation ICPMS in the Earth Sciences: Current Practices and Outstanding Issues. Vol. 40 of Mineralogical Association of Canada Short Course series. pp. 343–348.

Hennebelle, P., Mac Low, M., Vazquez-Semadeni, E., 2007. Diffuse interstellar medium and the formation of molecular clouds. ArXiv e-prints.

Herzog, G. F., 2003. Treatise on Geochemistry. In: Davis, A. W. (Ed.), Treatise on Geochemistry. Vol. 1. Oxford: Elsevier-Pergamon, Ch. 13, pp. 347–380.

Hevey, P. J., Sanders, I. S., 2006. A model for planetesimal meltdown by ^{26}Al and its implications for meteorite parent bodies. Meteoritics and Planetary Science 41, 95–106.

Hewins, R. H., Connolly, Jr., H. C., 1996. Peak temperatures of flash-melted chondrules. In: Chondrules and the Protoplanetary Disk. pp. 197–204.

Horwitz, E. P., McAlister, D. R., Bond, A. H., Barrans, R. E., 2005. Novel extraction of chromatographic resins based on tetraalkyldiglycolamides: Characterization and potential applications. Solvent Extraction and Ion Exchange 23, 319–344.

Hsu, W., Crozaz, G., 1997. Mineral chemistry and the petrogenesis of eucrites: II. Cumulate eucrites. Geochimica et Cosmochimica Acta 61, 1293–1302.

Hsu, W., Guan, Y., Leshin, L., Ushikubo, T., Wasserburg, G., 2006. A late episode of irradiation in the early solar system: Evidence from extinct ^{36}Cl and ^{26}Al in meteorites. The Astrophysical Journal 640, 525–529.

Hudson, G., Kennedy, B., Podosek, F., Hohenberg, C., 1989. The early solar system abundance of ^{244}Pu as inferred from the St. Severin chondrite. Lunar and Planetary Science Conference Proceedings 19, 547–557.

Ireland, T., Fegley, B., 2000. The Solar System's earliest chemistry: Systematics of refractory inclusions. International Geology Review 42, 865–894.

Jacobsen, B., Yin, Q.-Z., Moynier, F., Amelin, Y., Krot, A. N., Nagashima, K., Hutcheon, I. D., Palme, H., 2008. ^{26}Al-^{26}Mg and ^{207}Pb-^{206}Pb systematics of Allende CAIs: Canonical solar initial ^{26}Al/^{27}Al ratio reinstated. Earth and Planetary Science Letters 272, 353–364.

Jarosewich, E., Nelen, J., Norberg, J., 1980. Reference samples for electron microprobe analysis. Geostandard Newsletter 4, 43 – 47.

Jeffery, P. M., Reynolds, J. H., 1961. Origin of excess Xe129 in stone meteorites. Journal of Geophysical Research 66, 3582 pp.

Jochum, K., Willbold, M., Raczek, I., Stoll, B., Herwig, K., 2005. Chemical characterisation of the USGS reference glasses GSA-1G, GSC-1G, GSD-1G, GSE-1G, BCR-2G, BHVO-2G and BIR-1G using EPMA, ID-TIMS, ID-ICP-MS and LA-ICP-MS. Geostandards Geoanalytical Research 29, 285–302.

Keil, K., 1968. Mineralogical and chemical relationships among enstatite chondrites. Journal of Geophysical Research 73, 6945–6976.

Keil, K., Ntaflos, T., Taylor, G., Brearley, A., Newsom, H., Romig Jr, A., 1989. The Shallowater aubrite - Evidence for origin by planetesimal impacts. Geochimica et Cosmochimica Acta 53, 3291–3307.

Keil, K., Stoeffler, D., Love, S., Scott, E., 1997. Constraints on the role of impact heating and melting in asteroids. Meteoritics 32, 349–363.

Kimura, M., Goresy, A. E., Palme, H., Zinner, E., 1993. Ca-, Al-rich inclusions in the unique chondrite ALH85085: Petrology, chemistry and isotopic compositions. Geochimica et Cosmochimica Acta 57, 2329 – 2359.

Kiriishi, M., Tomeoka, K., 2008. Northwest Africa 1232 - A CO3 carbonaceous chondrite with two lithologies. Journal of Mineralogical and Petrological Sciences 103, 161–165.

Kita, N. T., Nagahara, H., Togashi, S., Morshita, Y., 2000. A short duration of chondrule formation in the solar nebula: Evidence from Al-26 in Semarkona ferromagnesian chondrules. Geochimica et Cosmochimica Acta 64, 3913–3922.

Kleine, T., Mezger, K., Münker, C., Palme, H., Bischoff, A., 2004. Hf-182-W-182 isotope systematics of chondrites, eucrites, and martian meteorites: Chronology of core formation and early mantle differentiation in Vesta and Mars. Geochimica et Cosmochimica Acta 68, 2935–2946.

Kleine, T., Mezger, K., Palme, H., Scherer, E., Münker, C., 2005a. Early core formation in asteroids and late accretion of chondrite parent bodies: Evidence from Hf-182-W-182 in CAIs, metal-rich chondrites, and iron meteorites. Geochimica et Cosmochimica Acta 69, 5805–5818.

Kleine, T., Mezger, K., Palme, H., Scherer, E., Münker, C., 2005b. The W isotope composition of eucrite metals: constraints on the timing and cause of the thermal metamorphism of basaltic eucrites. Earth and Planetary Science Letters 231, 41–52.

Kleine, T., Münker, C., Mezger, K., Palme, H., 2002. Rapid accretion and early core formation on asteroids and the terrestrial planets from Hf–W chronometry. Nature 418, 952–955.

Kleine, T., Touboul, M., Bourdon, B., Mezger, K., Palme, H., Nimmo, F., Jacobsen, S. B., Yin, Q. Z., 2007. ^{182}Hf-^{182}W chronometry and the origin and evolution of planetary bodies. In: Chronology of Meteorites and the Early Solar System. pp. 94–95.

Komatsu, M., Krot, A. N., Petaev, M. I., Ulyanov, A. A., Keil, K., Miyamoto, M., 2001. Mineralogy and petrography of amoeboid olivine aggregates from the reduced CV3 chondrites Efremovka, Leoville and Vigarano: Products of nebular condensation, accretion and annealing. Meteoritics and Planetary Science 36, 629–641.

Krot, A., Amelin, Y., Cassen, P., Meibom, A., 2005. Young chondrules in CB chondrites from a giant impact in the early Solar System. Nature 436, 989–992.

Krot, A., Keil, K., Scott, E., Goodrich, C., Weisberg, M., 2007. Classification of meteorites. In: Holland, H. D., Turekian, K. K. (Eds.), Treatise on Geochemistry. Pergamon, Oxford, pp. 1 – 52.

Krot, A. N., Meibom, A., Weisberg, M. K., Keil, K., 2002. The CR chondrite clan: implications for early solar system processes. Meteoritics and Planetary Science 37, 1451–1490.

Lada, C., Lada, E., 2003. Embedded clusters in molecular clouds. Annual Review of Astronomy and Astrophysics 41, 57–115.

Larimer, J. W., 1995. Core Formation in Asteroid-sized Bodies. Meteoritics 30, 533.

LaTourrette, T., Wasserburg, G. J., 1998. Mg diffusion in anorthite: implications for the formation of early solar system planetesimals. Earth and Planetary Science Letters 158, 91–108.

Lattimer, J. M., Schramm, D. N., Grossman, L., 1978. Condensation in supernova ejecta and isotopic anomalies in meteorites. The Astrophysical Journal 219, 230–249.

Lee, T., Papanastassiou, D. A., Wasserburg, G. J., 1976. Demonstration of Mg-26 excess in Allende and evidence for Al-26. Geophysical Research Letters 3, 41–44.

Lee, T., Papanastassiou, D. A., Wasserburg, G. J., 1977. Al-26 in the early Solar-System - fossil or fuel. The Astrophysical Journal 211, L107–L110.

Lee, T., Shu, F., Shang, H., Glassgold, A., Rehm, K., 1998. Protostellar cosmic rays and extinct radioactivities in meteorites. The Astrophysical Journal 506, 898–912.

Leya, I., Wieler, R., Halliday, A., 2003. The influence of cosmic-ray production on extinct nuclide systems. Geochimica et Cosmochimica Acta 67, 529–541.

Lin, Y., Guan, Y., Leshin, L. A., Ouyang, Z., Wang, D., 2005. Short-lived chlorine-36 in a Ca- and Al-rich inclusion from the Ningqiang carbonaceous chondrite. Proceedings of the National Academy of Sciences of the United States of America 102, 1306–1311.

Lissauer, J., 1987. Timescales for planetary accretion and the structure of the protoplanetary disk. Icarus 69, 249–265.

Liu, M.-C., McKeegan, K. D., Goswami, J. N., Marhas, K. K., Sahijpal, S., Ireland, T. R., Davis, A. M., 2009. Isotopic records in CM hibonites: Implications for timescales of mixing of isotope reservoirs in the solar nebula. Geochimica et Cosmochimica Acta 73, 5051 – 5079.

Lofgren, G. E., 1996. A dynamic crystallization model for chondrule melts. In: Chondrules and the Protoplanetary Disk. pp. 187–196.

Ludwig, K. R., 2003. Isoplot 3.00. A geochronological toolkit for Microsoft Excel. Berkeley Geochronology Center Special Publication, pp. 74.

Lugmair, G., Shimamura, T., Lewis, R., Anders, E., 1983. Samarium-146 in the early solar system: Evidence from neodymium in the Allende meteorite. Science 222, 1015–1018.

Lugmair, G. W., Galer, S. J. G., 1992. Age and isotopic relationships among the angrites Lewis Cliff 86010 and Angra dos Reis. Geochimica et Cosmochimica Acta 56, 1673–1694.

Lugmair, G. W., Shukolyukov, A., 1998. Early solar system timescales according to Mn-53-Cr-53 systematics. Geochimica et Cosmochimica Acta 62, 2863–2886.

Lugmair, G. W., Shukolyukov, A., 2001. Early solar system events and timescales. Meteoritics and Planetary Science 36, 1017–1026.

MacPherson, G., 2007. Calcium-aluminum-rich inclusions in chondritic meteorites. In: Holland, H. D., Turekian, K. K. (Eds.), Treatise on Geochemistry. Pergamon, Oxford, pp. 1 – 47.

MacPherson, G. J., Davis, A. M., Zinner, E. K., 1995. The distribution of Al-26 in the early Solar-System - A Reappraisal. Meteoritics 30, 365–386.

Manhes, G., Allegre, C. J., Provost, A., 1984. U-Th-Pb systematics of the eucrite Juvinas - precise age-determination and evidence for exotic lead. Geochimica et Cosmochimica Acta 48, 2247–2264.

Markowski, A., Leya, I., Quittè, G., Ammon, K., Halliday, A. N., Wieler, R., 2006a. Correlated helium-3 and tungsten isotopes in iron meteorites: Quantitative cosmogenic corrections and planetesimal formation times. Earth and Planetary Science Letters 250, 104–115.

Markowski, A., Quitte, G., Halliday, A. N., Kleine, T., 2006b. Tungsten isotopic compositions of iron meteorites: Chronological constraints vs. cosmogenic effects. Earth and Planetary Science Letters 242, 1–15.

Markowski, A., Quittè, G., Kleine, T., Halliday, A. N., Bizzarro, M., Irving, A. J., 2007. Hafnium-tungsten chronometry of angrites and the earliest evolution of planetary objects. Earth and Planetary Science Letters 262, 214–229.

Marsh, C., Della-Giustina, D., Giacalone, J., Lauretta, D., 2006. Experimental tests of the induction heating hypothesis for planetesimals. Lunar and Planetary Science Conference Abstracts 37, 2078.pdf.

McCaughrean, M. J., O'Dell, C. R., 1996. Direct imaging of circumstellar disks in the Orion Nebula. The Astronomical Journal 111, 1977–1986.

McCoy, T., Keil, K., Clayton, R., Mayeda, T., Bogard, D., Garrison, D., Huss, G., Hutcheon, I., Wieler, R., 1996. A petrologic, chemical, and

isotopic study of Monument Draw and comparison with other acapulcoites: Evidence for formation by incipient partial melting. Geochimica et Cosmochimica Acta 60, 2681–2708.

McCoy, T., Keil, K., Muenow, D., Wilson, L., 1997. Partial melting and melt migration in the acapulcoite-lodranite parent body. Geochimica et Cosmochimica Acta 61, 639–650.

McKeegan, K., Davis, A., 2007. Early solar system chronology. In: Holland, H. D., Turekian, K. K. (Eds.), Treatise on Geochemistry. Pergamon, Oxford, pp. 1–38.

McKeegan, K. D., Chaussidon, M., Robert, F., 2000. Incorporation of short–lived ^{10}Be in a calcium–aluminium–rich inclusion from the Allende meteorite. Science 289, 1334–1337.

Mendybaev, R., Beckett, J., Grossman, L., Stolper, E., Cooper, R., Bradley, J., 2002. Volatilization kinetics of silicon carbide in reducing gases: An experimental study with applications to the survival of presolar grains in the solar nebula. Geochimica et Cosmochimica Acta 66, 661–682.

Mittlefehldt, D., Bogard, D., Berkley, J., Garrison, D., 2003. Brachinites: Igneous rocks from a differentiated asteroid. Meteoritics and Planetary Science 38, 1601–1625.

Mittlefehldt, D., Lindstrom, M., 1991. Generation of abnormal trace element abundances in Antarctic eucrites by weathering processes. Geochimica et Cosmochimica Acta 55, 77–87.

Mittlefehldt, D., McCoy, T., Goodrich, C., Kracher, A., 1998. Nonchondritic meteorites from asteroidal bodies. Reviews in Mineralogy and Geochemistry 36, 4–1.

Mittlefehldt, D. W., 2002. Geochemistry of the ungrouped carbonaceous chondrite Tagish Lake, the anomalous CM chondrite Bells, and compar-

ison with CI and CM chondrites. Meteoritics and Planetary Science 37, 703–712.

Mittlefehldt, D. W., 2007. Treatise on Geochemistry. Vol. 1. Oxford: Elsevier-Pergamon, Ch. 11, pp. 291–324.

Mittlefehldt, D. W., Killgore, M., Lee, M. T., 2002. Petrology and geochemistry of D'Orbigny, geochemistry of Sahara 99555, and the origin of angrites. Meteoritics and Planetary Science 37, 345–369.

Mittlefehldt, D. W., Lindstrom, M. M., 2003. Geochemistry of eucrites: genesis of basaltic eucrites, and Hf and Ta as petrogenetic indicators for altered antarctic eucrites. Geochimica et Cosmochimica Acta 67, 1911–1934.

Mostefaoui, S., Kita, N. T., Togashi, S., Tachibana, S., Nagahara, H., Morishita, Y., 2002. The relative formation ages of ferromagnesian chondrules inferred from their initial aluminum-26/aluminum-27 ratios. Meteoritics and Planetary Science 37, 421–438.

Mostefaoui, S., Lugmair, G., Hoppe, P., 2005. ^{60}Fe: A heat source for planetary differentiation from a nearby supernova explosion. The Astrophysical Journal 625, 271–277.

Mostefaoui, S., Lugmair, G., Hoppe, P., El Goresy, A., 2004. Evidence for live ^{60}Fe in meteorites. New Astronomy Reviews 48, 155–159.

Mukherjee, A. B., Bulatov, V., Kotelnikov, A., 1990. New high P-T experimental results on orthopyroxene-chrome spinel equilibrium and a revised orthopyroxene-spinel cosmothermometer. In: V. L. Sharpton & G. Ryder (Ed.), Lunar and Planetary Science Conference Proceedings. Vol. 20. pp. 299–308.

National Nuclear Data Center, B. N. L., 2010.
URL http://www.nndc.bnl.gov

Nehru, C., Prinz, M., Weisberg, M., Ebihara, M., Clayton, R., Mayeda, T., 1992. Brachinites: A new primitive achondrite group. Meteoritics 27, 267.

Nehru, C., Prinz, M., Weisberg, M., Ebihara, M., Clayton, R., Mayeda, T., 1996. A new brachinite and petrogenesis of the group. Lunar and Planetary Science Conference Abstracts 27, 1472.pdf.

Nelson, A., Benz, W., Adams, F., Arnett, D., 1998. Dynamics of circumstellar disks. The Astrophysical Journal 502, 342–371.

Nelson, A., Benz, W., Ruzmaikina, T., 2000. Dynamics of circumstellar disks. II. Heating and cooling. The Astrophysical Journal 529, 357–390.

Nielsen, S., Rehkämper, M., Halliday, A., 2006. Large thallium isotopic variations in iron meteorites and evidence for lead-205 in the early solar system. Geochimica et Cosmochimica Acta 70, 2643–2657.

Nishiizumi, K., 2004. Preparation of ^{26}Al AMS standards. Nuclear Instruments and Methods in Physics Research Section B: Beam Interactions with Materials and Atoms 223-224, 388–392.

Nyquist, L. E., Reese, Y., Wiesmann, H., Shih, C. Y., Takeda, H., 2003. Fossil Al-26 and Mn-53 in the Asuka 881394 eucrite: evidence of the earliest crust on asteroid 4 Vesta. Earth and Planetary Science Letters 214, 11–25.

Ouellette, N., Desch, S., Bizzarro, M., Boss, A., Ciesla, F., Meyer, B., 2009. Injection mechanisms of short-lived radionuclides and their homogenization. Geochimica et Cosmochimica Acta 73, 4946 – 4962.

Ouellette, N., Desch, S., Hester, J., 2010. Injection of supernova dust in nearby protoplanetary disks. The Astrophysical Journal 711, 597–612.

Ouellette, N., Desch, S. J., Hester, J. J., 2007. Interaction of supernova ejecta with nearby protoplanetary disks. The Astrophysical Journal 662, 1268–1281.

Palme, H., Jones, A., 2003. Solar system abundances of the elements. In: Holland, H. D., Turekian, K. K. (Eds.), Treatise on Geochemistry. Pergamon, Oxford, pp. 41–61.

Palme, H., O'Neill, H., 2007. Cosmochemical estimates of mantle composition. In: Holland, H. D., Turekian, K. K. (Eds.), Treatise on Geochemistry. Pergamon, Oxford, pp. 1–38.

Podosek, F. A., Cassen, P., 1994. Theoretical, observational, and isotopic estimates of the lifetime of the solar nebula. Meteoritics 29, 6–25.

Quittè, G., Oberli, F., 2006. Quantitative extraction and high precision isotope measurements of nickel by MC-ICPMS. Journal of Analytical Atomic Spectrometry 21, 1249–1255.

Regelous, M., Elliott, T., Coath, C., 2008. Nickel isotope heterogeneity in the early Solar System. Earth and Planetary Science Letters 272, 330–338.

Righter, K., Drake, M. J., 1997. A magma ocean on Vesta: Core formation and petrogenesis of eucrites and diogenites. Meteoritics and Planetary Science 32, 929–944.

Rotaru, M., Birck, J. L., Allègre, C. J., 1992. Clues to early solar-system history from chromium isotopes in carbonaceous chondrites. Nature 358, 465–470.

Rubin, A., 1989. Size-frequency distributions of chondrules in CO3 chondrites. Meteoritics 24, 179–189.

Rugel, G., Faestermann, T., Knie, K., Korschinek, G., Poutivtsev, M., Schumann, D., Kivel, N., Gunther-Leopold, I., Weinreich, R., Wohlmuther,

M., 2009. New Measurement of the Fe-60 Half-Life. Physical Review Letters 103, 072502.

Russell, S. S., Srinivasan, G., Huss, G. R., Wasserburg, G. J., MacPherson, G. J., 1996. Evidence for Widespread ^{26}Al in the Solar Nebula and Constraints for Nebula Time Scales. Science 273, 757–762.

Ruzicka, A., Hutson, M., 2005. Portales Valley: Not just another ordinary chondrite. Meteoritics and Planetary Science 40, 261295.

Ruzicka, A., Snyder, G., Taylor, L., 1997. Vesta as the HED parent body: Implications for the size of a core and for large-scale differentiation. Meteoritics and Planetary Science 32, 825–840.

Safronov, V. S., 1954. On the growth of planets in the protoplanetary cloud. Astronomicekij Zhurnal 31, 499–510.

Sahijpal, S., Gupta, G., 2009. The plausible source(s) of ^{26}Al in the early solar system: A massive star or the X-wind irradiation scenario? Meteoritics and Planetary Science 44, 879–890.

Sahijpal, S., Soni, P., Gupta, G., 2007. Numerical simulations of the differentiation of accreting planetesimals with Al-26 and Fe-60 as the heat sources. Meteoritics and Planetary Science 42, 1529–1548.

Sanders, I. S., Hill, H. G. M., 1994. Multistage compound chondrules and molded chondrules in the Bovedy (L3) meteorite. Meteoritics 29, 527–528.

Sanders, I. S., Taylor, G. J., 2005. Implications of ^{26}Al in nebular dust: Formation of chondrules by disruption of molten planetesimals. In: Krot, A. N., Scott, E. R. D., Reipurth, B. (Eds.), Chondrites and the Protoplanetary Disk ASP Conference Series. Vol. 341. pp. 915–932.

Schersten, A., Elliott, T., Hawkesworth, C., Russell, S., Masarik, J., 2006. Hf-W evidence for rapid differentiation of iron meteorite parent bodies. Earth and Planetary Science Letters 241, 530–542.

Schiller, M., Baker, J. A., Bizzarro, M., 2010a. ^{26}Al-^{26}Mg dating asteroidal magmatism in the young Solar System. Geochimica et Cosmochimica Acta, in review.

Schiller, M., Handler, M. R., Baker, J., 2010b. High precision Mg isotopic systematics of bulk chondrites. Earth And Planetary Science Letters in review.

Schönbachler, M., Rehkamper, M., Halliday, A., Lee, D., Bourot-Denise, M., Zanda, B., Hattendorf, B., Gunther, D., 2002. Niobium-zirconium chronometry and early solar system development. Science 295, 1705.

Scott, E., Haack, H., Love, S., 2001. Formation of mesosiderites by fragmentation and reaccretion of a large differentiated asteroid. Meteoritics and Planetary Science 36, 869–882.

Scott, E., Krot, A., 2007. Chondrites and their components. In: Holland, H. D., Turekian, K. K. (Eds.), Treatise on Geochemistry. Pergamon, Oxford, pp. 1 – 72.

Scott, E. R. D., Krot, A. N., 2001. Oxygen isotopic compositions and origins of calcium-aluminum-rich inclusions and chondrules. Meteoritics and Planetary Science 36, 1307–1319.

Shearer, C., Fowler, G., Papike, J., 1997. Petrogenetic models for magmatism on the eucrite parent body: Evidence from orthopyroxene in diogenites. Meteoritics and Planetary Science 32, 877–890.

Shu, F., Shang, H., Lee, T., 1996. Toward an astrophysical theory of chondrites. Science 271, 1545–1552.

Shu, F. H., Shang, H., Glassgold, A. E., Lee, T., 1997. X-rays and fluctuating x-winds from protostars. Science 277, 1475–1479.

Shukolyukov, A., Lugmair, G., 2007. The Mn-Cr isotope systematics of bulk angrites. Lunar and Planetary Science Conference Abstracts 38, 1423.pdf.

Shukolyukov, A., Lugmair, G. W., Irving, A. J., 2009. Mn – Cr isotope systematics of angrite Northwest Africa 4801. Lunar and Planetary Science Conference Abstracts 40, 1381.pdf.

Smoliar, M., 1993. A survey of Rb-Sr systematics of eucrites. Meteoritics 28, 105–113.

Sonett, C. P., Colburn, D. S., Schwartz, K., 1968. Electrical heating of meteorite parent bodies and planets by dynamo induction from a pre-main dequence T Tauri "solar wind". Nature 219, 924–926.

Spivak-Birndorf, L., Wadhwa, M., Janney, P., 2009. ^{26}Al-^{26}Mg systematics in D'Orbigny and Sahara 99555 angrites: Implications for high-resolution chronology using extinct chronometers. Geochimica et Cosmochimica Acta 73, 5202–5211.

Spivak-Birndorf, L., Wadhwa, M., Janney, P. E., Foley, C. N., 2005. Al-Mg isotopic systematics in the angrite Sahara 99555 and the primitive achondrite Brachina. Lunar and Planetary Science Conference Abstracts 36, 2201.pdf.

Srinivasan, G., Goswami, J. N., Bhandari, N., 1999. Al-26 in eucrite Piplia Kalan: Plausible heat source and formation chronology. Science 284, 1348–1350.

Srinivasan, G., Sahijpal, S., Ulyanov, A., Goswami, J., 1996. Ion microprobe studies of Efremovka CAIs: II. Potassium isotope composition and ^{41}Ca

in the early solar system. Geochimica et Cosmochimica Acta 60, 1823–1835.

Srinivasan, G., Ulyanov, A., Goswami, J., 1994. ^{41}Ca in the early solar system. The Astrophysical Journal 431, L67–L70.

Stolper, E., 1977. Experimental petrology of eucritic meteorites. Geochimica et Cosmochimica Acta 41, 587–611.

Strelow, F. W. E., Victor, A. H., Vanzyl, C. R., Eloff, C., 1971. Distribution coefficients and cation exchange behavior of elements in hydrochloric acid-acetone. Analytical Chemistry 43, 870–876.

Sugiura, N., Miyazaki, A., Yanai, K., 2005. Widespread magmatic activities on the angrite parent body at 4562 Ma ago. Earth Planets Space 57, E13–E16.

Sugiura, N., Yamaguchi, A., 2007. Al-Mg and Mn-Cr Ages of Northwest Africa 011 Achondrite. Lunar and Planetary Science Conference Abstracts 38, 1431.pdf.

Tachibana, S., Huss, G., 2003. The initial abundance of ^{60}Fe in the solar system. The Astrophysical Journal 588, L41–L44.

Tachibana, S., Huss, G. R., Kita, N. T., Shimoda, G., Morishita, Y., 2006. ^{60}Fe in chondrites: Debris from a nearby supernova in the early Solar System? The Astrophysical Journal Letters 639, L87–L90.

Teng, F. Z., Wadhwa, M., Helz, R. T., 2007. Investigation of magnesium isotope fractionation during basalt differentiation: Implications for a chondritic composition of the terrestrial mantle. Earth and Planetary Science Letters 261, 84–92.

Tera, F., Carlson, R.W., 1999. Assessment of the Pb-Pb and U-Pb chronometry of the early solar system. Geochimica et Cosmochimica Acta 63, 1877–1889.

Tera, F., Carlson, R. W., Boctor, N. Z., 1997. Radiometric ages of basaltic achondrites and their relation to the early history of the Solar System. Geochimica et Cosmochimica Acta 61, 1713–1731.

Terasaki, H., Frost, D., Rubie, D., Langenhorst, F., 2008. Percolative core formation in planetesimals. Earth and Planetary Science Letters 273, 132–137.

Thrane, K., Bizzarro, M., Baker, J. A., 2006. Extremely brief formation interval for refractory inclusions and uniform distribution of ^{26}Al in the early solar system. The Astrophysical Journal 646, L159–L162.

Tipper, E. T., Louvat, P., Capmas, F., Galy, A., Gaillardet, J., 2008. Accuracy of stable Mg and Ca isotope data obtained by MC-ICP-MS using the standard addition method. Chemical Geology 257, 65–75.

Touboul, M., Kleine, T., Bourdon, B., 2008. Hf-W systematics of cumulate eucrites and the chronology of the eucrite parent body. Lunar and Planetary Science Conference Abstracts 39, 2336.pdf.

Treiman, A., 1997. The parent magmas of the cumulate eucrites: A mass balance approach. Meteoritics 32, 217–230.

Trinquier, A., Birck, J.-L., Allègre, C., Göpel, C., Ulfbeck, D., 2008. ^{53}Mn-^{53}Cr systematics of the early Solar System revisited. Geochimica et Cosmochimica Acta 72, 5146 – 5163.

Trinquier, A., Birck, J. L., Allègre, C. J., 2007. Widespread Cr-54 heterogeneity in the inner solar system. The Astrophysical Journal 655, 1179–1185.

Trinquier, A., Elliott, T., Ulfbeck, D., Coath, C., Krot, A. N., Bizzarro, M., 2009. Origin of nucleosynthetic isotope heterogeneity in the solar protoplanetary disk. Science 324, 374–376.

Urey, H. C., 1954. On the dissipation of gas and volatilized elements from protoplanets. The Astrophysical Journal 1, 147–173.

Urey, H. C., 1955. The cosmic abundances of potassium, uranium, and thorium and the heat balances of the Earth, the Moon, and Mars. Proceedings of the National Academy of Sciences of the United States of America 41, 127–144.

Villeneuve, J., Chaussidon, M., Libourel, G., 2009. Homogeneous distribution of ^{26}Al in the solar system from the Mg isotopic composition of chondrules. Science 325, 985–988.

Wadhwa, M., Amelin, Y., Bogdanovski, O., Shukolyukov, A., Lugmair, G., Janney, P., 2009a. Ancient relative and absolute ages for a basaltic meteorite: Implications for timescales of planetesimal accretion and differentiation. Geochimica et Cosmochimica Acta 73, 5189 – 5201.

Wadhwa, M., Foley, C. N., Janney, P., Beecher, N. A., 2003a. Magnesium isotopic composition of the Juvinas eucrite: Implications for concordance of the Al-Mg and Mn-Cr chronometers and timing of basaltic volcanism on asteroids. Lunar and Planetary Science Conference Abstracts 34, 2055.pdf.

Wadhwa, M., Janney, P. E., Krot, A. N., 2009b. Evidence of disturbance in the ^{26}Al-^{26}Mg systematics of the Efremovka E60 CAI: Implications for the high-resolution chronology of the early solar system. Lunar and Planetary Science Conference Abstracts 40, 2495.pdf.

Wadhwa, M., Shukolyukov, A., Davis, A. M., Lugmair, G. W., Mittlefehldt, D. W., 2003b. Differentiation history of the mesosiderite parent body: Constraints from trace elements and manganese-chromium isotope systematics in Vaca Muerta silicate clasts. Geochimica et Cosmochimica Acta 67, 5047–5069.

Walker, F. W., Parrington, J. R., Feiner, F., 1989. Nuclides and Isotopes, 14th Edition. General Electric Co.

Walkiewicz, T. A., Raman, S., Jurney, E. T., Starner, J. W., Lynn, J. E., 1992. Thermal-neutron capture by magnesium isotopes. Physical Review C 45, 1597–1608.

Warren, P. H., 1997. MgO-FeO mass balance constraints and a more detailed model for the relationship between eucrites and diogenites. Meteoritics and Planetary Science 32, 945–963.

Wasserburg, G., Busso, M., Gallino, R., Nollett, K., 2006. Short-lived nuclei in the early Solar System: Possible AGB sources. Nuclear Physics A 777, 5–69.

Wasserburg, G., Lee, T., Papanastassiou, D., 1977. Correlated O and Mg isotopic anomalies in Allende inclusions. II- Magnesium. Geophysical Research Letters 4, 299–302.

Wasson, J., Yurimoto, H., Russell, S., 2001. ^{16}O-rich melilite in CO3.0 chondrites: Possible formation of common, ^{16}O-poor melilite by aqueous alteration. Geochimica et Cosmochimica Acta 65, 4539–4549.

Wasson, J. T., Kallemeyn, G. W., 1988. Compositions of chondrites. Philosophical Transactions of the Royal Society of London. Series A. Physical Sciences and Engineering 325, 535–544.

Wasson, J. T., Rubin, A. E., 1985. Formation of mesosiderites by low-velocity impacts as a natural consequence of planet formation. Nature 318, 168–170.

Weidenschilling, S., 2000. Formation of planetesimals and accretion of the terrestrial planets. Space Science Reviews 92, 295–310.

Weisberg, M., Prinz, M., 1998. Sahara 97096: A highly primitive EH3 chondrite with layered sulfide-metal-rich chondrules. Lunar and Planetary Science Conference Abstracts, 1741.pdf.

Welten, K., Lindner, L., van der Borg, K., Loeken, T., Scherer, P., Schultz, L., 1997. Cosmic-ray exposure ages of diogenites and the recent collisional history of the HED parent body/bodies. Meteoritics and Planetary Science 32, 891–902.

Wetherill, G., Stewart, G., 1993. Formation of planetary embryos: Effects of fragmentation, low relative velocity, and independent variation of eccentricity and inclination. Icarus 106, 190–209.

Wiechert, U., Halliday, A. N., 2007. Non-chondritic magnesium and the origins of the inner terrestrial planets. Earth and Planetary Science Letters 256, 360–371.

Willbold, M., Jochum, K., 2005. Multi-element isotope dilution sector field ICP-MS: A precise technique for the analysis of geological materials and its application to geological reference materials. Geostandards Geoanalytical Research 29, 63–82.

Wood, J., 1998. Meteoritic evidence for the infall of large interstellar dust aggregates during the formation of the solar system. The Astrophysical Journal 503, 101–104.

Wood, J., 2000. The beginning: Swift and violent. Space Science Reviews 92, 97–112.

Woodhead, J., Hellstrom, J., Paton, C., Hergt, J., Greig, A., Maas, R., 2008. A guide to depth profiling and imaging applications of LA-ICM-PS. In: P., S. (Ed.), Laser Ablation ICPMS in the Earth Sciences: Current Practices and Outstanding Issues. Vol. 40 of Mineralogical Association of Canada Short Course series. pp. 135–145.

Yamaguchi, A., Clayton, R. N., Mayeda, T. K., Ebihara, M., Oura, Y., Miura, Y. N., Haramura, H., Misawa, K., Kojima, H., Nagao, K., 2002. A new source of basaltic meteorites inferred from Northwest Africa 011. Science 296, 334–336.

Yang, W., Teng, F.-Z., Zhang, H.-F., 2009. Chondritic magnesium isotopic composition of the terrestrial mantle: A case study of peridotite xenoliths from the North China craton. Earth and Planetary Science Letters 288, 475–482.

Young, E., Galy, A., 2004. The isotope geochemistry and cosmochemistry of magnesium. Reviews in Mineralogy and Geochemistry 55, 197–230.

Young, E., Tonui, E., Manning, C. E., Schauble, E., Macris, C., 2008. Intermineral Magnesium isotope fractionation in the mantle and implications for the supra-chondritic $^{25}Mg/^{24}Mg$ of Earth. Eos Transactions AGU 89.

Young, E. D., Simon, J. I., Galy, A., Russell, S. S., Tonui, E., Lovera, O., 2005. Supra-canonical $^{26}Al/^{27}Al$ and the residence time of CAIs in the solar protoplanetary disk. Science 308, 223–227.

Zinner, E., 2007. Presolar grains. In: Holland, H. D., Turekian, K. K. (Eds.), Treatise on Geochemistry. Pergamon, Oxford, pp. 1–33.

Zinner, E., Nittler, L. R., Hoppe, P., Gallino, R., Straniero, O., Alexander, C. M., 2005. Oxygen, magnesium and chromium isotopic ratios of presolar spinel grains. Geochimica et Cosmochimica Acta 69, 4149–4165.

Appendix A

^{26}Mg* magma ocean evolution model

The ^{26}Mg* magma ocean evolution model takes into account that the formation of an achondrite from a chondritic precursor is likely to occur over time. Several variables influence the final ^{26}Mg anomaly in a basalt such as: (1) the initial ^{26}Al/^{27}Al abundance of the precursor; (2) the relative ^{26}Al/^{27}Al abundance of the precursor to Earth, to which the anomaly is measured relative to; (3) the initial ^{27}Al/^{24}Mg ratio of the magma; (4) the final ^{27}Al/^{24}Mg ratio of the parent magma at time of achondrite formation; (5) the ^{27}Al/^{24}Mg ratio of the achondrite; (6) the time of initial magma formation; (7) the time of achondrite crystallisation; and (8) the rate of change of the ^{27}Al/^{24}Mg ratio in the magma during the magmatic evolution.

In the simplest scenario, the initial ^{26}Al/^{27}Al abundance of the achondrite precursor is the same as Earth and CAIs [(5.21×0.12) x 10^{-5}], the initial ^{27}Al/^{24}Mg ratio is the same as the final ^{27}Al/^{24}Mg ratio, which means that time of melting is equal to the time of crystallisation. In this specific scenario the ^{26}Mg* anomaly can be used to construct a model age in combination with the chondritic composition (^{27}Al/^{24}Mg = 0.1, ^{26}Mg* = 0) and yield an age that represents the true formation age. However, in any other case ^{26}Mg* will evolve in the magma the achondrite crystallised from.

Apart from a the scenario in which the parent body has an elevated initial ^{26}Al/^{27}Al abundance relative to Earth, positive ^{26}Mg* anomalies can only be generated by increasing the ^{27}Al/^{24}Mg ratio of the precursor material or the evolving magma. Our model does not account for elevated ^{27}Al/^{24}Mg ratios of the precursor body as there is no evidence for highly elevated ^{26}Mg* anomalies in chondrites (see Chapter 4).

If the initial ^{26}Al/^{27}Al abundance is homogeneous, the initial and change of ^{27}Al/^{24}Mg ratio of the achondrite parent melt are the most important variables that influence the ^{26}Mg* anomaly before achondrite crystallisation where the remaining ^{26}Al will decay in situ adding to the final ^{26}Mg* anomaly. In a first instance, in order to simplify the model evolution of ^{26}Mg* in the parent magma we assume that the initial melt has a chondritic ^{27}Al/^{24}Mg ratio of 0.1 and the achondrite represents the final melt composition and hence the final ^{27}Al/^{24}Mg ratio.

In the example of Juvinas (Chapter 3), we assume a canonical ^{26}Al/^{27}Al abundance, starting from an initially chondritic ratio (0.1) and finishing with the ^{27}Al/^{24}Mg ratio as recorded in the basaltic meteorite (Juvinas = 1.7). The change of the ^{27}Al/^{24}Mg ratio occurs in 20 steps that linearly increase ^{27}Al/^{24}Mg ratio from 0.1 to 1.7 and for each step the amount of decayed 26Al and the respective increase of ^{26}* based on the ^{27}Al/^{24}Mg for the respective interval is calculated. The resulting ^{26}Mg* anomaly in this scenario is dependent on (A) the onset of the crystallisation in the fully molten body and hence the onset of increase in the ^{27}Al/^{24}Mg ratio. This onset with respect to CAIs controls the total amount of ^{26}Al that is still remaining and can contribute to an anomaly that is greater than 0, i.e., if the onset of differentiation is choosen to be 0 the initial ^{26}Al/^{27}Al is [(5.21 $\times$ 0.12) x 10^{-5}], if the onset is chosen to be indefinitely long the initial ^{26}Al/^{27}Al is 0 and ^{26}Al/^{27}Al decays exponentially in-between those extremes. The second variable (B) is the time the magma ocean evolves from the onset to the crystallisation of in this case Juvinas.

The ^{26}Mg* anomaly measured in Juvinas is 0.0303‰ and using the set

out conditions, there are infinite possibilities of combinations of onset of differentiation and time span of magma evolution as schematically shown in Fig. 3.7 that can produce such an anomaly., As a general rule, the earlier the onset of differentiation is chosen the longer the evolution of the magmatic system needs to be to produce the anomaly. This is independent of the rate of change of the $^{27}Al/^{24}Mg$ ratio in the magma, which can not be determined based on a single anomaly. An estimate of relative onset and time frame for the magma evolution can be made by using other constraints. For example, the combination of angrite isochron ages and bulk rock model ages allows to constrain the onset of differentiation based on the crystallisation age of these rocks. This is also exemplarily shown in Fig. 3.7 using the youngest allowable $^{53}Mn/^{53}Cr$ age to constrain the crystallisation age. In these cases the whole rock model age provides information about the onset of magmatic differentiation of the parent magma.

In the special case of the diogenites (Chapter 5), where the change of $^{26}Mg^*$ anomalies over time and information of the respective $^{27}Al/^{24}Mg$ ratios in the parent magma can be reconstructed, the rate of change of the $^{27}Al/^{24}Mg$ ratio in the magma can be evaluated. In this specific scenario the initial $^{26}Al/^{27}Al$ abundance is set to fit the oldest (most negative) $^{26}Mg^*$ anomalies and the time frame of magma evolution is adjusted to produce the youngest (most positive) $^{26}Mg^*$ anomalies. Then two different rates of change were used from the initial $^{27}Al/^{24}Mg$ ratio to the final $^{27}Al/^{24}Mg$ ratio: a linear change [($^{27}Al/^{24}Mg_{initial}$ + a $\times$ $^{27}Al/^{24}Mg_{final}$) - a $\times$ $^{27}Al/^{24}Mg_{final}$] and a double exponential approach [$^{27}Al/^{24}Mg_{initial}$ + b $\times$ $\exp^{c\times a}$], where a is a number between 0 and 1 and b and c are adequately chosen to result in $^{27}Al/^{24}Mg_{final}$. Those two approaches were chosen as the linear rate of change increases the $^{27}Al/^{24}Mg$ in the paren melt constant over time, while the double exponential rate of change extremely delays a change of $^{27}Al/^{24}Mg$ in the parent magma. Based on a polynomial fit (order = 3) of $^{26}Mg^*$ anomaly versus $^{27}Al/^{24}Mg$ ratio the predicted $^{27}Al/^{24}Mg$ ratios that would produce the measured $^{26}Mg^*$ anomaly in all

diogenites samples between the oldest and youngest diogenites samples were calculated. If the correct ^{27}Al/^{24}Mg rate of change in the diogenite producing magma has been chosen, the predicted ^{27}Al/^{24}Mg ratio should form a 1:1 correlation with the reconstructed ^{27}Al/^{24}Mg ratio (Fig. 5.7). In the case of diogenites there is a good correlation of the predicted and the reconstructed ^{27}Al/^{24}Mg ratio for a linear rate of change, while the double exponential change fails to correlate with the data. This suggests that at least in the case of diogenites a linear rate of change of the ^{27}Al/^{24}Mg ratio in the magma is a satisfactory assumption.

Appendix B

Electronic appendix

All raw data that has been used in chapters 3-5 can be found on the attached CD. For chapters 3 and 4 Mg isotope data can be found as Microsoft Excel files in their respective folders in the Appendix folder. Because all Mg isotope as well as laser ablation data for chapter 5 has been calculated off line using Iolite (http://iolite.earthsci.unimelb.edu.au/), these data are saved in form of Iolite experiments that can be used by installing the included trial version of Igor Pro and the free version of Iolite. Electron microprobe for diogenites and the $^{27}Al/^{24}Mg$ data for all samples with exception of the samples supplied by NASA are provided in Microsoft Excel 97-2000 format. $^{27}Al/^{24}Mg$ data for NASA samples are supplied as Iolite experiment. Detailed instructions to install Iolite can be found in the Iolite manual (http://iolite.earthsci.unimelb.edu.au/wiki/doku.php?id=manual_page). Both, Iolite and Igor Pro (for Pc and Mac), can also be found in the Appendix folder.